Instabilities in mechanics

Romain Lagrange

Institut Polytechnique de Paris

HABILITATION À DIRIGER DES RECHERCHES

Analyse de quelques problèmes d'instabilité en mécanique

par **Romain LAGRANGE**

le 12 décembre 2023

Commission d'examen :

M. Jean-Marc CHOMAZ	*Président du jury*
Mme Lydia BOUROUIBA	*Rapporteur*
M. Bruno COCHELIN	*Rapporteur*
M. Stéphane ETIENNE	*Rapporteur*
M. Xavier AMANDOLESE	*Examinateur*
Mme Marianna BRAZA	*Examinatrice*
M. Arnaud LAZARUS	*Examinateur*

REMERCIEMENTS

Mes premiers remerciements sont adressés à Patrick Le Tallec, référent en mécanique pour l'Habilitation à Diriger des Recherches (HDR) à l'Institut Polytechnique de Paris, pour ses conseils avisés et son accompagnement précieux tout au long du processus menant à la soutenance de l'HDR.

Je tiens ensuite à exprimer ma profonde gratitude envers les membres du jury de soutenance, en particulier les rapporteurs internationaux de ce travail, Lydia Bourouiba et Stéphane Etienne. Leur engagement et leur expertise ont été cruciaux, malgré leur découverte du processus spécifique de ce diplôme français. Parmi les rapporteurs, je tiens également à remercier chaleureusement Bruno Cochelin, dont l'influence dans ma formation à la mécanique des milieux continus, il y a maintenant une vingtaine d'années à l'École Centrale de Marseille, reste inestimable. Les rapports détaillés et circonstanciés témoignent de l'efficacité et du dévouement de Lydia Bourouiba, Stéphane Etienne et Bruno Cochelin à évaluer mon travail.

Mes remerciements s'étendent ensuite à Xavier Amandolèse, Arnaud Lazarus et Marianna Braza pour avoir accepté d'examiner mon travail d'HDR. Je tiens également à exprimer ma gratitude envers Jean-Marc Chomaz pour avoir accepté de présider le jury de soutenance. Présenter mes travaux a été un réel plaisir, et au-delà des enjeux liés au diplôme, j'ai particulièrement apprécié la bienveillance des membres du jury ainsi que la fluidité de nos échanges.

Ce travail d'HDR n'aurait pas été possible sans les interactions que j'ai eues avec de nombreux chercheurs rencontrés lors de mon parcours professionnel, notamment à l'IRPHE, à l'IFPEN, au MIT et au CEA. Je leur adresse donc un remerciement général, tout en soulignant le rôle essentiel de Maria-Adela Puscas dans la genèse de cette HDR. Je souhaite également remercier Natalie Lemaintec, secrétaire ultra efficace du laboratoire DYN, dont le soutien précieux a été déterminant pour l'organisation de la soutenance d'HDR.

"Last but not least", je remercie mes parents. Sans leur soutien indéfectible et leurs efforts constants pour me fournir les meilleures conditions de travail, rien (École d'Ingénieur, doctorat, HDR...) n'aurait été possible.

Table des matières

1. DOSSIER PERSONNEL

1.1 Research Interests

Fluid-Structure Interactions, Rotating Flows, Elasticity, Mechanical Instabilities, Nonlinear Dynamics and Chaos

1.2 Education

2009	**Ph.D.**, Fluid Mechanics, *Aix-Marseille Université*
2006	**M.Sc.**, Fluid Mechanics, *Aix-Marseille Université*. Magna Cum Laude
2006	**M.Eng.**, Solid Mechanics, *Centrale Marseille*, School of Engineering

1.3 Professional Experience

1.3.1 Teaching

2022-...	**Lecturer in Mechanics**, *E.N.P.C.*, Paris, France
Course	Introduction to continuum mechanics (Fall 2022)
2015-2018	**Lecturer in Mathematics and Mechanics**, *U.P.M.C.*, Paris, France
Courses	Instabilities (Fall 2018, 2017, 2016, 2015), Mathematics for engineers (Fall 2017, 2016), Numerical analysis (Spring 2018)
Recitations	Continuum Mechanics (Fall 2017), Mathematics for engineers (Fall 2017, 2016), Numerical analysis (Spring 2018)
2017-2018	**Lecturer in Mathematics**, *Université Paris-Saclay*, Orsay, France
Recitations	Mathematical tools (Fall 2017)
2017-2018	**Lecturer in Mathematics**, *C.N.A.M.*, Versailles, France
Courses	Linear algebra and geometry (Fall 2017)
2012-2015	**Instructor in Mathematics**, *M.I.T.*, Cambridge, U.S.A
Courses	Nonlinear Dynamics and Turbulence (Spring 2015, with Prof. L. Bourouiba), Nonlinear Dynamics: Chaos (Fall 2014, Fall 2013), Tensor Calculus (Jan. 2014)

Recitations	Differential Equations (Spring 2015, Spring 2014), Multivariable Calculus (Spring 2013, Fall 2012)
2007-2009	**Lecturer in Mechanics**, *Université Paul Cézanne*, Marseille, France
Hands-on works	Solid and Fluid Mechanics for Undergraduates (102 hours in two years)

1.3.2 Research

2015-	**Research Engineer**, *C.E.A.*, Gif-sur-Yvette, France
In progress	*Vibrations of tube bundles subject to two-phase cross-flows / Fluid-structure interactions problems*
	Main collaborators: Framatome/E.D.F, Y. Fraigneau (L.I.M.S.I.), C. Josserand (LadHyX)
2012-2015	**Instructor**, *M.I.T.*, Cambridge, U.S.A.
36 months	*Wrinkling on curved surface*
Details	Rationalized the effect of curvature on the wrinkling problem: stability analysis, Swift-Hohenberg model for pattern selection, crystallography properties of wrinkles.
	Collaborators: P. M. Reis, J. Dunkel, D. Terwagne, M. Brojan, F. L. Jiménez, N. Stoop
2010-2011	**Post-doctoral Researcher**, *I.F.P.E.N.*, Solaize, France
15 months	*Buckling of thin structures*
Details	Developed mathematical models and closed-form solutions for the buckling of slender structures used in the Offshore industry
	Advisors: D. Averbuch, M. Martinez
2006-2009	**Ph.D. Research Scholar**, *C.N.R.S., I.R.P.H.E.*, Marseille, France
36 months	*Dynamics inside a precessing fluid cylinder: theory and PIV experiments*
Details	Analyzed the Navier-Stokes equation in rotating frame: fixed points, stability, nature of bifurcations, model for transition to turbulence. Performed PIV measurements
	Advisors: P. Meunier, C. Eloy, F. Nadal
2006	**M.Sc. Student**, *C.N.R.S., I.R.P.H.E.*, Marseille, France
6 months	*Aeroelastic instability of a flag in uniform flow*
Details	Stability analysis and wind tunnel experiments
	Advisors: C. Eloy, L. Schouveiler

2005-2006 **M.Eng. Student**, *Centrale Marseille*, Marseille, France

90 hours *Heat transfer through a damaged material*

Details Set-up heat transfer models and performed Abaqus simulations

Advisors: S. Bourgeois, T. Desoyer

1.4 Students guidance

1.4.1 Ph.D. Research Scholars

2023-2026 Recruitment in progress, funding secured

36 months Modeling and numerical simulation of the aeroelasticity of a solar panel mounted on flexible cables

Supervised with B. Prabel and M. A. Puscas (C.E.A.)

Details The objective of this thesis is to conduct theoretical and numerical studies to determine the vibration characteristics of photovoltaic panels mounted on flexible cables. The results of these studies should ultimately allow optimal sizing of the photovoltaic panels and the system of attachment to flexible cables.

2021-2024 Maud Kocher, *I.P.P.*, Paris, France

36 months Vibrations of the primary circuit of a nuclear power plant

Supervised with P. Moussou (E.D.F.) and D. Panunzio (C.E.A.)

Details The objective of this thesis is to build, with the usual tools (CFD simulations, tests), an acoustic-mechanical model for the reactor vessel and its internals. The model shall describe the transmission of acoustic waves between the inlets/outlets of the vessel, taking into account the turbulence in the annular space and the oscillations of the core envelope.

2020-2023 Clément Bazin, *I.P.P.*, Paris, France

36 months Numerical and experimental studies of two-phase flows in interaction with a tube bundle

Supervised with C. Josserand (LadHyX) and M. G. Rodio (C.E.A.)

Details The objective of this thesis is to numerically simulate the fluid flow regimes and fluid-structure interactions in square tube bundles subject to two-phase cross-flows. The numerical results shall be corroborated experimentally and shall feed theoretical works on the modeling of random excitation forces.

1.4.2 M.Sc./M.Eng. Students

2022	Lazar Lorand, M.Eng. student at *E.S.T.A.C.A.*, Paris, France
4 months	Theoretical study of the interaction between a flexible cylindrical beam and a fluid at rest
2021	Erwan Beaugendre, M.Eng. student at *Polytech*, Orléans, France
6 months	Numerical study of the interaction of a transverse flow and a tube bundle
2021	Erika Diaferia, M.Sc. student at *E.N.S.A.M.*, Paris, France
6 months	Numerical simulation of the interaction between an axial flow and a slender cylinder
2020	Alexandre Epalle, M.Eng. student at *I.N.S.A.*, Lyon, France
6 months	Study of numerical dry friction modelling (modeling) in structural dynamics. Application to steam generator tubes in nuclear power plants.
2020	Matheus Melo Monteverde, M.Eng. student at *E.N.S.T.A.*, Paris, France
3 months	Interaction of two cylinders immersed in a viscous fluid
2020	Daniel Zegarra, M.Eng. student at *Sup. Galilée*, Paris, France
3 months	Numerical simulation with TrioCFD of the hydrodynamic interaction of two cylinders subjected to small oscillations
2020	Domenico Panunzio, M.Sc. student at *E.N.S.A.M.*, Paris, France
6 months	Numerical simulation of a single-phase flow around a vibrating cylindrical tube
2019	Salvatore Ambriola, M.Sc. student at *E.N.S.A.M.*, Paris, France
6 months	Numerical simulation of the turbulent force acting on a cylinder subjected to a two-phase flow
2013-2014	Stanislav Y. Tsitkov, undergraduate student (UROP) at *M.I.T.*, Cambridge, U.S.A.
12 months	Transition to chaos in a precessing fluid cylinder
2012	Alice Nasto, graduate student at *M.I.T.*, Cambridge, U.S.A.
2 months	Fluid-Structure Interactions: from Fluttering Flags to Flapping Wings

1.5 Ongoing professional activities

Examiner	Since 2020. CPGE maths program, Ecole Polytechnique Féminine, France
Examiner	Since 2017. Bachelor program, Ecole Polytechnique, France
Grader	2019-2020. Centrale Supélec national exam of mathematics, *French Grandes Ecoles*, France
Peer Review	Journal of Fluids and Structures, Physical Review Letters, Physics of Fluids, Chaos, Physical Review Fluids, European Journal of Mechanics - B/Fluids, Part C: Journal of Mechanical Engineering Science, Journal of Pressure Vessel Technology

1.6 Institutional/Administrative responsibilities

2023-2026	Responsible for the 'Fiche d'action' titled 'FLOW'. This intern document, produced annually, defines the orientations of specific research works conducted at C.E.A., anticipating human, material needs, and associated funding
2020-2023	Responsible for the 'Fiche d'action' titled 'Thèse diphasique', related to the Ph.D. work of C. Bazin
Since 2020	Responsible for the 'Fiche d'action' titled 'F.F.A.T.T.', related to the theoretical work on vibrations of tube bundles, conducted for the institute C.E.A./Framatome
2022	Member of the organizing committee, Flow-Induced Vibration conference, Paris-Saclay, 2022
2018-2020	Responsible for the 'Fiche d'action' titled 'F.S.A./F.F.E.', related to the theoretical work on vibrations of tube bundles, conducted for the institute C.E.A./Framatome/E.D.F.
2020	Representative of the Department of Systems and Structures Modeling (french acronym: D.M.2S.). Presentation of research activities on vibrations of tube bundles, for the evaluation of D.M.2S. by the scientific council of the Energy Division at Saclay (french acronym: D.E.S.)
2019	Representative of D.M.2S. for its evaluation by the H.C.E.R.E.S. committee. Interview and discussion with the committee
2019	Representative of the Laboratory of Dynamics at the general assembly of the Mechanical and Thermal Studies Service (french acronym: S.E.M.T.). Presentation of research activities on vibrations of tube bundles

2016-2019 Member of the Unit Council (french acronym: C.U.) of S.E.M.T. This advisory council aims to regulate the life of the research unit

1.7 Projects

Partner GO-VIKING European project. Modeling and simulation of vibrations in steam generators and fuel assemblies

1.8 Awards

2017 Nominated Specialist in Mechanics and Dynamics, *C.E.A.*

2009 Elected Main Presentation of the Vortex Session, *Congrès Français de Mécanique*

2008 Best Orator Award, *C.E.A./C.E.S.T.A.*

2006 Best Poster Award, *C.E.A./C.E.S.T.A.*

1.9 Languages

French Native

English Fluent, B2 level, T.O.E.I.C.

Spanish Fluent, B2 level, D.E.L.E.

1.10 Computer skills

Programming Matlab, Mathematica, Maple, basic knowledge in C/C++ language and Abaqus

Publishing Latex, Microsoft Office

1.11 Publications

Articles available here

Journal Publications

C. Bazin, M. G. Rodio, R. Lagrange, C. Josserand. Turbulence model effects on the two-phase all-regimes models prediction. ***Submitted to Int. J. Multiph. Flow***, 2023

R. Lagrange, D. Panunzio, P. Piteau, X. Delaune, J. Antunes. A new criterion for the instability threshold of a square tube bundle subject to an air–water cross-flow. ***J. Fluids Struct.***, vol. 122, 103980, 2023

P. Piteau, D. Panunzio, R. Lagrange, X. Delaune, J. Antunes. Experimental investigation of in-flow fluidelastic instability for rotated triangular tube bundles subjected to single-phase and two-phase transverse flows. ***Submitted to J. Fluids Struct., special issue***, 2023

M. A. Puscas, R. Lagrange. Interaction of two cylinders immersed in a viscous fluid. On the effect of moderate Keulegan-Carpenter numbers on the fluid forces. ***Eur. J. Mech. B Fluids***, vol. 101, 106-117, 2023

R. Lagrange, L. Lorand, M. A. Puscas. Forced beam vibrations of coaxial cylinders separated by a fluid gap of arbitrary size. Inviscid theory and numerical assessment of the fluid forces. ***J. Fluids Struct.***, vol. 120, 103899, 2023

R. Lagrange, M. A. Puscas. Viscous theory for the vibrations of coaxial cylinders. Analytical formulas for the fluid forces and the modal added coefficients. ***J. Appl. Mech.***, JAM-22-1411, 2023

R. Lagrange, M. A. Puscas, P. Piteau, X. Delaune, J. Antunes. Modal added-mass matrix of an elongated flexible cylinder immersed in a narrow annular fluid, considering various boundary conditions. New theoretical results and numerical validation. ***J. Fluids Struct.***, vol. 114, 103754, 2022

D. Panunzio, M. A. Puscas, R. Lagrange. FSI - Vibrations of immersed cylinders. Simulations with the engineering open source code TrioCFD. Test cases and experimental comparisons. ***C. R. Mecanique***, vol. 350, 451-476, 2022

R. Lagrange, M. A. Puscas. Hydrodynamic interaction between two flexible finite length coaxial cylinders: new theoretical formulation and numerical validation. ***J. Appl. Mech.***, 89(8): 081006, 2022

R. Lagrange, Y. Fraigneau. New estimations of the added mass and damping of two cylinders vibrating in a viscous fluid, from theoretical and numerical approaches. ***J. Fluids Struct.***, vol. 92, 102818, 2020

R. Lagrange, X. Delaune, P. Piteau, L. Borsoi, J. Antunes. A new analytical approach for modeling the added mass and hydrodynamic interaction of two cylinders subjected to large motions in a potential stagnant fluid. ***J. Fluids Struct.***, vol. 77, 102-114, 2018

F.L. Jiménez, N. Stoop, R. Lagrange, J. Dunkel, P. M. Reis. Curvature-controlled defect localization in elastic surface crystals. ***Phys. Rev. Lett.***, vol. 116, 104301, 2016

R. Lagrange, F.L. Jiménez, D. Terwagne, M. Brojan, P. M. Reis. From wrinkling to global buckling of a ring on a curved substrate. ***J. Mech. Phys. Solids***, vol. 89, 77-95, 2016

R. Lagrange, P. Meunier, C. Eloy. Triadic instability of a non-resonant precessing fluid cylinder. ***C. R. Mecanique***, vol. 344, 418-433, 2016

N. Stoop, R. Lagrange, D. Terwagne, P. M. Reis, J. Dunkel. Curvature-induced symmetry breaking of elastic surface patterns. ***Nature Mater.***, vol. 14, 337-342, 2015

M. Brojan, D. Terwagne, R. Lagrange, P.M. Reis. Wrinkling crystallography on spherical surfaces. ***Proc. Natl. Acad. Sci. U.S.A.***, vol. 112(1), 14-19, 2015

R. Lagrange. Limit point buckling of a finite beam on a nonlinear foundation. ***Theor. Appl. Mech. Lett.***, vol. 4, 031002, 2014

R. Lagrange. Compression-induced stiffness in the buckling of a one fiber composite. ***Theor. Appl. Mech. Lett.***, vol. 3, 061001, 2013

R. Lagrange, D. Averbuch. Solution methods for the growth of a repeating imperfection in the line of a strut on a nonlinear foundation. ***Int. J. Mech. Sci.***, vol. 63(1), 48-58, 2012

R. Lagrange, P. Meunier, C. Eloy, F. Nadal. Precessional instability of a fluid cylinder. ***J. Fluid Mech.***, vol. 666, 104-145, 2011

J.P. Lambelin, F. Nadal, R. Lagrange, A. Sarthou. Non-resonant viscous theory for the stability of a fluid-filled gyroscope. ***J. Fluid Mech.***, vol. 639, 167-194, 2009

R. Lagrange, P. Meunier, C. Eloy, F. Nadal. Dynamics of a fluid inside a precessing cylinder. ***Mec. Ind.***, EDP Sciences, vol. 10, 187-194, 2009

R. Lagrange, C. Eloy, F. Nadal, P. Meunier. Instability of a fluid inside a precessing cylinder. ***Phys. Fluids***, vol. 20, 081701, 2008

P. Meunier, C. Eloy, R. Lagrange, F. Nadal. A rotating fluid subject to weak precession. ***J. Fluid Mech.***, vol. 599, 405-440, 2008

C. Eloy, R. Lagrange, C. Souillez, L. Schouveiler. Aeroelastic instability of cantilevered flexible plates in uniform flow. ***J. Fluid Mech.***, vol. 611, 97-106, 2008

Conference publications

M. Kocher, S. Benhamadouche, P. Moussou, A. Joly, D. Panunzio, R. Lagrange. Fluid structure interaction in the annular gap of a nuclear reactor vessel: design of a test rig. *ERCOFTAC 2023 Symposium on Multiphysics critical flow dynamics involving moving/deformable structures with design applications*, Toulouse, 2023

J. Antunes, P. Piteau, X. Delaune, R. Lagrange. Spectral extrapolation of frequency-dependent fluidelastic coupling coefficients from causality enforcing. *Proceedings of the 26th International Conference on Structural Mechanics in Reactor Technology*, Berlin, 2022

R. Lagrange, D. Panunzio, P. Piteau, X. Delaune, J. Antunes. A new criterion for the instability threshold of a square tube bundle subject to an air-water cross-flow. *Proceedings of the Flow Induced Vibration conference*, Paris-Saclay, 2022

D. Panunzio, R. Lagrange, P. Piteau, X. Delaune, J. Antunes. Experimental investigation of out-of-flow fluidelastic instability for rotated triangular bundles subjected to single-phase and two-phase transverse flow. *Proceedings of the Flow Induced Vibration conference*, Paris-Saclay, 2022

J. Antunes, P. Piteau, X. Delaune, D. Panunzio, R. Lagrange. Experimental investigation of in-flow fluidelastic instability for rotated triangular bundles subjected to single-phase and two-phase transverse flow. *Proceedings of the Flow Induced Vibration conference*, Paris-Saclay, 2022

P. Moussou, M. Kocher, D. Panunzio, R. Lagrange, A. Joly. Fluid structure interaction in a pressure vessel: a multipole approach for acoustic analysis. *Proceedings of the Flow Induced Vibration conference*, Paris-Saclay, 2022

M. Kocher, P. Moussou, D. Panunzio, R. Lagrange, A. Joly. Fluid structure interaction in a pressure vessel: turbulent forcing. *Proceedings of the Flow Induced Vibration conference*, Paris-Saclay, 2022

J. Antunes, P. Piteau, X. Delaune, R. Lagrange. Spectral extrapolation of frequency-dependent fluidelastic coupling coefficients from causality enforcing. *Proceedings of the SMIRT-26 conference*, Berlin-Potsdam, 2022

R. Lagrange, P. Piteau, X. Delaune, J. Antunes. Fluid-elastic coefficients in single phase cross flow: dimensional analysis, direct and indirect experimental methods. *Proceedings of the ASME PVP conference*, San-Antonio, 93984, 2019

R. Lagrange, P. Meunier, C. Eloy, F. Nadal. Instability of a fluid inside a precessing cylinder. 12e Rencontre du non-linéaire (Eds. C. Josserand, M. Lefranc, C. Letellier), *Non-Linéaire Publications*, Paris, 103-108, 2009

R. Lagrange, P. Meunier, C. Eloy, F. Nadal. Instability of a fluid inside a precessing cylinder. 11e Rencontre du non-linéaire, *Non-Linéaire Publications*, Paris, 103-108, 2008

Technical notes

R. Lagrange. Analyse dimensionnelle des forces de couplage. Ecoulement diphasique eau-air, portance, pas carré. *NT/2021-67624/A, C.E.A.*, 2021

R. Lagrange, D. Panunzio. Bilan sur l'adimensionnement des forces fluides diphasiques en pas carré. *NT/2021-69276/A, C.E.A.*, 2021

R. Lagrange. Analyse dimensionnelle des forces aléatoires en portance, en écoulement diphasique eau-air et en faisceau à pas carré. *NT/2020-66059/A, C.E.A.*, 2020

R. Lagrange, P. Piteau, M. Bellanger. Instabilité fluide-élastique en faisceau à pas carré. Proposition d'une nouvelle loi pour le seuil de stabilité en écoulement diphasique. *NT/2019-65374/A, C.E.A.*, 2019

R. Lagrange. Analyse dimensionnelle des forces de couplage en écoulement diphasique eau-air. *NT/2018-63940/A, C.E.A.*, 2018

R. Lagrange. Potential theory for the fluid-elastic instability: application to the two cylinders problem. *NT/2018-62987/A, C.E.A.*, 2018

R. Lagrange. Analyse comparative du terme d'amortissement de la force de couplage mesuré par les méthodes directes et indirectes, en monophasique. *NT/2018-62652/A, C.E.A.*, 2018

R. Lagrange. Dimensional analysis of the fluid-elastic coefficients in monophasic fluid flow. *Technical note, NT/2017-62195/A, C.E.A.*, 2017

R. Lagrange. Potential-flow theory for the added mass and fluid force of two circular cylinders. *NT/16-018/A, C.E.A.*, 2016

R. Lagrange. Flambage d'armure : modèles analytiques. *Technical note, I.F.P.E.N.*, 70 pages, 2011

Course handout

R. Lagrange. Introduction to continuum mechanics. *E.N.P.C.*, 2022. Lecture notes available here

Book chapter

R. Lagrange, P. Piteau, X. Delaune, D. Panunzio, B. Prabel, M. A. Puscas, M. G. Rodio, G. Ricciardi, V. Faucher. *Chapitre 2, section 2. Vibrations sous écoulement. Monographie CEA, Mécanique des structures*, Publication in progress, 2023

1.12 Communications

2023

M. A. Puscas, R. Lagrange. Vibrations de deux cylindres flexibles coaxiaux dans un fluide visqueux. Formules analytiques pour les forces fluides et les coefficients modaux ajoutés. *SMAI 2023*, Le Gosier, Guadeloupe, France

M. A. Puscas, R. Lagrange. Vibrations of two coaxial flexible cylinders in a viscous fluid. *22nd Computational Fluids Conference*, Cannes, France

M. Kocher, P. Moussou, A. Joly, S. Benhamadouche, P. Panunzio, R. Lagrange. Fluid-structure interaction in the annular gap of a nuclear reactor vessel. *ERCOFTAC 2023 Symposium on Multiphysics critical flow dynamics involving moving/deformable structures with design applications*, Toulouse, France

C. Bazin, M. G. Rodio, R. Lagrange, C. Josserand. On the simulation of two-phase cross flow in a rod bundle guided by experimental forces spectra. *11th International Conference on Multiphase Flow*, Kobe, Japan

2022

C. Bazin, M. G. Rodio, R. Lagrange, C. Josserand. On the effect of turbulence models in the numerical simulation of bubbly flows in rectangular cross channels. *14 th European Fluid Mechanics Conference (EFMC14)*, Athens, Greece

R. Lagrange, D. Panunzio, P. Piteau, X. Delaune, J. Antunes. A new criterion for the instability threshold of a square tube bundle subject to an air-water cross-flow. *Flow Induced Vibration conference*, Paris-Saclay, France

D. Panunzio, R. Lagrange, P. Piteau, X. Delaune, J. Antunes. Experimental investigation of out-of-flow fluidelastic instability for rotated triangular bundles subjected to single-phase and two-phase transverse flow. *Flow Induced Vibration conference*, Paris-Saclay, 2022

J. Antunes, P. Piteau, X. Delaune, D. Panunzio, R. Lagrange. Experimental investigation of in-flow fluidelastic instability for rotated triangular bundles subjected to single-phase and two-phase transverse flow. *Flow Induced Vibration conference*, Paris-Saclay, 2022

P. Moussou, M. Kocher, D. Panunzio, R. Lagrange, A. Joly. Fluid structure interaction in a pressure vessel: a multipole approach for acoustic analysis. *Flow Induced Vibration conference*, Paris-Saclay, 2022

M. Kocher, P. Moussou, D. Panunzio, R. Lagrange, A. Joly. Fluid structure interaction in a pressure vessel: turbulent forcing. *Flow Induced Vibration conference*, Paris-Saclay, 2022

J. Antunes, P. Piteau, X. Delaune, R. Lagrange. Spectral extrapolation of frequency-dependent fluidelastic coupling coefficients from causality enforcing. *SMIRT-26 conference*, Berlin-Potsdam, 2022

M. A. Puscas, R. Lagrange. Fluid-structure interaction problem of a flexible cylinder in a narrow coaxial cylindrical duct. *WCCM-APCOM conference*, Yokohama, Japan

M. A. Puscas, R. Lagrange. Fluid-structure interaction problem of two coaxial vibrating flexible cylinders separated by a thin layer of fluid. *8th European Congress on Computational Methods in Applied Sciences and Engineering*, Oslo, Norway

M. A. Puscas, R. Lagrange. Scaling law for large motions of two cylinders vibrating in a viscous Fluid. *International Conference on Wave Mechanics and Vibrations (10th WMVC)*, Lisbon, Portugal

2021 M. A. Puscas, R. Lagrange. Numerical simulation of the hydrodynamic interaction of two cylinders vibrating in a viscous fluid. *Pan American Congress on Computational Mechanics 2021*, Rio, Brazil

2019 R. Lagrange, P. Piteau, X. Delaune, J. Antunes. Fluid-elastic coefficients in single phase cross flow: dimensional analysis, direct and indirect experimental methods. *P.V.P. Meeting*, San Antonio, U.S.A.

P. Piteau, X. Delaune, J. Antunes, L. Borsoi, R. Lagrange. Experiments on the flow-induced streamwise dynamics of a rotated triangular tube bundle subjected to single-phase and two-phase transverse flows. *P.V.P. Meeting*, San Antonio, U.S.A.

2017 R. Lagrange. Quelques exemples d'instabilité en mécanique. *L.I.M.S.I. Seminar*, Orsay, France

2015 R. Lagrange, P. Meunier, C. Eloy, F. Nadal. Dynamique d'un fluide dans un cylindre en précession. *I.M.F.T. Seminar*, Toulouse, France

N. Stoop, R. Lagrange, D. Terwagne, P. M. Reis, J. Dunkel. Curvature-induced symmetry breaking selects elastic wrinkling patterns. *Annual Meeting of the A.P.S. March Meeting*, San Antonio, U.S.A.

R. Lagrange, P. Meunier, C. Eloy, F. Nadal. Dynamique d'un fluide dans un cylindre en précession. *L.M.F.A. Seminar*, Lyon, France

R. Lagrange, P. Meunier, C. Eloy, F. Nadal. Dynamique d'un fluide dans un cylindre en précession. *Experimental Physics and Modelling Seminar*, E.N.S. Lyon, France

2014 F. L. Jimenez, R. Lagrange, P. M. Reis. Buckling of a thin film on a curved soft substrate. *ASME 2014 International Mechanical Engineering Congress and Exposition*, Montreal, Canada

P. M. Reis, D. Terwagne, M. Brojan, R. Lagrange. Smart Morphable Surfaces for Aerodynamic Drag Control. *17th U. S. National Congress on Theoretical and Applied Mechanics*, East Lansing, U.S.A.

P. M. Reis, M. Brojan, D. Terwagne, R. Lagrange. Wrinkling Crystallography on Curved Surfaces. *Annual Meeting of the A.P.S. March Meeting*, Denver, U.S.A.

2013 R. Lagrange. Wrinkling on a curved surface. *Fluid lab group meeting, Department of Applied Mathematics*, Cambridge, U.S.A.

R. Lagrange. Wrinkling on a curved surface. *E.G.S. lab group meeting, Department of Civil Engineering*, Cambridge, U.S.A.

R. Lagrange, D. Averbuch. Buckling of an imperfect beam on a nonlinear foundation . *3th Annual Meeting of the A.P.S. March Meeting*, Baltimore, U.S.A.

2012 R. Lagrange. Imperfect beam on foundation. *New England Workshop on the Mechanics of Materials and Structures, Brown University*, Providence, U.S.A.

R. Lagrange, P. Meunier, C. Eloy, F. Nadal. Fluid flow inside a precessing cylinder. *Fluid lab group meeting, Department of Applied Mathematics*, Cambridge, U.S.A.

R. Lagrange, D. Averbuch. Buckling of an imperfect beam on a nonlinear foundation. *E.G.S. lab group meeting, Department of Civil Engineering*, Cambridge, U.S.A.

2011 R. Lagrange, P. Meunier, C. Eloy, F. Nadal. Ecoulement d'un fluide dans un cylindre en précession. *Séminaire I.F.P.E.N.*, Solaize, France

R. Lagrange, D. Averbuch, M. Martinez. Flambage d'armure : modèles analytiques. *I.F.P.E.N.-Technip meeting*, Solaize, France

R. Lagrange, D. Averbuch. Explicit solutions for the buckling of an imperfect strut on a nonlinear elastic foundation. *Engineering Mechanics Institute Conference*, Boston, U.S.A.

R. Lagrange, P. Meunier, C. Eloy, F. Nadal. Fluid flow inside a precessing cylinder. *Engineering Mechanics Institute Conference*, Boston, U.S.A.

R. Lagrange, D. Averbuch, M. Martinez. Modèle de cinématique exacte pour le flambage des fils d'armure. *I.F.P.E.N.-Technip meeting*, Paris, France

R. Lagrange, D. Averbuch, M. Martinez. Comportement non-linéaire d'un fil d'armure sous compression puis flexion. *I.F.P.E.N.-Technip meeting*, Paris, France

2010 R. Lagrange, P. Meunier, C. Eloy, F. Nadal. Nonlinear dynamics of a fluid inside a precessing cylinder. *63th Annual Meeting of the A.P.S. Division of Fluid Dynamics*, Long Beach, U.S.A.

R. Lagrange, D. Averbuch, M. Martinez. Post-flambage d'une poutre avec défaut. *I.F.P.E.N.-Technip meeting*, Paris, France

R. Lagrange, P. Meunier, C. Eloy, F. Nadal. Dynamique d'un fluide dans un cylindre en précession. *Invited Presentation at O.N.E.R.A.*, Meudon, France

2009 R. Lagrange, P. Meunier, C. Eloy, F. Nadal. Dynamics of a fluid flow inside a precessing cylinder. *62th Annual Meeting of the A.P.S. Division of Fluid Dynamics*, Minneapolis, U.S.A.

R. Lagrange, P. Meunier, C. Eloy, F. Nadal. From laminar to turbulent flow in a precessing cylinder. *Workshop "Waves and Instabilities in Geophysical and Astrophysical Flows"*, Porquerolles, France

R. Lagrange, P. Meunier, C. Eloy, F. Nadal. Dynamics of a fluid inside a precessing cylinder. *19e Congrès Français de Mécanique*, Marseille, France

2008 P. Meunier, R. Lagrange, C. Eloy, F. Nadal. Chaotic dynamics of a fluid inside a precessing cylinder. *12e Rencontre du non-linéaire*, Paris, France

R. Lagrange, P. Meunier, C. Eloy, F. Nadal. Dynamics of a fluid inside a precessing cylinder. *IUTAM symposium "150 Years of Vortex Dynamics"*, Copenhagen, Denmark

P. Meunier, R. Lagrange, C. Eloy, F. Nadal. Dynamics of a fluid inside a precessing cylinder. *7th Euromech Fluid Mechanics Conference*, Manchester, U.K.

R. Lagrange, P. Meunier, C. Eloy, F. Nadal. Dynamics of a fluid inside a precessing cylinder. *22nd International Congress of Theoretical and Applied Mechanics (I.C.T.A.M.)*, Adelaide, Australia

R. Lagrange, P. Meunier, C. Eloy, F. Nadal. Dynamique d'un fluide dans un cylindre en précession. *I.R.P.H.E. Seminar*, Marseille, France

2007 R. Lagrange, P. Meunier, C. Eloy, F. Nadal. Instabilité d'un fluide dans un cylindre en précession. *11e Rencontre du non-linéaire*, Paris, France

R. Lagrange, P. Meunier, C. Eloy, F. Nadal. Stabilité d'un fluide dans un cylindre en précession. *18e Congrès Français de Mécanique*, Grenoble, France

C. Eloy, P. Meunier, R. Lagrange, F. Nadal. Rotating fluid cylinder submitted to a weak precession. *60th Annual Meeting of the A.P.S. Division of Fluid Dynamics*, Salt Lake City, U.S.A.

R. Lagrange, P. Meunier, C. Eloy, F. Nadal. Stability of a fluid flow inside a precessing cylinder. *3rd European S.C.A.T. Workshop and Summer School*, Porquerolles, France

C. Eloy, L. Schouveiler, R. Lagrange. Flag flutter. *Chaos complexity, and transport C.C.T.07*, Marseille, France

2. SYPNOSIS DES TRAVAUX DE RECHERCHE

Mon travail de recherche est consacré à l'analyse de phénomènes non linéaires (en particulier les instabilités, que j'ai commencé à étudier dès mon Master, avec l'instabilité de flottement d'un drapeau soumis à un écoulement parallèle à sa surface) dans le domaine de la mécanique des fluides et des structures. Mon objectif est de répondre à des problèmes pratiques tels que la dynamique des tubes en U dans les générateurs de vapeur, ou à des problèmes plus fondamentaux tels que la relation entre la géométrie et les instabilités dans les systèmes mécaniques (par exemple les structures élastiques minces). Que les problèmes soient pratiques ou fondamentaux, le fil conducteur de mon travail reste l'utilisation de techniques de modélisation pour comprendre des phénomènes complexes.

Je mène principalement des études théoriques en étroite collaboration avec des expérimentateurs, des experts en simulation numérique et des étudiants (stagiaires et 2 doctorants) que j'encadre. Un objectif qui me tient particulièrement à cœur est de déduire des formulations analytiques prédictives, en considérant des modèles simplifiés de problèmes de mécanique intrinsèquement complexes. En général, ces modèles simplifiés se réduisent à un ensemble d'équations aux dérivées partielles comportant des termes non linéaires et plusieurs paramètres physiques. Les non-linéarités peuvent provenir de diverses sources, notamment des charges mécaniques externes, des changements de géométrie ou de position du système modélisé (non-linéarités géométriques) ou, plus rarement dans mes travaux, de comportements spécifiques des matériaux (non-linéarités matérielles).

En général, les termes non linéaires produisent un ensemble riche et complexe de solutions dont l'existence et la stabilité dépendent de nombres sans dimension. Pour découvrir ces solutions, déchiffrer leurs propriétés dynamiques, élucider les mécanismes de base et les paramètres de gouvernance, j'utilise des techniques classiques de mathématiques appliquées et de mécanique : analyse dimensionnelle, minimisation de fonctionnelles, analyses linéaires de stabilité et faiblement non-linéaires, expansions asymptotiques, théorie des écoulements potentiels, décomposition de Helmholtz des écoulements...

Pour illustrer mes contributions à l'analyse des phénomènes non linéaires en mécanique, j'ai choisi de présenter dans ce mémoire les résultats que j'ai obtenus dans les travaux de recherche qui suivent.

2.1 Instabilité d'un fluide dans un cylindre en précession

Les écoulements forcés par un mouvement de précession deviennent instables lorsque les vitesses de rotation et/ou l'angle de précession dépassent un seuil critique[1]. Pendant ma thèse (I.R.P.H.E., 2006-2009), j'ai effectué une analyse linéaire de stabilité de ces écoulements, en me concentrant sur le cas particulier d'un cylindre résonnant (cylindre avec un rapport d'aspect spécifique pour lequel l'écoulement de base se réduit à un unique mode hydrodynamique forcé). J'ai continué ce travail lors de mon séjour postdoctoal au M.I.T. (2012-2015), afin de développer une nouvelle théorie, valable quel que soit le rapport d'aspect du cylindre. J'ai montré que l'écoulement de base, induit par la précession du cylindre, est une superposition d'un écoulement de cisaillement (vertical ou horizontal) et d'une somme infinie de modes forcés. J'ai ensuite effectué une analyse linéaire de stabilité de cet écoulement de base en considérant sa résonance triadique avec deux modes de Kelvin libres (solutions homogènes des équations de Navier-Stokes linéarisées). J'ai dérivé les équations d'amplitude des modes de Kelvin libres et obtenu une expression analytique du seuil d'instabilité et du taux de croissance. Ensuite, j'ai étudié la transition vers la turbulence en supervisant pendant un an un étudiant de premier cycle au M.I.T. Ensemble, nous avons effectué des simulations MATLAB des équations faiblement non linéaires que j'avais établies théoriquement. Les simulations ont montré que l'écoulement instable stationnaire devient périodique par le biais d'une bifurcation de Hopf supercritique. En augmentant davantage le nombre de Reynolds, nous avons montré que l'écoulement périodique subit de nombreuses bifurcations de doublement de période ainsi qu'un phénomène d'intermittence (coexistence de fenêtres périodiques et de chaos avec un attracteur étrange). Certains de ces résultats sont maintenant utilisés par P. Meunier (ancien directeur de thèse à l'I.R.P.H.E.) et R. Manasseh (Swinburne University of Technology) dans le cadre du développement d'un mélangeur sans pales, utilisant la précession pour assurer un mélange puissant pour un faible cisaillement (brevets FR1651703, US11311848). Mes travaux de recherche sur l'instabilité de précession ont été publiés dans les journaux suivants :

- R. Lagrange, P. Meunier, C. Eloy. Triadic instability of a non-resonant precessing fluid cylinder. C. R. Mecanique, 344, 418-433, 2016.
- R. Lagrange, P. Meunier, C. Eloy, F. Nadal. Precessional instability of a fluid cylinder. J. Fluid Mech., vol. 666, 104-145, 2011.
- J.P. Lambelin, F. Nadal, R. Lagrange, A. Sarthou. Non resonant viscous theory for the stability of a fluid–filled gyroscope. J. Fluid Mech., vol. 639, 167-194, 2009. PDF
- R. Lagrange, P. Meunier, C. Eloy, F. Nadal. Dynamics of a fluid inside a precessing cylinder. Mec. Ind., EDP Sciences, 10, 187-194, 2009.

[1] Vidéo I.R.P.H.E. de l'instabilité d'un fluide dans un cylindre en précession, visualisation avec des particules (kalliroscope) réfléchissantes : ici.

- R. Lagrange, C. Eloy, F. Nadal, P. Meunier. Instability of a fluid inside a precessing cylinder. Phys. Fluids, vol. 20, 081701, 2008.
- P. Meunier, C. Eloy, R. Lagrange, F. Nadal. A rotating fluid subject to weak precession. J. Fluid Mech., vol.599, 405-440, 2008.

2.2 Instabilités de flambage/plissement

Les deux instabilités, flambage et plissement, appartiennent à la catégorie générique des instabilités de structures élastiques, élancées et/ou minces, soumises à des contraintes de compression ou de traction (i.e. compression transverse via l'effet Poisson). Lorsque la contrainte devient trop importante, la structure peut subir une instabilité se traduisant par une déformation hors-plan. Bien que la dénomination ne soit pas universelle, on parle généralement de flambage (buckling en Anglais) dans le cas d'une déformation globale de la structure. Le plissement (wrinkling en Anglais) est en général associé à un mode de flambage localisé (déformation exhibant une petite longueur d'onde), se traduisant par l'apparition de rides ou de plis au niveau de la surface de la structure.

2.2.1 Flambage d'une poutre imparfaite sur fondation non-linéaire

Dans le cadre d'une collaboration avec l'industrie parapétrolière (Technip), je me suis intéressé, avec D. Averbuch (I.F.P.E.N., 2010-2011), à la déformation des fils d'armure (tensile armours/wires en Anglais) qui assurent la tenue mécanique des risers flexibles aux efforts axiaux. Nous avons considéré le problème modèle d'une poutre imparfaite (défaut de courbure), soumise à un effort de compression axial et à une force de rappel transverse. L'imperfection est introduite pour prendre en compte la courbure géodésique du fil d'armure. La force de rappel (type bilinéaire ou régularisée) modélise quant à elle l'interaction non-linéaire d'un fil d'armure avec son support (type Winkler). La minimisation d'une énergie potentielle (incluant une énergie de déformation de flexion et les travaux des efforts extérieurs) conduit à une équation différentielle d'ordre 4 pour le déplacement transverse, non-linéaire, avec un terme de forçage directement lié à l'amplitude de l'imperfection. Pour résoudre cette équation différentielle (avec des conditions aux limites de type appui-appui) et déterminer les états d'équilibre statiques du système, nous avons proposé deux méthodes théoriques. La première méthode, applicable uniquement dans le cas d'une force de rappel de type bilinéaire, est basée sur la recherche d'une solution par morceaux de l'équation d'équilibre. Cette méthode, bien que contraignante car nécessitant des conditions de raccordement (continuité du déplacement, de la tangeante, de la courbure et de l'effort tranchant) en deux points de la structure, conduit à une solution exacte du problème d'équilibre. La deuxième méthode, valable quel que soit le type de force de rappel (bilinéaire ou régularisée), est basée sur une procédure de Galerkin (recherche d'une solution ayant la même forme que l'imperfection) et la minimisation d'un résidu. Cette approche, simple à mettre en place, produit une relation explicite entre la charge de compression et l'amplitude du déplacement, mais conduit à une solution approximative du problème

d'équilibre. Quelle que soit la méthode utilisée, nous avons montré que le système est sensible à l'imperfection et que la déformée est une amplification du défaut. De plus, nous avons montré l'existence d'une taille critique d'imperfection gouvernant l'existence d'une charge limite (i.e. un point limite) dans les courbes d'équilibre du système. Une expression analytique de cette imperfection critique et des lois d'évolution pour la charge limite ont été proposées et vérifiées numériquement (outil O.D.E. 45 de Matlab). Les travaux de recherche sur l'instabilité de flambage ont été publiés dans les journaux suivants :

- R. Lagrange. Limit point buckling of a finite beam on a nonlinear foundation. Theor. Appl. Mech. Lett.,vol. 4, 031001, 2014.
- R. Lagrange. Compression-induced stiffness in the buckling of a one fiber composite. Theor. Appl. Mech. Lett., vol. 3, 061001, 2013.
- R. Lagrange, D. Averbuch. Solution methods for the growth of a repeating imperfection in the line of a strut on a nonlinear foundation. Int. J. Mech. Sci., vol. 63(1), 48-58, 2012.

2.2.2 Flambage/plissement d'un film mince sur substrat circulaire

Pour mieux comprendre l'instabilité de plissement, je me suis intéressé avec mes collègues du M.I.T. (P. Reis, J. Dunkel et al., 2012-2015), au cas de la déformation d'un film mince attaché à un substrat élastique circulaire (2D) contenant une cavité interne dépressurisée[2]. L'effet du substrat sur le film a été modélisé par une force de rappel, déterminée à partir d'une fonction d'Airy (résolution du problème statique d'élasticité linéaire 2D pour le substrat). A partir des équations d'Euler-Lagrange (obtenues via la minimisation d'une énergie potentielle) et d'un développement asymptotique du déplacement, j'ai déterminé les états d'équilibre du film (ordre 0, déformation purement radiale), la pression critique et les modes de l'instabilité (analyse linéaire de stabilité, ordre 1). Les modes de l'instabilité correspondent à un plissement local ou à un flambage global du film. J'ai établi un diagramme de phase montrant que la sélection d'un mode d'instabilité dépend du rayon effectif (rapport entre le rayon du substrat et l'épaisseur du film), du rapport des modules d'Young et de la taille de la cavité interne. Ce diagramme de phase a été corroboré par des simulations ABAQUS. Les résultats pour un substrat circulaire (2D) ont ensuite été étendus au cas d'un substrat sphérique (3D). Une théorie de coque et une minimisation d'une énergie de déformation ont permis d'obtenir une équation de Swift-Hohenberg généralisée pour les états d'équilibre du système. Nous avons montré, via une résolution numérique et une étude paramétrique de cette équation, l'existence d'une variété d'états d'équilibre caractérisés par différents patterns (hexagonaux, labyrinthiques). Nous avons montré que la sélection d'un pattern dépend du rayon effectif, du rapport des modules d'Young et de la contrainte excédentaire (contrainte de compression au-delà du seuil critique) appliquée au film.

[2] Vidéo M.I.T. de l'instabilité de plissement, cas d'un substrat semi-sphérique possédant une cavité intérieure dépressurisée : ici.

Finalement, nous avons réduit l'équation de Swift-Hohenberg généralisée à une forme standard à partir de laquelle nous avons établi un diagramme de bifurcation et de phase des motifs de plissement. Les travaux de recherche sur l'instabilité de plissement ont été publiés dans les journaux suivants :

- F. Lopez Jimenez, N. Stoop, R. Lagrange, J. Dunkel, P.M. Reis. Curvature controlled defect localization in elastic surface crystals. Phys. Rev. Lett., 116, 104301, 2016.
- R. Lagrange, F. Lopez Jimenez, D. Terwagne, M. Brojan, P. Reis, From wrinkling to global buckling of a ring on a curved substrate. J. Mech. Phys. Solids, 89, 77-95, 2016.
- N. Stoop, R. Lagrange, D. Terwagne, P.M. Reis, J. Dunkel. Curvature induced symmetry breaking selects elastic surface patterns. Nature Materials, 14, 337-342, 2015.
- M. Brojan, D. Terwagne. R. Lagrange, P.M. Reis. Wrinkling crystallography on spherical surfaces. Proc. Natl. Acad. Sci. U.S.A., 112(1), 14-19, 2015.

2.3 Instabilité fluide-élastique d'un faisceau de tubes

L'instabilité fluide-élastique se produit lorsque des structures élastiques sont soumises à l'écoulement d'un fluide. Dans certains cas, la dynamique du fluide peut entraîner des vibrations de la structure, qui à leur tour modifient l'écoulement, créant ainsi un couplage fluide-structure. En tant que structures minces et flexibles, les tubes en U des générateurs de vapeur sont sensibles aux mécanismes d'interaction fluide-structure, en particulier dans leur partie supérieure, soumise à un écoulement transverse diphasique eau-vapeur. Dans ce contexte, je dirige depuis mon arrivée au C.E.A. en 2015 une activité de recherche sur la modélisation des forces fluide-élastiques (et des forces turbulentes) dans des faisceaux de tubes soumis à un écoulement transverse. Dans le cas d'un tube flexible, situé au centre d'un faisceau rigide à pas carré, j'ai montré que ce dernier devient instable dans la direction de portance, lorsqu'il est soumis à un écoulement monophasique caractérisé par un nombre de Reynolds élevé[3]. À partir d'une analyse dimensionnelle, alimentée par des résultats expérimentaux obtenus sur des maquettes à échelle réduite, j'ai fourni une expression analytique du nombre de Reynolds critique. J'ai montré que le seuil d'instabilité dépend du nombre de Scruton (c'est-à-dire de l'effet masse-amortissement) et du nombre de Stokes (c'est-à-dire de l'effet fréquence/rigidité) du tube : i) pour un nombre de Scruton donné, le tube est d'autant plus stable que le nombre de Stokes est grand, ii) pour un nombre de Stokes donné, un tube est d'autant plus stable que le nombre de Scruton est grand. À la suite de ces résultats obtenus en écoulement monophasique, j'ai dérivé un nouveau critère pour le seuil d'instabilité en écoulement diphasique. Ce critère établit un lien direct avec le

[3] Vidéo C.E.A. de l'instabilité fluide-élastique en portance, faisceau à pas carré, écoulement monophasique : ici.

seuil d'instabilité en écoulement monophasique, ne dépend pas des régimes d'écoulement diphasique, et est corroboré par des expériences en écoulement air-eau. Ce nouveau critère doit être testé pour différentes géométries de faisceaux de tubes (par exemple en pas triangulaire) et pour des fluides diphasiques différents (eau-freon, vapeur-eau), avant sa mise en œuvre dans le code numérique thermo-hydraulique développé par Framatome et le C.E.A. Ce nouveau critère de stabilité a été présenté lors de la conférence internationale "Fluid-Induced Vibrations" que j'ai coorganisée en 2022 à Paris et a été retenu pour faire l'objet d'une publication dans un numéro spécial du journal "J. Fluids and Struct". Les travaux de recherche sur l'instabilité fluide-élastique ont été publiés/soumis dans les journaux suivants :

- R. Lagrange, D. Panunzio, P. Piteau, X. Delaune, J. Antunes. A new criterion for the instability threshold of a square tube bundle subject to two-phase cross-flow. Submitted to J. Fluids Struct., special issue, 2023.
- P. Piteau, D. Panunzio, R. Lagrange, X. Delaune, J. Antunes. Experimental investigation of in-flow fluidelastic instability for rotated triangular tube bundles subjected to single-phase and two-phase transverse flows. Submitted to J. Fluids Struct., special issue, 2023.
- R. Lagrange, P. Piteau, X. Delaune, J. Antunes. Fluid-elastic coefficients in single phase cross flow : dimensional analysis, direct and indirect experimental methods. Proceedings of the ASME, PVP2019, 93984, 2019.

Je développe dans la suite de ce mémoire les thèmes de recherche associés à ces trois types d'instabilité. Chaque chapitre commence par une introduction générale sur le phénomène d'instabilité considéré, suivie d'une publication (post-docotorale, identifiée par une couleur bleue ci-dessus) représentative du travail réalisé et de la méthodologie mise en place pour comprendre, modéliser et prédire les caractéristiques de cette instabilité. Les publications identifiées par une couleur rouge sont reportées en annexes A et B.

3. INSTABILITÉ D'UN FLUIDE DANS UN CYLINDRE EN PRÉCESSION

La compréhension de l'écoulement engendré par un mouvement de précession revêt une importance critique dans différents domaines. En aéronautique, certains engins volants contiennent un carburant liquide qui peut être mis en rotation par frottement sur les parois du réservoir. En l'absence de perturbation externe, ce liquide est en rotation solide. Toutefois, en raison de facteurs tels qu'une asymétrie dans la géométrie de l'engin volant, un petit angle de précession peut apparaître et entraîner un changement de direction de l'axe de rotation propre $\mathbf{\Omega}_1$. L'axe peut se mettre à tourner autour d'un second axe, noté $\mathbf{\Omega}_2$, donnant ainsi à l'engin volant un mouvement de précession par rapport à un référentiel galiléen. Dans le cas où l'écoulement du fluide carburant est en résonance, l'angle initial de précession peut augmenter, ce qui peut avoir une incidence considérable sur la stabilité de l'engin volant. Les problèmes de mécanique des fluides tournants ont également un impact significatif sur de nombreux phénomènes atmosphériques tels que les cyclones et les tornades. La dynamique de ces phénomènes est étroitement liée à la force de Coriolis, qui est omniprésente dans les fluides en rotation et qui agit perpendiculairement à la vitesse d'un corps en déplacement dans un référentiel en rotation. Un cyclone (i.e. une dépression) correspond à une structure fluide en forme de spirale, localisée à la surface de la Terre, en rotation autour de la verticale locale à la vitesse angulaire $\Omega_1 = \Omega_2 \sin\alpha$; Ω_2 étant la vitesse de rotation de la Terre et α la latitude du cyclone. L'axe $\mathbf{\Omega}_1$ du cyclone est lui-même en rotation autour de l'axe polaire et précesse donc à la vitesse angulaire Ω_2. Ce mouvement de précession s'effectue alors avec un angle $\theta = 90 - \alpha$ degrés. Dans ce contexte, une question importante est de savoir comment la précession via la force de Coriolis influence la dynamique de ce cyclone. Un autre grand domaine d'application des fluides tournants concerne la géophysique interne liée à la précession terrestre (rotation de la Terre autour de l'axe polaire, lui même en rotation autour d'un axe perpendiculaire au plan de l'écliptique). Le mouvement de précession de la Terre joue un rôle clé dans la dynamique de son noyau liquide (composé de métaux en fusion, principalement de fer et de nickel). Ce mouvement crée un forçage sur le noyau liquide qui génère des écoulements de fluides. Ces écoulements peuvent produire des courants électriques, donnant naissance à des champs magnétiques. Ces derniers renforcent alors à leur tour les courants, créant ainsi un effet dynamo. La maîtrise de la mécanique des fluides tournants est donc essentielle pour comprendre le processus de génération du champ magnétique terrestre.

La dynamique d'un fluide Newtonien (masse volumique ρ, viscosité cinéma-

tique ν) dans un cylindre (hauteur H, rayon R) en précession est gouvernée par l'équation de Navier–Stokes

$$\frac{\partial \mathbf{U}}{\partial T} + (\mathbf{U}\cdot\nabla)\,\mathbf{U} = -\nabla\left(\frac{P}{\rho}\right) - 2\boldsymbol{\Omega}\times\mathbf{U} - \boldsymbol{\Omega}\times(\boldsymbol{\Omega}\times\mathbf{R}) - \left(\frac{d\boldsymbol{\Omega}}{dT}\right)_a \times\mathbf{R} + \nu\Delta\mathbf{U}, \tag{3.1}$$

avec $\mathbf{R}$ le vecteur position, $\mathbf{U}$ la vitesse du fluide dans le repère en rotation (représenté par le vecteur rotation $\boldsymbol{\Omega} = \boldsymbol{\Omega_1} + \boldsymbol{\Omega_2}$ et par sa variation temporelle $(d\boldsymbol{\Omega}/dT)_a$ par rapport à un repère absolu). Dans cette équation le terme $\boldsymbol{\Omega}\times(\boldsymbol{\Omega}\times\mathbf{R})$ correspond à la force centrifuge. La composante $2\boldsymbol{\Omega}\times\mathbf{U}$ correspond à la force de Coriolis. Le terme $(d\boldsymbol{\Omega}/dT)_a \times\mathbf{R}$ correspond à l'accélération du repère tournant par rapport au repère absolu et est appélé accélération de Poincaré. Ce terme est essentiel dans un mouvement de précession car il représente un terme de forçage spécifique sur le fluide. Une analyse dimensionnelle de l'équation de Navier-Stokes montre que la dynamique du fluide est gouvernée par quatre nombres sans dimension

- le rapport d'aspect du cylindre, $h = H/R$,
- le rapport de fréquence, $\omega = \Omega_1/\Omega$,
- le nombre de Reynolds, $Re = \Omega R^2/\nu$, représentant le rapport entre les ordres de grandeur du terme de Coriolis et du terme visqueux de l'équation de Navier-Stokes,
- le nombre de Rossby, $Ro = U/(\Omega R)$, représentant le rapport entre les ordres de grandeurs du terme de transport convectif de l'équation de Navier-Stokes et du terme de force de Coriolis.

Pour des nombres de Reynolds et de Rossby modérés, nous avons montré que l'écoulement d'un fluide dans un cylindre en précession est une superposition d'un cisaillement et d'une infinité d'ondes hydrodynamiques, appelées modes de Kelvin. L'amplitude d'un mode de Kelvin diverge lorsque sa fréquence propre (fonction du rapport d'aspect h) est égale à la fréquence de précession Ω. On dit alors que le cylindre de rapport d'aspect h est résonnant. Dans un tel cylindre, le mode divergeant devient prépondérant devant le cisaillement et les autres modes de Kelvin. Il constitue alors l'écoulement de base à l'intérieur du cylindre en précession, voir Fig. 3.1. Lorsque le nombre de Reynolds augmente, cet écoulement de base devient instable. Grâce à des mesures PIV (Particle Image Velocimetry), nous avons montré que cette instabilité est due à une interaction entre le mode résonnant et deux modes de Kelvin libres (solutions de l'équation de Navier–Stokes linéarisée et homogène), voir Fig. 3.2. Une analyse linéaire de stabilité basée sur un mécanisme de résonance triadique entre modes de Kelvin (i.e. interaction entre trois modes de Kelvin via le terme non-linéaire de l'équation de Navier-Stokes) permet de prédire correctement le taux de croissance et le seuil de l'instabilité, voir Fig. 3.3. Une analyse faiblement non-linéaire permet de plus de prédire la saturation des modes instables qui forcent un mode axisymétrique (mode géostrophique) au travers des couches limites. Ce mode limite alors l'amplitude de l'instabilité en modifiant la fréquence des modes instables.

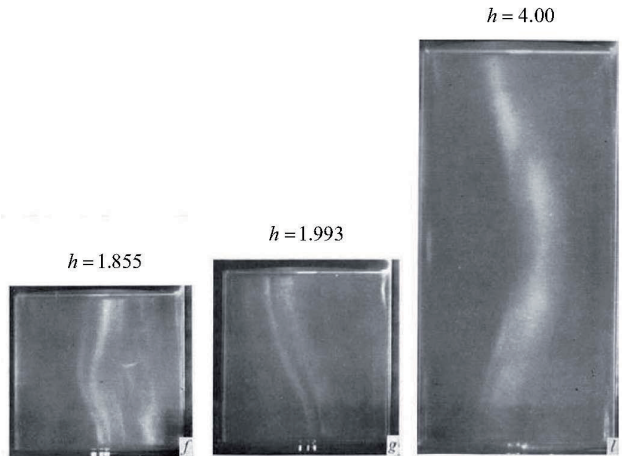

FIGURE 3.1 : Visualisations avec des particules réfléchissantes des modes de Kelvin dans un cylindre résonnant, obtenues pour différents rapports d'aspect h, par McEwan (1970).

En plus de prédire la saturation de l'instabilité, la théorie faiblement non-linéaire prédit également des régimes d'intermittence et une transition vers le chaos. La prédiction de l'instabilité et de sa saturation sont en excellent accord avec les résultats expérimentaux, même pour des nombres de Reynolds une décade au dessus du seuil. Les résultats de cette analyse, obtenus dans le cadre de ma thèse, sont cependant uniquement valables dans le cas d'un cylindre résonnant.

L'extension de l'analyse de stabilité au cas d'un cylindre quelconque a été réalisée lors de mon séjour postdocoral au M.I.T., et est l'objet de la publication qui suit, parue dans la revue *Comptes Rendus Mécanique*, sous le titre "Triadic instability of a non-resonant precessing fluid cylinder".

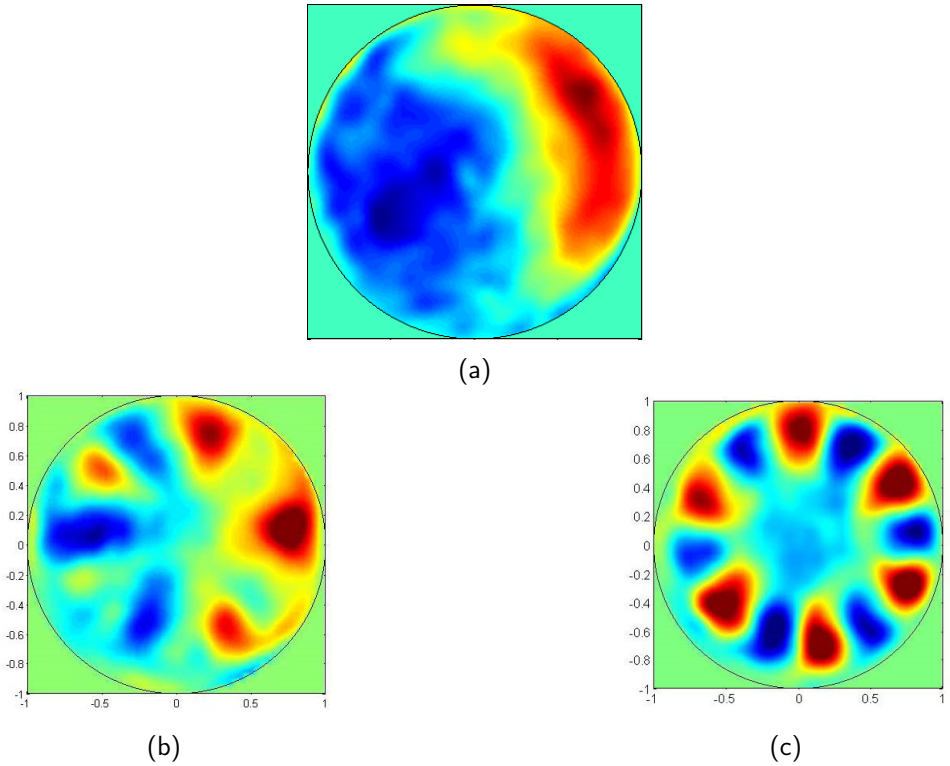

(a) (b) (c)

FIGURE 3.2 : Champs de vorticité axial instantané (PIV) des modes de Kelvin dans un cylindre en précession. Mode de base résonnant forcé par la précession (a) et modes de l'instabilité (b et c). Les modes (a), (b) et (c) interagissent via un mécanisme de résonance triadique. Vidéo I.R.P.H.E. de l'instabilité de précession : ici.

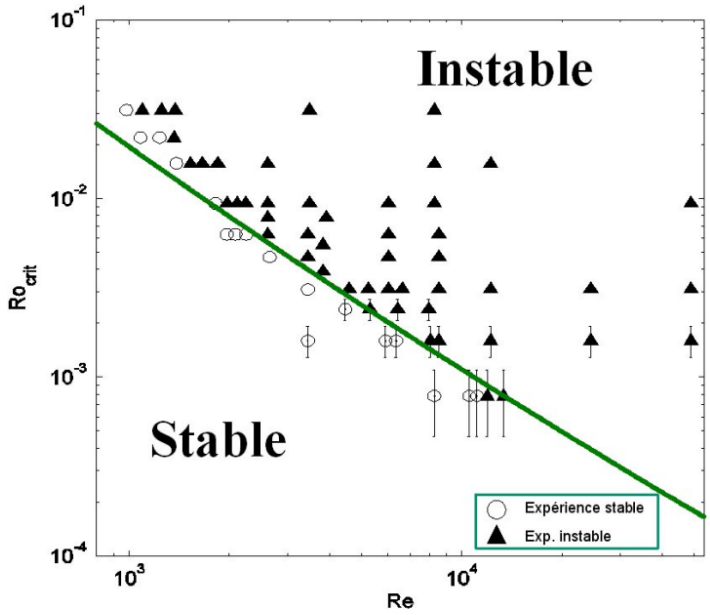

FIGURE 3.3 : Diagramme de stabilité d'un fluide dans un cylindre en précession, cas d'un cylindre résonnant. La droite verte correspond à la prédiction théorique du seuil d'instabilité.

Abstract

Flows forced by a precessional motion can exhibit instabilities of crucial importance, whether they concern the fuel of a flying object or the liquid core of a telluric planet. So far, stability analyses of these flows have focused on the special case of a resonant forcing. Here, we address the instability of the flow inside a precessing cylinder in the general case. We first show that the base flow forced by the cylinder precession is a superposition of a vertical or horizontal shear flow and an infinite sum of forced modes. We then perform a linear stability analysis of this base flow based on the mechanism of triadic resonance between a forced mode and two free Kelvin modes. Finally, we derive the amplitude equations of the free Kelvin modes and obtain an expression of the instability threshold and growth rate.

3.1 Introduction

Knowing the flow forced by precessional motion is of critical importance in several domains. In aeronautics, liquid propellants contained in flying objects can become resonant for specific geometries of their tank. The resulting flow can then create a destabilizing torque on the objects and dangerously modify their trajectories Stewartson (1958); Karpov (1965); Gans (1984); Garg *et al.* (1986); Herbert (1986); Pocha (1987); Agrawal (1993); Bao & Pascal (1997); Lambelin *et al.* (2009). Modeling the flow inside a precessing cylinder is thus a necessary step to design tank geometries that avoid these unwanted resonances.

In geophysics, most planets have a motion of slow precession, which is mainly governed by the planet aspect ratio. In the presence of a liquid core, this precessional motion creates a weak forcing that can drastically modify the flow inside the core due to the presence of resonances and critical layers. Flows inside liquid planet cores are of primordial interest to understand the generation of magnetic field by dynamo effect. For the present-day Earth, the magnetic field is likely due to the convection between the hot solid inner core and the colder mantle Malkus (1989); Grote *et al.* (1999, 2000); Grote & Busse (2001). However, a magnetic field was present on the early Earth although a solid inner core was not yet present. At that time, other mechanisms have generated and sustained the Earth's magnetic field. Tides (leading to elliptic streamlines) have often thought to be a source of energy sufficient for geodynamo Malkus (1989); Cébron *et al.* (2011), but recently it has also been shown numerically that precession could generate a magnetic field Tilgner (2005); Nore *et al.* (2011) (although this was not clearly proven for the case of the Earth). Besides, there is still some debate as to whether the production of kinetic energy due to precession is sufficient to balance the Ohmic energy loss induced by the magnetic field Rochester *et al.* (1975); Loper (1975); Roberts & Gubbins (1987); Vanyo *et al.* (1995); Kerswell (1996); Gans (1970); Tilgner (2000); Gailitis *et al.* (2002). In any case, even if precession is not the cause of magnetic field production on Earth, it might be different on other telluric planets.

To study the flow driven by a precessional motion, the cylindrical geom-

etry offers a good alternative to a planet-like spheroidal geometry because of its simplicity. In a precessing cylinder, the base flow is a sum of a shear flow and an infinite set of forced modes Kelvin (1880); Greenspan (1968). For particular precessional frequencies, a forced mode may become resonant when the height of the cylinder equals an odd number of half wavelengths Fultz (1959); McEwan (1970); Kerswell & Barenghi (1995); Meunier *et al.* (2008). In the framework of an inviscid and linear theory, this resonance leads to a divergence of the forced mode amplitude. Viscous effects however may saturate this amplitude to a value scaling as the inverse square root of the Ekman number (due to Ekman layers) (Gans, 1970). Nonlinear effects can also saturate the amplitude at a value scaling as the cubic root of the forcing (Meunier *et al.*, 2008). This nonlinear saturation is due to the presence of a strong axisymmetric zonal flow (also called geostrophic flow), which tends to decrease the solid body rotation and thus detune the resonance of the forced mode Kong *et al.* (2015).

When the Ekman number is decreased or the precessing angle is increased above a critical value, a resonant forced mode can become unstable McEwan (1970); Thompson (1970); Manasseh (1992, 1994); Kobine (1995); Manasseh (1996). For small tilt angles, we have shown that this instability is due to a triadic resonance between the resonant forced mode and two free Kelvin modes Lagrange *et al.* (2008, 2009, 2011). However, outside of resonances, the forced modes have a small amplitude and the base flow is not made of a single mode anymore. Here, our principal objective is to perform a stability analysis of the complete base flow (made of a shear flow and a sum of forced modes) in the case of a non-resonant precessing fluid cylinder. We will consider the triadic interaction of the base flow with two free Kelvin modes to determine the conditions of instability and derive an expression for the growth rate.

This paper is organized as follows. Section 3.2 presents the problem of a precessing cylinder by introducing the governing equations. In this section we determine the off-resonance base flow and discuss the symmetry properties of the problem. In § 3.3, we develop a linear stability analysis of the complete base flow, based on the mechanism of triadic resonance. We discuss the conditions of resonance, derive the amplitude equations of the instability modes and provide an analytical expression of the instability growth rate and threshold. In § 3.4 we present an application for a particular case, and determine its stability diagram. Finally, some conclusions are drawn and discussed in the context of the transition to turbulence in precessing flows.

3.2 Formulation of the problem

Consider a cylinder of radius R, height H, axis of revolution along $\hat{\mathbf{k}}$, entirely filled with a Newtonian fluid of kinematic viscosity ν. The cylinder rotates at the angular speed Ω_1 about $\hat{\mathbf{k}}$, which also rotates at the angular speed Ω_2 about the vertical axis and we denote by θ the precession angle, i.e. the angle between these two axes of rotation (Fig. 3.4).

To make the problem dimensionless, we introduce four numbers: the aspect ratio $h = H/R$, the frequency ratio $\omega = \Omega_1/\Omega$, with $\Omega = \Omega_1 + \Omega_2 \cos\theta$,

the Ekman number $Ek = \nu/(\Omega R^2)$ and the Rossby number $Ro = \Omega_2 \sin\theta/\Omega$, which will be assumed asymptotically small, i.e. $Ro \ll 1$ (weak precession). The dimensionless flow velocity in the cylinder's frame of reference $(O, \hat{\mathbf{i}}, \hat{\mathbf{j}}, \hat{\mathbf{k}})$ is denoted by $\mathbf{u} = \mathbf{U}/(R\Omega)$. The dimensionless cylindrical coordinates are (r, φ, z), where $z = 0$ corresponds to the mid-height section of the cylinder and we note $\mathbf{r}$ the position vector of a fluid particle. In the cylinder's frame of reference, the dimensionless Euler equations (assuming an inviscid fluid) are Meunier *et al.* (2008); Lagrange *et al.* (2011)

$$\frac{\partial \mathbf{u}}{\partial t} + 2\left(\hat{\mathbf{k}} + Ro\,\boldsymbol{\delta}\right) \times \mathbf{u} + \boldsymbol{\nabla} p = -2Ro\,\omega r\,\cos(\omega t + \varphi)\,\hat{\mathbf{k}} + \mathbf{u} \times (\boldsymbol{\nabla} \times \mathbf{u}), \quad (1a)$$

$$\boldsymbol{\nabla} \cdot \mathbf{u} = 0, \quad (1b)$$

with $\boldsymbol{\delta} = \cos(\omega t)\,\hat{\mathbf{i}} - \sin(\omega t)\,\hat{\mathbf{j}}$. On the left hand side (LHS) of (1a), the first term is inertia, the second term is the Coriolis force and p is the dimensionless pressure field defined as

$$\begin{aligned} p = {} & \frac{P}{\rho\Omega^2 R^2} - \frac{1}{2} r^2 + Ro|1-\omega| r z \cos(\omega t + \varphi) + \boldsymbol{\gamma}_O \cdot \mathbf{r} \\ & - \frac{1}{2} Ro^2 [z^2 + r^2 \sin^2(\omega t + \varphi)] \\ & + \frac{1}{2}\mathbf{u}^2, \end{aligned} \quad (2)$$

where $\boldsymbol{\gamma}_O = \boldsymbol{\Gamma}_O/R\Omega^2$ is the dimensionless acceleration of the cylinder centroid O. On the right hand side (RHS) of (1a), the first term is the forcing due to precession, the second term is the convective nonlinear term. At this point, it is convenient to introduce the four components vector $\mathbf{v} = (\mathbf{u}, p)^T$ and recast equations (1) into a matrix formulation

$$\left(\frac{\partial}{\partial t}\mathcal{I} + \mathcal{M}\right)\mathbf{v} = 2Ro\,\mathbf{F}_0 \cos(\omega t + \varphi) + \mathbf{N}(\mathbf{v}, \mathbf{v}) + Ro\,(\mathcal{D}^{\,\mathrm{i}(\omega t + \varphi)} + \text{c.c.})\mathbf{v}, \quad (3)$$

where operators $\mathcal{I}$, $\mathcal{M}$, $\mathcal{D}$, the forcing vector $\mathbf{F}_0$ and the bilinear function $\mathbf{N}$ are reported in Appendix 3.6.1. The symbol c.c. stands for the complex conjugate.

3.2.1 Base flow

In the limit of small Rossby numbers, the base flow forced by the precessional motion can be found by solving the Euler equations (3) at first order. We thus have to solve the following inhomogeneous linear differential equation for $\mathbf{v}$

$$\left(\frac{\partial}{\partial t}\mathcal{I} + \mathcal{M}\right)\mathbf{v} = 2Ro\,\mathbf{F}_0 \cos(\omega t + \varphi)\,. \quad (4)$$

Projecting this equation onto $\hat{\mathbf{k}}$ yields

$$\frac{\partial v_z}{\partial t} + \frac{\partial v_p}{\partial z} = -2Ro\,r\omega\cos(\omega t + \varphi). \quad (5)$$

There are two particular solutions of this equation, which can be found by assuming either $p = 0$ or $u_z = 0$. The first assumption leads to a vertical shear given by

$$\mathbf{v} = Ro\ \mathbf{v}^{\mathrm{V}}_{\mathrm{shear}}\ e^{\mathrm{i}(\omega t+\varphi)} + \mathrm{c.c.} \qquad \text{with} \qquad \mathbf{v}^{\mathrm{V}}_{\mathrm{shear}} = \begin{pmatrix} 0 \\ 0 \\ \mathrm{i}r \\ 0 \end{pmatrix}. \tag{6}$$

This vertical shear is schematically shown in Fig. 3.4 (middle) and corresponds to the flow that would be found in a cylinder with infinite height. However, there is an alternative particular solution given by the second assumption ($u_z = 0$) which leads to a horizontal shear flow

$$\mathbf{v} = Ro\ \mathbf{v}^{\mathrm{H}}_{\mathrm{shear}}\ e^{\mathrm{i}(\omega t+\varphi)} + \mathrm{c.c.} \qquad \text{with} \qquad \mathbf{v}^{\mathrm{H}}_{\mathrm{shear}} = \frac{\omega z}{2-\omega} \begin{pmatrix} \mathrm{i} \\ -1 \\ 0 \\ r\,(\omega-2) \end{pmatrix}. \tag{7}$$

This horizontal shear is schematically shown in Fig. 3.4 (right). None of these particular solutions satisfy the boundary conditions on the cylinder walls, and they have to be completed with homogeneous solutions of (4). In the case of the vertical shear $\mathbf{v}^{\mathrm{V}}_{\mathrm{shear}}$, the full solution with proper boundary conditions has been found to be (e.g. Meunier *et al.* (2008))

$$\mathbf{v} = Ro\,\mathbf{v}^{\mathrm{V}}_{\mathrm{base}} = Ro\left(\mathbf{v}^{\mathrm{V}}_{\mathrm{shear}} + \sum_{j=1}^{\infty} a^{\mathrm{V}}_j \mathbf{v}^{\mathrm{V}}_j\right) e^{\mathrm{i}(\omega t+\varphi)} + \mathrm{c.c.}, \tag{8}$$

where $\mathbf{v}^{\mathrm{V}}_j$ are forced modes of azimuthal wavenumber $m = 1$, frequency ω, and axial wavenumbers k^{V}_j. The amplitudes a^{V}_j and the structure of the forced modes are given in Appendix 3.6.1. Since here, these forced modes compensate the normal flow on the top and bottom walls of the cylinder, they have zero radial velocity $u_r = 0$ at $r = 1$. This boundary condition forces the axial wavenumbers k^{V}_j through the dispersion relation $D(1, \omega, k^{\mathrm{V}}_j) = 0$ given in Appendix 3.6.1 (it is stressed that the wavenumbers k^{V}_j are not a multiple of π/h since the forced modes do not satisfy the boundary condition $u_z = 0$ on the top and bottom wall).

In the case of a horizontal shear $\mathbf{v}^{\mathrm{H}}_{\mathrm{shear}}$, a similar procedure yields the following base flow solution

$$\mathbf{v} = Ro\,\mathbf{v}^{\mathrm{H}}_{\mathrm{base}} = Ro\left(\mathbf{v}^{\mathrm{H}}_{\mathrm{shear}} + \sum_{j=1}^{\infty} a^{\mathrm{H}}_j \mathbf{v}^{\mathrm{H}}_j\right) e^{\mathrm{i}(\omega t+\varphi)} + \mathrm{c.c.}. \tag{9}$$

The amplitudes a^{H}_j and the structure of the forced modes $\mathbf{v}^{\mathrm{H}}_j$ are given in Appendix 3.6.1. In this case, note that the axial wavenumbers k^{H}_j are odd multiples of π/h ($k^{\mathrm{H}}_j = (2j-1)\pi/h$). Here, the forced modes $\mathbf{v}^{\mathrm{H}}_j$ satisfy the boundary conditions on the top and bottom walls, but not on the lateral walls ($u_r \neq 0$ at $r = 1$), because these forced modes have been added to compensate an horizontal shear flow.

In both cases ($\mathbf{v}^{\mathrm{V}}_{\mathrm{base}}$ or $\mathbf{v}^{\mathrm{H}}_{\mathrm{base}}$), the base flow can be written as a superposition of a shear flow (vertical or horizontal respectively) and a sum of forced modes. These forced modes are similar to Kelvin modes Kelvin (1880); Greenspan (1968). However, we do not consider them as "real" Kelvin modes because they do not satisfy the free-slip boundary condition on all the cylinder walls. Figure 3.5 shows the two base flow solutions with an increasing number of forced modes. It is clear that both solutions tend to be equal $\mathbf{v}^{\mathrm{V}}_{\mathrm{base}} = \mathbf{v}^{\mathrm{H}}_{\mathrm{base}} = \mathbf{v}_{\mathrm{base}}$ when the number of forced modes is increased.

3.2.2 Symmetry properties

The stability analysis of the base flow described above will be presented below in §3. Before that, it is worth recalling some symmetry properties of the problem. It can first be noted that the vertical shear flow $\mathbf{v}^{\mathrm{V}}_{\mathrm{shear}}$ has only a vertical velocity component v_z, which is an even function of z. In contrast, the horizontal shear flow $\mathbf{v}^{\mathrm{H}}_{\mathrm{shear}}$ has no vertical component but its radial, azimuthal, and pressure components are odd functions of z. Both quadrivectors are thus of the type:

$$\mathbf{v}^- = \begin{pmatrix} f^-(z,r,\varphi,t) \\ f^-(z,r,\varphi,t) \\ f^+(z,r,\varphi,t) \\ f^-(z,r,\varphi,t) \end{pmatrix}, \tag{10}$$

where f^+ (resp. f^-) denotes even (resp. odd) functions of z. Equation (42) shows that the forced modes $\mathbf{v}^{\mathrm{V}}_j$ and $\mathbf{v}^{\mathrm{H}}_j$ also have the same z-parity. As a consequence, the base flow calculated above is of the type $\mathbf{v}^-$. This could have been anticipated since the first order terms of the Navier–Stokes equations only force this symmetry. However, at higher orders, the operators can generate a flow with the opposite symmetry of the type

$$\mathbf{v}^+ = \begin{pmatrix} f^+(z,r,\varphi,t) \\ f^+(z,r,\varphi,t) \\ f^-(z,r,\varphi,t) \\ f^+(z,r,\varphi,t) \end{pmatrix}. \tag{11}$$

It is easy to show that the operators $\mathcal{D}$, $\overline{\mathcal{D}}$, and $\mathbf{N}$ have the following properties

$$\mathcal{D}\mathbf{v}^- \sim \overline{\mathcal{D}}\mathbf{v}^- \sim \mathbf{v}^+, \tag{12a}$$

$$\mathbf{N}\left(\mathbf{v}_{\mathrm{base}}, \mathbf{v}^-\right) \sim \mathbf{N}\left(\overline{\mathbf{v}_{\mathrm{base}}}, \mathbf{v}^-\right) \sim \mathbf{v}^+, \tag{12b}$$

$$\mathbf{N}\left(\mathbf{v}^-, \mathbf{v}_{\mathrm{base}}\right) \sim \mathbf{N}\left(\mathbf{v}^-, \overline{\mathbf{v}_{\mathrm{base}}}\right) \sim \mathbf{v}^+, \tag{12c}$$

where the symbol $\sim$ means "same parity as" and $\mathbf{v}_{\mathrm{base}}$ corresponds to either the vertical base flow $\mathbf{v}^{\mathrm{V}}_{\mathrm{base}}$ or the horizontal base flow $\mathbf{v}^{\mathrm{H}}_{\mathrm{base}}$. This means that, even if the base flow is of the type $\mathbf{v}^-$ at first order, the nonlinear terms may introduce a different symmetry in the problem. It is actually easy to show that the previous equations remain valid under the permutation of signs $(+,-) \to (-,+)$.

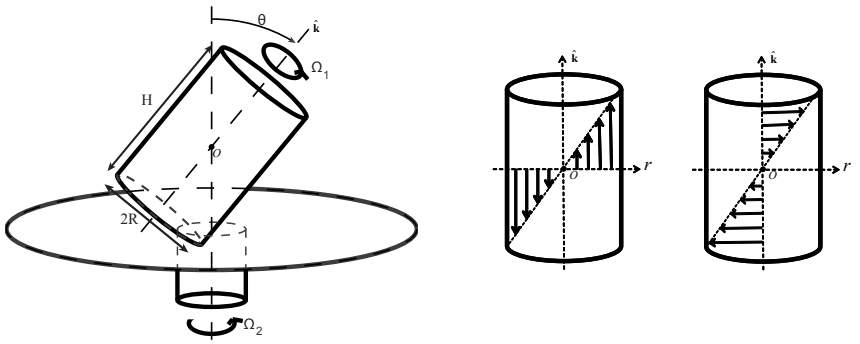

Figure 3.4: Sketch of a precessing cylinder of radius R and height H (left). The cylinder is rotating around its own axis with angular velocity Ω_1, and this axis itself rotates around a second axis with angular velocity Ω_2. The precession forces a shear flow which can be taken vertical (middle) or horizontal (right), but which does not respect the boundary conditions.

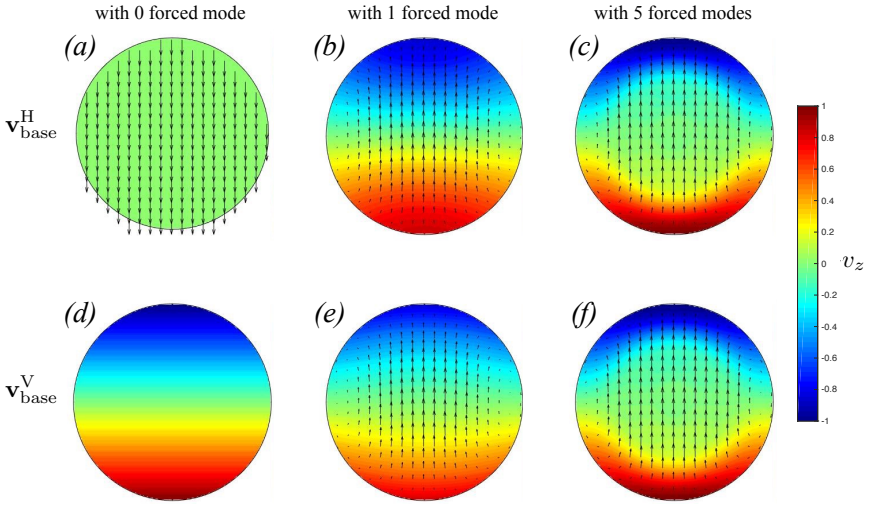

Figure 3.5: Comparisons of the base flows computed from eqns. (8) and (9) for $h = 2.3$, $\omega = 1.34$, $t = 0$. *(a-c)* Flow $\mathbf{v}^{\mathsf{H}}_{\mathsf{base}}$ obtained from eqn. (9) when the sum of forced modes is truncated to 0, 1, and 5 modes respectively. *(d-f)* Same plots for $\mathbf{v}^{\mathsf{V}}_{\mathsf{base}}$ from eqn. (8). In both cases, the vectors show the projection of the velocity field in the plane $z = h/3$ and the color-coded map shows v_z in the same plane.

A direct consequence of these symmetry properties is that a triadic resonance cannot develop if the perturbation has a single parity ($\mathbf{v}^+$ or $\mathbf{v}^-$). Indeed, in a mechanism of triadic resonance, the base flow interacts with two free Kelvin modes $\mathbf{v}_1$ and $\mathbf{v}_2$ through the nonlinear operator $\mathbf{N}$. Let us assume that the free Kelvin modes have the same symmetry $\mathbf{v}^-$. The growth of the first free Kelvin mode is due to the nonlinear interaction of the second free Kelvin mode with the base flow, via the terms $\mathbf{N}(\mathbf{v}_{\text{base}}, \mathbf{v}_{\mathbf{2}}^-)$, $\mathbf{N}(\mathbf{v}_{\mathbf{2}}^-, \mathbf{v}_{\text{base}})$ and $\mathcal{D}\mathbf{v}_2^-$ which have the opposite symmetry $\mathbf{v}^+$. These forcing terms are thus perpendicular to the first free Kelvin mode and such a triadic resonance is non constructive. This can be properly shown by defining the dot product

$$\langle \mathbf{X}, \mathbf{Y} \rangle = \int_V \left(\overline{X_r} Y_r + \overline{X_\varphi} Y_\varphi + \overline{X_z} Y_z + \overline{X_p} Y_p \right) d^3V, \tag{13}$$

where $\overline{X}$ refers to the conjugate of X and V is the volume of the cylinder. It is then straightforward to show, using (12a-c) that the dot products $\left\langle \mathbf{v}_1^-, \mathbf{N}(\mathbf{v}_{\mathbf{2}}^-, \mathbf{v}_{\text{base}}) \right\rangle$, $\left\langle \mathbf{v}_1^-, \mathbf{N}(\mathbf{v}_{\text{base}}, \mathbf{v}_{\mathbf{2}}^-) \right\rangle$ and $\left\langle \mathbf{v}_1^-, \mathcal{D}\mathbf{v}_2^- \right\rangle$ vanish because they only contain terms of the form

$$\langle \mathbf{v}^+, \mathbf{v}^- \rangle = \int_{-h/2}^{h/2} f^+(z) f^-(z) dz = 0. \tag{14}$$

The same reasoning applies to free Kelvin modes with a symmetry $\mathbf{v}^+$. The general conclusion is that the constructive triadic resonances must couple an even free Kelvin mode $\mathbf{v}^+$ with an odd free Kelvin mode $\mathbf{v}^-$. We will now use this property to restrict the number of possible instabilities that may arise in the linear stability analysis.

3.3 Linear stability analysis

To study the stability of the base flow, we introduce a small perturbation in form of a four-components vector $\widetilde{\mathbf{v}} = (\widetilde{\mathbf{u}}, \widetilde{p})^T$, so that the total flow is

$$\mathbf{v} = Ro\, \mathbf{v}_{\text{base}} + \widetilde{\mathbf{v}} + o\left(Ro\right), \tag{15}$$

where $\mathbf{v}_{\text{base}}$ is either $\mathbf{v}_{\text{base}}^{\text{V}}$ or $\mathbf{v}_{\text{base}}^{\text{H}}$. Inserting this expansion into (3) yields an equation for the perturbation vector

$$\left(\frac{\partial}{\partial t} \mathcal{I} + \mathcal{M} \right) \widetilde{\mathbf{v}} = Ro \left[\mathbf{N}(\mathbf{v}_{\text{base}}, \widetilde{\mathbf{v}}) + \mathbf{N}(\widetilde{\mathbf{v}}, \mathbf{v}_{\text{base}}) + \left(\mathcal{D}^{\,\mathrm{i}(\omega t + \varphi)} + \text{c.c.} \right) \widetilde{\mathbf{v}} \right] + o\left(Ro\right) + o\left(|\widetilde{\mathbf{v}}|\right), \tag{16}$$

where $|\widetilde{\mathbf{v}}| = \sqrt{\langle \widetilde{\mathbf{v}}, \widetilde{\mathbf{v}} \rangle}$ is the magnitude of $\widetilde{\mathbf{v}}$. The first two terms on the RHS of (16) represent the nonlinear interactions between the base flow and the perturbation. The third term represents the interaction between the forcing due to precession and the perturbation. The perturbation vector satisfies the inviscid boundary condition

$$\widetilde{\mathbf{u}} \cdot \mathbf{n} = 0 \text{ at the walls } \left(r = 1 \text{ or } z = \pm h/2 \right). \tag{17}$$

To solve (16) and (17), we use a multiscale expansion in time with t a rapid time scale and $\tau = Ro\, t$ a slow time scale. We then expand $\widetilde{\mathbf{v}}$ as

$$\widetilde{\mathbf{v}} = \widetilde{\mathbf{v}}_0(\mathbf{r}, \tau, t) + Ro\, \widetilde{\mathbf{v}}_1(\mathbf{r}, \tau, t) + o(Ro). \tag{18}$$

Inserting (18) into (16) yields two equations: one of order 1 and one of order Ro that shall be studied now. The equation at order one gives the form of the free Kelvin modes, and the equation at order Ro gives their slow time dynamics, hence their stability properties.

3.3.1 Order 1: free Kelvin modes

At first order, the equation (16) and the inviscid boundary condition $\widetilde{\mathbf{u}} \cdot \mathbf{n}$ are

$$\left(\frac{\partial \mathcal{I}}{\partial t} + \mathcal{M}\right) \widetilde{\mathbf{v}}_0 = \mathbf{0}, \tag{19a}$$

$$\widetilde{\mathbf{u}}_0 \cdot \mathbf{n} = 0 \quad \text{at the walls } (r = 1 \text{ or } z = \pm h/2). \tag{19b}$$

The solution to this homogenous problem is a linear combination of free Kelvin modes with different z-parities Lagrange *et al.* (2011)

$$\widetilde{\mathbf{v}}_0 = \sum_{l=1}^{\infty} A_l{}^{+} \mathbf{v}_l^{+} e^{\mathrm{i}(\omega_l t + m_l \varphi)} + \sum_{l=1}^{\infty} A_l{}^{-} \mathbf{v}_l^{-} e^{\mathrm{i}(\omega_l t + m_l \varphi)} + \text{c.c.} \tag{20}$$

Vectors $\mathbf{v}_l^{+}$ (resp. $\mathbf{v}_l^{-}$) have axial wavenumbers k_l^{+} (resp. k_l^{-}) which are even (resp. odd) multiple of π/h in order to respect the condition of no normal flow at the top and bottom ($z = \pm h/2$). This property is interesting because the wavenumbers are separated into two families, which will restrict the number of possible triadic resonances. The components of the free Kelvin modes are given in Appendix 3.6.1. In (20), $A_l^{\pm}$, m_l, and ω_l are the amplitude, azimuthal wavenumber, and angular frequency of the free Kelvin mode $\mathbf{v}_l{}^{\pm} e^{\mathrm{i}(\omega_l t + m_l \varphi)}$. The wavenumbers are connected through the dispersion relation $D(m_l, \omega_l, k_l^{\pm})$ such that the radial velocity of the mode vanishes at the cylinder wall $r = 1$.

To examine the mechanism of triadic resonance, the perturbation $\widetilde{\mathbf{v}}_0$ is reduced to a combination of two free Kelvin modes $\mathbf{v}_1$ and $\mathbf{v}_2$ with unknown amplitudes $A_1(\tau)$ and $A_2(\tau)$

$$\widetilde{\mathbf{v}}_0 = A_1 \mathbf{v}_1 e^{\mathrm{i}(\omega_1 t + m_1 \varphi)} + A_2 \mathbf{v}_2 e^{\mathrm{i}(\omega_2 t + m_2 \varphi)} + \text{c.c.}. \tag{21}$$

From now on, we attribute index 2 to the mode with the highest azimuthal wavenumber (i.e. $m_2 > m_1$).

3.3.2 Triadic resonance

We know from the symmetry properties presented in §3.2.2 that a triadic resonance between the base flow and the two free Kelvin modes can be constructive only if it involves free Kelvin modes with different z-parities. Therefore, the wavenumbers k_1 and k_2 must be integer multiple of π/h with

different parities. It follows that the difference between the two wavenumbers must be an odd multiple of π/h:

$$k_2 - k_1 = (2p-1)\pi/h, \tag{22}$$

with p an integer.

In addition, the base flow will interact with two free Kelvin modes if the operator $\mathbf{N}$ appropriately couples their time and azimuthal Fourier components. Thus the coupling term $\mathbf{N}(\mathbf{v}_{\text{base}}, \widetilde{\mathbf{v}}_0) + \mathbf{N}(\widetilde{\mathbf{v}}_0, \mathbf{v}_{\text{base}})$ in (16) has to contain the same Fourier components as $\mathbf{v}_l e^{\mathrm{i}(\omega_l t + m_l \varphi)}$, $l = 1, 2$. Since these terms have the following time and azimuthal Fourier components

$$\mathbf{v}_l e^{\mathrm{i}(\omega_l t + m_l \varphi)} : \text{Fourier components } (m_l, \omega_l), \tag{23a}$$

$$\mathbf{N}(\mathbf{v}_{\text{base}}, \widetilde{\mathbf{v}}_0) + \mathbf{N}(\widetilde{\mathbf{v}}_0, \mathbf{v}_{\text{base}}) : \text{Fourier components } (m_l + 1, \omega_l + \omega), (m_l - 1, \omega_l - \omega), \tag{23b}$$

the base flow will interact with the two free Kelvin modes if

$$m_2 - m_1 = 1, \tag{24a}$$

$$\omega_2 - \omega_1 = \omega. \tag{24b}$$

We recognize on the RHS the azimuthal wavenumber $m_{\text{base}} = 1$ and the angular frequency $\omega_{\text{base}} = \omega$ of the base flow. The conditions (24a-b) are characteristic of triadic resonances occurring in various domains (surface waves, plate vibrations, etc.), and are the key ingredient of weak (or wave) turbulence theory.

To find a pair of free Kelvin modes that fulfill the conditions of resonance (24a-b), we proceed as shown in Fig 3.6. In the plane (k_2, ω_2) we plot the dispersion relation of the free Kelvin modes (m_2, ω_2, k_2) and the dispersion relation of the free Kelvin modes (m_1, ω_1, k_1) translated horizontally by $(2p-1)\pi/h$ (with p an arbitrary integer) and vertically by ω. The intersection points correspond to free Kelvin modes satisfying the conditions of resonance (24a-b) and the condition induced by parity (22). In addition, the free Kelvin modes have to fit in the cylinder, so their axial wavenumbers need to be multiple of π/h. It means that the intersection point has to lie on the vertical dotted line of Fig 3.6. Such a tuned triadic resonance only occurs for particular aspect ratios (for a given forcing frequency ω). Otherwise, in most cases, the three curves do not intersect at the same point. Figure 3.6 shows an example of a tuned triadic resonance for $h = 2.3$, $\omega = 1.34$ with $m_1 = 2$ and $m_2 = 3$. The label for these points is (m_2, l_1, l_2), where $l_{1,2}$ is the branch number of the dispersion relations. There are an infinity of possible triadic resonances and they can all be studied in the inviscid case. However, when viscous effects are taken into account, the highest wavenumbers will be damped, such that in practice only the lowest axial, azimuthal and radial wavenumbers may be treated.

The procedure outline above shows how the axial, azimuthal and radial wavenumbers of two free Kelvin modes can be found to permit triadic resonance. In the next section, we consider the Euler equations at the next order in Ro, in order to calculate the slow temporal evolution of these free Kelvin modes and determine their stability.

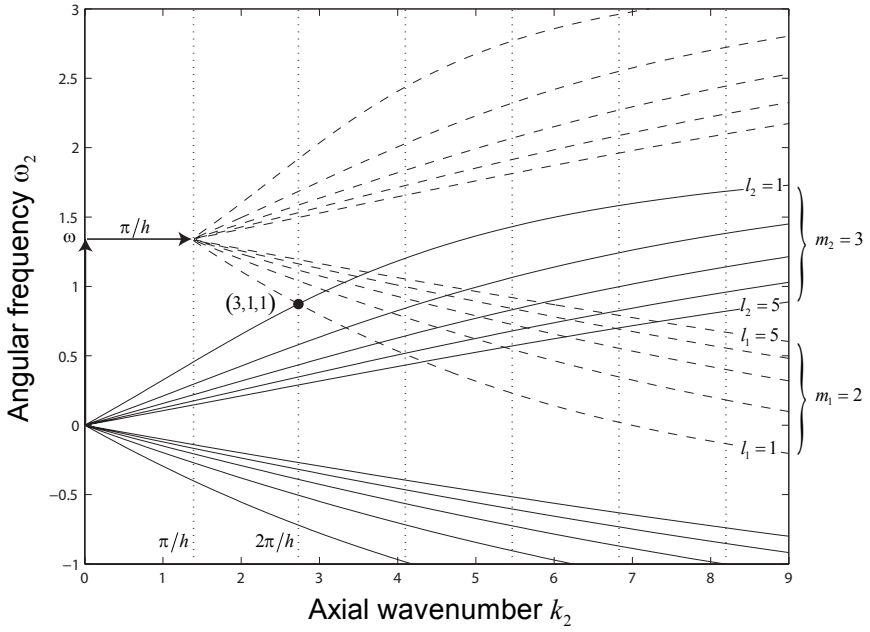

Figure 3.6: Dispersion relations of the free Kelvin modes with azimuthal wavenumbers $m_1 = 2$ (dashed lines) and $m_2 = 3$ (solid lines). The dispersion relation for $m_1 = 2$ is translated by π/h ($h = 2.3$) along the abscissae and by $\omega = 1.34$ along the ordinate. Vertical dotted lines indicate the discretisation of the axial wavenumber as a multiple of π/h imposed by the inviscid boundary condition at the top and bottom of the cylinder. A point lying at the intersection of the branches of the dispersion relations and a vertical line corresponds to a pair of resonant free Kelvin modes. The combination $(m_2 = 3, l_1 = 1, l_2 = 1)$ (marked with a black circle) is an example of resonant free Kelvin modes. Coordinates for this point are $k_2 = 2\pi/h$ and $\omega_2 = 0.874$.

3.3.3 Order *Ro*: slow time equations

At order Ro, equation (16) becomes

$$\left(\frac{\partial \mathcal{I}}{\partial t}+\mathcal{M}\right)\widetilde{\mathbf{v}}_1=\mathbf{N}\left(\mathbf{v}_{\text{base}},\widetilde{\mathbf{v}}_0\right)+\mathbf{N}\left(\widetilde{\mathbf{v}}_0,\mathbf{v}_{\text{base}}\right)+\left[\left(\mathcal{D}e^{\mathrm{i}(\omega t+\varphi)}+\text{c.c.}\right)-\frac{\partial \mathcal{I}}{\partial \tau}\right]\widetilde{\mathbf{v}}_0. \tag{25}$$

This $O(Ro)$ problem is linear, with a forcing term given by the RHS of (25). To avoid secular terms in the solution $\widetilde{\mathbf{v}}_1$, the RHS must be orthogonal to the kernel of the LHS operator. This kernel being spanned by the free Kelvin modes, themselves given by the $O(1)$ problem solved above, a solvability condition is obtained by taking the dot product of (25) with $\mathbf{v}_l e^{\mathrm{i}(\omega_l t+m_l\varphi)}$, $l=1,2$. Since the problem is self-adjoint, i.e. $\left\langle \mathbf{v}_l e^{\mathrm{i}(\omega_l t+m_l\varphi)},\left(\partial\mathcal{I}/\partial t+\mathcal{M}\right)\widetilde{\mathbf{v}}_1\right\rangle = 0$, we show in Appendix 3.6.2 that the slow time equations for A_1 and A_2 are

$$\frac{dA_1}{d\tau}=c_1A_2 \qquad \text{with} \qquad c_1=\frac{\overline{d}_{12}+n_{1s}+\sum_j \overline{a_j}n_{1j}}{\langle \mathbf{v}_1,\mathcal{I}\mathbf{v}_1\rangle}, \tag{26a}$$

$$\frac{dA_2}{d\tau}=c_2A_1 \qquad \text{with} \qquad c_2=\frac{d_{21}+n_{2s}+\sum_j a_jn_{2j}}{\langle \mathbf{v}_2,\mathcal{I}\mathbf{v}_2\rangle}. \tag{26b}$$

The terms $dA_l/d\tau$ come from the dot products $\left\langle \mathbf{v}_l e^{\mathrm{i}(\omega_l t+m_l\varphi)},\frac{\partial\mathcal{I}}{\partial\tau}\widetilde{\mathbf{v}}_0\right\rangle$. The terms $\overline{d}_{12}$ and d_{21} represent the interaction between the resonant free Kelvin modes and the forcing due to precession. They come from the dot products

$$\left\langle \mathbf{v}_l e^{\mathrm{i}(\omega_l t+m_l\varphi)},\left(\mathcal{D}e^{\mathrm{i}(\omega t+\varphi)}+\text{c.c.}\right)\widetilde{\mathbf{v}}_0\right\rangle. \tag{27}$$

The terms n_{1s} and n_{2s} represent the nonlinear interactions between the resonant free Kelvin modes and the shear part of the base flow. They come from the dot products

$$n_{ls}=\left\langle \mathbf{v}_l e^{\mathrm{i}(\omega_l t+m_l\varphi)},\mathbf{N}\left(\mathbf{v}_s e^{\mathrm{i}(\omega t+\varphi)}+\text{c.c.},\widetilde{\mathbf{v}}_0\right)+\mathbf{N}\left(\widetilde{\mathbf{v}}_0,\mathbf{v}_s e^{\mathrm{i}(\omega t+\varphi)}+\text{c.c.}\right)\right\rangle. \tag{28}$$

where $\mathbf{v}_s$ may be the vertical shear given by (6) or the horizontal shear given by (7). Finally, the terms n_{1j} and n_{2j} represent the nonlinear interactions between the resonant free Kelvin modes and the j-th forced mode of the base flow. They come from the dot products

$$n_{lj}=\left\langle \mathbf{v}_l e^{\mathrm{i}(\omega_l t+m_l\varphi)},\mathbf{N}\left(\mathbf{v}_j e^{\mathrm{i}(\omega t+\varphi)}+\text{c.c.},\widetilde{\mathbf{v}}_0\right)+\mathbf{N}\left(\widetilde{\mathbf{v}}_0,\mathbf{v}_j e^{\mathrm{i}(\omega t+\varphi)}+\text{c.c.}\right)\right\rangle. \tag{29}$$

Simplified expressions for all these terms are given in Appendix 3.6.2.

Seeking solutions to the amplitude equations (26) as growing exponentials, $A_j\sim e^{\sigma t}$, yields an analytical prediction for the complex growth rate σ of the instability

$$\sigma=|Ro|\sqrt{c_1c_2}. \tag{30}$$

The temporal growth rate σ_r is then obtained by taking the real part of σ, i.e. $\sigma_r=|Ro|\mathrm{Re}\left(\sqrt{c_1c_2}\right)$. A resonant combination of free Kelvin modes is unstable if σ_r is positive. This is always the case for combinations issued from the intersection of dispersion relations with opposite slopes Fukumoto (2003).

3.3.4 Amplitude equations using the horizontal shear decomposition

Amplitude equations (26) apply to any decomposition, $\mathbf{v}^{\mathrm{V}}_{\mathrm{base}}$ or $\mathbf{v}^{\mathrm{H}}_{\mathrm{base}}$, of the base flow. If the vertical shear decomposition $\mathbf{v}^{\mathrm{V}}_{\mathrm{base}}$ is chosen for the base flow, the formula for the growth rate contains infinite summations (corresponding to n_{1j} and n_{2j}). This is because, in this case, axial wavenumbers k^{V}_j are not integer multiples of π/h and the integral from $z=-\pi/h$ to π/h in the dot products (29) cannot be easily simplified.

However, if the horizontal decomposition $\mathbf{v}^{\mathrm{H}}_{\mathrm{base}}$ is chosen, it is possible to achieve such a simplification. In this case, the forced modes have axial wavenumbers k^{H}_j that are odd multiples of π/h. These forced modes will interact with the resonant free Kelvin modes if the dot product between $\mathbf{N}\left(\mathbf{v}^{\mathrm{H}}_j e^{\mathrm{i}(\omega t+\varphi)}+\mathrm{c.c.},\widetilde{\mathbf{v}}_0\right)$ and $\mathbf{v}_l e^{\mathrm{i}(\omega_l t+m_l\varphi)}$ lead to a non-zero integral over z. Since these terms have the following z-Fourier components

$$\mathbf{v}_l : z\text{-Fourier components } \pm k_l, \tag{31a}$$

$$\mathbf{N}\left(\mathbf{v}^{\mathrm{H}}_j e^{\mathrm{i}(\omega t+\varphi)}+\mathrm{c.c.},\widetilde{\mathbf{v}}_0\right) : z\text{-Fourier components } k^{\mathrm{H}}_j \pm k_l, -k^{\mathrm{H}}_j \pm k_l, \tag{31b}$$

and since k_1 and k_2 have different parities and k^{H}_j is an odd multiple of π/h, the axial wavenumber of the dot product only contains even multiple of π/h, i.e. multiple of $2\pi/h$. As a consequence, the integral over z is non-zero only if the axial wavenumber of the dot product is equal to zero. It follows that only two forced modes of $\mathbf{v}^{\mathrm{H}}_{\mathrm{base}}$ will interact with the resonant free Kelvin modes and their axial wavenumbers are

$$k^{\mathrm{H}}_j = k_{j_1} = |k_2 - k_1| \quad \text{and} \quad k^{\mathrm{H}}_j = k_{j_2} = |k_2 + k_1|\,. \tag{32}$$

It means that there are only two forced modes j_1 and j_2 which give non zero coefficients n_{1j} and n_{2j} such that the infinite summations in (26) becomes sum of only two terms. The coefficients c_1 and c_2 thus simplify to

$$c_1 = \frac{\overline{d}_{12} + n_{1s} + \overline{a^{\mathrm{H}}_{j_1}} n_{1j_1} + \overline{a^{\mathrm{H}}_{j_2}} n_{1j_2}}{\langle \mathbf{v}_1, \mathcal{I}\mathbf{v}_1\rangle}, \tag{33a}$$

$$c_2 = \frac{d_{21} + n_{2s} + a^{\mathrm{H}}_{j_1} n_{2j_1} + a^{\mathrm{H}}_{j_2} n_{2j_2}}{\langle \mathbf{v}_2, \mathcal{I}\mathbf{v}_2\rangle}. \tag{33b}$$

3.3.5 Case of a resonant cylinder

In a resonant cylinder, the precession forces a flow that is dominated by a single forced mode, which is a Kelvin mode (i.e. a forced mode which satisfies the no-slip boundary conditions on the cylinder walls). In that case, the flow can become unstable if this forced Kelvin mode interacts constructively with two free Kelvin modes. As we have shown in a previous work, amplitude equations can be derived for a resonant cylinder Lagrange *et al.* (2011). In this section, we want to explain how to recover these amplitude equations from the amplitude equations of a non-resonant precessing fluid cylinder derived here in (26a,b) .

When a forced mode is resonant, its amplitude a_j predicted by the linear theory diverges. As shown by the equation (45), it happens when the dispersion relation $D(1,\omega,k_j)=0$ holds for an axial wavenumber k_j which is an odd multiple of π/h. For large Ekman numbers, the viscous effects saturate the amplitude of the forced Kelvin mode to an order $Ek^{-1/2}$ larger than the amplitudes of the shear flow and the others forced modes, see refs.(Gans, 1970; Meunier *et al.*, 2008). Thus, at main order the base flow $\mathbf{v}_{\text{base}}$ is a single forced Kelvin mode with amplitude $|\varepsilon| = O(RoEk^{-1/2})$. It follows that the summations in (26) are truncated to the index of that mode and the amplitude a_j must be replaced by ε/Ro. Since the terms $\overline{d}_{12}$, n_{1s}, d_{21} and n_{2s} are of order $O(1)$, they are negligible compared to ε/Ro and can be dropped in (26). The amplitude equations when the j-th forced mode is resonant thus become

$$\frac{dA_1}{d\tau} = A_2 \frac{\overline{\varepsilon} n_{1j}}{\langle \mathbf{v}_1, \mathcal{I}\mathbf{v}_1 \rangle} = n_1 \overline{\varepsilon} A_2, \tag{34a}$$

$$\frac{dA_2}{d\tau} = A_1 \frac{\varepsilon n_{2j}}{\langle \mathbf{v}_2, \mathcal{I}\mathbf{v}_2 \rangle} = n_2 \varepsilon A_1. \tag{34b}$$

As explained in §3.3.4, terms n_1 and n_2 are non-zeros only if the condition of resonance $|k_2 - k_1| = k_j = (2j-1)\pi/h$ or $|k_2 + k_1| = k_j = (2j-1)\pi/h$ is satisfied (together with similar conditions on m and ω: $m_2 - m_1 = 1$ and $\omega_2 - \omega_1 = \omega$).

Seeking solutions to the amplitude equations (34a,b) as growing exponentials $A_j \sim e^{\sigma t}$, yields an expression for the growth rate

$$\sigma = |\varepsilon| \sqrt{n_1 n_2}, \tag{35}$$

similar to the one obtained in Lagrange *et al.* (2011). As expected (based on similarities with the elliptic instability), the growth rate scales as the amplitude of the forced Kelvin mode. For large Ekman number, the growth rate of a resonant precessing fluid cylinder is thus an order $Ek^{-1/2}$ larger than the growth rate of the non-resonant case.

For example, for $h = 1.62$ and $\omega = 1.18$, the first Kelvin mode is forced at its first resonance and we recover (see Table 3 in Lagrange *et al.* (2011)) that the resonant combination $(6,1,1)$ has $n_1 = -1.672$, $n_2 = -2.456$, leading to a growth rate $\sigma = 2.026|\varepsilon|$.

3.3.6 Viscous effects

Amplitude equations (26a,b) have been derived under the assumption of an inviscid fluid. Accounting for viscosity, they modify to Lagrange *et al.* (2011)

$$\frac{dA_1}{d\tau} = c_1 A_2 - \alpha_1 A_1, \tag{36a}$$

$$\frac{dA_2}{d\tau} = c_2 A_1 - \alpha_2 A_2, \tag{36b}$$

with $\alpha_l = s_l Ek^{1/2} + v_l Ek$. The coefficients s_l represent the surface viscous damping of the free Kelvin modes due to Ekman layers on the cylinder walls.

They are complex numbers with a positive real part Lagrange *et al.* (2011). The coefficients v_l are real and represent the volume viscous damping of the free Kelvin modes. They come from the Laplace operator of the Navier-Stokes equations, and are proportional to $k_l^2 + \delta_l^2$, such that they strongly damp the free Kelvin modes with large axial and radial wavenumbers Lagrange *et al.* (2011).

The critical Rossby number for which the instability appears can be determined from the condition of a vanishing growth rate, leading to

$$|Ro_{\text{crit}}| = \left\{ \frac{\alpha_1^{\text{r}} \alpha_2^{\text{r}}}{c_1 c_2} \left[1 + \left(\frac{\alpha_1^{\text{i}} - \alpha_2^{\text{i}}}{\alpha_1^{\text{r}} + \alpha_2^{\text{r}}} \right)^2 \right] \right\}^{1/2}, \tag{37}$$

where α_l^{r} and α_l^{i} are respectively the real and imaginary parts of α_l. For large Ek, the volume viscous effects (which scale as Ek) are larger than the surface viscous effects (which scale as $Ek^{1/2}$), such that Ro_{crit} scales as $Ek^{3/2}$. On the contrary, for low Ek, surface viscous effects are dominant and Ro_{crit} scales as Ek Lagrange *et al.* (2011).

3.4 Numerical application far from a resonance

In this section we compute the inviscid growth rate of the precessing instability, given by (30), when the forced modes are not resonant. To do so, we first determine an aspect ratio h and a frequency ratio ω, such that the first 4 forced modes are away from a resonance, and such that combination of free Kelvin modes ($m_2 = 3, l_1 = 1, l_2 = 1$) forms a perfect triadic resonance with the first forced mode (see Fig. 3.6). These two conditions are illustrated in Fig. 3.7: the first 5 resonances of the first 4 forced modes are noted $\omega_{j,n}$ (n-th resonance of the j-th forced Kelvin mode) and are solutions to the dispersion relation

$$D\left(m_j, \omega_{j,n}, \frac{(4 - {\omega_{j,n}}^2)^{1/2}}{|\omega_{j,n}|} (2n-1)\frac{\pi}{h} \right) = 0. \tag{38}$$

The thick blue curve in Fig. 3.7 gives the aspect ratio and the frequency ratio for which the combination $(3, 1, 1)$ is resonant. This curve is the solution of the equation

$$\omega_2(k_2 = 2\pi/h, l_2 = 1, m_2 = 3) = \omega_1(k_1 = \pi/h, l_1 = 1, m_{1r} = 2) + \omega_{i,n}, \tag{39}$$

where $\omega_2(k_2 = 2\pi/h, l_2 = 1, m_2 = 3)$ means: the value of ω_2 for $k_2 = 2\pi/h$ and $l_2 = 1$ (first branch of the dispersion relation $m_2 = 3$).

In the present numerical investigations, we choose $h = 2.3$ and $\omega = 1.34$. It can be checked that for these aspect and frequency ratios, $(3, 1, 1)$ is a resonant point (Fig. 3.6). The theoretical axial vorticity fields of the corresponding free Kelvin modes, $m_1 = 2$ and $m_2 = 3$, are shown in Fig. 3.8. Since these modes correspond to the first branches of the dispersion relation ($l_1 = l_2 = 1$), their vorticity fields exhibit only one ring of 4 (for $m_1 = 2$) or 6 (for $m_2 = 3$) counter-rotating vortices.

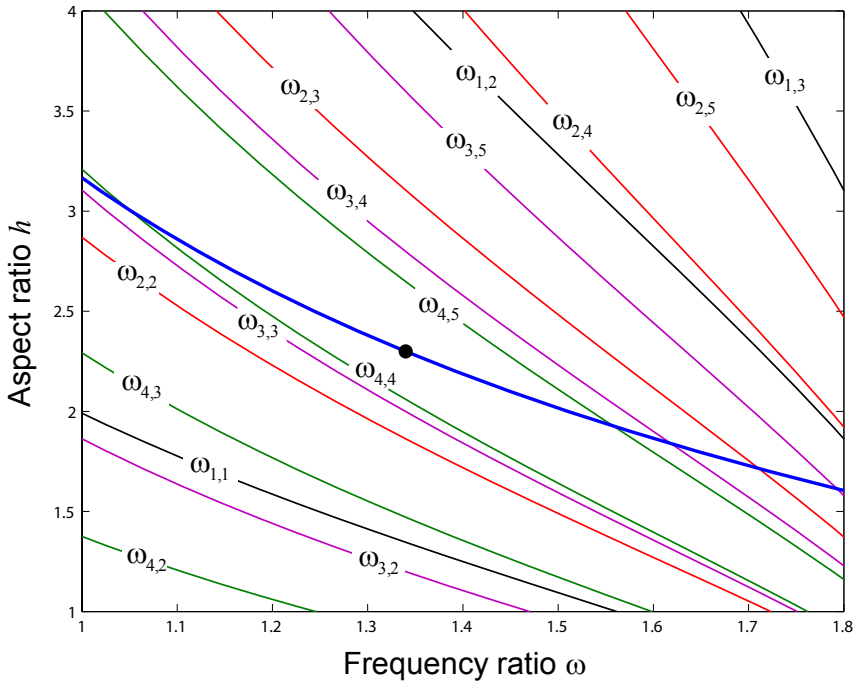

Figure 3.7: Resonance location in the ω–h plane. The resonances of the 1st (black curves), 2nd (red curves), 3rd (pink curves), 4th (green curves) forced modes are shown. The notation $\omega_{j,n}$ refers to the n-th resonance of the j-th forced mode. The blue thick line indicates the values of ω and h for which the unstable modes combination $(3, 1, 1)$ forms a perfect triadic resonance with the first forced mode (see Fig. 3.6). The black circle $(\omega = 1.34, h = 2.3)$ is the choice for the numerical application.

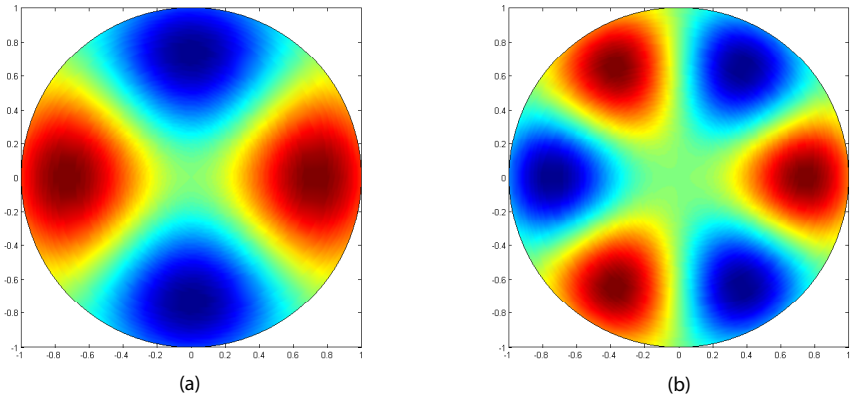

Figure 3.8: Theoretical axial vorticity fields of the free Kelvin modes $m_1 = 2$ (a) and $m_2 = 3$ (b) which are expected to grow for $h = 2.3$ and $\omega = 1.34$.

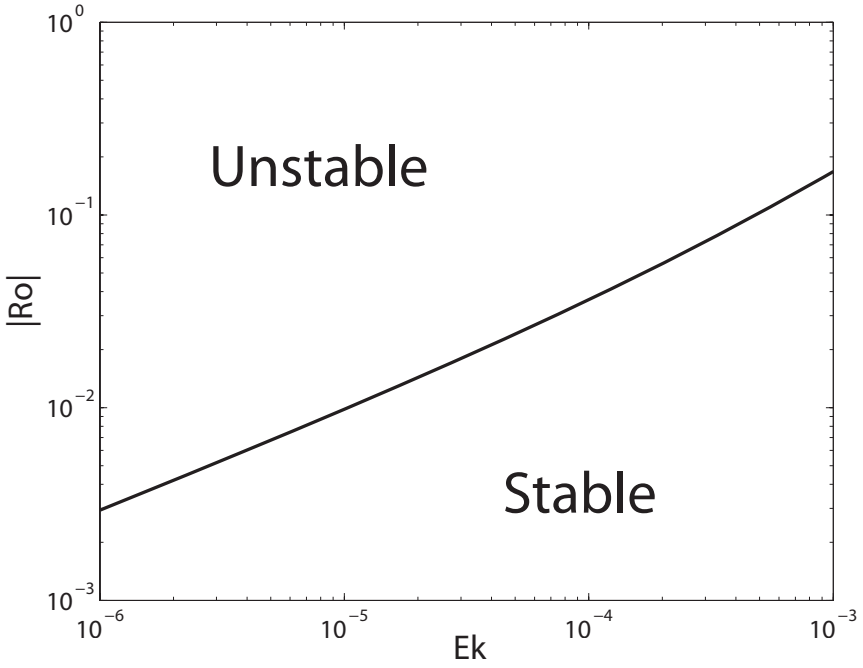

Figure 3.9: Stability diagram of the flow inside a precessing cylinder, for $h = 2.30$ and $\omega = 1.34$. The stable and unstable domains are separated by the solid line corresponding to the prediction (37).

$\langle \mathbf{v}_1, \mathcal{I}\mathbf{v}_1 \rangle$	$\overline{d}_{12}$	n_{1s}	n_{1j1}	n_{1j2}
27.1230	6.8448	1.1623	-12.7524	3.6628
		c_1	s_1	v_1
		-0.3940	$1.22 - 0.15\mathrm{i}$	34.37
$\langle \mathbf{v}_2, \mathcal{I}\mathbf{v}_2 \rangle$	d_{21}	n_{2s}	n_{2j1}	n_{2j2}
35.2671	-6.8448	21.8624	-23.9177	6.8697
		c_2	s_2	v_2
		-0.5683	$1.50 + 0.027\mathrm{i}$	39.08

Table 3.1: Values of the parameters appearing in the amplitude equations. The aspect ratio and the frequency ratio are $h = 2.30$ and $\omega = 1.34$. For these values, the combination $(m_2 = 3, l_1 = 1, l_2 = 1)$ is resonant and corresponds to a pair of free Kelvin modes $(m_1 = 2, \omega_1 = -0.466, k_1 = \pi/h)$ and $(m_2 = 3, \omega_2 = 0.874, k_2 = 2\pi/h)$. The forced modes are those with indices $j_1 = 1$, $j_2 = 2$ and have axial wavenumbers $k_{j_1} = \pi/h$ and $k_{j_2} = 3\pi/h$. Their amplitudes are $a^{\mathrm{H}}_{j_1} = 1.4983$ and $a^{\mathrm{H}}_{j_2} = 0.1130$.

The values needed to compute the inviscid growth rate given by (30) are listed in Table 5.1. For $h = 2.3$ and $\omega = 1.34$, we obtain a growth rate $\sigma_r = |Ro|\left(\sqrt{c_1 c_2}\right) = 0.4732|Ro|$. Since the combination $(3, 1, 1)$ corresponds to free Kelvin modes with simple radial and axial structures, volume viscous damping (which scale as $k_l^2 + \delta_l^2$) is small, which make these modes the perfect candidates for an instability. The stability diagram of the resonant combination $(3, 1, 1)$ is shown in Fig. 3.9 in the *Ek*–*Ro* plane: in this graph, the prediction from (37) is represented by a solid line that splits the *Ek*–*Ro* plane into a stable and an unstable domain.

3.5 Conclusion

In this paper, the instability of a fluid inside a precessing cylinder has been addressed theoretically. First, we have shown that the base flow can be written as a superposition of a vertical or horizontal shear flow and a sum of forced modes. The stability of this base flow has then been studied for a forcing at a non-resonant frequency, thus completing previous studies performed for resonant or near-resonant frequencies Lagrange *et al.* (2008, 2011). We have shown that the non-resonant base flow can trigger a triadic instability with two free Kelvin modes only if these modes have different axial parities. We also have obtained a prediction of the instability growth rate, showing that the inviscid growth rate is proportional to the Rossby number, *Ro*, and an order $Ek^{-1/2}$ smaller than the growth rate obtained for a resonant base flow. Finally, introducing viscous damping, we have given a prediction of Ro_{crit}, the critical Rossby number for which the flow becomes unstable, as a function of *Ek*: for large (resp. low) *Ek* numbers, Ro_{crit} scales as $Ek^{3/2}$ (resp. *Ek*).

We believe that the theoretical predictions provided in this paper will be valuable for future experimental and numerical studies of precessing flows performed at arbitrary frequencies. We shall note however that our analysis relies on the assumption of a small Rossby number, i.e. a small precession angle. For strong forcing, very different phenomena are expected (e.g. Kelvin-Helmholtz, centrifugal, or boundary layer instabilities), due to the generation of powerful zonal flows.

In closing, the precessional instability is typical of transition to turbulence in rotating flows. The presence of rotation ensures that energy is continuously provided to the flow. It also supports the existence of inertial waves that can lead to several instabilities (elliptic instability, libration instability, etc.). The structure of turbulence is also modified by the presence of the rotation because of the anisotropy induced. There is much more work to be done on this fascinating topic if we want to understand the mechanisms at play in turbulent rotating flows.

This study was carried out under CEA-CNRS contract No. 012171.

3.6 Appendix

3.6.1 Operators of the Euler equations, forced mode vector $\mathbf{v}_j$, amplitudes a_j^{V} and a_j^{H}, free Kelvin modes vectors $\mathbf{v}_l^+$ and $\mathbf{v}_l^-$

Operators used for the matrix formulation (3) of the Euler equations are

$$\mathcal{I} = \begin{pmatrix} 1 & 0 & 0 & 0 \\ 0 & 1 & 0 & 0 \\ 0 & 0 & 1 & 0 \\ 0 & 0 & 0 & 0 \end{pmatrix}, \mathcal{D} = \begin{pmatrix} 0 & 0 & -\mathrm{i} & 0 \\ 0 & 0 & 1 & 0 \\ \mathrm{i} & -1 & 0 & 0 \\ 0 & 0 & 0 & 0 \end{pmatrix},$$
$$\mathcal{M} = \begin{pmatrix} 0 & -2 & 0 & \frac{\partial}{\partial r} \\ 2 & 0 & 0 & \frac{1}{r}\frac{\partial}{\partial \varphi} \\ 0 & 0 & 0 & \frac{\partial}{\partial z} \\ \frac{\partial}{\partial r} + \frac{1}{r} & \frac{1}{r}\frac{\partial}{\partial \varphi} & \frac{\partial}{\partial z} & 0 \end{pmatrix}, \tag{40}$$

and

$$\mathbf{F}_0 = \begin{pmatrix} 0 \\ 0 \\ -r\omega \\ 0 \end{pmatrix}, \mathbf{N}\left(\mathbf{v}_1, \mathbf{v}_2\right) = \begin{pmatrix} \mathbf{u}_1 \times (\nabla \times \mathbf{u}_2) \\ 0 \end{pmatrix}. \tag{41}$$

The forced modes quadri-vector $\mathbf{v}_j^{\mathrm{V}}$ and $\mathbf{v}_j^{\mathrm{H}}$ are given by the same expression

$$\mathbf{v}_j^{\mathrm{V}} = \mathbf{v}_j^{\mathrm{H}} = 2 \begin{pmatrix} \left(\mathbf{w}_{1,\omega,k_j}\right)_r \mathrm{i} \sin\left(k_j z\right) \\ \left(\mathbf{w}_{1,\omega,k_j}\right)_\varphi \mathrm{i} \sin\left(k_j z\right) \\ \left(\mathbf{w}_{1,\omega,k_j}\right)_z \cos\left(k_j z\right) \\ \left(\mathbf{w}_{1,\omega,k_j}\right)_p \mathrm{i} \sin\left(k_j z\right) \end{pmatrix}, \tag{42}$$

with

$$\mathbf{w}_{m,\omega,k} = \begin{pmatrix} \frac{-1}{4-\omega^2}\left(\omega\delta J_m'\left(\delta r\right) + 2\frac{m}{r} J_m\left(\delta r\right)\right) \\ \frac{-\mathrm{i}}{4-\omega^2}\left(2\delta J_m'\left(\delta r\right) + \frac{\omega m}{r} J_m\left(\delta r\right)\right) \\ \mathrm{i}\frac{k}{\omega} J_m\left(\delta r\right) \\ -\mathrm{i} J_m\left(\delta r\right) \end{pmatrix}, \tag{43}$$

and where J_m is the Bessel function of the first kind, J_m' its derivative and $\delta = \sqrt{4-\omega^2}k/|\omega|$. However, they have been named differently since they have different boundary conditions and thus different axial wavenumbers k_j^{V} or k_j^{H}. For the vertical shear, the radial wavenumber δ is imposed by the boundary conditions and k is deduced from the dispersion relation whereas for the horizontal shear, the axial wavenumber is imposed by the boundary conditions and δ is given again by $\delta = \sqrt{4-\omega^2}k/|\omega|$.

The dispersion relation is

$$D(m,\omega,k) = \omega\delta J_m'\left(\delta\right) + 2m J_m\left(\delta\right). \tag{44}$$

The amplitudes of the forced modes are

$$a_j^{\mathrm{V}} = \frac{\omega^2}{(\omega-2)(k_j^2+1)k_j J_1(\delta_j)\cos(k_j h/2)}, \tag{45a}$$

$$a_j^{\mathrm{H}} = -\frac{2h(-1)^j\omega(2+\omega)}{\pi^2(2j-1)^2(\omega\delta_j J_1'(\delta_j) + 2J_1(\delta_j))}. \tag{45b}$$

Vectors $\mathbf{v}_l^+$ and $\mathbf{v}_l^-$ appearing in (20) are

$$\mathbf{v}_l^+ = 2\begin{pmatrix} \left(\mathbf{w}_{m_l,\omega_l,k_l^+}\right)_r \cos\left(k_l^+ z\right) \\ \left(\mathbf{w}_{m_l,\omega_l,k_l^+}\right)_\varphi \cos\left(k_l^+ z\right) \\ \left(\mathbf{w}_{m_l,\omega_l,k_l^+}\right)_z \mathrm{i}\sin\left(k_l^+ z\right) \\ \left(\mathbf{w}_{m_l,\omega_l,k_l^+}\right)_p \cos\left(k_l^+ z\right) \end{pmatrix}, \quad \mathbf{v}_l^- = 2\begin{pmatrix} \left(\mathbf{w}_{m_l,\omega_l,k_l^-}\right)_r \mathrm{i}\sin\left(k_l^- z\right) \\ \left(\mathbf{w}_{m_l,\omega_l,k_l^-}\right)_\varphi \mathrm{i}\sin\left(k_l^- z\right) \\ \left(\mathbf{w}_{m_l,\omega_l,k_l^-}\right)_z \cos\left(k_l^- z\right) \\ \left(\mathbf{w}_{m_l,\omega_l,k_l^-}\right)_p \mathrm{i}\sin\left(k_l^- z\right) \end{pmatrix}. \tag{46}$$

3.6.2 Derivation of amplitude equations

In this Appendix, we derive the amplitude equations (26), starting from the order *Ro* equation (25) that we report here

$$\left(\frac{\partial \mathcal{I}}{\partial t} + \mathcal{M}\right)\widetilde{\mathbf{v}}_1 = \mathbf{N}\left(\mathbf{v}_{\text{base}}, \widetilde{\mathbf{v}}_0\right) + \mathbf{N}\left(\widetilde{\mathbf{v}}_0, \mathbf{v}_{\text{base}}\right) + \left[\left(\mathcal{D}e^{\mathrm{i}(\omega t+\varphi)} + \text{c.c.}\right) - \frac{\partial \mathcal{I}}{\partial \tau}\right]\widetilde{\mathbf{v}}_0. \tag{47}$$

As explained in the core of the manuscript, a solvability condition is obtained by taking the dot product of this equation with $\mathbf{v}_l e^{\mathrm{i}(\omega_l t + m_j \varphi)}$, $l = 1, 2$. The problem being self adjoint, we have $\left\langle \mathbf{v}_l e^{\mathrm{i}(\omega_l t + m_l \varphi)}, \left(\partial \mathcal{I}/\partial t + \mathcal{M}\right)\widetilde{\mathbf{v}}_1 \right\rangle = 0$, so that, we are left with

$$\begin{aligned} \left\langle \mathbf{v}_l e^{\mathrm{i}(\omega_l t + m_l \varphi)}, \frac{\partial \mathcal{I}}{\partial \tau}\widetilde{\mathbf{v}}_0 \right\rangle = & \left\langle \mathbf{v}_l e^{\mathrm{i}(\omega_l t + m_l \varphi)}, \left(\mathcal{D}e^{\mathrm{i}(\omega t+\varphi)} + \text{c.c.}\right)\widetilde{\mathbf{v}}_0 \right\rangle \\ & + \left\langle \mathbf{v}_l e^{\mathrm{i}(\omega_l t + m_l \varphi)}, \mathbf{N}\left(\mathbf{v}_{\text{base}}, \widetilde{\mathbf{v}}_0\right) \right\rangle \\ & + \left\langle \mathbf{v}_l e^{\mathrm{i}(\omega_l t + m_l \varphi)}, \mathbf{N}\left(\widetilde{\mathbf{v}}_0, \mathbf{v}_{\text{base}}\right) \right\rangle. \end{aligned} \tag{48}$$

The computation of the LHS term is straightforward and follows from the linearity of the dot product and the orthogonality of the free Kelvin modes.

Introducing the expression of $\widetilde{\mathbf{v}}_0$ given by (21) gives a LHS term equal to

$$
\begin{aligned}
&\left\langle \mathbf{v}_l e^{\mathrm{i}(\omega_l t+m_l\varphi)}, \sum_{l=1}^{2} \frac{dA_j}{d\tau}\mathcal{I}\left(\mathbf{v}_j e^{\mathrm{i}(\omega_j t+m_j\varphi)}\right)\right\rangle \\
&+\left\langle \mathbf{v}_l e^{\mathrm{i}(\omega_l t+m_l\varphi)}, \sum_{j=1}^{2} \frac{d\overline{A_j}}{d\tau}\mathcal{I}\left(\overline{\mathbf{v}_j} e^{-\mathrm{i}(\omega_j t+m_j\varphi)}\right)\right\rangle \\
&=\sum_{j=1}^{2}\frac{dA_j}{d\tau}\left\langle \mathbf{v}_l e^{\mathrm{i}(\omega_l t+m_l\varphi)}, e^{\mathrm{i}(\omega_j t+m_j\varphi)}\mathcal{I}\mathbf{v}_j\right\rangle \\
&+\sum_{j=1}^{2}\frac{d\overline{A_j}}{d\tau}\left\langle \mathbf{v}_l e^{\mathrm{i}(\omega_l t+m_l\varphi)}, e^{-\mathrm{i}(\omega_j t+m_j\varphi)}\mathcal{I}\overline{\mathbf{v}_j}\right\rangle, \qquad (49a)\\
&=\sum_{j=1}^{2}\frac{dA_j}{d\tau}\underbrace{\left\langle \mathbf{v}_l, e^{\mathrm{i}[(-\omega_l+\omega_j)t+(-m_l+m_j)\varphi]}\mathcal{I}\mathbf{v}_j\right\rangle}_{\neq 0 \text{ if } j=l} \\
&+\sum_{j=1}^{2}\frac{d\overline{A_j}}{d\tau}\underbrace{\left\langle \mathbf{v}_l, e^{\mathrm{i}[(-\omega_l-\omega_j)t+(-m_l-m_j)\varphi]}\mathcal{I}\overline{\mathbf{v}_j}\right\rangle}_{0 \text{ because } \propto \int_0^{2\pi} e^{-\mathrm{i}\left(m_l+m_j\right)\varphi}d\varphi}, \qquad (49b)\\
&=\frac{dA_l}{d\tau}\left\langle \mathbf{v}_l, \mathcal{I}\mathbf{v}_l\right\rangle. \qquad (49c)
\end{aligned}
$$

Eq. (49b) shows that it is not necessary to take into account the c.c. part of $A_j\mathbf{v}_j e^{\mathrm{i}(\omega_j t+m_j\varphi)}$ in (48) since it leads to 0 integral terms. This observation still holds for computations with operators $\mathcal{D}$, $\overline{\mathcal{D}}$ and $\mathbf{N}$ since they do not change the wavenumbers in the exponential when applied to $\mathbf{v}_l e^{\mathrm{i}(\omega_l t+m_l\varphi)}$. Therefore, the c.c. part of $A_j\mathbf{v}_j e^{\mathrm{i}(\omega_j t+m_j\varphi)}$ will be omitted in the next computations.

Plugging (49c) into (48) yields the amplitude equations

$$
\begin{aligned}
\frac{dA_l}{d\tau} &= \frac{\left\langle \mathbf{v}_l e^{\mathrm{i}(\omega_l t+m_l\varphi)}, \left(\mathcal{D}e^{\mathrm{i}(\omega t+\varphi)}+\text{c.c.}\right)\widetilde{\mathbf{v}}_0\right\rangle}{\left\langle \mathbf{v}_l, \mathcal{I}\mathbf{v}_l\right\rangle} \\
&+\frac{\left\langle \mathbf{v}_l e^{\mathrm{i}(\omega_l t+m_l\varphi)}, \mathbf{N}\left(\mathbf{v}_{\text{base}}, \widetilde{\mathbf{v}}_0\right)+\mathbf{N}\left(\widetilde{\mathbf{v}}_0, \mathbf{v}_{\text{base}}\right)\right\rangle}{\left\langle \mathbf{v}_l, \mathcal{I}\mathbf{v}_l\right\rangle}. \qquad (50)
\end{aligned}
$$

We now proceed with the calculation of the RHS terms of (50). Computations are performed with $l=1$ so that results for $l=2$ will follow from the permutation of indices $(1,2)\to(2,1)$. Also, from the operators properties presented in §3.2.2, we know that the free Kelvin modes $\mathbf{v}_1 e^{\mathrm{i}(\omega_1 t+m_1\varphi)}$ and $\mathbf{v}_2 e^{\mathrm{i}(\omega_2 t+m_2\varphi)}$ must have different z-parities to give nonzero coupling terms. Thus, for $l=1$ we can directly substitute in (50) vector $\widetilde{\mathbf{v}}_0$ by $\mathbf{v}_2 e^{\mathrm{i}(\omega_2 t+m_2\varphi)}$

and (50) writes

$$\begin{aligned}\frac{dA_1}{d\tau} &= \frac{\left\langle \mathbf{v}_1 e^{\mathrm{i}(\omega_1 t+m_1\varphi)}, \left(\mathcal{D}e^{\mathrm{i}(\omega t+\varphi)}+\text{c.c.}\right)\mathbf{v}_2 e^{\mathrm{i}(\omega_2 t+m_2\varphi)}\right\rangle}{\langle \mathbf{v}_1, \mathcal{I}\mathbf{v}_1\rangle} \\ &+ \frac{\left\langle \mathbf{v}_1 e^{\mathrm{i}(\omega_1 t+m_1\varphi)}, \mathbf{N}\left(\mathbf{v}_{\text{base}}, \mathbf{v}_2 e^{\mathrm{i}(\omega_2 t+m_2\varphi)}\right)\right\rangle}{\langle \mathbf{v}_1, \mathcal{I}\mathbf{v}_1\rangle} \\ &+ \frac{\left\langle \mathbf{v}_1 e^{\mathrm{i}(\omega_1 t+m_1\varphi)}, \mathbf{N}\left(\mathbf{v}_2 e^{\mathrm{i}(\omega_2 t+m_2\varphi)}, \mathbf{v}_{\text{base}}\right)\right\rangle}{\langle \mathbf{v}_1, \mathcal{I}\mathbf{v}_1\rangle}. \end{aligned} \tag{51}$$

In what follows we compute each of the terms in the RHS of (51) and we assume that the resonance conditions (24) are fulfilled in order to drop the exponential terms.

3.6.3 Computation of $\left\langle \mathbf{v}_1 e^{\mathrm{i}(\omega_1 t+m_1\varphi)}, \left(\mathcal{D}e^{\mathrm{i}(\omega t+\varphi)}+\text{c.c.}\right)\left(\mathbf{v}_2 e^{\mathrm{i}(\omega_2 t+m_2\varphi)}\right)\right\rangle$

Expanding the complex conjugate leads to 2 terms

$$\begin{aligned}&\left\langle \mathbf{v}_1 e^{\mathrm{i}(\omega_1 t+m_1\varphi)}, e^{\mathrm{i}(\omega t+\varphi)} e^{\mathrm{i}(\omega_2 t+m_2\varphi)}\mathcal{D}\mathbf{v}_2\right\rangle \\ &\left\langle \mathbf{v}_1 e^{\mathrm{i}(\omega_1 t+m_1\varphi)}, e^{-\mathrm{i}(\omega t+\varphi)} e^{\mathrm{i}(\omega_2 t+m_2\varphi)}\overline{\mathcal{D}}\mathbf{v}_2\right\rangle. \end{aligned} \tag{52}$$

The first term vanishes because the azimuthal Fourier components are different on each side of the dot product such that the integral over φ gives zero. In contrast, in the second term, the azimuthal Fourier components are equal and can thus be dropped. This term can thus be written as

$$\overline{d}_{12} = \langle \mathbf{v}_1, \overline{\mathcal{D}}\mathbf{v}_2\rangle. \tag{53}$$

3.6.4 Computation of $\left\langle \mathbf{v}_1 e^{\mathrm{i}(\omega_1 t+m_1\varphi)}, \mathbf{N}\left(\mathbf{v}_{\text{base}}, \mathbf{v}_2 e^{\mathrm{i}(\omega_2 t+m_2\varphi)}\right)\right\rangle$

Here $\mathbf{v}_{\text{base}} = \mathbf{v}_b e^{\mathrm{i}(\omega t+\varphi)} + \text{c.c.}$ is the base flow given either by (8) or (9) depending on which decomposition (vertical or horizontal shear) is used to express the base flow. We have

$$\begin{aligned}&\left\langle \mathbf{v}_1 e^{\mathrm{i}(\omega_1 t+m_1\varphi)}, \mathbf{N}\left(\mathbf{v}_{\text{base}}, \mathbf{v}_2 e^{\mathrm{i}(\omega_2 t+m_2\varphi)}\right)\right\rangle \\ &= \left\langle \mathbf{v}_1 e^{\mathrm{i}(\omega_1 t+m_1\varphi)}, \mathbf{N}\left(\mathbf{v}_b e^{\mathrm{i}(\omega t+\varphi)}+\text{c.c.}, \mathbf{v}_2 e^{\mathrm{i}(\omega_2 t+m_2\varphi)}\right)\right\rangle, &\text{(54a)} \\ &= \left\langle \mathbf{v}_1 e^{\mathrm{i}(\omega_1 t+m_1\varphi)}, \mathbf{N}\left(\mathbf{v}_b e^{\mathrm{i}(\omega t+\varphi)}, \mathbf{v}_2 e^{\mathrm{i}(\omega_2 t+m_2\varphi)}\right)\right\rangle \\ &+ \left\langle \mathbf{v}_1 e^{\mathrm{i}(\omega_1 t+m_1\varphi)}, \mathbf{N}\left(\overline{\mathbf{v}_b} e^{-\mathrm{i}(\omega t+\varphi)}, \mathbf{v}_2 e^{\mathrm{i}(\omega_2 t+m_2\varphi)}\right)\right\rangle, &\text{(54b)} \\ &= \left\langle \mathbf{v}_1 e^{\mathrm{i}(\omega_1 t+m_1\varphi)}, e^{\mathrm{i}(\omega t+\varphi)} e^{\mathrm{i}(\omega_2 t+m_2\varphi)}\mathbf{N}_{\mathrm{i}m_2}\left(\mathbf{v}_b, \mathbf{v}_2\right)\right\rangle \\ &+ \left\langle \mathbf{v}_1 e^{\mathrm{i}(\omega_1 t+m_1\varphi)}, e^{-\mathrm{i}(\omega t+\varphi)} e^{\mathrm{i}(\omega_2 t+m_2\varphi)}\mathbf{N}_{\mathrm{i}m_2}\left(\overline{\mathbf{v}_b}, \mathbf{v}_2\right)\right\rangle, &\text{(54c)} \end{aligned}$$

where $\mathbf{N}_{\mathrm{i}m_2}$ corresponds to operator $\mathbf{N}$ where $d/d\varphi$ has been replaced by $\mathrm{i}m_2$. As previously, the first term vanishes and the exponential can be dropped

from the second term. Introducing the expression of $\mathbf{v}_b$ makes this whole term equal to

$$\left\langle \mathbf{v}_1, \mathbf{N}_{\mathrm{i}m_2}\left(\overline{\mathbf{v}_s} + \sum_{j=1}^{\infty} \overline{a_j \mathbf{v}_j}, \mathbf{v}_2\right)\right\rangle = n_{1\bar{s}2} + \sum_{j=1}^{\infty} \overline{a_j} n_{1\bar{j}2}, \tag{55a}$$

$$\text{with} \quad n_{1\bar{s}2} = \left\langle \mathbf{v}_1, \mathbf{N}_{\mathrm{i}m_2}\left(\overline{\mathbf{v}_s}, \mathbf{v}_2\right)\right\rangle \qquad \text{and} \quad n_{1\bar{j}2} = \left\langle \mathbf{v}_1, \mathbf{N}_{\mathrm{i}m_2}\left(\overline{\mathbf{v}_j}, \mathbf{v}_2\right)\right\rangle, \tag{55b}$$

3.6.5 Computation of $\left\langle \mathbf{v}_1 e^{\mathrm{i}(\omega_1 t + m_1\varphi)}, \mathbf{N}\left(\mathbf{v}_2 e^{\mathrm{i}(\omega_2 t + m_2\varphi)}, \mathbf{v}_{\text{base.}}\right)\right\rangle$

We have

$$\begin{aligned}
&\left\langle \mathbf{v}_1 e^{\mathrm{i}(\omega_1 t + m_1\varphi)}, \mathbf{N}\left(\mathbf{v}_2 e^{\mathrm{i}(\omega_2 t + m_2\varphi)}, \mathbf{v}_{\text{base}}\right)\right\rangle \\
&= \left\langle \mathbf{v}_1 e^{\mathrm{i}(\omega_1 t + m_1\varphi)}, \mathbf{N}\left(\mathbf{v}_2 e^{\mathrm{i}(\omega_2 t + m_2\varphi)}, \mathbf{v}_b e^{\mathrm{i}(\omega t + \varphi)} + \text{c.c.}\right)\right\rangle, \qquad (56a)\\
&= \left\langle \mathbf{v}_1 e^{\mathrm{i}(\omega_1 t + m_1\varphi)}, \mathbf{N}\left(\mathbf{v}_2 e^{\mathrm{i}(\omega_2 t + m_2\varphi)}, \mathbf{v}_b e^{\mathrm{i}(\omega t + \varphi)}\right)\right\rangle \\
&+ \left\langle \mathbf{v}_1 e^{\mathrm{i}(\omega_1 t + m_1\varphi)}, \mathbf{N}\left(\mathbf{v}_2 e^{\mathrm{i}(\omega_2 t + m_2\varphi)}, \overline{\mathbf{v}_b} e^{-\mathrm{i}(\omega t + \varphi)}\right)\right\rangle, \qquad (56b)\\
&= \left\langle \mathbf{v}_1 e^{\mathrm{i}(\omega_1 t + m_1\varphi)}, e^{\mathrm{i}(\omega_2 t + m_2\varphi)} e^{\mathrm{i}(\omega t + \varphi)} \mathbf{N}_{\mathrm{i}}\left(\mathbf{v}_2, \mathbf{v}_b\right)\right\rangle \\
&+ \left\langle \mathbf{v}_1 e^{\mathrm{i}(\omega_1 t + m_1\varphi)}, e^{\mathrm{i}(\omega_2 t + m_2\varphi)} e^{-\mathrm{i}(\omega t + \varphi)} \mathbf{N}_{-\mathrm{i}}\left(\mathbf{v}_2, \overline{\mathbf{v}_b}\right)\right\rangle, \qquad (56c)
\end{aligned}$$

where $\mathbf{N}_{\mathrm{i}}$ and $\mathbf{N}_{-\mathrm{i}}$ correspond to operator $\mathbf{N}$ where $d/d\varphi$ has been replaced by i and $-\mathrm{i}$, respectively. As previously, the first term vanishes and the exponentials can be dropped from the second term. Introducing the expression of $\mathbf{v}_b$ makes this whole term equal to

$$\left\langle \mathbf{v}_1, \mathbf{N}_{-\mathrm{i}}\left(\mathbf{v}_2, \overline{\mathbf{v}_s} + \sum_{j=1}^{\infty} \overline{a_j \mathbf{v}_j}\right)\right\rangle = n_{12\bar{s}} + \sum_{j=1}^{\infty} \overline{a_j} n_{12\bar{j}}, \tag{57a}$$

$$\text{with} \quad n_{12\bar{s}} = \left\langle \mathbf{v}_1, \mathbf{N}_{-\mathrm{i}}\left(\mathbf{v}_2, \overline{\mathbf{v}_s}\right)\right\rangle \qquad \text{and} \quad n_{12\bar{j}} = \left\langle \mathbf{v}_1, \mathbf{N}_{-\mathrm{i}}\left(\mathbf{v}_2, \overline{\mathbf{v}_j}\right)\right\rangle \tag{57b}$$

3.6.6 Conditions of resonance and amplitude equations

Collecting (53), (55b) and (57b) together, the amplitude equations (50) rewrite

$$\frac{dA_1}{d\tau} = A_2 \frac{\overline{d}_{12} + n_{1s} + \sum_{j=1}^{\infty} \overline{a_j} n_{1j}}{\langle \mathbf{v}_1, \mathcal{I}\mathbf{v}_1\rangle}, \tag{58a}$$

$$\frac{dA_2}{d\tau} = A_1 \frac{d_{21} + n_{2s} + \sum_{j=1}^{\infty} a_j n_{2j}}{\langle \mathbf{v}_2, \mathcal{I}\mathbf{v}_2\rangle}, \tag{58b}$$

where coefficients in (58a) are

$$\overline{d}_{12} = \left\langle \mathbf{v}_1, \overline{\mathcal{D}}\mathbf{v}_2\right\rangle, \tag{59a}$$

$$n_{1s} = n_{1\bar{s}2} + n_{12\bar{s}} = \left\langle \mathbf{v}_1, \mathbf{N}_{\mathrm{i}m_2}\left(\overline{\mathbf{v}_s}, \mathbf{v}_2\right)\right\rangle + \left\langle \mathbf{v}_1, \mathbf{N}_{-\mathrm{i}}\left(\mathbf{v}_2, \overline{\mathbf{v}_s}\right)\right\rangle, \tag{59b}$$

$$n_{1j} = n_{1\bar{j}2} + n_{12\bar{j}} = \left\langle \mathbf{v}_1, \mathbf{N}_{\mathrm{i}m_2}\left(\overline{\mathbf{v}_j}, \mathbf{v}_2\right)\right\rangle + \left\langle \mathbf{v}_1, \mathbf{N}_{-\mathrm{i}}\left(\mathbf{v}_2, \overline{\mathbf{v}_j}\right)\right\rangle. \tag{59c}$$

Coefficients in (58b) are

$$d_{21} = \langle \mathbf{v}_2, \mathcal{D}\mathbf{v}_1 \rangle = -\overline{d}_{12}, \tag{60a}$$

$$n_{2s} = n_{2s1} + n_{21s} = \langle \mathbf{v}_2, \mathbf{N}_{\mathrm{i}m_1}(\mathbf{v}_s, \mathbf{v}_1) \rangle + \langle \mathbf{v}_2, \mathbf{N}_{\mathrm{i}}(\mathbf{v}_1, \mathbf{v}_s) \rangle, \tag{60b}$$

$$n_{2j} = n_{2j1} + n_{21j} = \langle \mathbf{v}_2, \mathbf{N}_{\mathrm{i}m_1}(\mathbf{v}_j, \mathbf{v}_1) \rangle + \langle \mathbf{v}_2, \mathbf{N}_{\mathrm{i}}(\mathbf{v}_1, \mathbf{v}_j) \rangle. \tag{60c}$$

Bibliography

Agrawal, B. N. 1993 Dynamics characteristics of liquid motion in partially filled tanks of a spinning spacecraft. *J. Guid. Control Dynam.* **16** (4), 636–640.

Bao, G. W. & Pascal, M. 1997 Stability of a spinning liquid filled spacecraft. *Appl. Mech.* **67**, 407–421.

Cébron, D., Bars, M. L. & Maubert, P. 2011 Magnetohydrodynamic simulations of the elliptical instability in triaxial ellipsoids. *Geophys. and Astrophys. Fluid Dyn.* **106**, 524–546.

Fukumoto, Y. 2003 The three dimensional instability of a strained vortex tube revisited. *J. Fluid Mech.* **493**, 287–318.

Fultz, D. 1959 A note on overstability and elastoid-inertia oscillations of kelvin, solberg and bjerknes. *J. Meteorol.* **16**, 199–208.

Gailitis, A., Lielaussis, O., Platacis, E., Stefani, F. & Gerbeth, G. 2002 Laboratory experiments on hydromagnetic dynamos. *Rev. Mod. Phys.* **74**, 973.

Gans, R. F. 1970 On the precession of a resonant cylinder. *J. Fluid Mech.* **476**, 865–872.

Gans, R. F. 1984 Dynamics of a near-resonant fluid-filled gyroscope. *AIAA J.* **22**, 1465–1471.

Garg, S. C., Furunoto, N. & Vanyo, J. P. 1986 Spacecraft nutational instability prediction by energy dissipation measurments. *J. Guid.* **9** (3), 357–361.

Greenspan, H. P. 1968 *The theory of rotating fluids*. Cambridge University Press.

Grote, F. & Busse, H. 2001 Dynamics of convection and dynamos in rotating spherical fluid shells. *Fluid Dyn. Res.* **28**, 349–368.

Grote, F., Busse, H. & Tilgner, A. 1999 Convection driven quadrupolar dynamos in rotating spherical shells. *Phys. Rev. E* **60**, R5025.

Grote, F., Busse, H. & Tilgner, A. 2000 Regular and chaotic spherical dynamos. *Phys. Earth Planet. Inter.* **117**, 259.

Herbert, T. 1986 Viscous fluid motion in a spinning and nutating cylinder. *J. Fluid Mech.* **167**, 181–198.

Karpov, B. G. 1965 *Ballistic Research Labs. Maryland, U. S., Report BRL R 1302* .

Kelvin, L. 1880 Vibrations of a columnar vortex. *Phil. Mag.* **10**, 155–168.

Kerswell, R. R. 1996 Upper bounds on the energy dissipation in turbulent precession,. *J. Fluid Mech.* **321**, 335–370.

Kerswell, R. R. & Barenghi, C. F. 1995 On the viscous decay rates of inertial waves in a rotating cylinder. *J. Fluid Mech.* **285**, 203–214.

Kobine, J. J. 1995 Inertial wave dynamics in a rotating and precessing cylinder. *J. Fluid Mech.* **303**, 233–252.

Kong, D., Cui, Z., Liao, X. & Zhang, K. 2015 On the transition from the laminar to disordered flow in a precessing spherical-like cylinder. *Geophys. Astrophys. Fluid Dyn.* **109**, 62–83.

Lagrange, R., Eloy, C., Nadal, F. & Meunier, P. 2008 Instability of a fluid inside a precessing cylinder. *Physics of Fluids.* **20(8)**, 081701.

Lagrange, R., Meunier, P., Eloy, C. & Nadal, F. 2009 Dynamics of a fluid inside a precessing cylinder. *Mechanics and Industry.* **10**, 187–194.

Lagrange, R., Meunier, P., Nadal, F. & Eloy, C. 2011 Precessional instability of a fluid cylinder. *Journal of Fluid Mechanics* **666**, 104–145.

Lambelin, J. P., Nadal, F., Lagrange, R. & Sarthou, A. 2009 Non-resonant viscous theory for the stability of a fluid-filled gyroscope. *Journal of Fluid Mechanics* **639**, 167–194.

Loper, D. E. 1975 Torque balance and energy budget for the precesionally driven dynamo. *Phys. Earth Planet. Inter.* **43**, 43.

Malkus, W. V. R. 1989 An experimental study of global instabilities due to tidal (elliptical) distortion of a rotating elastic cylinder. *Geophys. Astrophys. Fluid Dynamics* **48**, 123–134.

Manasseh, R. 1992 Breakdown regimes of inertia waves in a precessing cylinder. *J. Fluid Mech.* **243**, 261–296.

Manasseh, R. 1994 Distorsions of inertia waves in a precessing cylinder forced near its fundamental mode resonance. *J. Fluid Mech.* **265**, 345–370.

Manasseh, R. 1996 Nonlinear behaviour of contained inertia waves. *J. Fluid Mech.* **315**, 151–173.

McEwan, A. D. 1970 Inertial oscillations in a rotating fluid cylinder. *J. Fluid Mech.* **40** (3), 603–640.

Meunier, P., Eloy, C., Lagrange, R. & Nadal, F. 2008 A rotating fluid cylinder subject to weak precession. *J. Fluid Mech.* **599**, 405–440.

Nore, C., Léorat, J., Guermond, J. & Luddens, F. 2011 Nonlinear dynamo action in a precessing cylindrical container. *Phys. Rev. E* **84**, 016317.

Pocha, J. J. 1987 An experimental investigation of spacecraft sloshing. *Space Commun. Broadcasting* **5**, 323–332.

Roberts, P. H. & Gubbins, D. 1987 Origin of the main field: Kinematics. *Geomagnetism, Ed. J. A. Jacobs, Academic Press* **2**, 185–249.

Rochester, M. G., Jacobs, J. A., Smylie, D. E. & Chong, K. F. 1975 Can precession power the geomagnetic dynamo? *Geophys. J. R. Astron. Soc.* **43**, 661.

Stewartson, K. 1958 On the stability of a spinning top containing liquid. *J. Fluid Mech.* **5**, 577–592.

Thompson, R. 1970 Diurnal tides and shear instabilities in a rotating cylinder. *J. Fluid Mech.* **40**, 737–751.

Tilgner, A. 2000 Oscillatory shear layer in source driven flows in an unbounded rotating fluid. *Phys. Fluids* **12**, 1101–1111.

Tilgner, A. 2005 Precession driven dynamos. *Phys. Fluids* **17**, 034104.

Vanyo, J. P., Wilde, P. & Cardin, P. 1995 Experiments on precessing flows in the earth's liquid core. *Geophys. J. Int.* **121**, 136–142.

4. INSTABILITÉS DE FLAMBAGE/PLISSEMENT

Une structure constituée d'un film mince (épaisseur h_F, module d'Young E_F, coefficient de Poisson ν_F) attaché à un substrat plan semi-infini (épaisseur h_S, module d'Young E_S, coefficient de Poisson ν_S), devient instable lorsqu'elle est soumise à une contrainte (axiale ou bi-axiale) supérieure à un chargement critique.

Lorsque le substrat est beaucoup plus épais que le film, des plis, voir Fig. 4.1, se forment à la surface de ce dernier : on parle alors d'une instabilité (locale) de plissement (wrinkling en Anglais). Le principal objectif des approches analytiques est de caractériser l'effet des paramètres, comme le rapport des épaisseurs h_F/h_S ou le type de chargement (uniaxial, équi-bi-axial, bi-axial), sur la sélection du mode de plissement, sur sa longueur d'onde, sur son amplitude et sur sa stabilité. Généralement, les approches reposent sur la définition d'une énergie potentielle

$$\mathcal{E} = \mathcal{E}_S + \mathcal{E}_B - W_{ext}, \tag{1}$$

incluant une énergie de déformation de membrane $\mathcal{E}_S$ (stretching energy en Anglais), de flexion $\mathcal{E}_B$ (bending energy) et un terme associé au travail W_{ext} des efforts extérieurs, supposés conservatifs. La minimisation de cette énergie potentielle conduit alors, suivant la cinématique adoptée, à une ou plusieurs équations aux dérivées partielles non-linéaires pour le champ de déplacement et les états d'équilibre statiques associés. Les premiers modèles analytiques pour prédire les instabilités de plissement ont été principalement développés à partir des équations d'équilibre de Von-Karman (équations différentielles partielles non-linéaires, obtenues via la minimisation d'une énergie potentielle construite sous l'hypothèse de déformations planes, où toutes les non-linéarités liées aux composantes du déplacement dans le plan sont négligées). Une analyse linéaire de stabilité par Allen (1969) montre alors que la configuration plane devient instable par plissement pour un chargement critique

$$\sigma_c^{(W)} = \frac{\overline{E_F}}{4}\left(3\frac{\overline{E_S}^*}{\overline{E_F}}\right)^{2/3}. \tag{2}$$

Dans cette équation, $\overline{E_S}^* = 4E_S/(3-4\nu_S)$ et $\overline{E_F} = E_F/(1-{\nu_F}^2)$ représentent respectivement les rigidités effectives du substrat et du film. Le mode de l'instabilité est de la forme $w \sim \cos(2\pi/\lambda x)$ (mode cylindrique, voir Fig.

4.1) avec

$$\lambda = 2\pi h_F \left(\frac{1}{3} \frac{\overline{E_F}}{\overline{E_S}^*} \right)^{1/3}, \tag{3}$$

sa longueur d'onde. Ce mode cylindrique devient à son tour instable lorsque le chargement de compression dépasse un nouveau seuil critique. Le mode d'instabilité secondaire (mode ondulant ou carré, i.e. herringbone or square-checkerboard mode en Anglais) dépend alors de l'isotropie de la contrainte, voir le diagramme de stabilité de Audoly & Boudaoud (2008*a*), Fig. 4.1.

Lorsque l'épaisseur du substrat diminue, l'ensemble de la structure peut également fléchir selon un mode global de flambage, voir Fig. 4.2, apparaissant pour un chargement critique $\sigma_c^{(B)}$. Il existe alors une compétition (voire parfois une co-existence) entre le mode de plissement cylindrique et le mode de flambage. Dans le cas d'un film mince attaché à un substrat plan semi-infini, les limites de cette compétition peuvent être établies, voir Wang *et al.* (2008), en calculant la charge critique de flambage $\sigma_c^{(B)}$ du film et du substrat, modélisés sous la forme d'une poutre composite. La limite $\sigma_c^{(W)} = \sigma_c^{(B)}$ permet alors de définir un diagramme de phase entre l'instabilité de plissement et l'instabilité de flambage, voir Fig. 4.2.

L'extension de cette analyse au cas d'un substrat non-plan[1] a été réalisée lors de mon séjour postdocoral au M.I.T., et est l'objet de la publication qui suit, parue dans la revue *Journal of the Mechanics and Physics of Solids*, sous le titre "From wrinkling to global buckling of a ring on a curved substrate".

[1] Vidéo M.I.T. de l'instabilité de plissement, cas d'un substrat semi-sphérique possédant une cavité intérieure dépressurisée : ici.

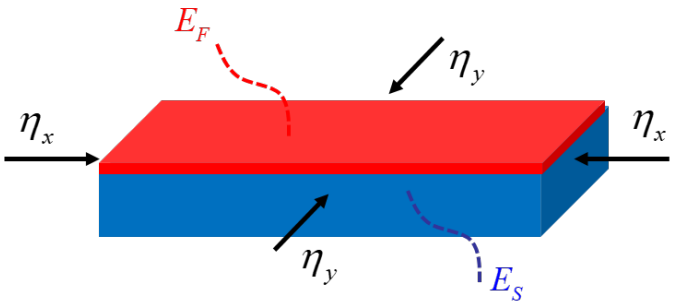

(a)

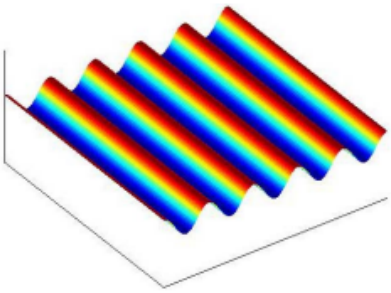

(b) Mode cylindrique (C).

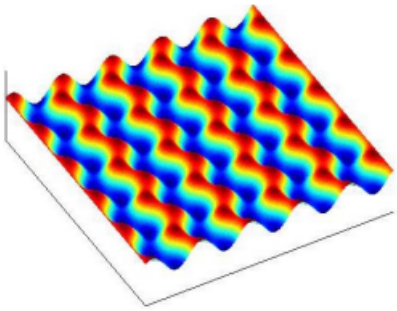

(c) Mode ondulant (U).

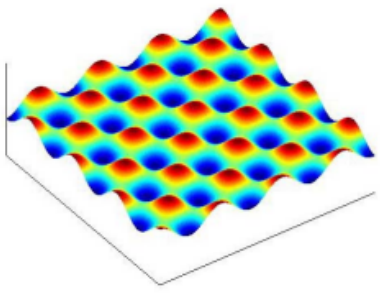

(d) Mode carré (K).

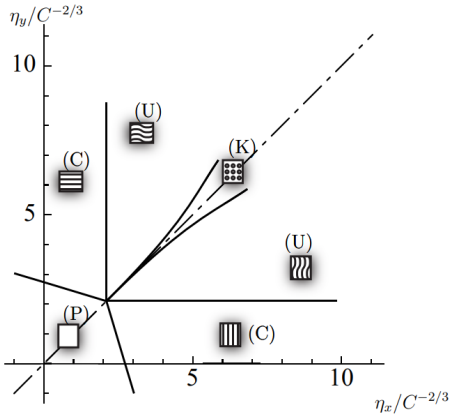

(e)

FIGURE 4.1 : (a) Schéma d'un film mince attaché à un substrat élastique plan, sous compression bi-axiale. Modes de l'instabilité de plissement (par Cai *et al.* (2011)) : mode cylindrique (b), ondulant (c), carré (d). (e) Diagramme de phase par Audoly & Boudaoud (2008*a*) dans le cas général d'une compression bi-axiale non isotrope (compressions directionnelles adimensionnées η_x et η_y). La configuration plane est notée (P).

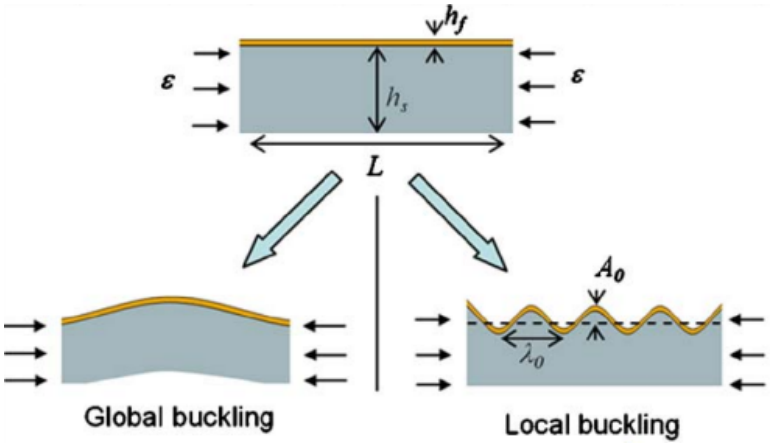

(a)

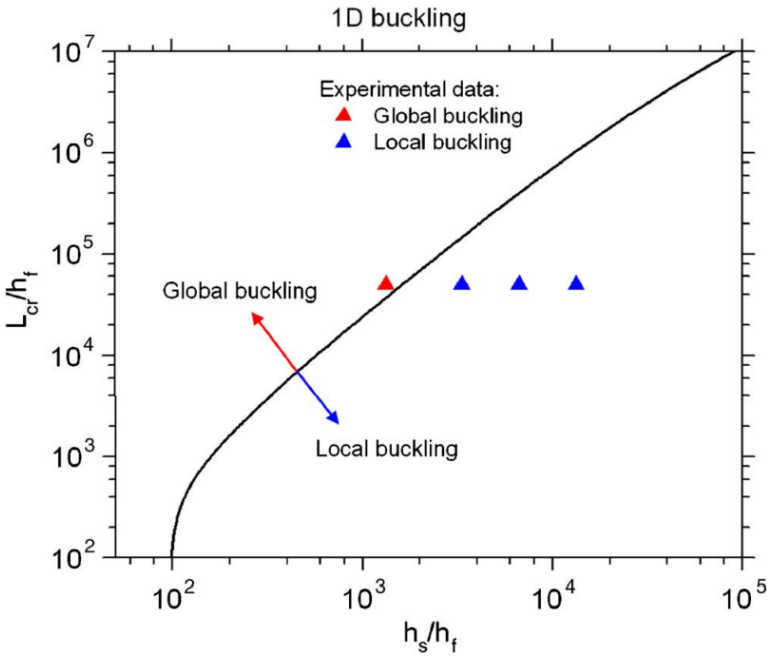

(b)

FIGURE 4.2 : (a) Schéma d'un film mince attaché à un substrat élastique plan, sous compression axiale. (b) Diagramme de phase dans le plan h_S/h_F (rapport des épaisseurs) - L/h_F (rapport d'aspect du film). La courbe indique la transition entre instabilité de flambage et instabilité de plissement, établie théoriquement par Wang *et al.* (2008).

Abstract

We present a combined analytical approach and numerical study on the stability of a ring bound to an annular elastic substrate, which contains a circular cavity. The system is loaded by applying a pressure differential between the inside of the cavity and the outside of the sample. The ring is modeled as an Euler-Bernoulli beam and its equilibrium equations are derived from the mechanical energy which takes into account both stretching and bending contributions. The curvature of the substrate is considered explicitly to model the work done by its reaction force on the ring. We distinguish two different instabilities: periodic wrinkling of the ring or global buckling of the structure. Our model provides an expression for the critical pressure, as well as a phase diagram that rationalizes the transition between instability modes. Towards assessing the role of curvature, we compare our results for the critical stress and the wrinkling wavelength to their planar counterparts. We show that the critical stress is insensitive to the curvature of the substrate, while the wavelength is only affected by the discrete values of the azimuthal wavenumber imposed by the geometry of the problem. Throughout, we contrast our analytical predictions against finite element simulations.

4.1 Introduction

Wrinkling is a stress-driven mechanical instability that occurs when a stiff and slender surface layer bonded to a compliant substrate is subject to compression. This universal instability phenomenon spans from numerous natural and technological/engineering examples. It can be observed over a wide range of length scales, for example: carbon nanotubes (Lourie *et al.*, 1998), pre-stretched elastomers used in flexible electronics applications (Kim *et al.*, 2011), human skin (Chen & Yin, 2010), drying fruit (Yin *et al.*, 2009), surface morphology of the brain (Budday *et al.*, 2014) and mountain topographies generated due to tectonic stresses (Price & Cosgrove, 1990; Huddleston & Lan, 1993).

Over the past decade, there has been an upsurge of interest in the study of the mechanics of wrinkling, along with a change of paradigm in regarding surface instabilities as an opportunity for functionality, instead of a first step in the route to structural failure (Genzer & Groenewold, 2006; Li *et al.*, 2012). The first mechanical studies of wrinkling were motivated by the stability of sandwich panels (Allen, 1969), used in lightweight structural applications, in which the core acts as a soft substrate for the much stiffer skin. More recently, Bowden *et al.* (1998) showed how the wrinkling of a thin film on an elastomeric substrate can be used to produce complex self-organized patterns. Their seminal work has instigated the realization of wrinkling through several different actuation mechanisms, including thermal mismatch (Huck *et al.*, 2000), tissue growth/atrophy (Ben Amar & Goriely, 2005; Li *et al.*, 2011*a*; Budday *et al.*, 2014), swelling of a liquid (Chan & Crosby, 2006*b*) or vapor solvent (Breid & Crosby, 2009), and pneumatics (Terwagne *et al.*, 2014). The opportunities opened by such a wide range of external stimuli have enabled the usage of wrinkling in various applications in photonics (Kim

et al., 2012), optics (Chan & Crosby, 2006*a*), self-assembly (Yoo *et al.*, 2002), microfluidics (Yin *et al.*, 2012) or morphogenesis (Efimenko *et al.*, 2005).

In order to provide a theoretical background to these recent developments, several authors have builded on the pioneering work of Allen (1969), who first provided close form solutions for the critical stress and wavelength obtained when an initially straight beam adhered to an infinite plane substrate is placed under a state of uniaxial compression. Chen & Hutchinson (2004) extended this work to consider the case of a plate adhered to a flat substrate under equi-biaxial compression and performed a nonlinear analysis of the Föppl-von Kármán equations (Landau & Lifshitz, 1959; Timoshenko & Gere, 1961). Huang *et al.* (2005) further refined these efforts by considering the effect of a finite substrate. Both studies showed the existence of multiple buckling modes associated with the same value of critical stress. The stability of these modes under different loadings conditions has been addressed by Audoly & Boudaoud (2008*a*,*b*,*c*), who produced a stability diagram covering the complete evolution from low to high values of overstress. However, experiments by Cai *et al.* (2011) found disagreement at low values of overstress, suggesting that a finite intrinsic curvature of the system, even if small, may play an important role in dictating the pattern selection.

Early studies of wrinkling on curved substrates, as in the flat configuration, were also motivated by a structural problem, in this case the stability of the outer shell of rockets (Kachman, 1959; Seide & Weingarten, 1961; Seide, 1962). More recent studies that consider instabilities as a possible source of functionality have led to applications of curved configurations in adhesion (Kundu *et al.*, 2011), microfluidics (Mei *et al.*, 2010), morphogenesis of microparticles (Yin *et al.*, 2014), optics (Breid & Crosby, 2013) and aerodynamic drag reduction (Terwagne *et al.*, 2014). Curvature also plays a relevant role in the growth of biological systems (Li *et al.*, 2011*b*). Despite these important emerging applications, the mechanics of wrinkling on curved substrates remains weakly understood, when compared to the planar counterpart.

Systematic Finite Element simulations simulations have been performed (Yin *et al.*, 2009; Chen & Yin, 2010; Li *et al.*, 2011*c*; Cao *et al.*, 2012) that highlighted a complex pattern formation process and suggested the possibility of curvature to affect the selected patterns and modify the relevant characteristic length scales, which calls for a robust theoretical backing. Analytical predictions are challenged by the difficulty of modeling the stiffness of the substrate, even in two-dimensional configurations. Cheng (1996) and Cai *et al.* (2011) used the stiffness provided by Allen (1969) for the flat case, such that their model therefore neglects the contribution of curvature on the response of the substrate. Yin *et al.* (2009) used the prediction provided by Brush & Almroth (1975), which accounts for curvature but does not consider the influence of the wrinkling wavelength and their prediction does not converge to the classical planar case as the curvature tends to zero. As such, there is a need to quantify the effect of curvature on the stiffness of the substrate and its subsequent influence on wrinkling.

Here, to the best of our knowledge, we provide the first analytical work that accounts for both the curvature of a (2D) shell-substrate system, as

well as the finite size of the substrate. As an initial step, we focus our study on a curved film adhered to a cylindrical substrate, instead of dealing with non-zero Gaussian curvature geometries, which is left for a future study. We assume axial–symmetry to further simplify the system to the 2D problem of a ring on an annular substrate. Mechanical loading is applied by depressurizing a circular cavity inside the substrate, which places the system under a homogenous state of compression. This geometry is motivated by recent experiments (Terwagne *et al.*, 2014) that demonstrated the usage of wrinkling on spherical samples for switchable and tunable aerodynamic drag reduction. In our simplified 2D system, we solve the elasticity problem for the substrate and derive a close form expression for its stiffness, which is then used in the stability analysis of the ring to quantify the buckling patterns.

The paper is organized as follows: in § 4.2 we describe our system along with its material and geometrical parameters. We also describe the possible instability modes, and present a simplified phase diagram, with the aim of providing physical insight on the problem. In § 4.3 we then introduce the kinematics of the ring attached to the substrate and determine the stiffness of the later. We proceed by defining a strain energy that includes both bending and stretching of the ring, as well as the effect of the substrate. Energy minimization yields the equilibrium equations of the problem. An asymptotic expansion is then used to calculate the principal solution and the bifurcation at the onset of instability. In § 4.4, we describe the finite element simulations that we have performed for this same system.

The results of our investigation are presented in § 4.5. Throughout, we directly compare the analytical predictions to the numerical simulations. We start with the fundamental solution and the critical conditions that lead to instability. We then construct a phase diagram which rationalizes the dependence of the instability modes on the governing parameters. The results for our system are then quantitatively compared to those for wrinkling of a film on a planar substrate, highlighting the effect of curvature. Finally, § 4.6 summarizes our findings and provides perspectives for potential extensions of our work in future studies.

4.2 Definition of the problem

We study the stability of a thin elastic ring, bound to an equally curved 2D substrate that contains an inner cavity, a schematic diagram of which is presented in Fig. 4.3(a). The system is loaded by applying a pressure differential, P, between the inside of the cavity and the outside of the ring. The thickness of the ring is H, its Young's modulus E_F and its Poisson's ratio ν_F. We refer to $\overline{E_F} = E_F/(1-{\nu_F}^2)$ as the reduced Young's modulus of the filmß. The substrate is made of a linearly elastic material with Young's modulus E_S, Poisson's ratio ν_S and reduced Young's modulus $\overline{E_S} = E_S/(1-{\nu_S}^2)$. The thickness of the substrate is $R-R_0$, where R_0 is the radius of the inner cavity.

For convenience, we now introduce new rescaled quantities to reduce the number of parameters of the problem. As such, we use R and $\overline{E_F}$ to

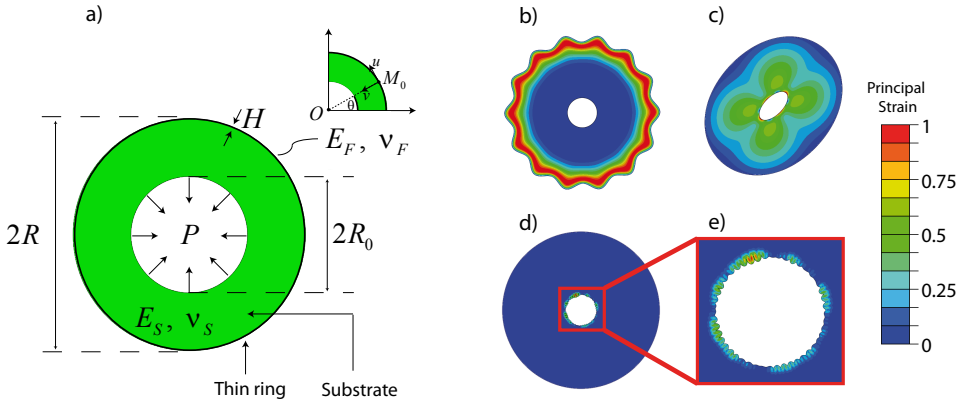

Figure 4.3: (a) Schematic diagram of our system: a ring is bound to a curved substrate which contains a circular cavity. The system is loaded by applying a pressure differential between the inside of the cavity and the outside of the ring. (b-d) Representative examples of the three possible instability modes of a ring on a curved substrate which contains a cavity that is depressurized. (b) Wrinkling mode ($h = 10^{-2}$ and $\xi = 10^3$), (c) global buckling mode ($h = 10^{-2}$ and $\xi = 10^6$) and (d) Biot mode ($h = 10^{-2}$ and $\xi = 10^2$). (e) is a zoom in of (d) that exhibits the deformation of the surface of the inner cavity in the Biot mode. The colorbar refers to the principal component of the strain tensor of the mode, which has been normalized.

normalize lengths and pressures and define

$$h = \frac{H}{R}, \quad \beta = \frac{R_0}{R}, \quad \xi = \frac{\overline{E_F}}{\overline{E_S}}, \quad p = \frac{P}{\overline{E_F}}, \tag{1}$$

as the dimensionless thickness, cavity size, stiffness ratio, and pressure, respectively.

In Fig. 4.3(b-e) we show representative results, obtained from Finite Element Modeling (FEM), of the three possible instability configurations of the ring-substrate system for different values of the dimensionless ring thickness h and ratio of stiffness ξ. All the other mechanical properties are kept constant: the Poisson's ratios are $\nu_F = \nu_S = 0.5$, and the cavity size is $\beta = 0.2$. In the simulations this is achieved by taking fixed values for $R = 100$ units of length and $E_S = 1$ units of pressure, while changing the values of H, R_0 and E_F accordingly. More details on our numerical simulations are provided in §4.4.

The first mode, a representative example of which is shown in Figure 4.3(b) for $h = 10^{-2}$ and $\xi = 10^3$, corresponds to periodic wrinkling of the film with a well defined wavelength. The strain in the bulk of the substrate is negligible, and no deformation of the inner cavity is observed. The second mode, for example at $h = 10^{-2}$ and $\xi = 10^6$ in Figure 4.3(c), corresponds to a global buckling of the structure, where both the ring and the cavity deform into an ellipse such that the wavelength is $\lambda = \pi R$.

In addition to these two instability modes (wrinkling and global buckling), we have also numerically observed an instability on the inner surface

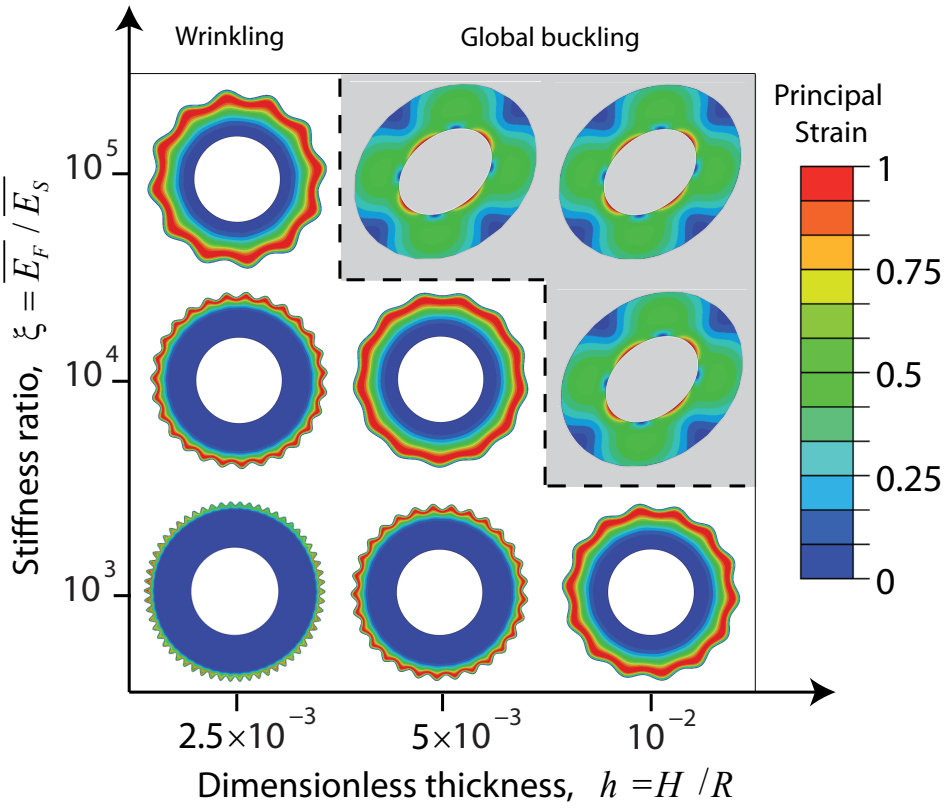

Figure 4.4: Schematic phase diagram of the instability modes of the system, obtained for a critical value of the pressure differential: i) wrinkling of the ring or ii) global buckling of the structure (shaded regions). The primary parameters that govern this transition are the stiffness and thickness ratios: $\xi = \overline{E_F}/\overline{E_S}$ and $h = H/R$, respectively. The depicted examples from FEM simulations are for an incompressible film and substrate, $\nu_F = \nu_S = 0.5$. They were obtained for $R = 100$ units of length and $E_S = 1$ units of pressure, while varying H and E_F. The colorbar refers to the principal component of the strain tensor of the mode, which has been normalized.

of the cavity. However, this third mode does not affect the ring and is found for low values of cavity size and stiffness ratio ($\xi = 10^2$ and $h = 10^{-2}$ in Fig. 4.3c-d). This instability was first discussed by Biot (1965) and we therefore refer to it as the *Biot mode*; it is local in nature and only depends on the compressive strain at the surface. This type of instability mode has been recently studied in the case of elastomeric materials with voids by Michel *et al.* (2007) and Cai *et al.* (2010). Understanding the specifics of this Biot mode is however outside the scope of our work and we shall not take it into account in our analytical model and systematic numerical investigation.

A schematic phase diagram of our system is provided in Fig. 4.4. For low values of h and ξ the ring wrinkles with a short wavelength. As either h or ξ are increased, the wavelength also increases. Once these parameters reach a critical value, represented by the dashed line in Fig. 4.4, the instability transitions from wrinkling to global buckling. In what follows, we focus on rationalizing how the wavelength of the wrinkling mode, and the threshold value for the transition to global buckling, evolve with the elastic and geometrical parameters of the system.

4.3 Analytical approach

In this section we present our analytical approach. The ring is treated as an Euler-Bernoulli beam. The effect of the substrate is modeled as a restoring force that acts on the ring and is determined by solving the elasticity problem of the substrate with adequate boundary conditions. Minimization of the potential energy provides the equilibrium equations of the problem, which are solved using an asymptotic expansion that yields the principal and bifurcated solutions.

4.3.1 Kinematics, energy formulation and equations of equilibrium

We model the ring as an extensible Euler-Bernoulli beam made of an homogeneous and isotropic material. Polar coordinates are used to track the position of the ring center-line, C. The initial configuration of the ring, prior to depressurization, is assumed to be circular. The origin, O, is located at the center of the cavity, and the initial and equilibrium configurations of an arbitrary point of C are represented by M_0 and M, respectively. Vectors are expressed in the physical base $(\mathbf{e_r}, \mathbf{e}_\theta)$, derived from the polar coordinates (r, θ). The initial position of C is $\mathbf{OM}_0 = (R, 0)$, as shown in the inset of Fig.4.3(a). When the system is loaded by depressurizing the cavity, C deforms to a new configuration given by the position vector $\mathbf{OM} = R\,(1 + v\,(\theta)\,, u\,(\theta))$, where v and u are the dimensionless radial and orthoradial displacements, respectively.

The infinitesimal arclength of C in the initial and deformed configurations are denoted by $ds_0 = |d\mathbf{OM}_0|$ and $ds = |d\mathbf{OM}|$, respectively. Moreover, defining the tangent vector $\mathbf{T} = d\mathbf{OM}/ds$, allows us to express the curvature of C in the deformed configuration as $\kappa/R = |d\mathbf{T}/ds|$. Here, κ is

dimensionless and can be written in terms of v and u as

$$\kappa = 1 + \left(-1 + 2u' + 2v\right) v'' + v^2 - v - u'^2 + \left(-u + v'\right) u'' + \frac{1}{2}\left(v'^2 - u^2\right) + \text{h.o.t.}, \tag{2}$$

where the prime notation represents derivation with respect to θ and high order terms (h.o.t.) are neglected under the assumption of small displacements and moderate rotations. We now define the elongation of the ring as $e = ds/ds_0$ to express the stretching deformation, $\eta = \left(e^2 - 1\right)/2$, in terms of v and u as

$$\eta = \frac{1}{2}\left[u'^2 + v^2 + \left(u - v'\right)^2\right] + \left(1 + v\right) u' + v, \tag{3}$$

so that the hoop stress in the film is $\sigma_0 = \overline{E_F}\eta$.

Following Euler-Bernoulli beam theory (Timoshenko & Gere, 1961), the total energy of deformation $\mathcal{E}$ of the ring is the sum of a stretching energy $\mathcal{E}_S$ and a bending energy $\mathcal{E}_B$,

$$\mathcal{E} = \mathcal{E}_S + \mathcal{E}_B = \int_0^{2\pi R} \overline{\mathcal{E}} ds_0, \tag{4}$$

with

$$\mathcal{E}_S = \int_0^{2\pi R} \frac{\overline{E_F} H}{2} \eta^2 ds_0, \tag{5a}$$

$$\mathcal{E}_B = \int_0^{2\pi R} \frac{\overline{E_F} H^3}{24 R^2} (\kappa - 1)^2 ds_0, \tag{5b}$$

and $\overline{\mathcal{E}}$ the energy of deformation per unit length of the initial configuration of the ring. Assuming that the reaction force of the substrate derives from a potential $\int_0^{2\pi R} \overline{W} ds_0$, the equilibrium states of the ring are the solutions of

$$\delta\mathcal{E}_S + \delta\mathcal{E}_B - \int_0^{2\pi R} \delta\overline{W} ds_0 = 0, \tag{6}$$

where $\delta\mathcal{A}$ is the variation of quantity $\mathcal{A}$, for an arbitrary displacement field $R\left(\delta v, \delta u\right)$, which is 2π periodic. The computation of the variations in Eq. (6) leads to the Euler-Lagrange equations for the equilibrium of the ring,

$$\frac{\partial\overline{\mathcal{E}}}{\partial v} - \left(\frac{\partial\overline{\mathcal{E}}}{\partial v'}\right)' + \left(\frac{\partial\overline{\mathcal{E}}}{\partial v''}\right)'' - \left(\frac{\partial\overline{\mathcal{E}}}{\partial v'''}\right)''' + \left(\frac{\partial\overline{\mathcal{E}}}{\partial v''''}\right)'''' - \frac{\partial\overline{\delta W}}{\partial \delta v} = 0, \tag{7a}$$

$$\frac{\partial\overline{\mathcal{E}}}{\partial u} - \left(\frac{\partial\overline{\mathcal{E}}}{\partial u'}\right)' + \left(\frac{\partial\overline{\mathcal{E}}}{\partial u''}\right)'' - \left(\frac{\partial\overline{\mathcal{E}}}{\partial u'''}\right)''' + \left(\frac{\partial\overline{\mathcal{E}}}{\partial u''''}\right)'''' - \frac{\partial\overline{\delta W}}{\partial \delta u} = 0, \tag{7b}$$

along with static boundary conditions that are naturally satisfied due to the 2π periodicity condition on the displacements v and u.

4.3.2 Asymptotic expansion and reactive force of the substrate

We seek a solution of Eq. (7) as an expansion of the form

$$v = v_0 + \varepsilon A \sin(m\theta) + O\left(\varepsilon^2\right), \tag{8a}$$

$$u = \varepsilon B \cos(m\theta) + O\left(\varepsilon^2\right), \tag{8b}$$

where $(v_0, 0)$ corresponds to a radial pre-buckling deformation and the term $\varepsilon(A\sin(m\theta), B\cos(m\theta))$ represents an instability of azimuthal wavenumber m. From the requirement of 2π periodic functions v and u, m has to be an integer. Also, we consider $m > 1$ since $m = 1$ corresponds to a solid body translation of the ring. The instability displacement field has amplitudes εA and εB, where ε is a small parameter.

Before substituting Eq. (8) into Eq. (7) and solving at each order in ε, we first need to determine the work, $\overline{\delta W}$, done by the reaction force, $\mathbf{F} = -\left(\sigma\mathbf{e}_\perp + \tau\mathbf{e}_\parallel\right)$, that the substrate exerts on the ring. The normal stress σ and the tangential stress τ at the interface between the ring and the substrate are computed by solving the corresponding two-dimensional elasticity problem using an Airy function, with pressure P at $r = R_0$ and the displacement field given by Eq. (8), at $r = R$. It is worth to note that in our computation we thus enforce the continuity of the displacement field at the interface ring/substrate, contrarily to Seide (1962), who assumed zero shear stress and continuity of normal stress. Both computations can be carried out in a similar way using an Airy function, but they lead to significantly different estimates for the bending and stretching energy in the ring. Audoly & Boudaoud (2008*a*) have shown that it is preferable to enforce the continuity of the displacement, since the continuity of the stress yields a stretching energy in the ring much larger than the bending energy, in contradiction to what is expected in the wrinkling of a thin film. Our explicit solution for the boundary value problem of the substrate is reported in 4.7.1. In short, we find that the stresses σ and τ at the interface are

$$\frac{\sigma}{\overline{E_F}} = k_0 v_0 + k\varepsilon A \sin(m\theta) - \gamma p, \tag{9a}$$

$$\frac{\tau}{\overline{E_F}} = \mu\varepsilon B \sin(m\theta), \tag{9b}$$

with the following governing parameters

$$k_0 = \frac{(1-\nu_S)\left(1-\beta^2\right)}{1-2\nu_S+\beta^2}\frac{1}{\xi}, \tag{10a}$$

$$k = \frac{(1-\nu_S)}{2}\left(S_A + S_B\frac{B}{A}\right)\frac{1}{\xi}, \tag{10b}$$

$$\mu = \frac{(1-\nu_S)}{2}\left(S_B\frac{A}{B} + T_B\right)\frac{1}{\xi}, \tag{10c}$$

$$\gamma = \frac{2\beta^2(1-\nu_S)}{1-2\nu_S+\beta^2}. \tag{10d}$$

Here, k_0, k, and μ are the dimensionless pre-wrinkling, wrinkling and shear stiffnesses of the substrate, respectively. The coefficient γ quantifies the effect

of pressure, p, on the ring through the term $-\gamma p$ in Eq. (9a). The value of γ is smaller than one, reflecting the fact that the transmitted pressure decreases within the substrate. There are however two exceptions for which $\gamma = 1$: the limit where there is no substrate, $\beta \to 1$, and the limit of a perfectly incompressible substrate, $\nu_S \to 0.5$, in which the volumetric pressure remains constant throughout the substrate. The quantities S_A, S_B and T_B used in Eq. (10) are functions of both the cavity size β and the azimuthal wavenumber m, and their full expressions are reported in 4.7.1.

Depending on which configuration of the ring is used (initial or deformed), two cases need to be considered to define the normal and tangential vectors $\mathbf{e}_\perp$ and $\mathbf{e}_\parallel$, respectively. If we define these vectors from the initial configuration, then $(\mathbf{e}_\perp, \mathbf{e}_\parallel) = (\mathbf{e_r}, \mathbf{e}_\theta)$, so that the reaction force $\mathbf{F}$ keeps a constant direction while the ring deforms. If we use the deformed configuration, then $\mathbf{F}$ is modeled as a follower force whose direction changes with the ring deformation. In this case, $(\mathbf{e}_\perp, \mathbf{e}_\parallel) = (\mathbf{N}, \mathbf{T})$, where $\mathbf{N}$ is the inward normal vector orthogonal to the ring center-line, in its deformed state. In order to take both of these options into account in the same model, we define a parameter, χ, which can take the values $\chi = 1$ or $\chi = 0$, when either the undeformed or deformed configurations are used. Thus, we express the reaction force and its elementary work per unit length of the ring as

$$\mathbf{F} = -\left[(\sigma \mathbf{e_r} + \tau \mathbf{e}_\theta)\,\chi + (\sigma \mathbf{N} + \tau \mathbf{T})\,(\chi - 1)\right], \tag{11a}$$

$$\overline{\delta W} = \mathbf{F} \cdot R\,(\delta v \mathbf{e_r} + \delta u \mathbf{e}_\theta). \tag{11b}$$

where $\cdot$ is the Euclidean dot product.

The principal solution: order 0 in ε

We now proceed to obtain the principal solution and the critical instability modes by substituing Eq. (8) into Eq. (7) and solving the resulting equations for each order of ε. At order 0, Eq. (3) for the stretching deformation η yields $\eta_0 = v_0 = \sigma_0/\overline{E_F}$ and the linear approximation of the Euler-Lagrange Eq. (7a)

$$v_0 = \frac{\gamma p}{h + h^3/12 + k_0} = \frac{\sigma_0}{\overline{E_F}}, \tag{12}$$

relates the dimensionless pressure, p, and the dimensionless hoop stress, $\sigma_0/\overline{E_F}$, in the ring. Note that Eq. (7b) is automatically satisfied at order 0 in ε. In the absence of a substrate, the ratio σ_0/P reads

$$\lim_{\beta \to 1} \left(\frac{\sigma_0}{P}\right) = \frac{1}{h} + O\,(h)\,, \tag{13}$$

and in the limit of the ring that is much stiffer than the substrate we obtain

$$\lim_{\xi \to \infty} \left(\frac{\sigma_0}{P}\right) = \frac{\gamma}{h} + O\,(h)\,, \tag{14}$$

so that $\frac{\sigma_0}{P} < \lim\limits_{\xi \to \infty} \left(\frac{\sigma_0}{P}\right) \leq \lim\limits_{\beta \to 1} \left(\frac{\sigma_0}{P}\right)$. For $\nu_S = 0.5$, we have $\gamma = 1$ through the definition in Eq. (10d) and both limits in Eqs. (13) and (14) are equal. Thus, the hoop stress in a very stiff ring lying on a soft incompressible substrate is the same as the hoop stress in a ring with no substrate, which serves as a verification of the rationale thus far.

The instability: order 1 in ε

At order 1 in ε, the Euler-Lagrange Eqs. (7) write

$$\left(a_1 p + \widetilde{a_1}\right) A + \left(b_1 p + \widetilde{b_1}\right) B = 0, \tag{15a}$$

$$\left(a_2 p + \widetilde{a_2}\right) A + \left(b_2 p + \widetilde{b_2}\right) B = 0, \tag{15b}$$

where a_i, $\widetilde{a_i}$, b_i and $\widetilde{b_i}$ are functions of the azimuthal wavenumber m, the stiffness ratio ξ, the cavity size β and the substrate Poisson's ratio ν_S, reported in full in 4.7.2. The linear system in Eq. (15) has a nontrivial solution when its determinant vanishes, which for a given value of m occurs at the dimensionless pressure

$$p_m = \frac{P_m}{E_F} = \frac{-\widetilde{a_1}\widetilde{b_2} + \widetilde{b_1}\widetilde{a_2}}{a_1\widetilde{b_2} + \widetilde{a_1}b_2 - b_1\widetilde{a_2} - \widetilde{b_1}a_2}. \tag{16}$$

The critical azimuthal wavenumber and the dimensionless critical pressure can now be obtained from Eq. (16) by minimizing over all possible values of m

$$[m_c, p_c] = \min_{m=2,3,\ldots} (p_m). \tag{17}$$

For the general case, this minimization must be performed numerically. However, in the absence of the substrate, we obtain that $m_c = 2$ and Eq. (16) simplifies to

$$\lim_{\beta\to 1}(p_c) = \lim_{\beta\to 1}(p_2) = -\frac{1}{4-\chi}h^3 - \frac{4}{(4-\chi)^2}h^5 + O\left(h^7\right). \tag{18a}$$

The term of order h^3 corresponds to the classical dimensionless critical pressure for a ring with no substrate (Lévy, 1884; Carrier, 1947; Timoshenko & Gere, 1961; Combescure, 1981). The term in h^5 is a correction also reported by Atanackovic (1998). In the limit of a ring much stiffer than the substrate, we also have $m = 2$, with

$$\begin{aligned}\lim_{\xi\to\infty}(p_c) &= \lim_{\xi\to\infty}(p_2)\\ &= -\frac{1}{2}\frac{\left(-1+2\nu_S-\beta^2\right)h^3}{\beta^2\left(-1+\nu_S\right)(4-\chi)} - \frac{2\left(-1+2\nu_S-\beta^2\right)h^5}{\beta^2\left(-1+\nu_S\right)(4-\chi)^2} + O\left(h^7\right),\end{aligned} \tag{19}$$

so that $\lim_{\xi\to\infty}(p_c) \leq \lim_{\beta\to 1}(p_c) < 0$. Again, for $\nu_S = 0.5$ we observe that the limits equal, corroborating the physical intuition that as the stiffness ratio ξ increases, the effect of the substrate becomes negligible.

4.3.3 Critical stress, wavelength and comparison to wrinkling on a planar substrate

To determine the effect of curvature on the instability, we compare the critical hoop stress, σ_c, in the ring, given by Eq. (12) with $p = p_c$, as well as the

wavelength $\lambda_c = 2\pi R/m_c$ of the wrinkling mode, against their counterparts for an initially planar film on an infinite plane substrate (Chen & Hutchinson, 2004)

$$\sigma_{Plane} = \frac{\overline{E_F}}{4}\left(3\frac{\overline{E_S}^*}{\overline{E_F}}\right)^{2/3} = \frac{\overline{E_F}}{4}\left(\frac{4(1-\nu_S)^2}{3-4\nu_S}\frac{3}{\xi}\right)^{2/3}, \tag{20a}$$

$$\lambda_{Plane} = 2\pi H\left(\frac{1}{3}\frac{\overline{E_F}}{\overline{E_S}^*}\right)^{1/3} = 2\pi H\left(\frac{1}{3}\frac{3-4\nu_S}{4(1-\nu_S)^2}\xi\right)^{1/3}, \tag{20b}$$

where $\overline{E_S}^* = 4\overline{E_S}(1-\nu_S)^2/(3-4\nu_S)$ is the effective stiffness of the substrate. Together, Eqs. (20) and (12) yield

$$\frac{\sigma_c}{\sigma_{Plane}} = \frac{4\gamma p_c}{h + h^3/12 + k_0}\left(\frac{12(1-\nu_S)^2}{3-4\nu_S}\frac{1}{\xi}\right)^{-2/3}, \tag{21a}$$

$$\frac{\lambda_c}{\lambda_{Plane}} = \frac{1}{hm_c}\left(\frac{3-4\nu_S}{12(1-\nu_S)^2}\xi\right)^{-1/3}, \tag{21b}$$

and, in the limit of absence of the substrate, Eq. (21a) reduces to

$$\lim_{\beta\to 1}\left(\frac{\sigma_c}{\sigma_{Plane}}\right) = \lim_{\beta\to 1}\left(\frac{\sigma_2}{\sigma_{Plane}}\right) = \frac{4}{4-\chi}\left(\frac{12(1-\nu_S)^2}{(3-4\nu_S)\,\xi}\right)^{-2/3} h^2 + O\left(h^4\right). \tag{22}$$

In § 4.5.4, we shall make use of Eqs. (21) and Eq. (22) to further quantify the sensitivity of the stress and wavelength to the curvature of the substrate.

4.4 Numerical simulations

In § 4.5, we will contrast the predictions from the above analysis with the results of a series of finite element simulations performed in the commercial package Abaqus, using the `BUCKLE` analysis, which provides the buckling load and the corresponding eigenmodes.

As in the analytical study, the cylindrical structure was modeled as an annulus of a soft substrate with a stiffer thin film adhered to its exterior, under plane strain conditions. The bonding between the substrate and the film is assumed to be perfect, such that both share nodes. Negative pressure is applied on the interior surface, to model the effect of the pressure differential between the inner surface of the annulus (the cavity) and the exterior of the system. The buckling analysis provides the value of the critical pressure, p_c, as well as the corresponding critical mode. Rigid body motions are removed by constraining the displacement of two points on the film.

Both substrate and film are modeled as incompressible linearly elastic materials, $\nu_S = \nu_F = 0.5$. These results were compared to additional simulations using a Neo-Hookean model but no difference was observed given the low values of strain involved. The substrate was modeled using quadrilateral plane strain elements. Due to the incompressibility, the corresponding hybrid element, CPE4H, was used. The film was modeled using B21 beam

elements. In order to account for the effect of plane strain, the stiffness of the beam is defined as $E_F/\left(1-\nu_F^2\right)$.

All of the results presented were obtained using 1000 elements in the circumferential direction, and $150\,(R-R_0)$ elements in the radial direction. The mesh size was validated with a convergence analysis. By way of example, differences less than 0.5% in critical pressure were obtained when comparing results for a mesh with twice the elements in each direction, even in the case of wrinkling with very short wavelengths. The deviations between the two meshes were, however, larger ($\sim$ 5%) for the case when the critical buckling mode is a Biot instability, due to the infinite number of wavelengths associated to the same buckling mode. However, as stated in § 4.2, this mode shall not be studied in detail as we focus on the wrinkling and global buckling loads.

4.5 Results

Having introduced our analytical and numerical methods, we now present the results of a systematic exploration of the mechanical response of our system for different geometric and material parameters. Throughout, we provide a direct comparison between analytical results and numerical simulations, finding good agreement, and instances of discrepancies will be discussed where appropriate.

For the geometric parameters, we have varied the cavity size, $\beta = R_0/R$, and the dimensionless thickness, $h = H/R$. Three representative values were chosen for β (depicted in the insets of Fig. 4.5a-c): a small cavity, $\beta = 0.2$; a cavity with size half the external radius, $\beta = 0.5$; and a large cavity, $\beta = 0.8$. Moreover, h was varied in the range 10^{-3} to 10^{-1}. This parameter has two different physical interpretations. On one hand, for a substrate with given curvature, *i.e.* fixed R, increasing h is equivalent to increasing the thickness of the ring. On the other hand, for a ring of given thickness H, the value of h decreases with the curvature, $1/R$.

For the material properties, we have considered values for the stiffness ratio between the film and the substrate, $\xi = \bar{E}_F/\bar{E}_S$, spanning over five orders of magnitude, from 10^2 to 10^7. The substrate is taken to be incompressible, $\nu_S = 0.5$, since most of the relevant experiments that have motivated our study (Bowden *et al.*, 1998; Huck *et al.*, 2000; Yu & Jiang, 2010; Terwagne *et al.*, 2014) use nearly incompressible elastomeric substrates. Moreover, it is important to note that, even if the analytical model has been derived assuming a general value of ν_S, it is expected to be less accurate for increasing deviations from incompressibility, as discussed previously by Cai *et al.* (2011). The reason for these discrepancies is that, since the ring is modeled as a beam, it is not possible to enforce both displacement and traction continuity at the interface. In the present work, we impose displacement continuity, as discussed in § 4.3.2.

In the presentation of our results, we first consider the effect of h and ξ on the hoop-stress and on the critical pressure. Then, we rationalize the transition from wrinkling to global buckling, shown in Fig. 4.3. We finally compare the critical stress and wavelength of the wrinkling mode to their

planar substrate counterparts and discuss the effect of curvature.

4.5.1 Hoop stress prior to wrinkling

In Fig. 4.5, we plot the hoop stress in the ring, normalized by the pressure, σ_0/P, as a function of the dimensionless thickness, $h = H/R$. We find that the hoop stress decreases monotonically with the dimensionless thickness, and increases with both the stiffness ratio and the cavity size. When the ring is much stiffer than the substrate (i.e. $\xi \to \infty$), the hoop stress scales as $\sigma_0/P \sim (H/R)^{-1}$, with a prefactor given by Eq. (14). For a given thickness of the ring and a given cavity size, the hoop stress in the ring decreases as the curvature of the substrate increases. This observation is consistent with the classic result for the hoop stress, $\sigma_0 = PR/H$, for a depressurized thin-walled cylindrical pressure vessel. This result can be recovered from Eq. (12) by taking $\gamma = 1$, $k_0 = 0$ and performing a Taylor expansion in h, about 0.

4.5.2 Critical pressure

In Fig. 4.6, we plot the dimensionless critical pressure, $|p_c| = |P_c|/\overline{E_F}$, as a function of the dimensionless thickness, h, and observe two different regimes. For low values of h, the ring wrinkles with an azimuthal wavenumber $m_c \gg 2$, with a critical pressure $|p_c|$ that increases with h. When h reaches a threshold value, h^*, the wavenumber decreases suddenly; the nature of the instability changes from a wrinkling to a global buckling mode with $m_c = 2$. In this regime, there is a clear asymptote as $\xi \to \infty$, given by Eq. (19), which corresponds to the buckling of a ring with no substrate.

Depending on the model used for the reaction force of the substrate (constant direction force, $\chi = 1$, or follower force, $\chi = 0$, see § 4.3.2), Eq. (11) yields two different analytical predictions, shown in Fig. 4.6 as a solid line for $\chi = 0$, and a dashed line for $\chi = 1$. We note that the agreement between FEM simulations and analytical predictions is superior for $\chi = 0$, in particular for the global mode. In other words, it is better to model the reaction force of the substrate as a pressure field which remains normal to the ring center-line C as it deforms, than a force with constant direction. Thus, from now on, all analytical results will be only presented for $\chi = 0$.

Despite the overall good agreement between analytical and numerical predictions, there are noticeable discrepancies in the global modes for low values of the stiffnesses ratio, for example when $\xi = 10^2$. The reason is the impossibility of our model to enforce both displacement and traction continuity at the interface, as discussed at the beginning of § 4.5. For the wrinkling modes, the shear between ring and substrate is negligible, and consequently inaccuracies in modeling the interface do not affect the model (Audoly & Boudaoud, 2008*a*). For the global modes, however, the shear stress plays a crucial role, which is underestimated in our model. This leads to discrepancies in the critical pressure with the numerical results, where continuity of both displacement and stress is enforced. The disagreement is more pronounced when the ring and the substrate are of comparable stiffness (*e.g.* $\xi = 10^2$).

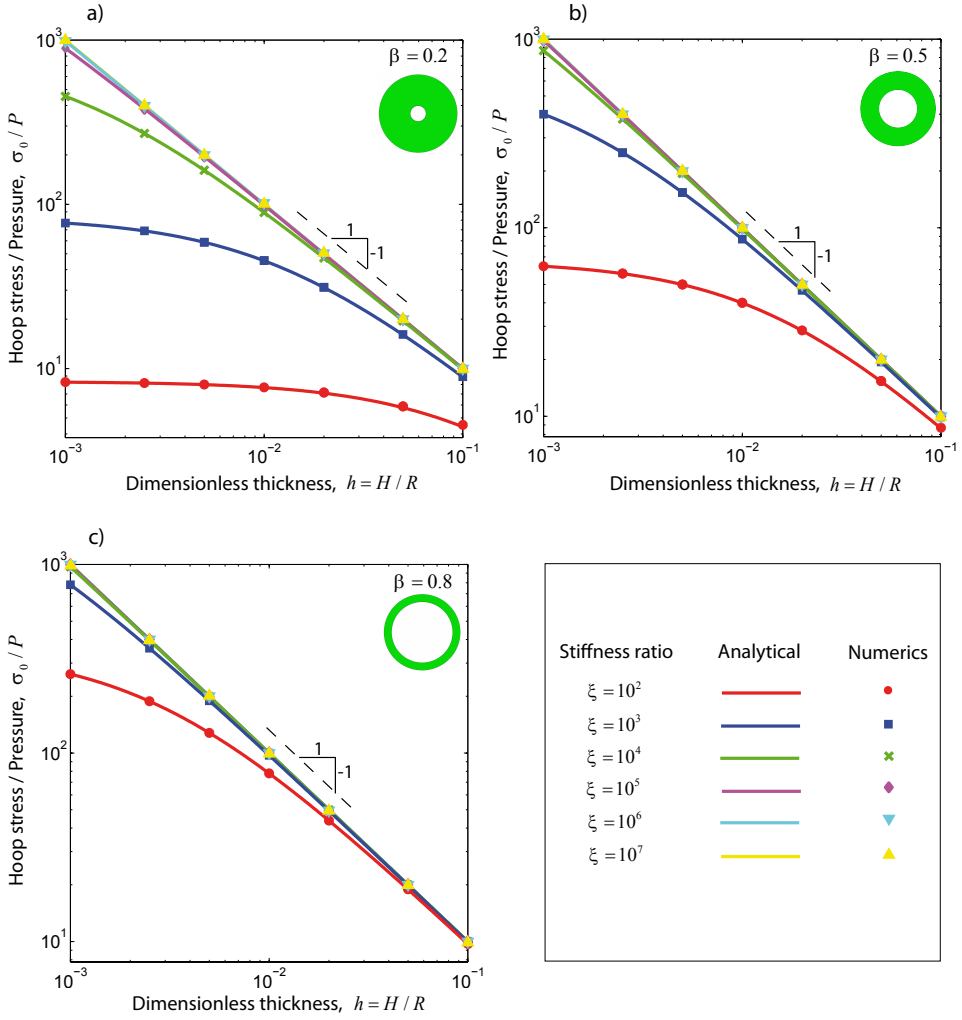

Figure 4.5: Pre-instability hoop stress, σ_0, in the ring, normalized by the pressure, P, as a function of the dimensionless ring thickness, $h = H/R$. Cavity sizes are: (a) $\beta = 0.2$, (b) $\beta = 0.5$, (c) $\beta = 0.8$. The Poisson's ratio of the substrate is $\nu_S = 0.5$. Analytical predictions are given by Eq. (12) as solid lines and FEM results are plotted as data points. The legend (bottom right) is common to all three plots.

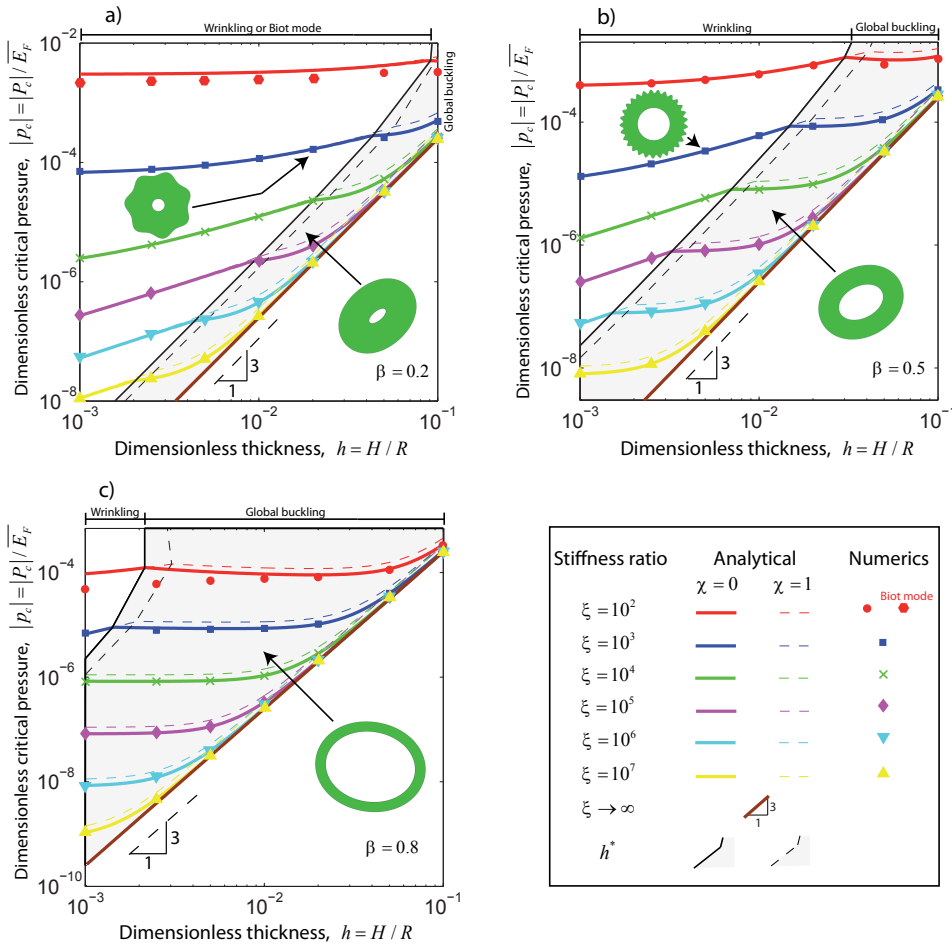

Figure 4.6: Dimensionless critical pressure $|p_c| = |P_c|/\overline{E_F}$ versus the dimensionless ring thickness $h = H/R$, for several stiffness ratios $\xi = \overline{E_F}/\overline{E_S}$ and cavity sizes β: (a) $\beta = 0.2$, (b) $\beta = 0.5$, (c) $\beta = 0.8$. Theory is given by Eq. (17). The Poisson's ratio of the substrate is $\nu_S = 0.5$. The legend (bottom right) is common to all three plots.

Another difference between the analytical predictions and the numerics is the appearance of Biot modes for $\beta = 0.2$ and $\xi = 10^2$. These modes, although possible, only occur in a small region of our parameter space and, as mentioned above, are beyond the scope of this work.

In short, our model exhibits limitations if the ring and the substrate have comparable stiffness and the system globally buckles, or when there is a Biot mode (small cavity). Apart from this extreme combination of parameters, rarely observed in experimental configurations, the model performs successfully.

4.5.3 Phase diagram

We proceed by focusing on the transition from wrinkling to global buckling, towards first constructing a phase diagram in the (ξ, h) parameter space and then quantifying the dependence of the boundary, $h^*(\xi)$, between the two modes on the size of the cavity, β. Given that we do not have a closed form expression for h^*, we use a numerical method which tracks any jump from $m_c = 2$ to $m_c^* > 2$ in Eq. (17), when h is decreased.

In Fig. 4.7(a), we plot h^* as a function of ξ, for $\beta = 0.5$. The boundary between modes is consistent with a power-law, $h^* \sim \xi^{-3}$, which divides the phase diagram into a wrinkling domain ($h < h^*$) and a global buckling domain ($h > h^*$, shaded region). Again, there is good agreement between numerical and analytical solutions.

In Fig. 4.7(b), we extend the phase diagram to cavity sizes from $\beta = 0.2$ to $\beta = 0.8$. We predict that the power-law with exponent -3, mentioned above for $\beta = 0.5$, is still valid as β increases, even if there are some deviations towards the higher values. To quantify the appropriateness of the -3 power-law, we fit a curve of the form $\xi = f_2 h^{f_1}$ to the analytically calculated boundaries. In Fig. 4.7(c) we plot the fitting parameters f_1 and f_2 as a function of β. We find that the exponent is $f_1 \approx -3$ for $\beta < 0.7$, and then decreases rapidly to a value of $f_1 \approx -4.25$ for $\beta = 0.8$. The decrease of the prefactor f_2 is more pronounced and reflects the fact that h^* decreases as β increases.

The evolution of m_c^* (i.e. azimuthal wavenumber of the wrinkling mode for $h = h^*$), as a function of β and ξ is presented in Fig. 4.7(d). Our prediction shows that m_c^* increases with β, while it is nearly insensitive to ξ. For example, for $\beta = 0.5$, we find that $m_c^* = 9$ for $\xi > 10^2$ and $m_c^* = 10$ for $\xi = 10^2$. Predictions for $\xi > 10^2$ are in relatively good agreement with finite element simulations, which have shown that $m_c^* = 10$. For $\xi = 10^2$, FEM simulations yield $m_c^* = 15$, pointing out again at the limitation of our analytical approach in the limit when the stiffness of the ring and the substrate become comparable.

4.5.4 Comparison of wrinkling in our curved system with that on infinite planar substrate

Thus far, we have shown that the ring may wrinkle or buckle globally, depending on the curvature and stiffness of the substrate. We now focus on the wrinkling mode of the ring, with the aim of comparing the critical stress and

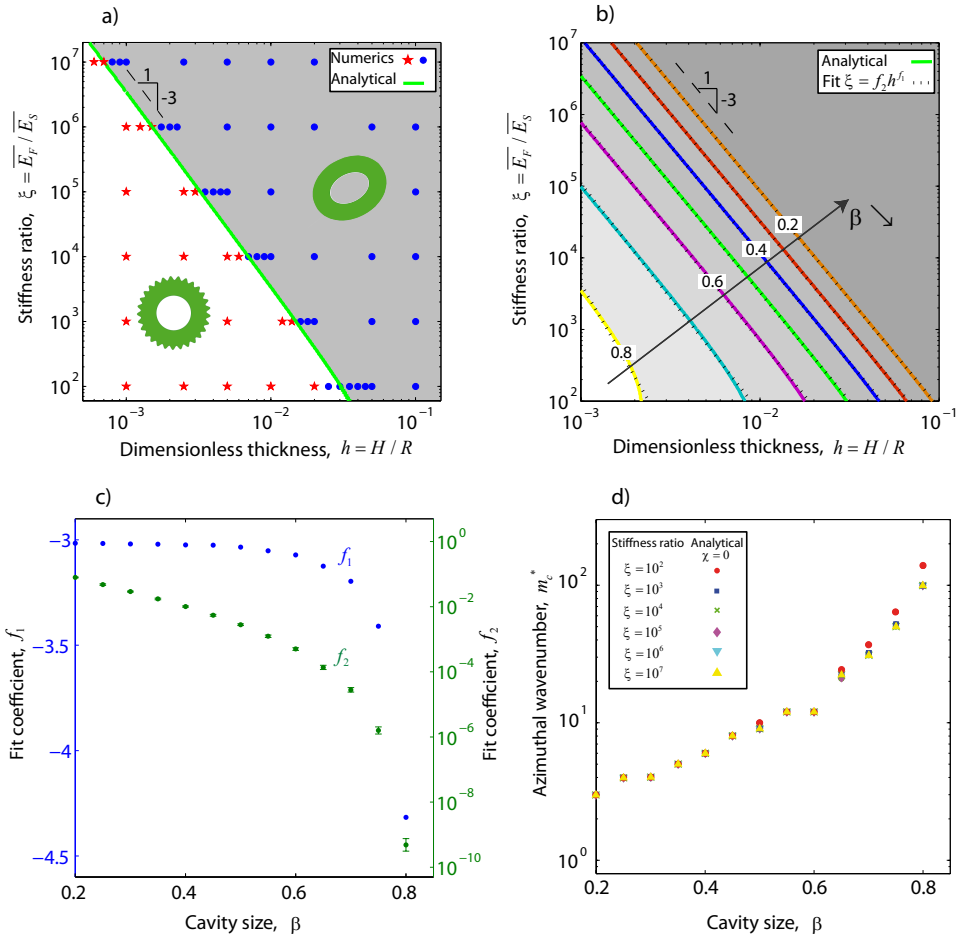

Figure 4.7: (a) Phase diagram in the (ξ, h) parameter space, showing the transition boundary, h^*, from wrinkling to global buckling, for $\beta = 0.5$. (b) Phase diagram for $\beta = 0.2$ to $\beta = 0.8$. Solid lines are analytical predictions and dotted lines correspond to a numerical fit $\xi = f_2 h^{f_1}$. (c) Fitting coefficients, f_1 and f_2, as functions of β. (d) Azimuthal wavenumber of the wrinkling mode for $h = h^*$, as a function of β. The Poisson's ratio of the substrate is $\nu_S = 0.5$.

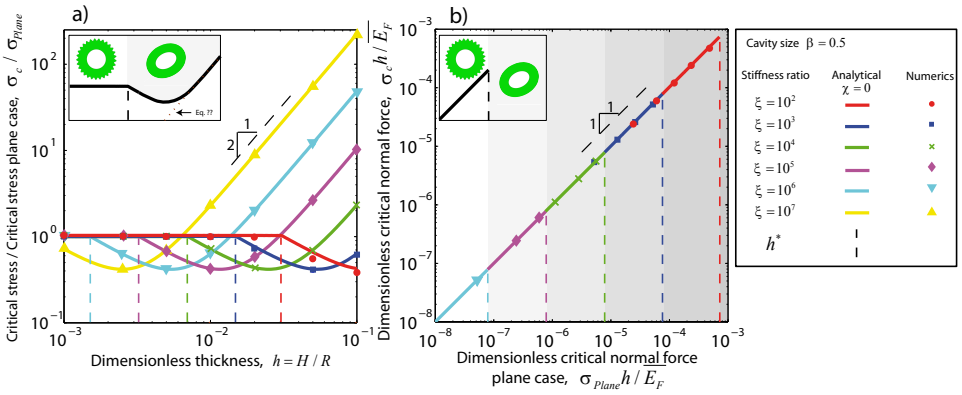

Figure 4.8: (a) Critical stress σ_c normalized by its planar substrate counterpart, σ_{Plane}, as a function of the dimensionless ring thickness $h = H/R$. (b) Dimensionless critical normal force versus planar substrate counterpart. Analytical predictions (solid lines) are given by Eq. (21a) and FEM results are shown as data points. Insets are sketches of the wrinkling and global buckling modes. The cavity size is $\beta = 0.5$ and the Poisson's ratio of the substrate is $\nu_S = 0.5$. The legend is common to both plots.

wavelength of our curved system to their counterparts for a infinite planar substrate. We shall center our discussion of this comparison for $\beta = 0.5$. In 4.7.3, we report the results for $\beta = 0.2$ and $\beta = 0.8$, which are qualitatively similar.

In Fig. 4.8(a), we plot σ_c/σ_{Plane} given by Eq. (21a), as a function of h. For $h < h^*$ (wrinkling domain), we find that $\sigma_c/\sigma_{Plane} \approx 1$, in agreement with the FEM simulations. To further quantify how close to unity is this ratio, in Fig. 4.8(b) we plot the dimensionless critical normal force $\sigma_c h/\overline{E_F}$ as a function of the planar result, $\sigma_{Plane}h/\overline{E_F}$. We obtain a line with unit slope, indicating that the substrate curvature has no significative effect on the critical stress for wrinkling. From this observation, and using Eq. (12) with $\sigma_0 = \sigma_{Plane}$, we write the following approximation for the dimensionless critical pressure,

$$|p_c| = \frac{h + k_0}{\gamma} \frac{\sigma_{Plane}}{\overline{E_F}} + O\left(h^3\right), \tag{23}$$

with k_0 and γ given by Eq. (10). Finally, back to Fig. 4.8(a), for $h > h^*$ (global buckling domain), we find that σ_c/σ_{Plane} first decreases with h, then reaches a local minimum and eventually increases as a power-law with slope 2, towards the asymptotic limit given by Eq. (22). The evolution of σ_c/σ_{Plane} in the global buckling domain is also reproduced well by FEM simulations.

We now investigate the effect of curvature on the wavelength of the instability mode. In Fig. 4.9(a), we plot $\lambda_c/\lambda_{Plane}$, given by Eq. (21b), as a function of h. Focusing on the wrinkling domain, we find that $\lambda_c/\lambda_{Plane} \approx 1$, in agreement with FEM simulations. In Fig. 4.9(b), once again, we quantify how close to unity this ratio is by plotting the critical wavelength λ_c as a function of the planar result, λ_{Plane}. To first approximation, noting the range of five orders of magnitude in both axes of the plot, we find a line with unit slope that passes through the origin, suggesting that the substrate cur-

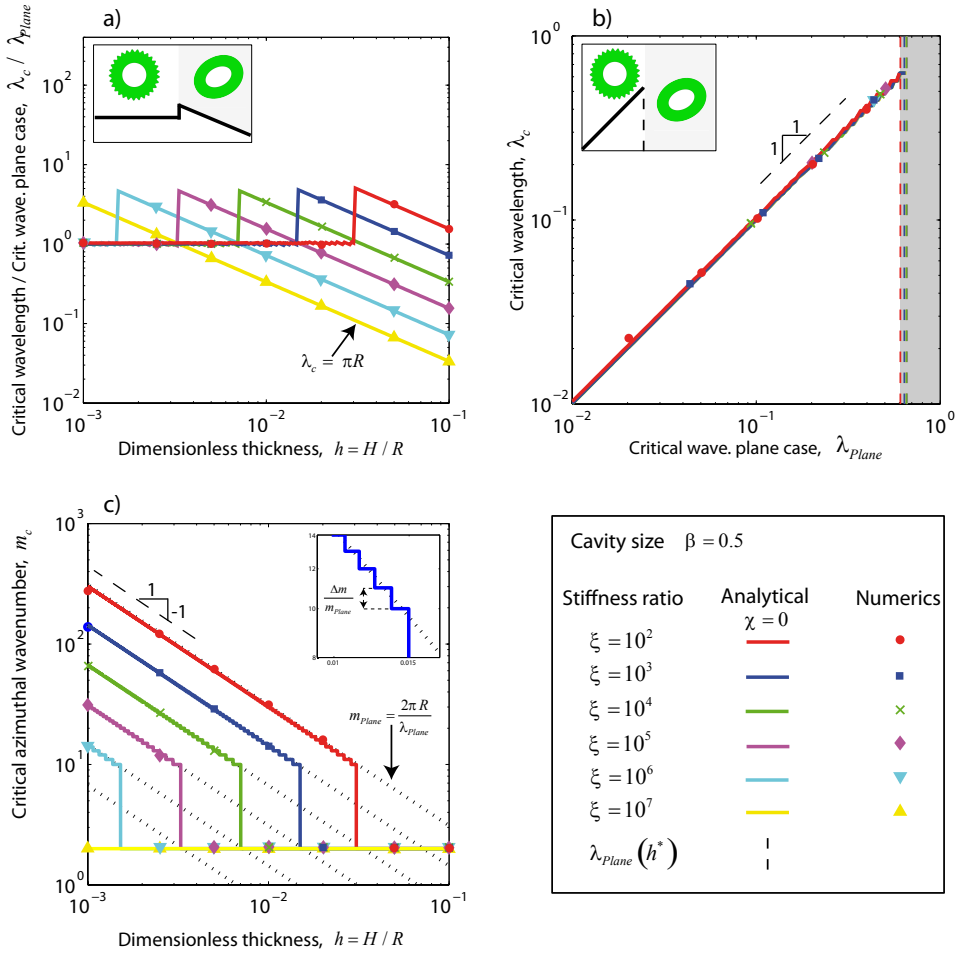

Figure 4.9: (a) Critical wavelength, λ_c, normalized by its planar substrate counterpart, λ_{Plane}, as a function of the dimensionless ring thickness $h = H/R$. Analytical predictions (solid lines) are given by Eq. (21b). (b) Zoom of the wrinkling domain by plotting λ_c versus λ_{Plane}. (c) Azimuthal wavenumber m_c of the wrinkling mode as a function of h. Analytical predictions (solid lines) are given by Eq. (17). Dotted lines show m_c for the planar substrate case. Insets on (a) and (b) are sketches of the wrinkling and global buckling modes. Inset on (c) is a zoom in showing the difference in m_c for the curved and planar substrates. The cavity size is $\beta = 0.5$ and the Poisson's ratio of the substrate is $\nu_S = 0.5$. FEM results shown as data points. The legend (bottom right) is common to all three plots.

vature has no significative effect on the wavelength of the wrinkling mode. The only deviations arise from the discrete nature of the wavenumber, since the geometry of the ring enforces 2π periodic wrinkling modes. To highlight this phenomenon, in Fig. 4.9(c), we plot the critical azimuthal wavenumber m_c, given by Eq. (17), as a function of h and we superimpose the planar substrate result (dashed line), $m_{Plane} = 2\pi R/\lambda_{Plane}$. We find that m_c is a decreasing stair function of h. The deviation in wavelength between the curved and planar cases scales as $(|\lambda_c - \lambda_{Plane}|)/\lambda_{Plane} \sim 1/m$, which is maximum for m_c^*. As shown previously in Fig. 4.7(d), m_c^* increases with β, hence the deviation $(|\lambda_c - \lambda_{Plane}|)/\lambda_{Plane}$ is maximum for a small cavity size. By way of example, for $\beta = 0.5$, Fig. 4.7(d) indicates that $m_c^* = 9$, leading to a maximum deviation $(|\lambda_c - \lambda_{Plane}|)/\lambda_{Plane} \approx 10\%$, that rapidly decreases as m increases.

4.6 Conclusion

We have considered the two-dimensional problem of a ring bound to an elastic substrate which contains a cavity that is depressurized. We have used an energy formulation to derive the Euler-Lagrange equations that govern the equilibrium of the ring, and solved them via an asymptotic expansion. As an improvement to previous results in the literature, our analytical approach accounts for the effect of curvature in modeling the reaction force of the substrate. The results have been compared with numerical simulations.

We first studied the principal solution, obtaining an expression for the hoop stress in the ring as a function of the applied pressure. We then performed a stability analysis of the problem to determine the critical pressure, P_c, and the corresponding instability mode. Depending on the dimensionless thickness and stiffness ratio (h and ξ) we have identified two different regimes: local wrinkling of the ring, and global buckling of the structure. The boundary between both regions of instability was described via a detailed phase diagram, which quantifies the value of h and ξ at which the transition between instabilities occurs and takes into account the cavity size, β. Our results can be used as a design guideline to target a desired mode. Finally, we have shown that the critical stress for wrinkling does not depend significantly on the curvature of the substrate. However, curvature imposes a discretization of the wrinkling wavelength due to the periodic closing conditions of the ring.

Our study focused on a 2D curved system which exhibits instability modes analogous to the cylindrical pattern found for uniaxial compression of a film on a flat infinite substrate. Considering more complex loading conditions (*e.g.* also introducing axial loading) or shells with non-zero Gaussian curvature, should lead to more complex patterns that deserve to be investigated further. Having validated the FEM analysis, as well as carefully considering the elastic response of the curved substrate, extending the study to these other scenarios and addressing the issue of pattern selection is an exciting avenue for future research.

4.7 Appendix

4.7.1 Response of the substrate

In this appendix we consider the boundary value problem of the substrate, subjected to the ring displacement $R\left(v\left(\theta\right),u\left(\theta\right)\right)$, v and u given by Eq. (8), at the interface $r=R$ between the ring and the substrate and to the pressure P at $r=R_0=\beta R$. The substrate is assumed to be in a plane strain state. We note $\alpha=3-4\nu_S$ and introduce the shear modulus $G=\overline{E_S}\left(1-\nu_S\right)/2$. The components of the stress in the substrate are represented by σ_{rr}, $\sigma_{r\theta}$, and the displacement field is (U_r,U_θ). The 2D problem of elasticity is solved by finding an Airy function of the form (Michell, 1899),

$$\begin{aligned}\phi_m\left(r,\theta\right)=&B_1r^2+B_2\ln\left(r\right)\\&+\varepsilon\left(A_1r^{m+2}+A_2r^{-m+2}+A_3r^m+A_4r^{-m}\right)\sin\left(m\theta\right),\end{aligned}\tag{24}$$

where A_i and B_i are unknown constants determined by the boundary conditions

$$\sigma_{rr}\left(R_0,\theta\right)=-P,\tag{25a}$$
$$\sigma_{r\theta}\left(R_0,\theta\right)=0,\tag{25b}$$
$$U_r\left(R,\theta\right)=Rv\left(\theta\right),\tag{25c}$$
$$U_\theta\left(R,\theta\right)=Ru\left(\theta\right),\tag{25d}$$

which are assumed to apply at $r=R_0$ and $r=R$. The first two equations stand for the continuity of the stress at the boundary of the cavity, whereas the last two stand for the continuity of the displacement at the interface between the substrate and the ring.

The stress and displacement fields resulting from the Airy function Eq. (24) are (Barber, 2002)

$$\sigma_{rr}\left(r,\theta\right)=2B_1+\frac{B_2}{r^2}+\begin{pmatrix}-A_1\left(m+1\right)\left(m-2\right)r^m\\-A_2\left(m+2\right)\left(m-1\right)r^{-m}\\-A_3m\left(m-1\right)r^{m-2}\\-A_4m\left(m+1\right)r^{-m-2}\end{pmatrix}\sin\left(m\theta\right),\tag{26}$$

$$\sigma_{r\theta}\left(r,\theta\right)=\begin{pmatrix}-A_1m\left(m+1\right)r^m+A_2m\left(m-1\right)r^{-m}\\-A_3m\left(m-1\right)r^{m-2}+A_4m\left(m+1\right)r^{-m-2}\end{pmatrix}\cos\left(m\theta\right),\tag{27}$$

$$U_r\left(r,\theta\right)=\frac{1}{2\mu}\left[B_1\left(\alpha-1\right)r+\begin{pmatrix}A_1\left(\alpha-m-1\right)r^{m+1}\\+A_2\left(\alpha+m-1\right)r^{-m+1}\\-A_3mr^{m-1}\\+A_4mr^{-m-1}\end{pmatrix}\sin\left(m\theta\right)\right],\tag{28}$$

$$U_\theta\left(r,\theta\right)=\frac{1}{2\mu}\left[B_1\left(\alpha-1\right)r+\begin{pmatrix}-A_1\left(\alpha+m+1\right)r^{m+1}\\+A_2\left(\alpha-m+1\right)r^{-m+1}\\-A_3mr^{m-1}\\-A_4mr^{-m-1}\end{pmatrix}\cos\left(m\theta\right)\right].\tag{29}$$

Applying the boundary conditions Eq. (25) to Eq. (26) yields a linear system for A_i and B_i, with solution

$$B_1 = \frac{1}{2\left(\beta^2+1-2\nu_S\right)}\left[\overline{E_S}v_0\left(1-\nu_S\right)-P\beta^2\right], \tag{30a}$$

$$B_2 = \frac{-R^2\beta^2}{\beta^2+1-2\nu_S}\left[\overline{E_S}v_0\left(1-\nu_S\right)+P\left(1-2\nu_S\right)\right], \tag{30b}$$

$$\begin{aligned} A_1 = & \\ & \frac{\left(m-1\right)\beta^{2m+2}+\left(\alpha-m+1\right)\beta^{2m}+\beta^2}{2\left(-m^2+1\right)\beta^{2m+2}+m^2\beta^{2m+4}+\beta^{4m+2}\alpha+\left(m^2-1+\alpha^2\right)\beta^{2m}+\alpha\beta^2} \\ & \times GR^{-m}A \\ & + \frac{\left(m-1\right)\beta^{2m+2}+\left(-m-\alpha+1\right)\beta^{2m}-\beta^2}{2\left(-m^2+1\right)\beta^{2m+2}+m^2\beta^{2m+4}+\beta^{4m+2}\alpha+\left(m^2-1+\alpha^2\right)\beta^{2m}+\alpha\beta^2} \\ & \times GR^{-m}B, \end{aligned} \tag{30c}$$

$$\begin{aligned} A_2 = & \\ & \frac{-\left(m+1\right)\beta^{2m+2}+\beta^{4m+2}+\beta^{2m}\left(\alpha+m+1\right)}{2\left(-m^2+1\right)\beta^{2m+2}+m^2\beta^{2m+4}+\beta^{4m+2}\alpha+\left(m^2-1+\alpha^2\right)\beta^{2m}+\alpha\beta^2} \\ & \times GR^{m}A \\ & + \frac{\left(m+1\right)\beta^{2m+2}+\beta^{4m+2}+\beta^{2m}\left(\alpha-m-1\right)}{2\left(-m^2+1\right)\beta^{2m+2}+m^2\beta^{2m+4}+\beta^{4m+2}\alpha+\left(m^2-1+\alpha^2\right)\beta^{2m}+\alpha\beta^2} \\ & \times GR^{m}B, \end{aligned} \tag{30d}$$

$$\begin{aligned} A_3 = & \\ & -\frac{\beta^2\left(\left(\alpha-m+1\right)\left(m+1\right)\beta^{2m}+m^2\beta^{2m+2}+\alpha+1+m\right)}{\left(2\left(-m^2+1\right)\beta^{2m+2}+m^2\beta^{2m+4}+\beta^{4m+2}\alpha+\left(m^2-1+\alpha^2\right)\beta^{2m}+\alpha\beta^2\right)m} \\ & \times GR^{-m+2}A \\ & -\frac{\beta^2\left(m^2\beta^{2m+2}-1+\left(-m-\alpha+1\right)\left(m+1\right)\beta^{2m}-m+\alpha\right)}{\left(2\left(-m^2+1\right)\beta^{2m+2}+m^2\beta^{2m+4}+\beta^{4m+2}\alpha+\left(m^2-1+\alpha^2\right)\beta^{2m}+\alpha\beta^2\right)m} \\ & \times GR^{-m+2}B, \end{aligned} \tag{30e}$$

$$\begin{aligned} A_4 = & \\ & -\frac{\left(-m^2\beta^{2m+2}+\left(m-1\right)\left(\alpha+m+1\right)\beta^{2m}-\left(\alpha-m+1\right)\beta^{4m}\right)\beta^2}{\left(2\left(-m^2+1\right)\beta^{2m+2}+m^2\beta^{2m+4}+\beta^{4m+2}\alpha+\left(m^2-1+\alpha^2\right)\beta^{2m}+\alpha\beta^2\right)m} \\ & \times GR^{m+2}A \\ & -\frac{\left(m^2\beta^{2m+2}+\left(m-1\right)\left(\alpha-m-1\right)\beta^{2m}-\left(-m-\alpha+1\right)\beta^{4m}\right)\beta^2}{\left(2\left(-m^2+1\right)\beta^{2m+2}+m^2\beta^{2m+4}+\beta^{4m+2}\alpha+\left(m^2-1+\alpha^2\right)\beta^{2m}+\alpha\beta^2\right)m} \\ & \times GR^{m+2}B. \end{aligned} \tag{30f}$$

Substituting A_i and B_i into Eq. (26) yields the stress at the interface $r = R$

$$\sigma_{rr}(R,\theta) = K_0 R v_0 + K R \varepsilon A \sin(m\theta) - \gamma P, \tag{31a}$$
$$\sigma_{r\theta}(R,\theta) = \mathrm{M} R \varepsilon B \cos(m\theta), \tag{31b}$$

where

$$K_0 = \overline{E_S}\frac{1}{R}\frac{(1-\nu_S)\left(1-\beta^2\right)}{1-2\nu_S+\beta^2}, \tag{32a}$$
$$K = \overline{E_S}\frac{1}{R}\frac{(1-\nu_S)}{2}\left(S_A + S_B\frac{B}{A}\right), \tag{32b}$$
$$\mathrm{M} = \overline{E_S}\frac{1}{R}\frac{(1-\nu_S)}{2}\left(S_B\frac{A}{B} + T_B\right), \tag{32c}$$
$$\gamma = \frac{2\beta^2(1-\nu_S)}{1-2\nu_S+\beta^2}, \tag{32d}$$

and

$$\begin{aligned}\psi S_A = {} & 2\left(-m^2\left(\beta^4+2+\alpha\right)+(3+\alpha)\left(m^2-1\right)\beta^2+2(\alpha+1)\right)\beta^{2m} \\ & -\left(((\alpha+1)m+\alpha-1)\beta^{4m}-(\alpha+1)m+\alpha-1\right)\beta^2,\end{aligned} \tag{33a}$$

$$\begin{aligned}\psi S_B = {} & -2m\left(-m^2\left(\beta^4+1\right)+2\left(m^2-1\right)\beta^2+1+\alpha\right)\beta^{2m} \\ & +\left(((\alpha-1)m+\alpha+1)\beta^{4m}+(\alpha-1)m-\alpha-1\right)\beta^2,\end{aligned} \tag{33b}$$

$$\begin{aligned}\psi T_B = {} & 2\left(-m^2\beta^4+(1-\alpha)\left(m^2-1\right)\beta^2+\alpha m^2\right)\beta^{2m} \\ & -\left(((\alpha+1)m+\alpha-1)\beta^{4m}-(\alpha+1)m+\alpha-1\right)\beta^2,\end{aligned} \tag{33c}$$

$$\psi = \left(m^2\beta^4-\left(m^2-1\right)\left(2\beta^2-1\right)+\alpha^2\right)\beta^{2m}+\alpha\beta^2\left(1+\beta^{4m}\right). \tag{33d}$$

The dimensionless stress at the interface and the dimensionless stiffness parameters are obtained from Eq. (31), by dividing it with $\overline{E_F}$,

$$\frac{\sigma}{\overline{E_F}} = k_0 v_0 + k\varepsilon A\sin(m\theta) - \gamma p, \tag{34a}$$
$$\frac{\tau}{\overline{E_F}} = \mu\varepsilon B\sin(m\theta), \tag{34b}$$
$$k_0 = \frac{K_0 R}{\overline{E_F}} = \frac{(1-\nu_S)\left(1-\beta^2\right)}{1-2\nu_S+\beta^2}\frac{1}{\xi}, \tag{34c}$$
$$k = \frac{KR}{\overline{E_F}} = \frac{(1-\nu_S)}{2}\left(S_A + S_B\frac{B}{A}\right)\frac{1}{\xi}, \tag{34d}$$
$$\mu = \frac{\mathrm{M}R}{\overline{E_F}} = \frac{(1-\nu_S)}{2}\left(S_B\frac{A}{B} + T_B\right)\frac{1}{\xi}, \tag{34e}$$

as indicated in Eq. (10).

We note that in the case of an inextensible wrinkling mode $A/B = m$, the stiffness K simplifies to $\widetilde{K}$ given by

$$\begin{aligned}\widetilde{K} &= \overline{E_S}\frac{1}{R}\frac{(1-\nu_S)}{2}\left(S_A + S_B\frac{1}{m}\right) \\ &= \overline{E_S}\frac{1}{mR}\frac{2(1-\nu_S)^2\left(\beta^{-2m}-\beta^{2m}+2m\left(1-\beta^{-2}\right)\right)\left(m^2-1\right)}{\left(\beta^{-1}-\beta\right)^2\left(m^2-1\right)+\left(\beta^{-m}-\beta^m\right)^2(3-4\nu_S)+\left(\frac{3-4\nu_S}{\beta}+\beta\right)^2},\end{aligned} \tag{35}$$

which, for a substrate with no cavity, leads to the limiting case

$$\lim_{\beta\to 0}\left(\widetilde{K}\right) = \overline{E_S}\frac{1}{mR}\frac{2(1-\nu_S)^2\left(m^2-1\right)}{3-4\nu_S}, \tag{36}$$

and, for an infinite plane substrate, yields

$$\lim_{R\to\infty}\left(\lim_{\beta\to 0}\left(\widetilde{K}\right)\right) = K_{Plane} = \overline{E_S}\frac{4(1-\nu_S)^2}{3-4\nu_S}\frac{\pi}{\lambda}, \tag{37}$$

in agreement with Audoly & Boudaoud (2008*a*).

4.7.2 Terms of the linear analysis of stability

The terms a_i, $\widetilde{a_i}$, b_i and $\widetilde{b_i}$ that appear in Eq. (16) are

$$a_1 = -4\xi h\left(\left(m^4+\frac{3}{2}-\frac{11}{4}m^2\right)h^2-9-3m^2\right)\frac{\gamma}{h+h^3/12+k_0}, \tag{38a}$$

$$\widetilde{a_1} = h\left(\left(m^2-1\right)^2h^2+12\right)\xi+6\left(1-\nu_S\right)S_A, \tag{38b}$$

$$b_1 = -4\xi h\left(\frac{1}{4}h^2m^3+12m\right)\frac{\gamma}{h+h^3/12+k_0}, \tag{38c}$$

$$\widetilde{b_1} = -12\xi hm+6\left(1-\nu_S\right)S_B, \tag{38d}$$

$$a_2 = -\left(h^3m^2+48h+12k_0\left(1-\chi\right)\right)m\xi\frac{\gamma}{h+h^3/12+k_0}+12\gamma\left(1-\chi\right)m\xi, \tag{38e}$$

$$\widetilde{a_2} = -12hm\xi+6\left(1-\nu_S\right)S_B, \tag{38f}$$

$$b_2 = \left(36hm^2+h^3+12h+12k_0\left(1-\chi\right)\right)\xi\frac{\gamma}{h+h^3/12+k_0}-12\gamma\left(1-\chi\right)\xi, \tag{38g}$$

$$\widetilde{b_2} = 12hm^2\xi+6\left(1-\nu_S\right)T_B \tag{38h}$$

where γ, k_0, S_A, S_B and T_B were given in 4.7.1.

4.7.3 Influence of the cavity size

In Figs. 4.10 and 4.11, we plot the h dependence of σ_c/σ_{Plane} and $\lambda_c/\lambda_{Plane}$, for cavity sizes $\beta = 0.2$ and $\beta = 0.8$, respectively. These plots are qualitatively similar to those obtained for $\beta = 0.5$ in Figs. 4.8 and 4.9, and discussed in 4.5.4 of the main text.

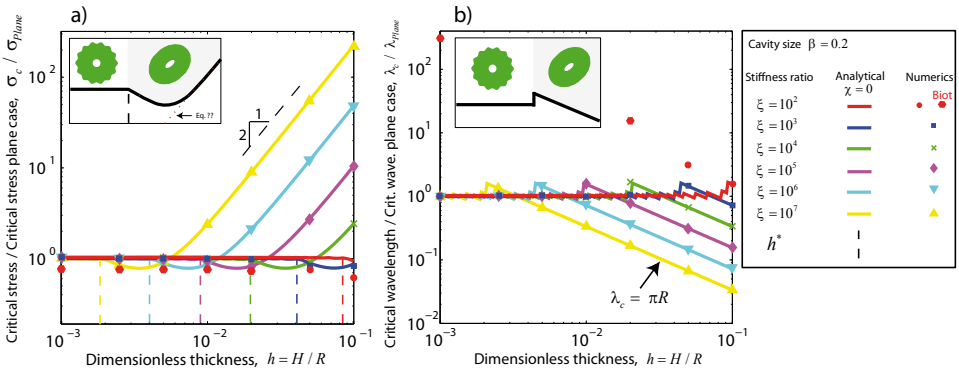

Figure 4.10: (a) Critical stress σ_c normalized by its planar substrate counterpart σ_{Plane}, as a function of the dimensionless ring thickness $h = H/R$. Analytical prediction is given by Eq. (21a). (b) Critical wavelength λ_c normalized by its planar substrate counterpart λ_{Plane}, as a function of h. Analytical prediction is given by Eq. (21b). Insets are sketches of the wrinkling and global buckling modes. The cavity size is $\beta = 0.2$ and the Poisson's ratio of the substrate is $\nu_S = 0.5$. The legend is common to both plots.

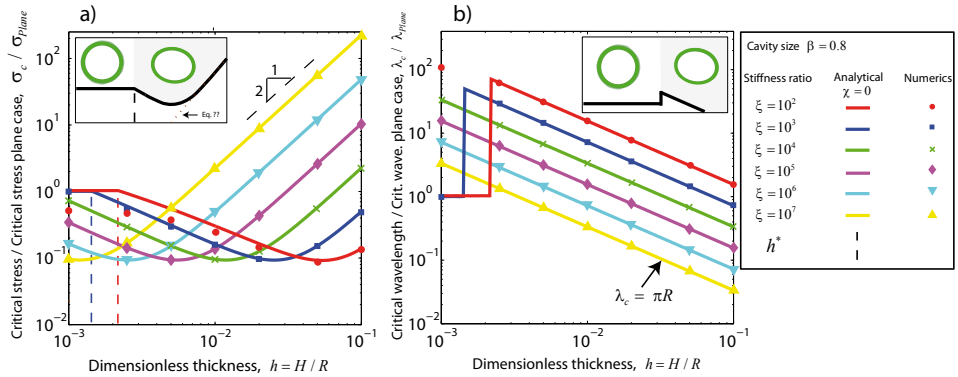

Figure 4.11: (a) Critical stress σ_c normalized by its plane substrate counterpart σ_{Plane}, as a function of the dimensionless ring thickness $h = H/R$. Analytical prediction is given by Eq. (21a). (b) Critical wavelength λ_c normalized by its plane substrate counterpart λ_{Plane}, as a function of h. Analytical prediction is given by Eq. (21b). Insets are sketches of the wrinkling and global buckling modes. The cavity size is $\beta = 0.8$ and the Poisson's ratio of the substrate is $\nu_S = 0.5$. The legend is common to both plots.

Bibliography

Allen, H. G. 1969 *Analysis and Design of Structural Sandwich Panels*. Pergamon, New York.

Atanackovic, T. M. 1998 Buckling of a compressible elastic ring. *Acta Mechanica* **127**, 121–134.

Audoly, B. & Boudaoud, A. 2008*a* Buckling of a thin film bound to a compliant substrate (part I). Formulation, linear stability of cylindrical patterns, secondary bifurcations. *Journal of the Mechanics and Physics of Solids* **56**, 2401–2421.

Audoly, B. & Boudaoud, A. 2008*b* Buckling of a thin film bound to a compliant substrate (part II). A global scenario for the formation of herringbone pattern. *Journal of the Mechanics and Physics of Solids* **56**, 2422–2443.

Audoly, B. & Boudaoud, A. 2008*c* Buckling of a thin film bound to a compliant substrate (part III). Herringbone solutions at large buckling parameter. *Journal of the Mechanics and Physics of Solids* **56**, 2444–2458.

Barber, J. R. 2002 *Elasticity: 2nd Edition*. Kluwer Academic Publishers.

Ben Amar, M. & Goriely, A. 2005 Growth and instability in elastic tissues. *Journal of the Mechanics and Physics of Solids* **53**, 2284–2319.

Biot, M. 1965 *Mechanics of Incremental Deformation*. Wiley, New York.

Bowden, N., Brittain, S., Evans, A. G., Hutchinson, J. W. & Whitesides, G. M. 1998 Spontaneous formation of ordered structures in thin films of metals supported on an elastomeric polymer. *Nature* **393**, 146–149.

Breid, D. & Crosby, A. J. 2009 Surface wrinkling behavior of finite circular plates. *Soft Matter* **5**, 425–431.

Breid, D. & Crosby, A. J. 2013 Curvature-controlled wrinkle morphologies. *Soft Matter* **9**, 3624–3630.

Brush, D. O. & Almroth, B. O. 1975 *Buckling of Bars, Plates and Shells*. McGraw–Hill, New York.

Budday, S., Steinmann, P. & Kuhl, E. 2014 The role or mechanics during brain development. *Journal of the Mechanics and Physics of Solids* **72**, 75–92.

Cai, S., Bertoldi, K., Wang, H. & Suo, Z. 2010 Osmotic collapse of a void in an elastomer: breathing, buckling and creasing. *Soft Matter* **6**, 5770–5777.

Cai, S., Breid, D., Crosby, A. J., Suo, Z. & Hutchinson, J. W. 2011 Periodic patterns and energy states of buckled films on compliant substrates. *Journal of the Mechanics and Physics of Solids* **59**, 1094–1114.

Cao, Y.-P., Li, B. & Feng, X.-Q. 2012 Surface wrinkling and folding of core–shell soft cylinders. *Soft Matter* **8**, 556.

Carrier, G. F. 1947 On the buckling of elastic rings. *Journal of Mathematics and Physics* **26**, 94–103.

Chan, E. P. & Crosby, A. J. 2006*a* Fabricating microlens arrays by surface wrinkling. *Advanced Materials* **18(24)**, 3238–3242.

Chan, E. P. & Crosby, A. J. 2006*b* Spontaneous formation of stable aligned wrinkling patterns. *Soft Matter* **2(4)**, 324–328.

Chen, X. & Hutchinson, J. W. 2004 Herringbone buckling patterns of compressed thin films on compliant substrates. *Journal of Applied Mechanics* **71(5)**, 597–603.

Chen, X. & Yin, J. 2010 Buckling patterns of thin films on curved compliant substrates with applications to morphogenesis and three-dimensional micro-fabrication. *Soft Matter* **22(6)**, 5667–5680.

Cheng, P. 1996 Weight optimization of cylindrical shells with cellular cores. Master of Science manuscript.

Combescure, A. 1981 Calcul analytique de la déformation d'un anneau avec défauts. DEMT/SMTS/BAMS/81-142 F.E. : 5423-05-000-09.

Efimenko, K., Rackaitis, M., Manias, E., Vaziri, A., Mahadevan, L. & Genzer, J. 2005 Nested self-similar wrinkling patterns in skins. *Nature Materials* **4**, 293–297.

Genzer, J. & Groenewold, J. 2006 Soft matter with hard skin: From skin wrinkles to templating and material characterization. *Soft Matter* **2**, 310–323.

Huang, Z., Hong, W. & Suo, Z. 2005 Nonlinear analyses of wrinkles in a film bonded to a compliant substrate. *Journal of the Mechanics and Physics of Solids* **53**, 2101–2118.

Huck, W. T. S., Bowden, N., Onck, P., Pardoen, T., Hutchinson, J. W. & Whitesides, G. M. 2000 Ordering of spontaneously formed buckles on planar surfaces. *Langmuir* **16**, 3497–3501.

Huddleston, P. J. & Lan, L. 1993 Information from fold shapes. *Journal of Structural Geology* **15**, 253–264.

Kachman, D. 1959 Test report on buckling of propellant cylinders under compressive loads. Space Technology Labs, Inc., GM-59-7520.6-24.

Kim, D. H., Lu, N., Ma, R., Kim, Y. S., Kim, R. H., Shuodao, W., Wu, J., Won, S. M., Kim, T. I., Chowdhury, R., Ying, M., Xu, L., Li, M., Chung, H. J., Keum, H., McCormick, M., Liu, P., Zhang, Y. W., Omenetto, F. G., Huang, Y., Coleman, T. & Rogers, J. A. 2011 Epidermal electronics. *Science* **333**, 838.

Kim, J. B., Kim, P., Pégard, N. C., Oh, S. J., Kagan, C. R., Fleischer, J. W., Stone, H. A. & Loo, Y. L. 2012 Wrinkles and deep folds as photonic structures in photovoltaics. *Nature Photonics* **6**, 327–332.

Kundu, S., Davis, C., Long, T., Sharma, R. & Crosby, A. 2011 Adhesion of nonplanar wrinkled surfaces. *Journal of Polymer Science Part B: Polymer Physics* **49**, 179–185.

Landau, L. D. & Lifshitz, E. M. 1959 *Theory of Elasticity*. Pergamon, London.

Lévy, M. M. 1884 Mémoire sur un nouveau cas intégrable du problème de l'élastique et de l'une de ses applications. *Journal de Mathématiques Pures et Appliquées* **3X**, 5–42.

Li, B., Cao, Y. P. & Feng, X. Q. 2011*a* Growth and surface folding of esophageal mucosa: a biomechanical model. *Journal of Biomechanics* **44**, 182–188.

Li, B., Cao, Y.-P., Feng, X.-Q. & Gao, H. 2011*b* Surface wrinkling of mucosa induced by volumetric growth : Theory, simulation and experiment. *Journal of the Mechanics and Physics of Solids* **59**, 758–774.

Li, B., Cao, Y.-P., Feng, X.-Q. & Gao, H. 2012 Mechanics of morphological instabilities and surface wrinkling in soft materials: a review. *Soft Matter* **8**, 5728.

Li, B., F, J., Cao, Y. P., Feng, X. Q. & Gao, H. 2011*c* Surface wrinkling patterns on a core–shell soft sphere. *Physical Review Letters* **106**, 234301.

Lourie, O., Cox, D. M. & Wagner, H. D. 1998 Buckling and collapse of embedded carbon nanotubes. *Physical Review Letters* **81**, 1638–1641.

Mei, Y., Kiravittaya, S., Harazim, S. & Schmidt, O. G. 2010 Principles and applications of micro and nanoscale wrinkles. *Materials Science and Engineering R* **70**, 209–224.

Michel, J., Lopez-Pamies, O., Ponte Castañeda, P. & Triantafyllidis, N. 2007 Microscopic and macroscopic instabilities in finitely strained porous elastomers. *Journal of the Mechanics and Physics of Solids* **55**, 900–938.

Michell, J. H. 1899 On the direct determination of stress in an elastic solid, with application to the theory of plates. *Proceedings of the London Mathematical Society* **s1-31(1)**, 100–124.

Price, N. J. & Cosgrove, J. W. 1990 *Analysis of Geological Structures*. Cambridge University Press, Cambridge.

Seide, P. 1962 The stability under axial compression and lateral pressure of circular-cylindrical shells with a soft elastic core. *Journal of the Aerospace Sciences* **29(7)**, 851–862.

Seide, P. & Weingarten, V. I. 1961 Buckling of circular rings and long cylinders enclosing an elastic material under uniform external pressure. *American Rocket Society Journal* **32(5)**, 680–687.

Terwagne, D., Brojan, M. & Reis, P. 2014 Smart morphable surfaces for aerodynamic drag control. *Advanced Materials* p. In press.

Timoshenko, S. P. & Gere, J. M. 1961 *Theory of Elastic Stability*. McGraw-Hill, New York.

Wang, S., Song, J., Kim, D., Huang, Y. & Rogers, J. 2008 Local versus global buckling of thin films on elastomeric substrates. *Applied Physics Letters* **93(2)**, 023126.

Yin, J., Chen, X. & Sheinman, I. 2009 Anisotropic buckling patterns in spheroidal film/substrate systems and their implications in some natural and biological systems. *Journal of the Mechanics and Physics of Solids* **57**, 1470–1484.

Yin, J., Han, X., Cao, Y. & Lu, C. 2014 Surface wrinkling on polydimethylsiloxane microspheres via wet surface chemical oxidation. *Scientific Reports* **4**, 5710.

Yin, J., Yagüe, J. L., Eggenspieler, D., Gleason, K. K. & Boyce, M. C. 2012 Deterministic order in surface micro-topologies through sequential wrinkling. *Advanced materials* **24**, 5441–5446.

Yoo, P. J., Suh, K. Y., Park, S. Y. & Lee, H. H. 2002 Physical self-assembly of microstructures by anisotropic buckling. *Advanced materials* **14**, 1383–1387.

Yu, C. & Jiang, H. 2010 Forming wrinkled stiff films on polymeric substrates at room temperature for strechable interconnects applications. *Thin Solid Films* **519**, 818–822.

5. INSTABILITÉ FLUIDE-ÉLASTIQUE D'UN FAISCEAU DE TUBES

Les phénomènes d'interaction fluide-structure (I.F.S.) sont omniprésents dans les installations industrielles où des structures solides sont en contact avec un fluide qui exerce un chargement mécanique. Pour des structures élancées et souples, l'I.F.S. peut induire des phénomènes vibratoires et des instabilités mécaniques à l'origine de grandes amplitudes de déplacements. L'industrie nucléaire est confrontée à cette problématique, notamment au niveau des tuyauteries, des assemblages de combustible, des commandes de grappe ou encore des générateurs de vapeur (G.V.). Un réacteur à eau préssurisée comprend habituellement trois ou quatre générateurs de vapeur, permettant le transfert de chaleur du circuit primaire vers le circuit secondaire, les deux circuits restant isolés. L'échange thermique entre les deux circuits se fait au travers de tubes en forme de U renversé. L'eau chaude du circuit primaire, pressurisée (155 bar) et chauffée (320 °C) par le cœur du réacteur nucléaire s'écoule à l'intérieur des tubes alors que l'eau froide du circuit secondaire s'écoule à l'extérieur des tubes. Cette eau, portée à ébullition, se transforme en vapeur qui alimente les turbines génératrices d'électricité. Un G.V. est constitué de plusieurs milliers de tubes (faisceau de tubes) représentant une surface d'échange de l'ordre de 5000 m^2. Ces tubes élancés sont encastrés en partie basse sur une plaque tubulaire et guidés par des plaques entretoises composées d'orifices qui permettent à l'eau liquide du circuit secondaire de s'écouler et de se transformer progressivement en vapeur. En tant que structures élancées et flexibles, les tubes de G.V. sont sensibles aux mécanismes de l'I.F.S., en particulier au niveau de la partie supérieure cintrée (chignon) soumise à un écoulement transverse diphasique eau-vapeur. Les vibrations liées à cette interaction induisent des phénomènes (fatigue et usure par frottement et chocs) pouvant entrainer de graves conséquences pour la sûreté nucléaire. Pour faire face aux différents modes de dégradation des tubes de G.V. et éviter des fuites entre le circuit primaire radioactif et le circuit secondaire, des contrôles avec des sondes passant dans les différents tubes sont réalisés lors des arrêts des réacteurs. En fonction des résultats de ces contrôles, des bouchages de tubes via l'obturation de leur entrées et sorties sont réalisés de manière préventive, voir Fig. 5.1. Enfin, lorsque les dégradations des tubes deviennent trop importantes, des opérations lourdes de remplacement de l'ensemble des générateurs de vapeur associés à un réacteur sont réalisées. Dans le cadre de la prévention des risques vibratoires des tubes de G.V., et afin d'améliorer le dimensionnement et évaluer les marges en fonctionnement normal ou dégradé des G.V., des études expérimentales, numériques et théoriques sont ainsi conduites par les acteurs du nucléaire. Pour les tubes

de G.V., ces études portent essentiellement sur les mécanismes de l'I.F.S. en écoulement transverse monophasique (I.F.S. en partie basse des tubes) ou diphasique (I.F.S. au niveau du chignon). L'étude des mécanismes d'I.F.S. dans ces deux zones est alors réalisée à l'aide de faisceaux analytiques de tubes droits soumis à un écoulement transverse, monophasique ou diphasique.

Dans le but de mieux appréhender et quantifier les phénomènes vibratoires des tubes de G.V., des travaux expérimentaux sont menés au sein du laboratoire d'Etudes de dynamique (DYN) du C.E.A., sur des maquettes à échelle réduite. Afin de limiter le coût des installations et dans un souci de sécurité, les études sont réalisées avec des fluides simulants, en l'occurrence de l'eau et de l'air. Les deux principales maquettes exploitées au sein du laboratoire DYN s'appellent DIVA et TITAN, voir Fig. 5.2. La maquette DIVA est principalement dédiée à l'étude des vibrations dans les faisceaux à pas carré. Elle reproduit ainsi à échelle réduite l'I.F.S. dans les générateurs de vapeur qui équipent actuellement les 32 réacteurs nucléaires de 900 MWe et les 20 réacteurs de 1300 MWe du parc Français. La maquette TITAN est, quant à elle, dédiée à l'étude des vibrations dans les faisceaux à pas triangulaire. Ces faisceaux permettent de placer un plus grand nombre de tubes au sein des G.V. qui équipent actuellement les 4 réacteurs de 1450 MWe de palier N4 du parc Français et équiperont les futurs EPR. Les deux maquettes sont alimentées par une boucle équipée d'une pompe pouvant débiter de 5 à 300 l/s d'eau et d 'un compresseur à air pouvant débiter jusqu'à 3000 m^3/h sous une pression absolue de 8 bar. La boucle peut ainsi fonctionner en écoulement d'eau, en écoulement d'air ou en écoulement diphasique eau-air. La maquette DIVA est constituée de 15 tubes en acier inox placés sur 5 rangées et de 10 demi-tubes pour limiter les effets de bord. Les tubes ont un diamètre $D = 30$ mm, une longueur $L = 300$ mm et le faisceau un pas carré (distance entre deux tubes) $P = 45$ mm. La maquette TITAN est, quant à elle, composée de tubes similaires à ceux utilisés pour DIVA, mais disposés selon un arrangement triangulaire parallèle et un pas $P = 43.2$ mm. Ces deux maquettes permettent d'étudier plusieurs configurations flexibles, notamment le cas d'un tube unique monté sur un bi-lame flexible et positionné au centre d'un faisceau rigide, voir Fig. 5.2 (a). Deux caractéristiques fondamentales de ces maquettes sont i) la possibilité de découpler le mouvement des tubes selon les directions de portance (direction perpendiculaire à l'écoulement) et de trainée (même direction que l'écoulement), ii) l'utilisation d'un système de contrôle actif sans contact (actionneur électro-dynamique), voir Fig. 5.2 (b), permettant d'amortir les vibrations des tubes afin d'explorer leur dynamique sous d'importantes vitesses d'écoulement. La mesure expérimentale de la force fluide s'exerçant sur un tube flexible est réalisée par la méthode directe ou indirecte. Dans la méthode directe, le déplacement du tube est imposé par un pot vibrant (actionneur PRODERA), voir Fig. 5.2 (b), et la force fluide est directement mesurée par un capteur piézoélectrique. Dans la méthode indirecte, le mouvement du tube est libre, piloté par son interaction naturelle avec l'écoulement incident. La force fluide est alors obtenue indirectement à partir de la mesure, via un capteur laser, du déplacement et de la vitesse du tube. Les variations de fréquence et d'amortissement de ces

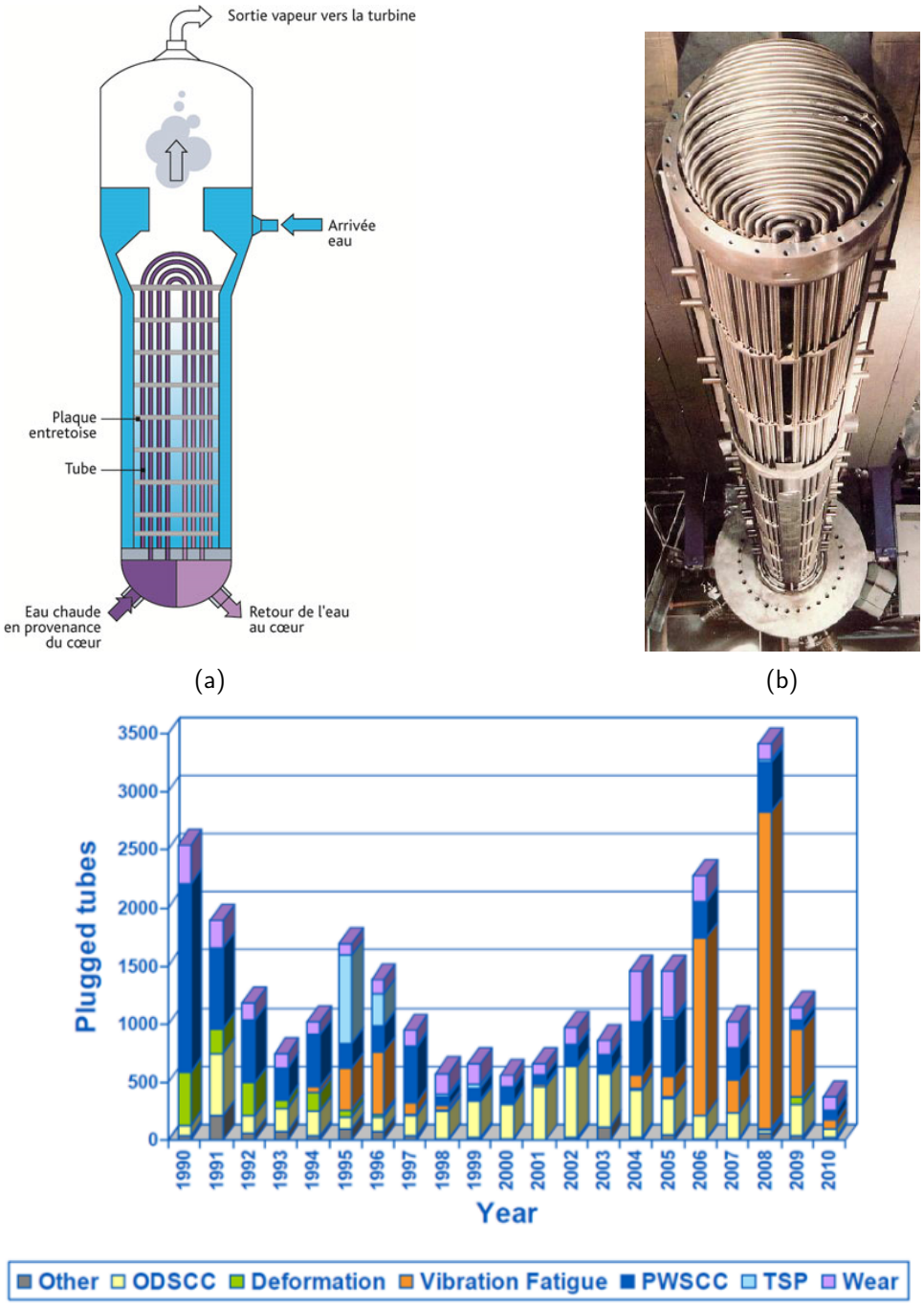

FIGURE 5.1 : (a) Schéma d'un générateur de vapeur, source IRSN. (b) Photo d'un assemblage de tubes de G.V. avec zoom sur le chignon. Vidéo Areva sur les vibrations des tubes de G.V. : ici. (c) Evolution du nombre de tubes bouchés en fonction des années, source EDF.

grandeurs par rapport aux références mesurées en fluide au repos permettent alors de remonter aux caractéristiques de la force fluide en écoulement.

En parallèle de son activité expérimentale, le laboratoire DYN conduit des études semi-analytiques pour déterminer le chargement mécanique exercé par un écoulement sur un tube flexible. La modélisation de ce chargement repose essentiellement sur l'hypothèse d'un découplage de la force fluide en deux phénomènes distincts

- les phénomènes aléatoires, modélisés par une force[1] fluide indépendante du mouvement du tube. Cette force, aussi appelée excitation aléatoire, est liée à l'intensité turbulente générée par l'écoulement. L'augmentation de cette intensité avec la vitesse de l'écoulement conduit à une croissance de l'amplitude vibratoire de la structure, voir Fig. 5.3.

- les phénomènes couplés, modélisés par une force fluide-élastique F_{FE} qui dépend du déplacement X, de la vitesse $\frac{dX}{dt}$ et de l'accélération $\frac{d^2X}{dt^2}$ du tube. Cette force est traditionnellement décomposée sous la forme

$$F_{FE} = -M_f \frac{d^2X}{dt^2} - C_f \frac{dX}{dt} - K_f X, \tag{1}$$

  où (M_f, C_f, K_f) représentent des coefficients de masse, d'amortissement et de rigidité ajoutés.

Sous l'hypothèse de décomposition de (1), le système couplé fluide-structure est alors caractérisé par un triplé de coefficients $M_s + M_f$, $C_s + C_f$, $K_s + K_f$, où M_s, C_s, K_s représentent la masse, l'amortissement et la rigidité du tube en air. Pour une vitesse d'écoulement critique V_c, l'amortissement total $C_T = C_s + C_f$ du système couplé devient nul, entrainant une instabilité fluide-élastique qui se manifeste sous la forme d'une croissance exponentielle de l'amplitude de vibration, voir Fig. 5.3. Ce type de phénomène peut conduire à une usure et un percement rapide des tubes de G.V. et a donc conditionné la plupart des études menées sur les faisceaux. Un adimensionnement est alors nécessaire pour transposer les résultats de ces études, réalisées sur des maquettes à échelle réduite, vers le cas du G.V. à échelle industrielle.

Les principaux nombres sans dimension permettant cette transposition d'échelle sont

- le rapport d'aspect, $l = L/D$, qui caractérise l'élancement des tubes sous écoulement,

- le pas réduit, $p = P/D$, qui caractérise la taille de l'espace libre utilisé par le fluide pour circuler entre les tubes,

- le nombre de Reynolds, $Re = DV/\nu$, avec V la vitesse de l'écoulement au sein du faisceau de tubes et ν la viscosité cinématique du fluide de densité ρ. Ce nombre caractérise principalement la vitesse de l'écoulement,

[1] Une collaboration (thèse de C. Bazin, 2020-2023) entre le laboratoire DYN (R. Lagrange, encadrant C.E.A.), le Laboratoire de Modélisation et Simulation en mécanique des Fluides (M. G. Rodio, encadrant C.E.A.) et le LadHyX (C. Josserand, directeur) est en cours pour reproduire numériquement cette force observée dans la maquette expérimentale DIVA.

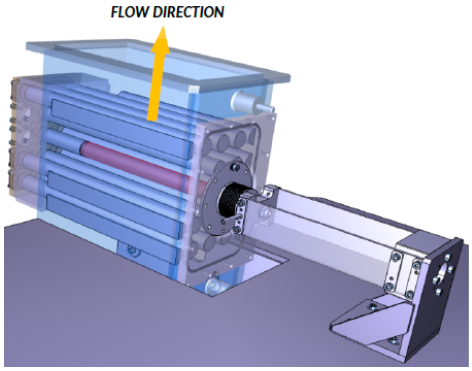

(a)

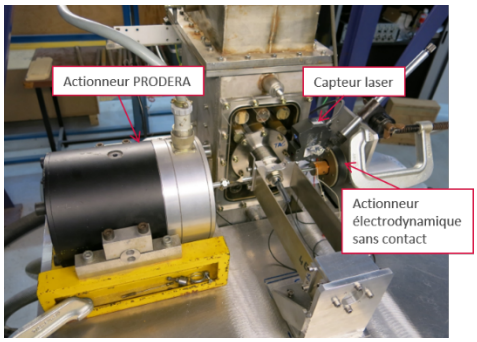

(b)

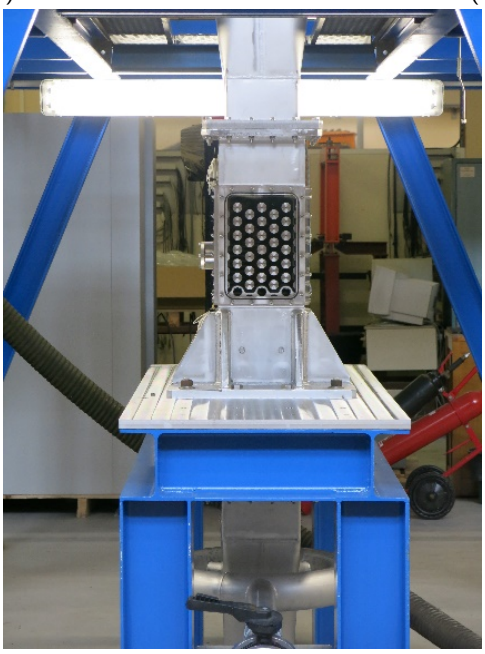

(c)

FIGURE 5.2 : (a) Schéma de la maquette DIVA (faisceau à pas carré). (b) Photo de l'instrumentation. Vidéo C.E.A. de l'instabilité fluide-élastique en portance, configuration DIVA, écoulement monophasique : ici. (c) Photo de la maquette TITAN (faisceau à pas triangulaire).

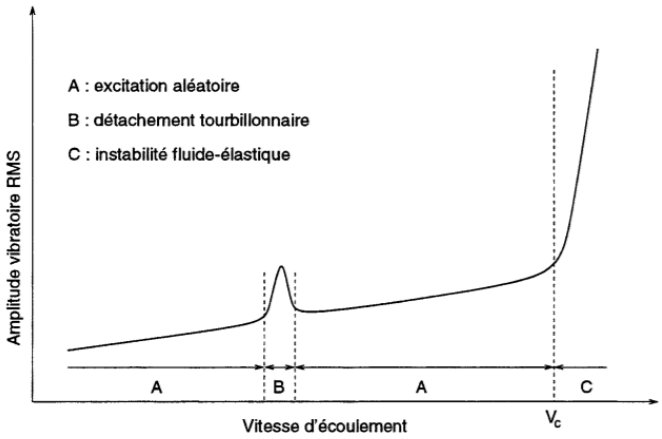

FIGURE 5.3 : Evolution de l'amplitude vibratoire en fonction du débit de l'écoulement. L'excitation aléatoire est liée à l'intensité turbulente de l'écoulement. Le détachement tourbillonnaire, absent en écoulement diphasique, correspond à une organisation périodique de l'écoulement autour du tube. L'instabilité fluide élastique est caractérisée par une croissance exponentielle de l'amplitude vibratoire. Source : S. Caillaud.

- le nombre de Stokes, $Sk = F_0 D^2/\nu$, avec F_0 la fréquence du tube en fluide au repos. Ce nombre caractérise principalement la flexibilité du tube,
- la vitesse réduite, $Vr = V/F_0 D$, qui caractérise le rapport entre la vitesse de l'écoulement et une vitesse caractéristique de vibration du tube. Ce nombre sans dimension s'exprime en fonction de Re et Sk sous la forme $Vr = Re/Sk$,
- le nombre de Scruton, $Sc = C_0/\left(2\rho D^2 L F_0\right)$ avec C_0 l'amortissement du tube en fluide au repos. Ce nombre caractérise principalement la masse et l'amortissement du tube et est parfois appelé paramètre masse-amortissement.

L'ensemble des nombres sans dimension caractérise alors le système couplé fluide-structure, en particulier l'évolution de son amortissement total $C_T = C_s + C_f$ et de son seuil de stabilité $C_T = 0$.

La détermination du seuil de stabilité $C_T = 0$ d'un tube flexible positionné au centre d'un faisceau rigide, à pas carré, soumis à un écoulement transverse monophasique et diphasique (eau-air), est l'objet de la publication qui suit, soumise dans la revue *Journal of Fluids and Structures*, sous le titre "A new criterion for the instability threshold of a square tube bundle subject to an air-water cross-flow".

Abstract

In this paper, we investigate the fluid-elastic instability of a square tube bundle subject to two-phase cross-flow. A dimensional analysis is carried out, leading to a new criterion of instability. This criterion establishes a direct link with the instability thresholds in single-phase flows. In parallel to the dimensional analysis, experimental work is carried out to i) determine the instability thresholds in single-phase flows (new relation between the Scruton, Stokes and Reynolds number), ii) to test the validity of the two-phase flow instability criterion, derived from the dimensional analysis. The experiments are carried out on a square tube bundle (pitch ratio of 1.5) consisting on 5 rows of 3 tubes (plus two end-rows of half tubes). The central tube is mounted on two flexible blades allowing a vibration in the transverse direction only, whereas all the other tubes are rigid. The instability threshold in single-phase (water) flow is obtained from a method of direct measurement of the fluid-elastic forces, in which the motion of the central tube is imposed. The instability threshold in two-phase (air-water) flow is obtained from a method of indirect measurement, with an active system stability control, of the fluid-elastic forces, in which the central tube vibrates freely. Three sets of blades with different stiffnesses are tested to investigate the stability of the central tube. The criterion of instability is in very good agreement with air-water experiments, predictive for all homogeneous void fractions, and so for all flow regimes (identified in our experiments with an optical probe). This new criterion is of theoretical interest for the understanding of complex two-phase flow excitations, as well as of practical significance for the predictive analysis of industrial components.

5.1 Introduction

The knowledge of the fluid force acting on a structure subject to a cross flow is a crucial information that must be accounted for when designing heat-exchanger tube bundles. The large vibrations resulting from a fluid-elastic instability may lead to some mechanical degradation of the concerned tube, which may affect the power plant operation and safety. This instability can be described as a self-excited feedback mechanism between the motion of the structure and the fluid forces.

The first work on fluid-elastic instability was published by Roberts (1962), who highlighted self-sustained oscillations within a row of cylinders subject to cross flow; the cylinders being alternately rigid and flexible in the direction of the flow. Connors Connors (1970) studied the interaction between a row of flexible cylinders and a transverse flow and developed a quasi-static model following the work of Roberts (1962). He proposed an estimation of the critical instability velocity for a tube as a function of a mass damping parameter and a constant called the Connors constant. Several other theoretical models were subsequently proposed for the study of the fluid-elastic instability: the inviscid or velocity potential model by Dalton & Helfinstine (1971), the quasi-steady model by Price & Paidoussis (1982, 1983), the unsteady model by Tanaka & Takahara (1980, 1981); Chen (1983*a*,*b*, 1987), the

quasi-unsteady model by Granger & Paidoussis (1996) or the flow channel model by Lever & Weaver (1986).

Following the work of Roberts (1962) and Connors (1970), a wealth of experimental studies were also carried out, primarily to refine Connors' model and determine the value of the Connors constant for various types of tube bundles. Initially, most of the experiments were performed in single-phase flows (liquid or gaseous) and it was not until the 1980s that studies on tube bundles subject to two-phase flow became widespread, see for e.g. Axisa *et al.* (1984, 1985); Nakamura *et al.* (1986*a*,*b*). Most experimental works were done in air-water flows due to the very high cost of steam-water loops. This however raised the question of the validity of experimental results for the tubes of a steam generator that actually operate in a steam-water mixture. To overcome this problem, some researchers as Pettigrew *et al.* (1995, 2002); Pettigrew & Taylor (2009) used a mixture of liquid-vapor freon due to the proximity of its density ratio to that of steam-water. The results have shown very little difference in terms of critical velocity whether a mixture of freon, an air-water or a steam-water flow is considered. It is therefore believed that the results in air-water are representative of what happens in a steam generator. Still, it should be mentioned that, apart from experimental Axisa *et al.* (1984, 1985); Nakamura *et al.* (1986*a*,*b*) and numerical Sadek *et al.* (2018, 2020) studies, most theoretical models have been developed for single-phase flows, whereas steam generators operate mainly in two-phase flows. Recently, Yasser *et al.* (2021) relied on the inviscid flow channel approach of Hassan & Weaver (2015, 2016) to develop a model to predict fluid-elastic instability in a square tube bundle subject to a two-phase bubbly cross-flow. In his work, Yasser *et al.* (2021) treated the liquid phase as a continuous medium and modeled gas bubbles as compressible dispersed particles. The continuity and momentum equations are solved numerically to calculate the fluid forces on the tube and the flow properties around it. The prediction of the stability threshold obtained from this model showed promising results compared to the experimental data. In our work, we present a very different approach, in which the two-phase instability threshold is not obtained from the implementation of a theoretical model in a numerical simulation code. This work, an augmented version of Lagrange *et al.* (2022), is based solely on dimensional analysis and on a hypothesis of similarity with single-phase flow.

5.2 Position of the problem and dimensional analysis

We consider the lift vibration of a flexible tube (diameter D, length L), part of a square tube bundle (pitch P), subject to a two-phase cross-flow characterized by the mass densities (ρ_1, ρ_2), the kinematic viscosities (ν_1, ν_2), the superficial gap velocities (J_1, J_2) of its two constitutive phases, as well as a surface tension σ, see Fig. 5.4. The homogeneous void fraction is defined as $\alpha = J_2/(J_1 + J_2)$. We note M_s, C_s and K_s the mass, damping and rigidity coefficients of the first mode of vibration of the flexible tube in vacuum. The modal displacement X in the lift direction is assumed to satisfy the equation

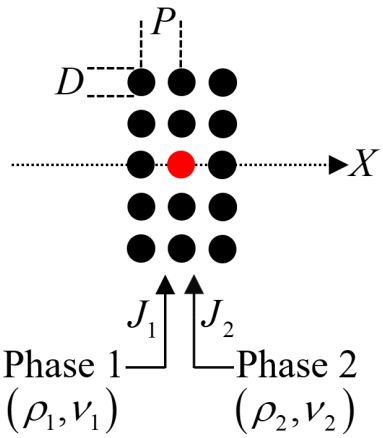

Figure 5.4: Sketch of a square tube bundle subject to two-phase cross-flow with superficial gap velocities J_1 and J_2. The two phases have mass densities (ρ_1, ρ_2) and kinematic viscosities (ν_1,ν_2). The central cylinder vibrates in the lift direction.

of motion

$$(M_s + M_f)\frac{d^2X}{dT^2} + (C_s + C_f)\frac{dX}{dT} + (K_s + K_f)X = F_t, \tag{1}$$

with T the time and where M_f, C_f and K_f are the fluid added mass, damping and rigidity terms, respectively. The right hand side term F_t is an excitation fluid force, considered as independent on the tube motion. According to this forced oscillator model, the flexible tube turns unstable when the total damping term $C_T = C_s + C_f$ vanishes, i.e. $C_T = 0$. Here, we consider that C_T is a function $H^{(j)}_{C_T}$ of $(C_j, F_j, \rho_1, \rho_2, \nu_1, \nu_2, \sigma, J_1, J_2, P, D, L)$ so that we can write

$$C_T = H^{(j)}_{C_T}\left(C_j, F_j, \rho_1, \rho_2, \nu_1, \nu_2, \sigma, J_1, J_2, P, D, L\right), \tag{2}$$

where C_j and F_j are the damping coefficient and frequency of the flexible tube immersed in the single-phase fluid j at rest. The relation (2) constitutes a minimal model, based on experimental observations, bibliography reporting and physical intuition. More advanced models would also consider the effect of some other parameters, for e.g. the roughness of the tubes. The dimensional analysis is based on the Vaschy-Buckingham theorem. The theorem states that an equation involving n physical variables with k fundamental units (usually $k = 3$ in classical mechanics) can be reduced to an equation involving $n-k$ dimensionless parameters. Thus, introducing a scale of length λ, mass M and time τ, the equation for the instability threshold $C_T = 0$ is physically meaningful if

$$h^{(j)}_{C_T}\left(\frac{C_j}{M\tau^{-1}}, \frac{F_j}{\tau^{-1}}, \frac{\rho_1}{M\lambda^{-3}}, \frac{\rho_2}{M\lambda^{-3}}, \frac{\nu_1}{\lambda^2\tau^{-1}}, \frac{\nu_2}{\lambda^2\tau^{-1}}, \right.$$
$$\left. \frac{\sigma}{M\tau^{-2}}, \frac{J_1}{\lambda\tau^{-1}}, \frac{J_2}{\lambda\tau^{-1}}, \frac{P}{\lambda}, \frac{D}{\lambda}, \frac{L}{\lambda}\right) = 0. \tag{3}$$

As Eq. (3) involves twelve dimensional quantities with three fundamental dimensions (length, mass and time), it can be reduced to a relation between nine dimensionless quantities. These dimensionless quantities are not unique and derive from a specific choice for the characteristic length λ, mass M and time τ. Picking $\lambda = D$, $M = \rho_j D^2 L$ and $\tau = D/J_j$ with j a free index, the dimensionless equation for the instability threshold can be rewritten as

$$h_{C_T}^{(j)}\left(Sc_j, Sk_j, m, \varepsilon, We_j, Re_1, Re_2, p, l\right) = 0, \tag{4}$$

with $l = L/D$, $p = P/D$, $m = \rho_2/\rho_1$ and $\varepsilon = \nu_2/\nu_1$ the tube aspect ratio, the pitch ratio, the density and viscosity ratios, respectively. The other dimensionless numbers appearing in Eq. (4), i.e.

$$Re_j = \frac{DJ_j}{\nu_j}, \quad Sk_j = \frac{D^2 F_j}{\nu_j}, \quad Sc_j = \frac{C_j}{2\rho_j D^2 L F_j}, \quad We_j = \frac{\rho_j L \nu_j^2}{\sigma D^2}, \tag{5}$$

are the Reynolds, Stokes, Scruton (i.e. mass-damping parameter) and Weber numbers, constructed from the physical properties of phase j. Once again, the choice for the dimensionless numbers is purely arbitrary, and other combinations are possible. For example, instead of Re_1 or Re_2, it is also possible to introduce the homogeneous void fraction α, via the relation $\alpha = \varepsilon Re_2/\left(Re_1 + \varepsilon Re_2\right)$. Similarly, one can replace in Eq. (4) the Reynolds number Re_j by a reduced velocity, $V_{rj} = Re_j/Sk_j$.

5.2.1 Single-phase flow instability threshold

A single-phase flow can be seen as a two-phase flow with two identical phases, i.e. $(\rho_1, \nu_1) = (\rho_2, \nu_2) = (\rho, \nu)$ and $\sigma = 0$. The density and viscosity ratios are then unitary, $m = 1, \varepsilon = 1$, while the Weber number diverges, $\mathrm{We} \to \infty$. In this case, the stability threshold (4) simplifies to

$$h_{C_T}^{(j)}\left(Sc, Sk, Re_1, Re_2, p, l\right) = 0, \tag{6}$$

with $Re_j = DJ_j/\nu$, $Sk = D^2 F/\nu$, $Sc = C/\left(2\rho D^2 L F\right)$, $C = C_1 = C_2$ and $F = F_1 = F_2$. As the two phases are identical, it is expected that Eq. (6) is in fact not a function of the two independent dimensionless numbers Re_1 and Re_2, but a function of the incident Reynolds number $Re = Re_1 + Re_2 = D\left(J_1 + J_2\right)/\nu$. Consequently, Eq. (6) reduces to an equation involving only five dimensionless numbers

$$h_{C_T}(Sc, Sk, Re, p, l) = 0. \tag{7}$$

For a given geometry of the bundle and for some given material properties of the tube and the fluid, the dimensionless numbers Sc, Sk, p and l are fixed and the instability threshold is the set of Reynolds numbers Re such that $Re =$ constant. In the plane (Re_1, Re_2), this threshold corresponds to a straight line of equation $Re = Re_1 + Re_2 = \text{constant} = Re_{\text{crit}}^{1\phi}$, i.e.

$$\frac{Re_1}{Re_{\text{crit}}^{1\phi}} + \frac{Re_2}{Re_{\text{crit}}^{1\phi}} = 1, \tag{8}$$

with $Re^{1\phi}_{\text{crit}} = H_{Re^{1\phi}_{\text{crit}}}\ (Sc, Sk, p, l)$ some function of (Sc, Sk, p, l), according to Eq. (7). Note that the instability threshold proposed by Connors (1970) is actually a special case of Eq. (7), corresponding to $h_{C_T}(Sc, Sk, Re, p, l) = Re - K(p,l)^{-1/2} Sc^{1/2} Sk = 0$, which is also similar to $H_{Re^{1\phi}_{\text{crit}}}\ (Sc, Sk, p, l) = K(p,l)^{-1/2} Sc^{1/2} Sk$. In this expression K is the Connors' constant, which is actually a function of (p, l), and possibly some other dimensionless numbers characteristics of the geometry of the tube bundle.

5.2.2 Two-phase flow instability threshold

The two-phase flow instability threshold is given by the implicit equation (4). For a given geometry of the bundle and for some given material properties of the tube and the fluid, the dimensionless numbers Sc_j, Sk_j, m, ε, We_j, p and l are fixed and the instability threshold is the set of Reynolds numbers Re_1 and Re_2 such that $h^{(j)}_{C_T} = 0$. In the plane (Re_1, Re_2), this set corresponds to a curve whose shape is unknown. By similarity with single-phase flows, we suppose that this curve is also a straight line. The hypothesis of continuity of the threshold between single-phase and two-phase flows requires this line to pass through the points $(Re_1, Re_2) = \left(0, Re^{1\phi}_{2,\text{ crit}}\right)$ and $(Re_1, Re_2) = \left(Re^{1\phi}_{1,\text{ crit}}, 0\right)$, where $Re^{1\phi}_{j,\text{ crit}}$ is the instability threshold in single-phase flows for the phase labeled j. These two hypotheses imply that Eq. (4) is finally independent of m, ε and We_j, and is explicitly expressed as

$$\frac{Re_1}{Re^{1\phi}_{1,\text{ crit}}} + \frac{Re_2}{Re^{1\phi}_{2,\text{ crit}}} = 1, \tag{9}$$

with $Re^{1\phi}_{j,\text{ crit}} = H_{Re^{1\phi}_{\text{crit}}}\ (Sc_j, Sk_j, p, l)$.

As expected (the stability threshold should not depend on how the label of the two phases), the relation (9) is invariant per index change $1 \leftrightarrow 2$ and establishes continuity with the single-phase thresholds, via the respective limits as $Re_2 \to 0$ and $Re_1 \to 0$

$$Re_1 \to Re^{1\phi}_{1,\text{ crit}} \quad \text{as} \quad Re_2 \to 0, \tag{10a}$$

$$Re_2 \to Re^{1\phi}_{2,\text{ crit}} \quad \text{as} \quad Re_1 \to 0. \tag{10b}$$

From the relation $\alpha = \varepsilon Re_2 / (Re_1 + \varepsilon Re_2)$, it is also possible to express the instability threshold in a form equivalent to Eq. (9), explicitly showing the homogeneous void fraction α and the viscosity ratio ε

$$Re_1 = \frac{Re^{1\phi}_{1,\text{ crit}}}{1 + \frac{\alpha}{1-\alpha}\frac{1}{\varepsilon}\frac{Re^{1\phi}_{1,\text{crit}}}{Re^{1\phi}_{2,\text{ crit}}}}, \quad Re_2 = \frac{Re^{1\phi}_{2,\text{ crit}}}{1 + \frac{1-\alpha}{\alpha}\varepsilon\frac{Re^{1\phi}_{2,\text{ crit}}}{Re^{1\phi}_{1,\text{ crit}}}}. \tag{11}$$

The above relationships remain invariant per index change $1 \leftrightarrow 2$ for $\alpha \to 1-\alpha$ and $\varepsilon \to 1/\varepsilon$. Similarly, the continuities with the single-phase thresholds

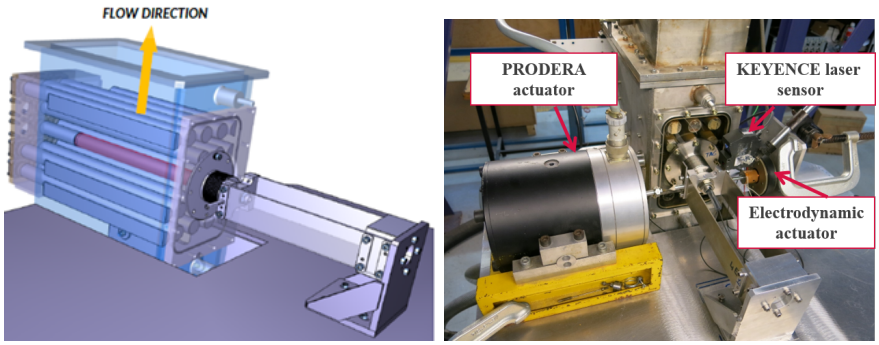

Figure 5.5: Left: 5×3 square tube bundle (pitch ratio $p = 1.5$) with a central tube mounted on two parallel blades, allowing vibrations in the lift direction only. Right: experimental setup and instrumentation. In the direct method of measurement of fluid-elastic forces, the PRODERA actuator is used to impose the harmonic vibration of the central tube.

are maintained as $\alpha \to 0$ and $\alpha \to 1$

$$Re_1 \to \begin{cases} Re^{1\phi}_{1,\,\mathrm{crit}} & \text{as} \quad \alpha \to 0 \\ 0 & \text{as} \quad \alpha \to 1 \end{cases}, \quad Re_2 \to \begin{cases} 0 & \text{as} \quad \alpha \to 0 \\ Re^{1\phi}_{2,\,\mathrm{crit}} & \text{as} \quad \alpha \to 1 \end{cases}. \tag{12}$$

5.3 Single-phase flow experiments

The formulation (9) expresses the two-phase flow instability threshold as a function of the two single-phase flow thresholds, $Re^{(1\phi)}_{1,\,\mathrm{crit}}$ and $Re^{(1\phi)}_{2,\,\mathrm{crit}}$, images of (Sc_1, Sk_1, p, l) and (Sc_2, Sk_2, p, l) by the unknown function $H_{Re^{1\phi}_{\mathrm{crit}}}$. To complete the formulation (9) it is therefore necessary to determine the function $H_{Re^{1\phi}_{\mathrm{crit}}}$, in particular by establishing its dependence on the Scruton and Stokes numbers. To do so, we measure experimentally the fluid-elastic forces acting on a flexible tube that is imposed a harmonic displacement (direct method of Tanaka & Takahara (1980), see also Lagrange *et al.* (2019)) and subject to a single-phase (water) cross-flow. Measurements are performed for various flow rates Q, i.e. different Reynolds numbers, and different forcing frequencies, i.e. different Stokes numbers. From the measured fluid-forces, the total damping coefficient C_T is extracted and the critical Scruton number, given by $C_T = 0$, is determined. This method makes it possible to map the instability threshold by independently varying the Reynolds number and the Stokes number.

5.3.1 Experimental setup and instrumentation

The experimental setup is sketched in Fig. 5.5 and described briefly in the following. Readers should refer to Caillaud *et al.* (1999, 2000, 2003); Piteau *et al.* (2012, 2019) for an extensive description of the experimental setup and to Lagrange *et al.* (2019) for a discussion on the methodology used to measure the fluid-elastic forces. The flexible tube is in the central

position of a 5×3 square bundle (pitch ratio $p = 1.5$) made of rigid tubes (plus two columns of 5 half-tubes at the boundaries). The tube bundle has immersed length $L = 300$ mm, diameter $D = 30$ mm, upstream cross section area $S = 6DL = 0.054$ m^2 and is subject to a water cross-flow (flow rate Q). The central tube is supported by two parallel flexible steel blades allowing vibrations in the lift direction. A PRODERA actuator is used to force the harmonic motion of the central tube (the forcing angular frequency ω and amplitude of the motion are imposed). A non-contact electrodynamic actuator is used for active speed control (system stability control of the first mode of vibration, via a feedback stabilizing force). The displacement and velocity of the flexible tube are provided by a KEYENCE laser sensor. The resultant force on the flexible tube is measured only in the lift direction by KISTLER sensors. This force, noted F_m, integrates the inertia, damping of the tube and the fluid-elastic forces, i.e.

$$F_m = (M_s + M_f)\,\frac{d^2X}{dT^2} + (C_s + C_f)\,\frac{dX}{dT} + K_f X. \tag{13}$$

It follows that the transfer function between the measured force and the imposed displacement is

$$H(\omega) = -\omega^2\,(M_s + M_f) + \mathrm{i}\omega\,(C_s + C_f) + K_f, \tag{14}$$

so that $C_T = C_s + C_f = \Im\{H\}/\omega$, with $\Im$ the imaginary part operator. Let C_0 be the value of C_T measured experimentally for a fluid at rest. Introducing $\overline{C_f} = C_T - C_0$, the critical Scruton number, defined by $C_T = 0$, is calculated as

$$Sc_{\mathrm{crit}} = -\frac{\overline{C_f}}{2\rho F D^2 L}. \tag{15}$$

Varying the Reynolds number, $Re = DQ/(S\nu)$, and the Stokes number, $Sk = D^2F/\nu$, we eventually obtain a set of points $(Re, Sk, Sc_{\mathrm{crit}})$ leading to a mapping of the instability threshold $h_{C_T}(Sc, Sk, Re, p, l) = 0$, and by extension of the unknown function $H_{Re^{1\phi}_{\mathrm{crit}}}$. In our experiments, measurements are performed for $Re \in \{27, 36, 45, 54, 72, 90, 117\} \times 10^3$. For each Re, 37 Stokes numbers, $Sk \in [3600, 36000]$, are tested (by continuous frequency sweep between 4 and 40 Hz).

5.3.2 Results and discussion

Figure 5.7 shows the evolution of the instability threshold, measured experimentally, represented in the planes (Sk, Sc) and $(Sc, V_r = Re/Sk)$, for $Re \in \{27, 36, 45, 54, 72, 90, 117\} \times 10^3$. The experimental data show that (i) for a given Scruton number, a tube is all the more stable (in the sense that the Reynolds number must be increased to reach the instability threshold) as the Stokes number is large, (ii) for a given Stokes number, a tube is all the more stable as the Scruton number is large, (iii) for a given Reynolds number, if the Scruton number is increased, then the Stokes number has be decreased to turn the flexible tube unstable, (iv) the instability threshold function $H_{Re^{1\phi}_{\mathrm{crit}}}$ is discontinuous at $Sc \approx 0.28$. All these observations

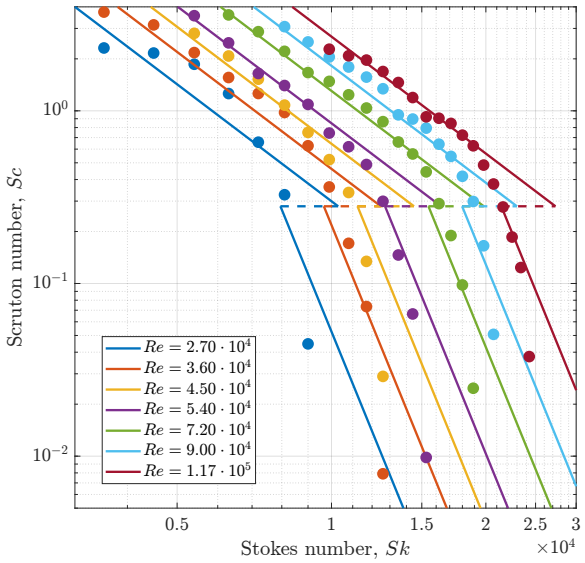

Figure 5.6: Log-Log graph of the instability threshold for a water cross-flow. The log-log scale is used to identify different power laws for the instability threshold, depending on the Scruton number. The points correspond to the experimental measurements. The curves correspond to the regression (17).

actually show that a tube is all the more stable as it is rigid and/or as its reduced mass-damping parameter (i.e. Scruton number) is large. Also, our experimental results show that the instability threshold is at least a function of three dimensionless parameters, for e.g. (Sc, Sk, Re), which can not be reduced to a function of only two parameters, for. e.g. Sc and $V_r = Re/Sk$, as suggested by Connors (1970) through the law $V_{r\mathrm{crit}} = K(p,l)Sc^{1/2}$. In other words, to correctly predict the instability threshold of a flexible tube subject to a single-phase flow, it is necessary to dissociate the fluid flow effects, represented by the Reynolds number, which will modify the fluid damping, and therefore affect the instability threshold, from structural frequency effects, represented by the Stokes number.

In order to obtain an analytical expression of the instability threshold, a non-linear regression of all the experimental points is carried out, in the form of two power laws, i.e.

$$Sc\,(d, b_1, b_2, b_3, c_1, c_2, c_3) = \left| \begin{array}{lll} Sc_1 = b_1 Re^{b_2} Sk^{b_3} & \text{if} & Sc < d \\ Sc_2 = c_1 Re^{c_2} Sk^{c_3} & \text{if} & Sc > d \end{array} \right. , \tag{16}$$

with b_i, c_i and d the fitting parameters. The discontinuity at $Sc = d$ is a pure mathematical artifact introduced to fit as much data as possible. This discontinuity is only used to take into account the possibility of different instability mechanisms for small and large Scruton numbers, as suggested by Chen (1983*b*). Indeed, a log-log plot of the data, see Fig. 5.6, tends to indicate the existence of different power laws for the instability threshold, depending on the Scruton number. At first glance, it seems reasonable to identify two regimes, with two different slopes. Obviously, a continuous non-

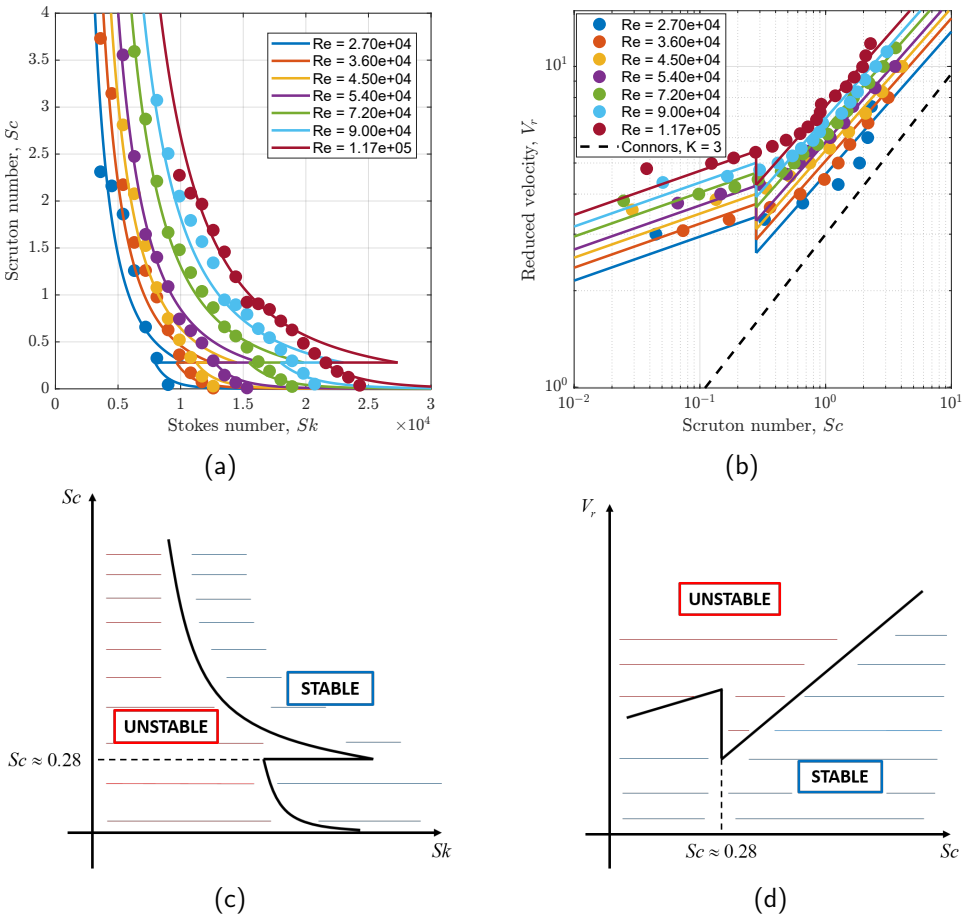

Figure 5.7: Graphs of the instability threshold for a water cross-flow. The points correspond to the experimental measurements. The curves correspond to the regressions (17) and (19). Subfigures (c) and (d) are representative diagrams of subfigures (a) and (b), respectively.

linear regression could be used to adjust the instability threshold, for example by imposing an additional constraint $Sc_1(d) = Sc_2(d)$ in the minimization process. This would make it possible to avoid introducing a non-physical discontinuity into the model, but this would also tend to unnecessarily complicate the expression of the instability threshold, in single-phase flow, and by extension in two-phase flow. Thus, in our study, guided by engineering applications, and following the example of Chen (1984), we stick to the model given by Eq. (16) (i.e. model based on power laws with a discontinuity), which has the merit of being simple. From the minimization process (least squares method), the discontinuity is obtained at $Sc = 0.28$ and the critical threshold writes

$$Sc_{\text{crit}} = \begin{cases} 9.78 \times 10^5 Re^{4.94} Sk^{-7.29} & \text{if} \quad Sc < 0.28 \\ 67.5 Re^{3/2} Sk^{-9/4} & \text{if} \quad Sc > 0.28 \end{cases}, \tag{17}$$

or equivalently

$$Re_{\text{crit}} = \begin{cases} 6.13 \times 10^{-2} Sc^{0.2} Sk^{1.48} & \text{if} \quad Sc < 0.28 \\ 6.03 \times 10^{-2} Sc^{2/3} Sk^{3/2} & \text{if} \quad Sc > 0.28 \end{cases}, \tag{18}$$

or equivalently

$$V_{r\,\text{crit}} = \begin{cases} 0.151 Sc^{0.137} Re^{0.322} & \text{if} \quad Sc < 0.28 \\ 0.154 Sc^{4/9} Re^{1/3} & \text{if} \quad Sc > 0.28 \end{cases}. \tag{19}$$

In Fig. 5.7, we show that the power laws (17) and (19) are in good agreement with experimental data. We conclude that Eq. (18) is a good prediction of the instability threshold in single-phase flow, that could be inserted in Eq. (9) to complete the criterion for the instability threshold in two-phase flow. Before going further, it should be noted that it is in fact possible to determine the total damping of the tube, C_T, for any Reynolds number, provided that Re_{crit} is known. Indeed, let k be an iso-value of the dimensionless coefficient $c_T = C_T/C_0$, so that

$$c_T = \frac{C_0 + \overline{C_f}}{C_0} = k \Leftrightarrow \frac{(1-k)\,C_0 + \overline{C_f}}{C_0} = 0. \tag{20}$$

This equation indicates that the point of coordinates $(Re, c_T = k)$, associated to the tube with modal damping C_0, corresponds to the critical threshold of a tube with modal damping $(1-k)\,C_0$, noted $Re_{\text{crit}}\left((1-k)\,C_0\right)$, i.e.

$$Re\left(C_0, c_T = k\right) = Re_{\text{crit}}\left((1-k)\,C_0\right). \tag{21}$$

In Eq. (21), the notation $Re\left(C_0, c_T = k\right)$ is used to define the Reynolds number for which the dimensionless total damping coefficient c_T of the tube with modal damping C_0 in still fluid equals k. According to Eq. (18), the instability threshold scales as $Re_{\text{crit}} \sim Sc^a$ with $Sc \propto C_0$ and $a = 0.2$ (resp. $2/3$) if $Sc < 0.28$ (resp. $Sc > 0.28$). Therefore, the right hand side term of Eq. (21) writes

$$Re_{\text{crit}}\left((1-k)\,C_0\right) = (1-k)^a Re_{\text{crit}}\left(C_0\right), \tag{22}$$

and Eq. (21) simplifies to

$$Re\left(C_0, c_T = k\right) = (1-k)^a Re_{\text{crit}}\left(C_0\right). \tag{23}$$

Replacing k by c_T and $Re\left(C_0, c_T = k\right)$ by Re in Eq. (23), the coefficient c_T can be written as

$$c_T = 1 - \left(\frac{Re}{Re_{\text{crit}}}\right)^{1/a}. \tag{24}$$

Finally, plugging Eq. (18) into Eq. (24) yields an expression of the total damping coefficient in single-phase flow

$$c_T = \left| \begin{array}{lll} 1 - \left(\frac{Re_1}{6.13\times10^{-2} Sc^{0.2} Sk^{1.48}}\right)^5 & \text{if} & Sc < 0.28 \\ 1 - \left(\frac{Re_1}{6.03\times10^{-2} Sc^{2/3} Sk^{3/2}}\right)^{3/2} & \text{if} & Sc > 0.28 \end{array} \right. . \tag{25}$$

Figure 5.8 shows the evolution of c_T as a function of Re for a set of blades with Scruton and Stokes numbers $Sc = 0.19$ and $Sk = 1.86 \times 10^4$ (blades with a frequency of 20.8 Hz in still fluid). The experimental points in Fig. 5.8 come from Lagrange *et al.* (2019) where c_T is obtained from the modal response of the tube mounted on the blades (indirect method of measuring forces). In Lagrange *et al.* (2019), experiments are performed well beyond the instability boundary of the system, using active control, allowing exploration of a significant range of Reynolds numbers. For $Sc < 0.28$, the proposed law (25) predicts quite satisfactorily the variations of c_T (as well as the prediction of the instability threshold $c_T = 0$) as a function of the Reynolds number, with the exception of the increasing part observed experimentally for the moderate Reynolds numbers, characteristic of tube stabilization. Since the approach is only valid for $k \leq 1$, the law does not in fact make it possible to predict a coefficient $c_T > 1$. For the interest of the reader, we have also plotted in Fig. 5.8 the variations of Eq. (25), considering $Sc > 0.28$. We show that the variations of c_T (as well as the prediction of the instability threshold $c_T = 0$) are not in good agreement with the experimental data, suggesting that it is better to fit the instability threshold with two power laws, possibly by introducing an artificial discontinuity, as done in our study.

5.4 Two-phase flow experiments

5.4.1 New criterion for the instability threshold

Introducing Eq. (18) into Eq. (9) yields a new criterion for the instability threshold in two-phase flow. This criterion writes

$$\frac{Re_1}{Re_{1,\text{ crit}}^{(1\phi)}} + \frac{Re_2}{Re_{2,\text{ crit}}^{(1\phi)}} = 1, \tag{26}$$

with

$$Re_{i,\text{crit}}^{(1\phi)} = \left| \begin{array}{lll} 6.13 \times 10^{-2} {Sc_i}^{0.2} {Sk_i}^{1.48} & \text{if} & Sc_i < 0.28 \\ 6.03 \times 10^{-2} {Sc_i}^{2/3} {Sk_i}^{3/2} & \text{if} & Sc_i > 0.28 \end{array} \right. . \tag{27}$$

To assess the validity of Eq. (26), along with Eq. (27), experimental measurements of the instability threshold in air-water cross-flow are carried out.

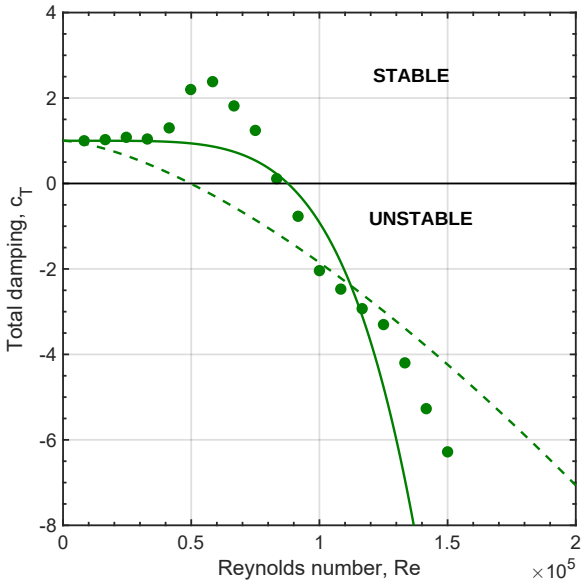

Figure 5.8: Evolution of the dimensionless total damping coefficient, c_T, as a function of the Reynolds number, for a set of blades characterized by $Sc = 0.19$ and $Sk = 1.86 \times 10^4$ (blades with a frequency of 20.8 Hz in still fluid). The points correspond to the experimental data of Lagrange *et al.* (2019), obtained with the indirect method and an active control system. The continuous (resp. dashed) line corresponds to the theoretical prediction (25) for $Sc < 0.28$ (resp. $Sc > 0.28$).

5.4.2 Experimental setup and methodology

The experimental setup for measurements in two-phase flow is the same as the one used in single-phase flow, see Fig. 5.5, except that the central flexible tube is not imposed a harmonic motion. Here, the tube is free to vibrate and the fluid-elastic force is extracted from the changes in the modal frequency and damping of the tube. This indirect measurement method of the fluid-elastic force is discussed in details in Caillaud *et al.* (1999, 2000, 2003); Piteau *et al.* (2012, 2019). The modal frequency of the central tube is set by changing the thickness of the blades. Three sets of blades, denoted L1C, L4C and L2C, whose modal properties in still air and water are reported in Table 5.1, have been tested. The tube bundle is subject to an air-water cross-flow with flow rates in the ranges $Q_{\text{water}} = [3, 300]$ L/s and $Q_{\text{air}} = [20, 3000]$ m^3/h. The measurement of the displacement and velocity of the flexible tube is provided by a laser transducer (Keyence LK-G500). A feedback control loop powered by an electro-dynamical shaker is used to ensure the stability of the tube, whatever the flow conditions. The principle of experimental determination of the instability threshold is as follows. For a given homogeneous void fraction, a modal identification is used to determine the reduced damping ξ_1 and the frequency F_1 of the coupled fluid-structure-shaker system. The total reduced damping ξ_T of the fluid-structure system is obtained by subtracting the control damping C_{ctrl} due to the electrodynamical shaker, by defining a mass of reference.

Blades	L1C	L4C	L2C
M_{air} (kg)	1.29	1.25	1.22
M_{water} (kg)	1.67	1.64	1.57
ξ_{air} (%)	0.56	0.46	0.38
ξ_{water} (%)	1.14	0.89	0.77
F_{air} (Hz)	14.11	22.06	29.18
F_{water} (Hz)	11.19	18.53	24.9
Sk_{air} ($\times 10^4$)	0.08140	0.12727	0.1683
Sk_{water} ($\times 10^4$)	1.000	1.656	2.225
Sc_{air}	140.1	111.5	89.90
Sc_{water}	0.4430	0.3397	0.2813

Table 5.1: Characteristics of the three sets of blades L1C, L4C and L2C.

In our case, two choices for this mass have been tested. The first choice is based on the homogeneous mass $M_h = M_{\text{air}} + \rho_h \left(M_{\text{water}} - M_{\text{air}}\right)/\rho_{\text{water}}$ with $\rho_h = \alpha\rho_{\text{air}} + (1-\alpha)\rho_{\text{water}}$. The second choice is based on a mass measurement $M_{2\phi}$ obtained from the frequency $F_{2\phi}$ of the tube motion for very low flow rates of water Q_{water} and air Q_{air}. Figure 5.9 shows that at first order the mass ratio $M_{\text{ratio}} = (M_{2\phi} - M_{\text{air}})/(M_{\text{water}} - M_{\text{air}})$ decreases linearly with the homogeneous void fraction, α. Similar trends were observed by Pettigrew *et al.* (1989); Carlucci (1980). Just like Pettigrew *et al.* (1989), however, we observe an oscillation of the mass ratio, which remains lower than $\rho_h/\rho_{\text{eau}} = (M_h - M_{\text{air}})/(M_{\text{water}} - M_{\text{air}})$ for $\alpha < 0.5$, then becomes higher for higher void fractions. The nature of this oscillation remains unknown but we suspect that it may be related to a non-uniform distribution of the local void fraction close to the tube and to a change in the flow regime for $\alpha \approx 0.5$. The two choices for a mass reference, M_h or $M_{2\phi}$, give two estimates of reduced damping, $\xi_T = \xi_{Th} = \xi_1 - C_{\text{ctrl}}/\left(2M_h\left(2\pi F_1\right)\right)$ or $\xi_T = \xi_{TMm} = \xi_1 - C_{\text{ctrl}}/\left(2M_{2\phi}\left(2\pi F_1\right)\right)$, which ultimately differ little from each other, i.e. $\xi_T \approx \xi_{Th} \approx \xi_{TMm}$. The instability threshold is then defined as the value of $Re = \left(Re_{\text{water}}^2 + Re_{\text{air}}^2\right)^{1/2}$ for which $\xi_{TMm} = 0$. In order to determine this critical value Re_{crit}, a linear interpolation between the last stable measuring point ($\xi_{TMm} > 0$) and the first unstable measuring point ($\xi_{TMm} < 0$) is performed. The repetition of this process for different void fractions α yields a set of points $(\alpha, Re_{\text{crit}})$. Once Re_{crit} has been determined, the results are reported in the planes $(Re_{\text{air}}, Re_{\text{water}})$, $(\alpha, Re_{\text{air}})$ and $(\alpha, Re_{\text{water}})$ with $\alpha = \varepsilon Re_{\text{air}}/\left(Re_{\text{water}} + \varepsilon Re_{\text{air}}\right)$.

5.4.3 Results and discussion

Figure 5.10 shows graphs of the instability threshold in air-water cross-flow, represented in planes $(Re_{\text{air}}, Re_{\text{water}})$, $\left(Re_{\text{air}}/Re_{\text{air,crit}}^{1\phi}, Re_{\text{water}}/Re_{\text{water,crit}}^{1\phi}\right)$, $(\alpha, Re_{\text{air}})$ and $(\alpha, Re_{\text{water}})$, for the three sets of blades, L1C, L4C and L2C. These blades are characterized by Scruton numbers Sc_{air} and Sc_{water} greater

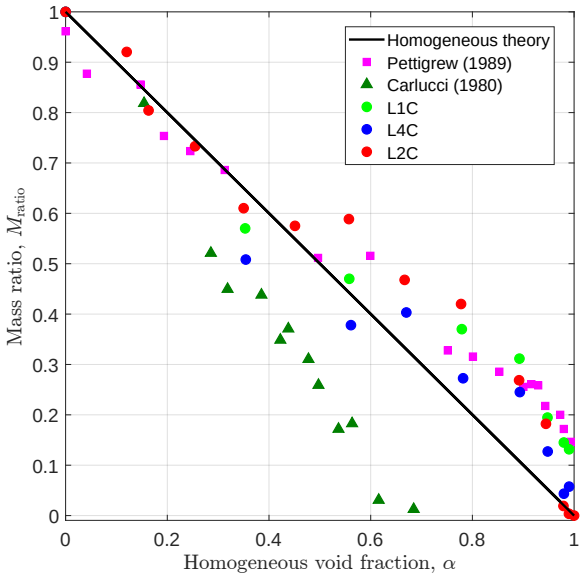

Figure 5.9: Evolution of the mass ratio $M_{\text{ratio}} = (M_{2\phi} - M_{\text{air}})/(M_{\text{water}} - M_{\text{air}})$ as a function of the homogeneous void fraction, α, for the three sets of blades tested, L1C, L4C and L2C. The straight line corresponds to the homogeneous theory, $M_{\text{ratio}} = \rho_h/\rho_{\text{water}}$, with $\rho_h = \alpha\rho_{\text{air}} + (1-\alpha)\,\rho_{\text{water}}$ the homogeneous mass density. Square symbols are experimental data from Pettigrew *et al.* (1989). Triangle symbols are experimental data from Carlucci (1980).

than 0.28, see Table 5.1, so that the criterion (26) reduces to

$$\frac{Re_{\text{water}}}{Sc_{\text{water}}^{2/3} Sk_{\text{water}}^{3/2}} + \frac{Re_{\text{air}}}{Sc_{\text{air}}^{2/3} Sk_{\text{air}}^{3/2}} = 6.03 \times 10^{-2}, \tag{28}$$

or equivalently

$$Re_{\text{air,crit}} = 6.03 \times 10^{-2} \frac{{Sc_{\text{air}}}^{2/3} {Sk_{\text{air}}}^{3/2}}{1 + \frac{1-\alpha}{\alpha} \frac{\nu_{\text{air}}}{\nu_{\text{water}}} \left(\frac{Sc_{\text{air}}}{Sc_{\text{water}}}\right)^{2/3} \left(\frac{Sk_{\text{air}}}{Sk_{\text{water}}}\right)^{3/2}}, \tag{29}$$

or equivalently

$$Re_{\text{water,crit}} = 6.03 \times 10^{-2} \frac{{Sc_{\text{water}}}^{2/3} {Sk_{\text{water}}}^{3/2}}{1 + \frac{\alpha}{1-\alpha} \frac{\nu_{\text{water}}}{\nu_{\text{air}}} \left(\frac{Sc_{\text{water}}}{Sc_{\text{air}}}\right)^{2/3} \left(\frac{Sk_{\text{water}}}{Sk_{\text{air}}}\right)^{3/2}}. \tag{30}$$

In the plane $(Re_{\text{air}}, Re_{\text{water}})$, experimental results nearly collapse on a straight line, as suggested by Eq. (28). Lines for the three sets of blades are staggered according to the frequency of the blades, reflecting the effect of the Stokes number on the single-phase flow critical Reynolds number, see Eq. (27). In the plane $\left(Re_{\text{air}}/Re^{1\phi}_{\text{air,crit}}\,, Re_{\text{water}}\,/Re^{1\phi}_{\text{water,crit}}\right)$, all experimental results align into a single line, as predicted by Eq. (26). Finally, in the plane $(\alpha, Re_{\text{air}}\,)$ (resp. $(\alpha, Re_{\text{water}})$), the graph of the instability threshold is an increasing (resp. decreasing) function of α, with $Re_{\text{air,crit}} \to 0$ as $\alpha \to 0$ and

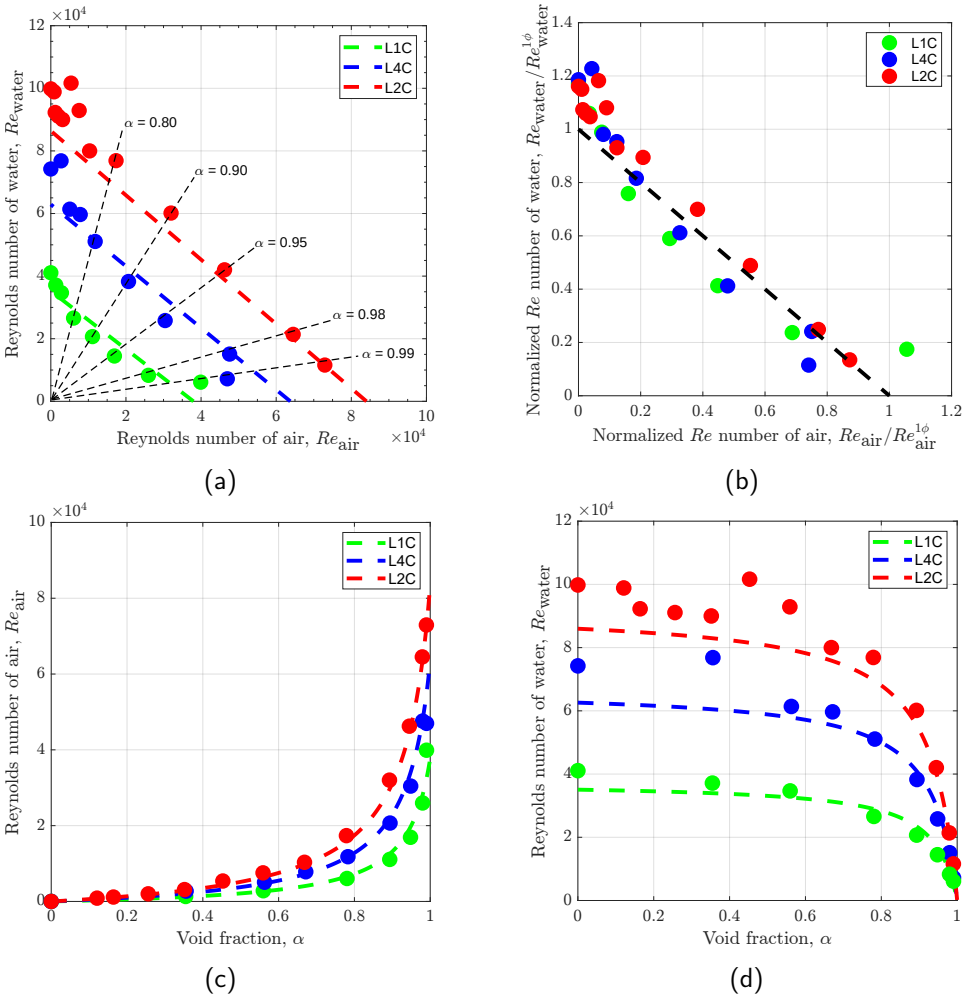

Figure 5.10: Graphs of the instability threshold for an air-water cross-flow. The points correspond to the experimental results. The curves correspond to the predictions from the criterion (26), which reduces to Eq. (28) for the three sets of blades L1C, L4C and L2C.

$Re_{\text{air,crit}} \to Re^{1\phi}_{\text{air,crit}}$ as $\alpha \to 1$ (resp. $Re_{\text{water,crit}} \to Re^{1\phi}_{\text{water,crit}}$ as $\alpha \to 0$ and $Re_{\text{water,crit}} \to 0$ as $\alpha \to 1$), as predicted by Eq. (29) (resp. Eq. (30)).

At first sight, the criterion for the instability threshold seems to perform worse for $\alpha < 0.80$ than for higher α. But this first impression actually depends on the plane of observation, the definition of the relative deviation, and the set of blades under consideration. To be more specific, in our experiments, the instability threshold is defined as the value of $Re = \left(Re^2_{\text{water}} + Re^2_{\text{air}}\right)^{1/2}$ for which the total damping of the system vanishes. Therefore, to correctly assess the performance of the criterion, it is necessary to compare the experimental value of Re_{crit}, noted $Re^{\text{Exp}}_{\text{crit}}$, with its prediction, $Re^{\text{Th}}_{\text{crit}}$. In Fig. 5.11, we then show the evolution of the relative deviation, $\iota\,(\%) = 100\left|Re^{\text{Exp}}_{\text{crit}} - Re^{\text{Th}}_{\text{crit}}\right| \Big/ Re^{\text{Exp}}_{\text{crit}}$, as a function of the homogeneous void fraction. For the stiffest blades L2C and L4C, we observe that the maximum relative deviation (approximately 20%) is reached for intermediate homogeneous void fractions $\alpha \in [0.3, 0.6]$. For such values of α, the regime map shown in Fig. 5.12 indicates that the instability threshold of these two sets of blades is located near a transition between a bubbly regime (identified by the probability density function (PDF) of a local void fraction, with a PDF characterized by a marked peak close to $\alpha = 0$) and a slug regime (PDF characterized by a peak close to $\alpha = 0$, which extends to higher values of α). On the contrary, for the most flexible set of blades L1C, we observe that the relative deviation decreases and hits a minimum in the range $\alpha \in [0.3, 0.6]$. For this set of blades, the regime map indicates that the instability threshold is located near a transition between a slug regime (PDF characterized by a peak close to $\alpha = 0$, which extends to higher values of α) and a churn regime (PDF characterized by a peak close to $\alpha = 1$, which extends to lower values of α). Interestingly, we also observe that the relative deviation increases in the range $\alpha \in [0.6, 1]$, which, according to the regime map, could be related to a transition from a churn to an annular regime (PDF characterized by a marked peak close to $\alpha = 1$). Let us note that the most flexible sets of blades, L1C and L4C, present a relative deviation greater than 15% for $\alpha = 0.99\%$. In fact, the existence of this peak is explained by the experimental difficulties associated with controlling a very low water flow (a few liters per second), while ensuring a high air flow. Also, additional measurements seem to indicate the possible existence of a cascade of bifurcations and hysteresis cycles, making the precise determination of the instability threshold very difficult for such high values of α and such flexible blades. Finally, despite some peaks in the relative deviation, the criterion (26), which does not take into account any tension surface effect, by including a Webber number for example, yields a rather accurate prediction of the instability threshold for all homogeneous voids fractions $\alpha \in [0.1]$.

5.5 Conclusion

In this work, we have studied the fluid-elastic instability of a tube bundle subject to a two-phase cross-flow. From a dimensional analysis, we have proposed a new criterion for the instability threshold, involving the

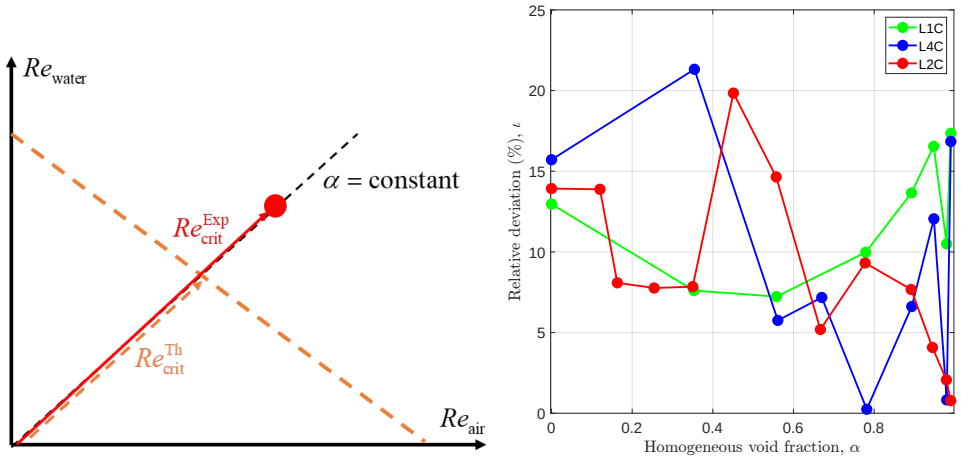

Figure 5.11: Left: geometrical interpretation of the relative deviation, $\iota\,(\%) = 100\left|Re^{\mathrm{Exp}}_{\mathrm{crit}} - Re^{\mathrm{Th}}_{\mathrm{crit}}\right| \Big/ Re^{\mathrm{Exp}}_{\mathrm{crit}}$. Right: evolution of the relative deviation, ι, as a function of the homogeneous void fraction, α.

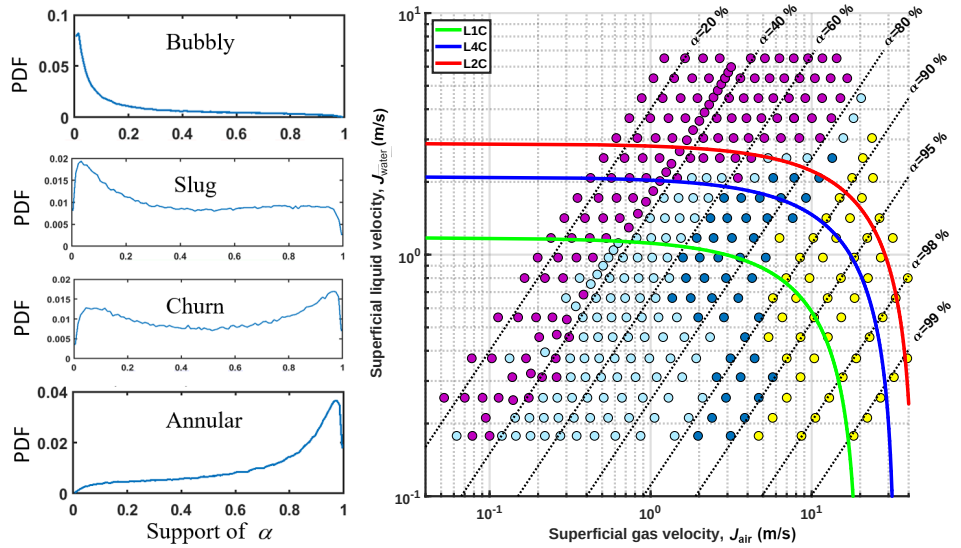

Figure 5.12: Left: probability density functions (PDF) of the void fraction, α, measured locally with an optical probe, in a rigid square tube bundle (5×3 full rigid square tube bundle, pitch ratio $p = 1.5$) subject to an air-water cross-flow. The optical probe is positioned halfway between the central cylinder $(3, 2)$ and the downstream cylinder $(2, 3)$. The superficial gap velocities are $(J_{\mathrm{water}}, J_{\mathrm{air}}) = (5.4, 1.79)$ m/s (bubbly, $\alpha = 0.25$), $(J_{\mathrm{water}}, J_{\mathrm{air}}) = (2.5, 5.86)$ m/s (slug, $\alpha = 0.70$), $(J_{\mathrm{water}}, J_{\mathrm{air}}) = (1.7, 4)$ m/s (churn, $\alpha = 0.70$), $(J_{\mathrm{water}}, J_{\mathrm{air}}) = (0.8, 22.1)$ m/s (annular, $\alpha = 0.965$). Right: regime map. The color of points is related to the experimental identifications of flow regimes: bubbly (purple), slug (light blue), churn (dark blue), annular (yellow). The curves correspond to the instability threshold given by Eq. (26), for the three sets of blades L1C, L2C and L4C.

Reynolds numbers of the two phases and the critical Reynolds number in single-phase flow. This new criterion has been established by similarity with single-phase flows, assuming that its representative curve is a straight line in the plane generated by the two Reynolds numbers. Experiments in water cross-flow (tube bundle with central tube mounted on two flexible blades, direct method of measurement of fluid-elastic forces) have shown that the critical Reynolds number in single-phase flow can be expressed in the form of a power law involving the Scruton and Stokes numbers. The instability criterion in two-phase flow has been corroborated with air-water experiments (indirect method of measurement of fluid-elastic forces). This criterion is shown to be predictive for homogeneous void fractions from 0 to 1, and so for all flow regimes (identified in experiments with an optical probe). The validity of the criterion has now to be tested for different tube bundle geometries (e.g. triangular pitch) and mixtures (e.g water-freon and ultimately steam-water).

Acknowledgements

This work was performed in the framework of a joint research program co-funded by FRAMATOME, EDF and CEA (France). A valuable contribution by M. Bellanger and T. Valin (CEA-Saclay) to the experimental work is gladly acknowledged.

Bibliography

Axisa, F., Boheas, M. A. & Villard, B. 1985 Vibration of tube bundles subjected to steam-water cross-flow: A comparative study of square and triangular arrays. In *8th International Conference on Structural Mechanics in Reactor Technology, Paper No. B1/2.*.

Axisa, F., Villard, B., Gibert, R. J., Hetsroni, G. & Sundheimer, P. 1984 Vibration of tube bundles subjected to air-water and steam-water cross flow: Preliminary results on fluidelastic instability. In *Symposium on Flow-Induced Vibrations, Volume 2: Vibration of Arrays of Cylinders in Cross Flow. Presented at the 1984 ASME Winter Annual Meeting. ASME New York NY USA.*

Caillaud, S., de Langre, E. & Baj, F. 2003 Active vibration control for the measurement of fluidelastic effects. *ASME Journal of Pressure Vessel Technology* **125**, 165–170.

Caillaud, S., de Langre, E. & Piteau, P. 1999 The measurement of fluidelastic effects at low reduced velocities using piezoelectric actuators. *ASME Journal of Pressure Vessel Technology* **121**, 232–238.

Caillaud, S., de Langre, E. & Piteau, P. 2000 Measurement of critical velocities for fluidelastic instability using vibration control. *ASME Journal of Pressure Vessel Technology* **122**, 341–345.

Carlucci, N. L. 1980 Damping and hydrodynamic mass of a cylinder in simulated two-phase flow. *Journal of Mechanical Design, Transactions of the ASME* **102**, 597–602.

Chen, S. S. 1983*a* Instability mechanisms and stability criteria of a group of circular cylinders subjected to cross-flow. part 1: Theory. *Journal of Vibration, Acoustics, Stress, and Reliability in Design* **105**, 51–58.

Chen, S. S. 1983*b* Instability mechanisms and stability criteria of a group of circular cylinders subjected to cross-flow. part ii: Numerical results and discussion. *Journal of Vibration, Acoustics, Stress, and Reliability in Design* **105**, 253–260.

Chen, S. S. 1984 Guidelines for the instability flow velocity of tube arrays in crossflow. *Journal of sound and Vibration* **93**, 439–455.

Chen, S. S. 1987 A general theory for dynamic instability of tube arrays in cross-flow. *Journal of Fluids Engineering, Transaction of the ASME* **1**, 35–53.

Connors, H. 1970 Fluidelastic vibration of tube arrays excited by cross-flows. *Flow-Induced Vibration in Heat Exchangers* pp. 42–56.

Dalton, C. & Helfinstine, R. A. 1971 Potential flow past a group of circular cylinders. *ASME Journal of Basic Engineering* **93**, 636–642.

Granger, S. & Paidoussis, M. P. 1996 An improvement to the quasi-steady model with application to cross-flow-induced vibration of tube arrays. *Journal of Fluid Mechanics* **320**, 163–184.

Hassan, M. & Weaver, D. S. 2015 The effect of flat bar supports on streamwise fluidelastic instability in heat exchanger tube arrays. *ASME. Journal of Pressure Vessel Technology* **137**, 061302.

Hassan, M. & Weaver, D. S. 2016 Modeling of streamwise and transverse fluidelastic instability in tube arrays. *ASME. Journal of Pressure Vessel Technology* **138**, 051304.

Lagrange, R., Panunzio, D., Piteau, P., Delaune, X. & Antunes, J. 2022 A new criterion for the instability threshold of a square tube bundle subject to an air-water cross-flow. In *Proceedings of the 12th International Conference on Flow-Induced Vibration*, L. Zimmer, Laboratoire EM2C, CNRS, CentraleSupélec, Université Paris-Saclay edn. (ed. C. Habchi & P. Moussou), pp. 391–399.

Lagrange, R., Piteau, P., Delaune, X. & Antunes, J. 2019 Fluidelastic coefficients in single phase cross flow: Dimensional analysis, direct and indirect experimental methods. In *Pressure Vessels and Piping Conference*, , vol. 4: Fluid-Structure Interaction, p. 93984.

Lever, J. & Weaver, D. S. 1986 On the stability of heat exchanger tube bundles, part 1: Modified theoretical model. *Journal of Sound and Vibration* **107**, 375–392.

Nakamura, T., Fujita, K., Kawanishi, K. & Saito, I. 1986*a* Study on the flow induced vibration of a tube array by a two-phase flow (2nd report, large amplitude vibration by steam - water flow). *Japan Society of Mechanical Engineers Part C.* **52**, 2790–2795.

Nakamura, T., Fujita, K., Yamaguchi, N., Sakata, K., Tsuge, A. & Saito, I. 1986*b* Study on flow induced vibration of a tube array by a two-phase flow. (1st report: large amplitude vibration by air-water flow). *Japan Society of Mechanical Engineers Part C.* **52**, 252–257.

Pettigrew, M. J. & Taylor, C. E. 2009 Vibration of a normal triangular tube bundle subjected to two-phase freon cross flow. *Journal of Pressure Vessel Technology, Transactions of the ASME* **131**, 051302.

Pettigrew, M. J., Taylor, C. E., Janzen, V. P. & Whan, T. 2002 Vibration behavior of rotated triangular tube bundles in two-phase cross flows. *Journal of Pressure Vessel Technology, Transactions of the ASME* **124**, 144–153.

Pettigrew, M. J., Taylor, C. E., Jong, J. H. & Currie, I. G. 1995 Vibration of a tube bundle in two-phase freon cross-flow. *Journal of Pressure Vessel Technology, Transactions of the ASME* **117**, 321–329.

Pettigrew, M. J., Taylor, C. E. & Kim, B. S. 1989 Vibration of tubes bundles in two-phase cross-flow: Part 1-hydrodynamic mass and damping. *Journal of Pressure Vessel Technology, Transactions of the ASME* **111**, 466–477.

Piteau, P., Delaune, X., Antunes, J. & Borsoi, L. 2012 Experiments and computations of a loosely supported tube in a rigid bundle subjected to single-phase flow. *Journal of Fluids and Structures* **28**, 56–71.

Piteau, P., Delaune, X., Borsoi, L. & Antunes, J. 2019 Experimental identification of fluid-elastic coupling forces on a flexible tube within a rigid square bundle subjected to single-phase cross-flow. *Journal of Fluids and Structures* **86**, 156–169.

Price, S. J. & Paidoussis, M. P. 1982 A theoretical investigation of the parameters affecting the fluidelastic instability of a double row of cylinders subject to a cross-flow. In *Vibration in Nuclear Plant. Proceedings of the 3rd International Conference. British Nucl. Energy Soc, London UK*.

Price, S. J. & Paidoussis, M. P. 1983 Fluidelastic instability of an infinite double row of circular cylinders subject to a uniform cross-flow. *Journal of Vibration Acoustics Stress Reliability in Design* **105**, 59–66.

Roberts, B. W. 1962 Low frequency, self-excited vibration in a row of circular cylinders mounted in an airstream. *Ph.D Thesis, University of Cambridge, Cambridge, UK.* .

Sadek, O., Mohany, A. & Hassan, M. 2018 Numerical investigation of the cross flow fluidelastic forces of two-phase flow in tube bundle. *Journal of Fluids and Structures* **79**, 171–186.

Sadek, O., Mohany, A. & Hassan, M. 2020 Numerical simulation of streamwise fluidelastic instability of tube bundles subjected to two-phase cross flow. *Journal of Fluids and Structures* **92**, 102816.

Tanaka, H. & Takahara, S. 1980 Unsteady fluid dynamic force on tube bundle and its dynamic effect on vibration. *American Society of Mechanical Engineers, Pressure Vessels and Piping Division (Publication) PVP* pp. 77–92.

Tanaka, H. & Takahara, S. 1981 Fluid elastic vibration of tube array in cross-flow. *Journal of Sound and Vibration* **77**, 19–37.

Yasser, S., Hassan, M., Mohany, A. & Ahmed, W. 2021 Modelling of fluidelastic instability in tube bundles under two-phase bubbly flow conditions. *Journal of Fluids and Structures* **103**, 103256.

6. PERSPECTIVES DE RECHERCHE

Dans ce mémoire ont été présentés quelques un de mes travaux de recherche post-doctoraux sur les instabilités en mécanique des fluides et des solides. Afin de conclure ce mémoire, je mets l'accent sur quelques projets qui seront privilégiés dans les années à venir. En tant qu'ingénieur-chercheur au Commissariat à l'Energie Atomique (C.E.A.), ces projets s'inscrivent dans le cadre d'une problématique industrielle, en partenariat avec les grands acteurs Français du nucléaire (E.D.F., Framatome), avec pour ligne directrice la modélisation fine des phénomènes d'interaction fluide-structure (I.F.S.). D'un point de vue recherche amont, ces travaux visent à améliorer la compréhension des mécanismes physiques de l'I.F.S.. D'un point de vue applicatif, ces travaux doivent alimenter les codes de calcul (par exemple TrioCFD[1], Neptune-CFD[2]) développés par le C.E.A. et ses partenaires, afin de disposer d'outils numériques fiables, qualifiés et prédictifs. In fine, ces outils doivent permettre de décrire efficacement le comportement mécanique de composants structurels utilisés dans le domaine nucléaire, pour améliorer leur dimensionnement, évaluer leurs marges et leurs incertitudes de fonctionnement. Dans ce contexte, j'ambitionne donc de poursuivre mon activité de recherche sur l'I.F.S. des écoulements transverses (monophasiques ou diphasiques), dans la continuité du travail présenté dans le chapitre 5, sur l'instabilité fluide-élastique d'un faisceau de tubes. Je souhaite également développer une activité sur l'I.F.S. des écoulements monophasiques axiaux, présents en partie basse des tubes de G.V., dans les assemblages combustibles, dans les in-

[1] TrioCFD est un code de calcul numérique développé au C.E.A. par le Laboratoire de Modélisation et Simulation en mécanique des Fluides (L.M.S.F.). Ce code, massivement parallèle, est principalement dédié à la thermohydraulique monophasique des réacteurs nucléaires, via la résolution des équations de Navier-Stokes incompressibles ou faiblement compressibles, éventuellement couplées à un modèle de turbulence. Une collaboration entre le laboratoire DYN (R. Lagrange) et le L.M.S.F. (M. A. Puscas) est en cours pour développer et éprouver les capactiés de TrioCFD et de son module A.L.E. (Arbitrary Lagrangian-Eulerian) pour la simulation de problèmes de mécanique impliquant un couplage entre des structures vibrantes et un fluide monophasique (au repos ou en écoulement).

[2] Neptune-CFD est un code de calcul numérique développé par E.D.F., le C.E.A., Framatome et l'Institut de Radioprotection et de Sûreté Nucléaire, pour la simulation des écoulements multiphasiques. Ce code repose sur la résolution des équations de Navier-Stokes pour chaque phase constitutive du fluide. Ces équations sont complétées par des modèles théoriques et/ou phénoménologiques permettant de décrire l'interaction entre les phases. Une collaboration (thèse de C. Bazin, 2020-2023) entre le laboratoire DYN (R. Lagrange, encadrant C.E.A.), le L.M.S.F. (M. G. Rodio, encadrant C.E.A.) et le LadHyX (C. Josserand, directeur) est en cours pour assurer la validation de ces modèles, via la simulation des régimes d'écoulement et des phénomènes aléatoires observés dans la maquette expérimentale DIVA, voir chapitre 5.

ternes de cuve[3], mais également responsables des vibrations des tubes guides du réacteur Jules Horowitz[4]. Pour cela, je compte m'appuyer sur la résolution de problèmes fondamentaux (couplage hydrodynamique entre deux cylindres concentriques ou parallèles, vibrant dans un fluide au repos ou en écoulement), exigeants d'un point de vue théorique mais aussi numérique. Ces problèmes modèles doivent permettre de tester les capacités des codes numériques, définir des pistes de développement, mais aussi de réaliser des études paramétriques pour établir de nouvelles formulations analytiques, par exemple pour les coefficients de masse, d'amortissement, de rigidité ajoutés, qui déterminent la stabilité des systèmes couplés. Une présentation synthétique d'un programme de recherche pluriannuel est proposée dans les tables 6.1 (I.F.S. en écoulement axial monophasique) et 6.2 (I.F.S. en écoulement transverse monophasique ou diphasique). Les premiers résultats de ce programme de recherche sont illustrés sur les figures 6.1, 6.2 et des publications représentatives sont reportées en annexes C et D.

TABLE 6.1 : Programme de recherche sur l'I.F.S. en écoulement axial monophasique.

Hydrodynamic interaction between two coaxial cylinders Free vibrations	
Goal	- Simulate and model the free oscillations of a slender and confined structure vibrating in a still fluid
References	- R. Lagrange et al., J. Appl. Mech., 89(8) : 081006, 2022. - R. Lagrange et al., J. Fluids Struct., 114, 103754, 2022. - R. Lagrange et al., J. Fluids Struct., 120, 103899, 2023. - R. Lagrange et al., J. Appl. Mech., 90(6) : 061009, 2023.
Actions	- Perform Helmholtz expansion and modal projection of the dynamical equations - Implement coupling models for beams in TrioCFD - Carry out parametric studies to determine new scaling laws for the frequency and damping characteristics of the free oscillations - Compare TrioCFD simulations to theoretical predictions

[3] Une collaboration (thèse de M. Kocher, 2021-2024) entre le laboratoire DYN (R. Lagrange et D. Panunzio, encadrants C.E.A.) et E.D.F. (Aurélien Joly, encadrant, et Pierre Moussou, directeur) est en cours afin de répondre aux objectifs conjoints du C.E.A. et d'E.D.F. sur le sujet des vibrations de circuit primaire principal. Le travail de thèse consiste à construire, avec les outils habituels (simulations numériques, essais), un modèle acoustique-mécanique représentatif de la cuve et de ses internes (modèle de transmission des ondes acoustiques entre les entrées et sorties de la cuve, via la prise en compte de la turbulence dans l'espace annulaire et des oscillations de l'enveloppe de cœur).

[4] Le réacteur Jules Horowitz est un réacteur d'essai principalement dédié aux études sur les comportements des matériaux et des combustibles utilisés dans le domaine nucléaire. Les tubes guides sont des structures cylindriques, en aluminium, qui assurent un positionnement précis des éléments à tester, permettant de contrôler et d'étudier leurs interactions avec les éléments combustibles. Les tubes guides sont insérés dans l'espace libre cylindrique entre les assemblages combustibles. Comme les éléments combustibles, ces tubes sont soumis à un écoulement axial monophasique provenant du circuit primaire, avec une vitesse caractéristique de 15 m/s dans la partie centrale.

Expected	- 2024
Abrupt change of section	
Goal	- Simulate and model the fluid forces acting on a rigid slender structure confined in an environment with an abrupt change of section
References	- R. Lagrange et al., J. Appl. Mech., 90(6) : 061009, 2023. - Hydro note by B. Molin (inviscid)
Actions	- Perform Helmholtz expansion with matching conditions - Perform simulations with the A.L.E. module and with the beam model (internal coupling) in TrioCFD - Carry out parametric studies to determine the effect of a change of section on the added-coefficients - Compare TrioCFD simulations to theoretical predictions
Expected	- 2024
Stability under axial flow	
Goal	- Simulate and model the coupled dynamics of slender structures subject to axial flow
References	- Internship E. Diaferia (2021) - R. Lagrange et al., J. Appl. Mech., 89(8) : 081006, 2022. - R. Lagrange et al., J. Fluids Struct., 114, 103754, 2022. - R. Lagrange et al., J. Fluids Struct., 120, 103899, 2023. - R. Lagrange et al., J. Appl. Mech., 90(6) : 061009, 2023.
Actions	- Couple the fluid equations (potential theory) with the Euler-Bernoulli beam equation - Perform simulations with the A.L.E. module and with the beam model (internal coupling) in TrioCFD - Carry out parametric studies to establish new Argand diagrams - Compare TrioCFD simulations to theoretical predictions
Expected	- 2025

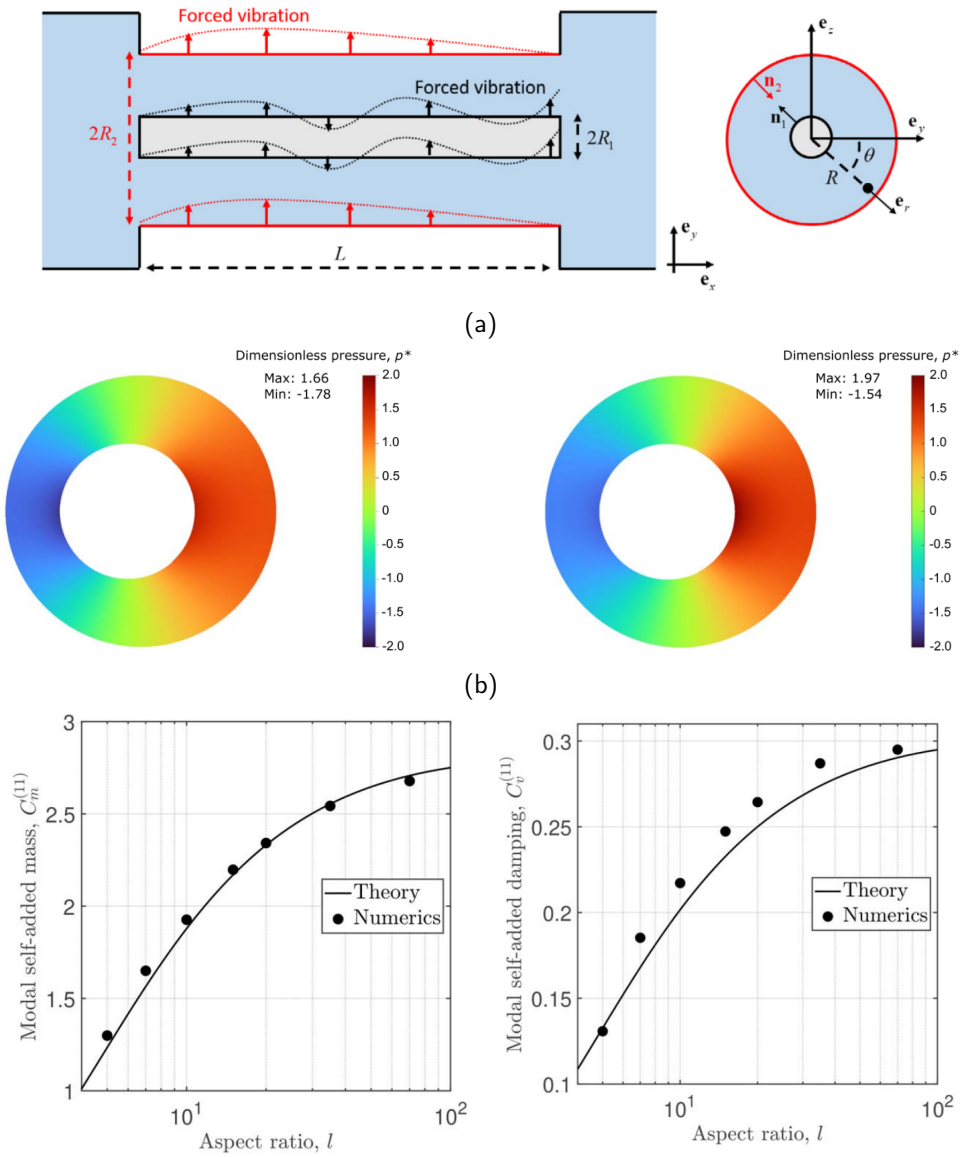

FIGURE 6.1 : Couplage hydrodynamique entre deux cylindres concentriques flexibles séparés par un fluide Newtonien au repos. (a) Schéma de principe de deux cylindres en vibrations imposées. (b) Exemple de champ adimensionné de pression généré par le déplacement rigide du cylindre intérieur, simulation numérique TrioCFD (figure de gauche), théorie potentielle 2D (figure de droite). Vidéo de l'I.F.S. entre deux cylindres concentriques (simulation TrioCFD) : ici. (c) Evolution des coefficients modaux adimensionnés ajoutés (masse et amortissement en fluide au repos) en fonction de l'élancement des cylindres. Le cylindre intérieur vibre selon le premier mode de flexion d'une poutre encastrée-libre, théorie visqueuse 3D.

TABLE 6.2 : Programme de recherche sur l'I.F.S. en écoulement transverse monophasique ou diphasique.

Hydrodynamic interaction between two parallel cylinders (single phase)	
Frequency effect	
Goal	- Simulate and model the Stokes effect, i.e. frequency and viscosity, on the forced oscillations of two slender structures immersed in still fluid
References	- Internships M. Monteverde and D. Zegarra (2020) - R. Lagrange et al., J. Fluids Struct., 77, 102-114, 2018. - R. Lagrange et al., J. Fluids Struct., 92, 102818, 2020.
Actions	- Perform Helmholtz expansion with 2D bipolar coord. - Perform simulations with the A.L.E. module of TrioCFD - Carry out parametric studies to determine new scaling laws for the added-coefficients - Compare TrioCFD simulations to theoretical predictions
Expected	- 2025
Three-dimensional and stiffness effects	
Goal	- Simulate and model the 3D and stiffness effects on the forced oscillations of two slender structures immersed in still fluid
References	- Internships M. Monteverde and D. Zegarra (2020) - R. Lagrange et al., J. Fluids Struct., 77, 102-114, 2018. - R. Lagrange et al., J. Fluids Struct., 92, 102818, 2020.
Actions	- Perform Helmholtz expansion with 3D bipolar coord. - Perform simulations with the A.L.E. module of TrioCFD - Carry out parametric studies to determine new scaling laws for the added-coefficients - Compare TrioCFD simulations to theoretical predictions
Expected	- 2025
Free vibrations	
Goal	- Simulate and model the free oscillations of a slender structure vibrating in a still fluid
References	- Internships M. Monteverde and D. Zegarra (2020) - R. Lagrange et al., J. Fluids Struct., 77, 102-114, 2018. - R. Lagrange et al., J. Fluids Struct., 92, 102818, 2020.
Actions	- Couple the fluid equations (potential theory) with the Euler-Bernoulli beam equation - Perform simulations with the beam model of TrioCFD - Carry out parametric studies to determine new scaling laws for the frequency and damping characteristics of free oscillations - Compare TrioCFD simulations to theoretical predictions
Expected	- 2026
Stability under cross-flow	
Goal	- Simulate and model the coupled dynamics of slender structures subject to cross-flow
References	- Internships M. Monteverde and D. Zegarra (2020)

	- Internship E. Beaugendre (2021) - R. Lagrange et al., J. Fluids Struct., 77, 102-114, 2018. - R. Lagrange et al., J. Fluids Struct., 92, 102818, 2020.
Actions	- Carry out potential flow theory with incident flow - Implement new turbulence models in TrioCFD - Carry out parametric studies to establish parametric Argand diagram - Compare TrioCFD simulations to theoretical predictions
Expected	- 2026
Nonlinear vibrations (large amplitudes)	
Goal	- Study the effect of large Keulegan-Carpenter numbers on the fluid forces and derive new power laws
References	- M. A. Puscas et al., Eur. J. Mech. B Fluids, 101, 106-117, 2023.
Actions	- Perform asymptotic development of the Navier-Stokes equations with the Keulegan-Carpenter number - Extend the amplitudes of the vibrations possible with the A.L.E. module of TrioCFD - Carry out parametric studies to determine new scaling laws for the fluid-elastic forces - Compare TrioCFD simulations to theoretical predictions
Expected	- 2027
Hydrodynamic interactions in tube bundles (single and two-phase)	
Goal	- Derive new scaling laws for the turbulent fluid forces and the fluid-elastic forces
References	- Technical notes on DIVA and TITAN - C. Bazin et al., submitted to Int. J. Multiph. Flow, 2023. - R. Lagrange et al., submitted to J. Fluids Struct., 2023. - P. Piteau et al., submitted to J. Fluids Struct., 2023. - Internships D. Panunzio (2020), E. Beaugendre (2021) - PhD, C. Bazin (2020-2023)
Actions	- Extend the theoretical studies performed with two parallel cylinders to the case of multiple cylinders, using complex analysis, symmetries and conformal mappings - Develop new law of walls in TrioCFD - Develop the all regimes model in Neptune-CFD - Carry out parametric studies to determine new scaling laws for the fluid forces (Stokes, Reynolds, Scruton effects) - Compare theoretical, numerical and experimental results - Extend the results to steam-water flows and to the industrial scale
Expected	- 2028

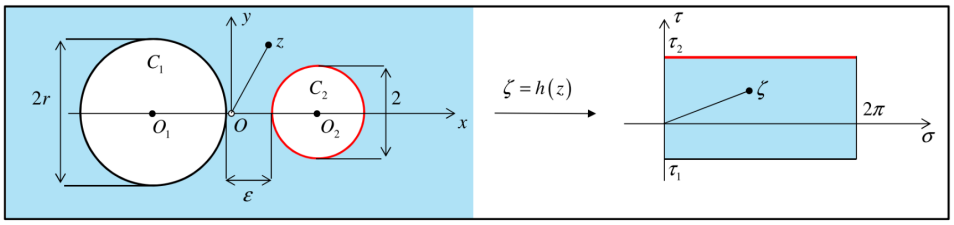

(a)

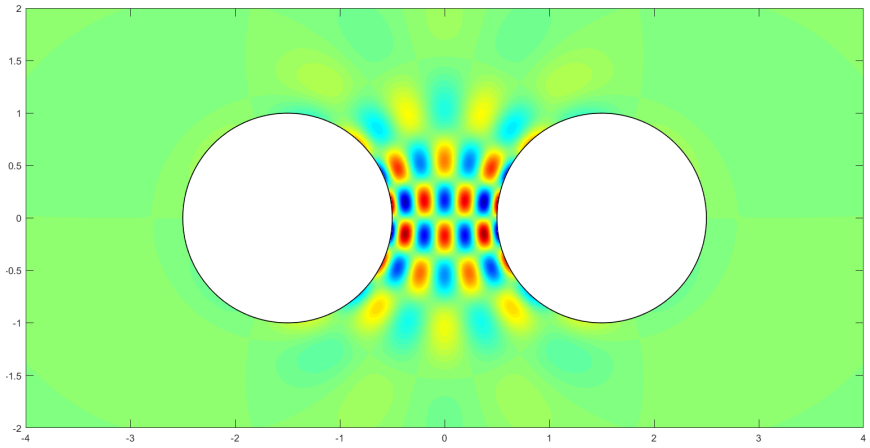

(b)

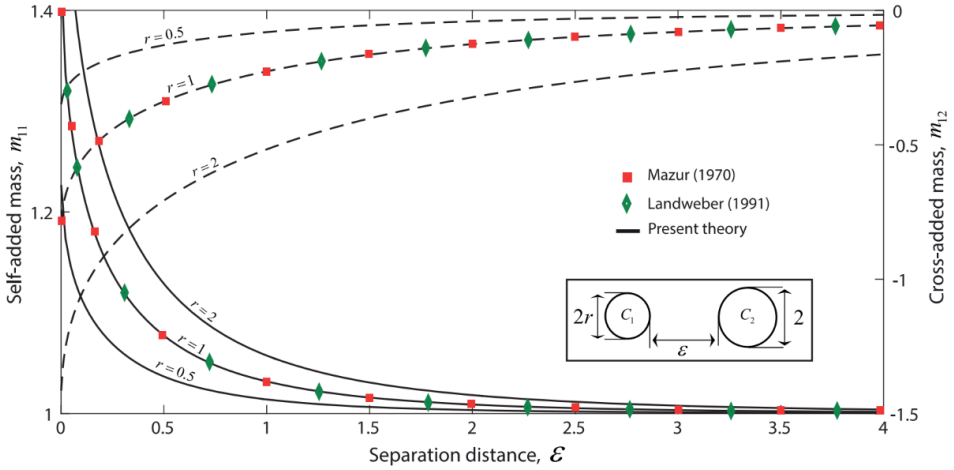

(c)

FIGURE 6.2 : Couplage hydrodynamique entre deux cylindres parallèles rigides immergés dans un fluide au repos. (a) Transformation conforme des coordonnées cartésiennes (x, y) en coordonnées bipolaires (σ, τ). (b) Exemple de champ de vorticité axiale d'un mode d'Helmholtz, théorie visqueuse 2D. (c) Evolution des coefficients adimensionnés de masse ajoutée (traits continus : m_{11}, traits discontinus : m_{12}) en fonction de la distance adimensionnée ε entre les deux cylindres et de leur rapport d'aspect r, théorie potentielle 2D. Vidéo de l'I.F.S. entre deux cylindres parallèles, théorie potentielle 2D : ici.

ANNEXES

A. FLAMBAGE D'UNE POUTRE IMPARFAITE SUR FONDATION NON-LINÉAIRE

Dans cette annexe, la publication parue dans la revue *International Journal of Mechanical Sciences*, sous le titre "Solution methods for the growth of a repeating imperfection in the line of a strut on a nonlinear foundation" est reproduite.

International Journal of Mechanical Sciences 63 (2012) 48–58

Contents lists available at SciVerse ScienceDirect

International Journal of Mechanical Sciences

journal homepage: www.elsevier.com/locate/ijmecsci

Solution methods for the growth of a repeating imperfection in the line of a strut on a nonlinear foundation

R. Lagrange *, D. Averbuch **

IFP Énergies nouvelles, Rond-point de l'échangeur de Solaize, BP3, 69360 Solaize, France

ARTICLE INFO

Article history:
Received 1 June 2011
Received in revised form
9 June 2012
Accepted 23 June 2012
Available online 29 June 2012

Keywords:
Buckling
Nonlinear elastic foundation
Imperfection
Stability and bifurcation

ABSTRACT

This paper is a theoretical and numerical study of the uniform growth of a repeating sinusoidal imperfection in the line of a strut on a nonlinear elastic Winkler-type foundation. The imperfection is introduced by considering an initially deformed shape which is a sine function with an half wavelength. The restoring force is either a bi-linear or an exponential profile. Periodic solutions of the equilibrium problem are found using three different approaches: a semi-analytical method, an explicit solution of a Galerkin method and a direct numerical resolution. These methods are found in very good agreement and show the existence of a maximum imperfection size which leads to a limit point in the equilibrium curve of the system. The existence of this limit point is very important since it governs the appearance of localization phenomena.

Using the Galerkin method, we then establish an exact formula for this maximum imperfection size and we show that it does not depend on the choice of the restoring force. We also show that this method provides a better estimate with respect to previous publications. The decrease in the maximum compressive force supported by the beam as a function of the imperfection magnitude is also determined. We show that the leading term of the development has a different exponent than in subcritical buckling of elastic systems, and that the exponent values depend on the choice of the restoring force.

1. Introduction

The subject of beam buckling can be found in several situations in industrial applications. Among the most studied are the thermal track buckling and the buckling of subsea pipelines under the effect of temperature and/or pressure. In the latter case, buckling can appear in both the vertical and horizontal planes, according to the existing restraints imposed by the environment and the backfill. Numerous authors have studied these two applications due to their high practical importance, and have proposed solution methods to determine buckling loads and post-buckling situations. Along time, the techniques used have progressed, based firstly on analytical analyses and latter on numerical methods mostly derived from finite elements models. Thus, based on some early work by Kerr [9,10] studying the stability of railway tracks subjected to thermal buckling, several authors such as Bournazel [1], Hobbs [4,5] have proposed solution methods where the equilibrium equations were solved in post-buckling configurations to establish relevant buckling loads. In these works, the soil was supposed to be rigid, while the external forces acting on the beam were assumed as constant as a dead weight or constant friction force. One of the key features of these theories is the fact that the loss of contact (or movement) induces a loss of global stiffness of the structure which leads to subcritical buckling and infinite buckling loads if no imperfection is assumed. Using slightly different arguments, other models were proposed in Croll [2] and Maltby and Calladine [14]. In the latter work, equilibrium equations were obtained by assuming sine deflections in the post-buckling situations and using an approximate Galerkin solution method. This method was compared with numerical solutions in Maltby and Calladine [13] and against experimental results in Maltby and Calladine [14]. Though using an approximate solution method, the approach showed good results with respect to the numerical simulation. In order to improve the earlier methods, numerical models were developed in Ju and Kyriakides [8], Klever et al. [11], Leroy and Putot [12], Yun and Kyriakides [25] to incorporate for instance additional nonlinear effects in the models, such as non linear geometric and material models. One of the key aspects of work related to the study of the upheaval buckling is the study of the localization phenomenon, which was suspected early in the pioneering work of Tveergard and Needleman [20,21]. This aspect was analyzed

* Principal corresponding author.
** Corresponding author. Tel.: +33 437 702 000.
E-mail addresses: romain.g.lagrange@gmail.com (R. Lagrange), daniel.averbuch@ifpen.fr (D. Averbuch).
URL: http://rlagrange.perso.centrale-marseille.fr/visible/Site/ (R. Lagrange).

0020-7403/$ - see front matter © 2012 Elsevier Ltd. All rights reserved.
http://dx.doi.org/10.1016/j.ijmecsci.2012.06.010

through numericalsimulations in these first papers and in Hunt and Wadee [7], Hunt and Blackmore [6], and through analytical approaches based on a double-scale expansion of the equilibrium equations in Potier-Ferry [16], for a beam resting on an elastic non-linear foundation. Based on these results, the study of the localization phenomenon was continued by using Galerkin techniques (see [22,24]) using the displacement envelopes obtained through the double-scale expansion of Potier-Ferry [16]. A lot of attention has also been paid to the estimation of the mechanical restraint induced by the soil friction and to the effect of backfill on the pipeline behavior, since the corresponding forces were found to highly influence the mechanical behavior of the pipe. In order to feed the corresponding models, experiments were performed (see [15,17–19]) either through centrifuge testing of small-scale pipeline models or through direct testing of buried full-scale pipe sections.

The present paper is an attempt to provide additional solutions for the study of the growth of a repeating imperfection in the line of a strut on a nonlinear foundation. In this work, the foundation is supposed to act through an either bi-linear or exponential regularized friction model relating the interaction line force to the transverse displacement (see Section 2). These two kinds of models are indeed found in the above mentioned papers describing the soil–pipe interaction models. In the former case, a solution method (piecewise solution) in Section 3 is proposed by explicitly solving the equilibrium equation in the regions where the foundation acts linearly and where the friction force is constant, and by connecting the two solutions by adequate boundary solutions. Alternatively, a Galerkin approach of the same problem is developed in Section 3 and leads to an explicit solution of the problem, which is developed for the two regularization models. The piecewise solution and the Galerkin approach are consequently compared together and with numerical solutions of the problem in Section 4. The post-buckling problem is then studied through the Galerkin approach which provides precise analytical solutions, focusing on the characteristics of a limit point (see Section 5) in the equilibrium curve depending on the magnitude of the initial imperfection.

2. Formulation of the differential equation

This section formulates the differential equation for the growth of an imperfection in the line of a strut on a nonlinear Winkler-type foundation, see Fig. 1. The imperfection is introduced by supposing an initially deformed shape W_0 whose form is

$$W_0 = A_0 \sin\left(\frac{\pi}{L}X\right), \tag{1}$$

with A_0 the amplitude of the imperfection, L its length and X the longitudinal coordinate. The compressive load is P and the restoring force per unit length is $\overline{P}$. These two forces are assumed to be conservative. The differential equation governing the deflection W may be derived either: directly by equilibration of forces; or from the Principal of Virtual Work; or using an energy formulation. The latter approach is adopted here; the total potential energy at first order being

$$V = \int_0^L \left[\frac{1}{2}EIW''^2 - P\left(\frac{1}{2}W'^2 + W_0'W'\right) - \int_0^W \overline{P}(t)\,\mathrm{d}t\right]\mathrm{d}X, \tag{2}$$

where a prime indicates differentiation with respect to X. The first term is the strain energy of bending (EI is the bending stiffness of the strut), the second is the work done by the load P and the remainder is the energy stored in the elastic foundation. Equilibrium is given by stationary values of V. In what follows the strut is assumed to be simply supported, such that the conditions at the boundaries are $W(0) = W(L) = 0$. The calculus of variations on (2) gives, for a virtual displacement δW such that $\delta W(0) = \delta W(L) = 0$

$$\delta V = EI[\delta W' W'']_0^L + \int_0^L [EIW'''' + P(W'' + W_0'') - \overline{P}(W)]\delta W\,\mathrm{d}X, \tag{3}$$

so that the Euler–Lagrange equation and the conditions at the boundaries for a simply supported strut are

$$EIW'''' + PW'' - \overline{P}(W) = -PW_0'', \tag{4a}$$

$$W(0) = 0, \tag{4b}$$

$$W''(0) = 0, \tag{4c}$$

$$W(L) = 0, \tag{4d}$$

$$W''(L) = 0. \tag{4e}$$

In Eq. (4a), P is the compressive load before buckling. The compressive load after buckling, considering a strut of section S, should be written as $N = P - (ES/2L)\int_0^L (W_{,X})^2\,dX$, last term of this expression being a geometric shortening which allows for the additional length introduced by the lateral movement. Therefore, N should be used in the equation for equilibrium. However, Tveergard and Needleman [21] have shown that the buckle will only become unstable if $N(y)$ has a maximum is correct for an isolated half-wave but is not correct for a long strut which contains a sequence of half-waves end-to-end. In such a case the key point is that a localization of the buckling, in which one particular half-wave grows at the expenses of its neighbors, can occur whenever the curve $P(y)$ has a maximum. Under this consideration, and as Maltby and Calladine [14] did, we use P instead of N as the load parameter.

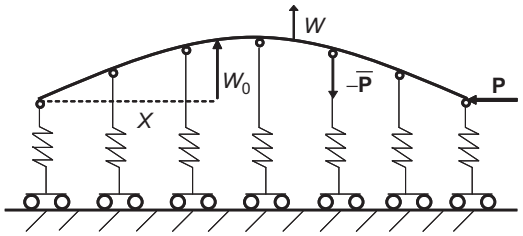

Fig. 1. Half-wavelength imperfection in the line of a strut resting on an elastic foundation. The imperfection is W_0, the compressive load is P and the buckling displacement is W. Springs have a nonlinear elastic force–displacement relationship $\overline{P}(W)$.

2.1. The restoring force

The restoring force per unit length is assumed to be nonlinear and two particular $\overline{P}$ functions are considered. The first one is referred as the bi-linear function and is defined by

$$\overline{P}(W) = \begin{cases} -KW & \text{if } |W| < \Delta, \\ -K\Delta & \text{if } W > \Delta, \\ K\Delta & \text{if } W < -\Delta, \end{cases} \tag{5}$$

where K is the linear stiffness and Δ the mobilization. These two constants are positive. The second $\overline{P}$ function considered in this paper is referred as the exponential profile and is defined by

$$\overline{P}(W) = \begin{cases} -K\Delta(1 - e^{-W/\Delta}) & \text{if } W > 0, \\ K\Delta(1 - e^{W/\Delta}) & \text{if } W < 0. \end{cases} \tag{6}$$

The two $\overline{P}$ functions share the same initial slope and limiting force (see Fig. 2(a)).

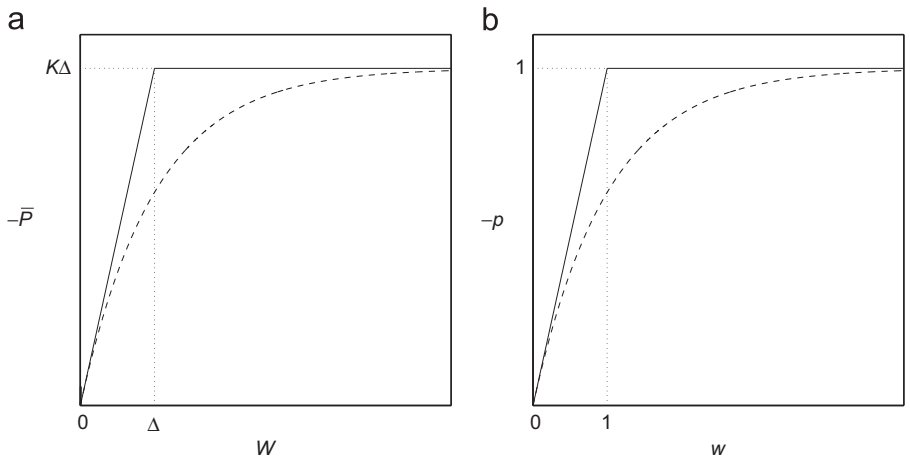

Fig. 2. (a) Restoring force. (b) Dimensionless restoring force. Bi-linear profile (solid line), exponential profile (dashed line). Dotted lines: limiting plateau (horizontal line), mobilization (vertical line).

2.2. Nondimensionalization

Let us introduce a characteristic length $L_{char}=(EI/K)^{1/4}$ and nondimensional quantities

$$l=\frac{L}{L_{char}},\quad x=\frac{X}{L_{char}},\quad w=\frac{W}{\Delta},\quad w_0=\frac{W_0}{\Delta},\quad \lambda=\frac{P}{KL_{char}^2},\quad p=\frac{\overline{P}}{K\Delta}. \tag{7}$$

Hence, from (4) the deflection w is the solution of the differential problem

$$w''''+\lambda w''-p(w)=-\lambda w_0'', \tag{8a}$$

$$w(0)=0, \tag{8b}$$

$$w''(0)=0, \tag{8c}$$

$$w(l)=0, \tag{8d}$$

$$w''(l)=0, \tag{8e}$$

the dimensionless imperfection being

$$w_0=a_0\sin\left(\frac{\pi}{l}x\right), \tag{9}$$

with $a_0=A_0/\Delta$.

After nondimensionalization, the bi-linear function rewrites

$$p(w)=\begin{cases}-w & \text{if } |w|<1,\\ -1 & \text{if } w>1,\\ 1 & \text{if } w<-1,\end{cases} \tag{10}$$

such that the dimensionless mobilization and limiting force equal 1. The nondimensional exponential profile is given by

$$p(w)=\begin{cases}-(1-e^{-w}) & \text{if } w>0,\\ 1-e^{w} & \text{if } w<0.\end{cases} \tag{11}$$

Fig. 2(b) shows the evolution of these two dimensionless restoring forces for $w>0$.

3. Theoretical resolution

In this paper, imperfections with dimensionless lengths $l<\sqrt{2}\pi$ are considered. In order to give a practical meaning to this inequation, let us consider the case of an imperfect railway. The most common rails in France (rail type 50E6) have a weight per meter of about $m=500\ \mathrm{N\,m^{-1}}$, a length from 10 to 400 m (length between two joints connection) and a bending stiffness of about $EI=4\times10^6\ \mathrm{N\,m^2}$. Considering a coefficient of friction φ between steel and concrete of 0.4 and a mobilization Δ from 0.1 to 1 mm it comes a linear stiffness $K=mg\varphi/\Delta$ (g being the gravity) from 2×10^5 to $2\times10^6\ \mathrm{N\,m^{-2}}$ and a characteristic length L_{char} from 1 to 2 m. Therefore $l<\sqrt{2}\pi$ would correspond to a repeating sinusoidal imperfection in the railway whose half-wavelength is no more than 10 m. In a more general way, $l<\sqrt{2}\pi$ deals with imperfections whose length does not exceed some meters. Therefore the specific calculations described in this paper have been made in the context of a small-scale experimental setup.

For $l<\sqrt{2}\pi$, the first buckling mode predicted by the linear analysis is excited when

$$\lambda=\lambda_c=\left(\frac{\pi}{l}\right)^2+\left(\frac{\pi}{l}\right)^{-2}, \tag{12}$$

and it has the same shape as the imperfection. In what follows we will also introduce the Euler load λ_e

$$\lambda_e=\left(\frac{\pi}{l}\right)^2, \tag{13}$$

which is the buckling load of the first mode when the restoring force equals 0.

Two theories are developed to solve the equilibrium problem. The first one, named piecewise solution theory is an exact resolution of the equilibrium problem when the bi-linear restoring force is considered. The second theory is based on a Galerkin method: it leads to an approximate resolution of the equilibrium problem by considering equally the bi-linear or the exponential restoring force. To initiate this method, the deflection shape is assumed to be a sinusoid, as the imperfection. Explicit solutions of the Galerkin equation are obtained without any assumptions.

3.1. Piecewise solution theory

The principle of the piecewise solution theory is to solve (8a) on each piece of the bi-linear function. Then, the solutions are connected thanks to the boundary conditions and assuming the continuity of w, w', w'' and w''' at two connecting points x_1 and x_2.

Substituting $p(w)$ by $-w$ and by -1 in (8a) yields respectively

$$w_1''''+\lambda w_1''+w_1=-\lambda w_0'', \tag{14a}$$

$$w_2''''+\lambda w_2''=-1-\lambda w_0''. \tag{14b}$$

The solutions w_1 and w_2 belong to two affine spaces of dimension 4 given by

$$w_1 = w_{1\mathrm{h}} + w_{1\mathrm{part}}, \tag{15a}$$

$$w_2 = w_{2\mathrm{h}} + w_{2\mathrm{part}}, \tag{15b}$$

where $w_{1\mathrm{h}}$ and $w_{2\mathrm{h}}$ satisfy the homogeneous equations

$$w''''_{1\mathrm{h}} + \lambda w''_{1\mathrm{h}} + w_{1\mathrm{h}} = 0, \tag{16a}$$

$$w''''_{2\mathrm{h}} + \lambda w''_{2\mathrm{h}} = 0. \tag{16b}$$

Inserting $w_{1\mathrm{h}} = Ae^{r_1 x}$ and $w_{2\mathrm{h}} = Be^{r_2 x}$ in (16) yields two algebraic equations

$$r_1^4 + \lambda r_1^2 + 1 = 0, \tag{17a}$$

$$r_2^4 + \lambda r_2^2 = 0, \tag{17b}$$

whose solutions are

$$r_1^{(1)} = \tfrac{1}{2}[-2\lambda + 2(\lambda^2-4)^{1/2}]^{1/2}, \tag{18a}$$

$$r_1^{(2)} = -\tfrac{1}{2}[-2\lambda + 2(\lambda^2-4)^{1/2}]^{1/2}, \tag{18b}$$

$$r_1^{(3)} = \tfrac{1}{2}[-2\lambda - 2(\lambda^2-4)^{1/2}]^{1/2}, \tag{18c}$$

$$r_1^{(4)} = -\tfrac{1}{2}[-2\lambda - 2(\lambda^2-4)^{1/2}]^{1/2}, \tag{18d}$$

and

$$r_2 = 0, \quad \pm\sqrt{\lambda}\mathrm{i}. \tag{19}$$

Let us introduce α_i and ω_i the real and imaginary parts of $r_1^{(i)}$. For $\lambda < 2$, the roots r_1 are complex numbers and the function $w_{1\mathrm{h}}$ is

$$w_{1\mathrm{h}} = A_1 e^{\alpha_1 x}\cos(\omega_1 x) + A_2 e^{\alpha_2 x}\cos(\omega_2 x) + A_3 e^{\alpha_1 x}\sin(\omega_1 x) + A_4 e^{\alpha_2 x}\sin(\omega_2 x), \tag{20}$$

with A_1, A_2, A_3 and A_4 four real constants. For $\lambda = 2$, the roots r_1 are double imaginary numbers ($r_1^{(1)} = r_1^{(3)}$ and $r_1^{(2)} = r_1^{(4)}$). The function $w_{1\mathrm{h}}$ is

$$w_{1\mathrm{h}} = (A_1 x + A_2)\cos(x) + (A_3 x + A_4)\sin(x). \tag{21}$$

For $\lambda > 2$, the roots r_1 are imaginary numbers. The solution $w_{1\mathrm{h}}$ is

$$w_{1\mathrm{h}} = A_1\cos(\omega_1 x) + A_2\cos(\omega_3 x) + A_3\sin(\omega_1 x) + A_4\sin(\omega_3 x). \tag{22}$$

For $\lambda \neq 0$ the function $w_{2\mathrm{h}}$ is given by

$$w_{2\mathrm{h}} = B_1 + B_2 x + B_3\cos(\sqrt{\lambda}x) + B_4\sin(\sqrt{\lambda}x), \tag{23}$$

with B_1, B_2, B_3 and B_4 four real constants.

Since $w_{1\mathrm{h}}$ and $w_{2\mathrm{h}}$ depend on four undetermined constants, these functions will be noted $w_{1\mathrm{h}}(x,A_1,A_2,A_3,A_4)$ and $w_{2\mathrm{h}}(x,B_1,B_2,B_3,B_4)$.

The functions $w_{1\mathrm{part}}$ and $w_{2\mathrm{part}}$ appearing in (15a) and (15b) are particular solutions of (14a) and (14b), with w_0 given by (9). Searching $w_{1\mathrm{part}}$ and $w_{2\mathrm{part}}$ as $w_{1\mathrm{part}} = Aw_0$ and $w_{2\mathrm{part}} = Cx^2 + Aw_0$ yields

$$w_{1\mathrm{part}} = \frac{\lambda}{\lambda_c - \lambda} w_0, \tag{24a}$$

$$w_{2\mathrm{part}} = -\frac{1}{\lambda}\frac{x^2}{2} + \frac{\lambda}{\lambda_e - \lambda} w_0. \tag{24b}$$

Finally, the functions w_1 and w_2, defined by (15a) and (15b), are

$$w_1 = w_{1\mathrm{h}}(x,A_1,A_2,A_3,A_4) + \frac{\lambda}{\lambda_c - \lambda} w_0, \tag{25a}$$

$$w_2 = w_{2\mathrm{h}}(x,B_1,B_2,B_3,B_4) - \frac{1}{\lambda}\frac{x^2}{2} + \frac{\lambda}{\lambda_e - \lambda} w_0. \tag{25b}$$

In what follows, we will introduce the function w_3 defined as

$$w_3 = w_{1\mathrm{h}}(x,C_1,C_2,C_3,C_4) + \frac{\lambda}{\lambda_c - \lambda} w_0. \tag{26}$$

This function is a solution of (14a), as w_1, but with four different undetermined constants C_1, C_2, C_3 and C_4.

The aim of the piecewise solution theory is to search for a deflection w solution of (8) by connecting the functions w_1, w_2 and w_3 at two unknown points x_1 and x_2 such that

$$w = \begin{cases} w_1 & \text{if } x \in [0,x_1[, \\ 1 & \text{if } x = x_1, \\ w_2 & \text{if } x \in]x_1,x_2[, \\ 1 & \text{if } x = x_2, \\ w_3 & \text{if } x \in]x_2,l]. \end{cases} \tag{27}$$

With these notations, the boundary conditions (8b), (8c), (8d) and (8e) rewrite as respectively

$$w_1(0) = 0, \tag{28a}$$

$$w'_1(0) = 0, \tag{28b}$$

$$w_3(l) = 0, \tag{28c}$$

$$w'_3(l) = 0. \tag{28d}$$

The continuity of the displacement, the tangent, the curvature and the shear at x_1 yields

$$w_1(x_1) - w_2(x_1) = 0, \tag{29a}$$

$$w'_1(x_1) - w'_2(x_1) = 0, \tag{29b}$$

$$w''_1(x_1) - w''_2(x_1) = 0, \tag{29c}$$

$$w'''_1(x_1) - w'''_2(x_1) = 0, \tag{29d}$$

and at x_2

$$w_2(x_2) - w_3(x_2) = 0, \tag{30a}$$

$$w'_2(x_2) - w'_3(x_2) = 0, \tag{30b}$$

$$w''_2(x_2) - w''_3(x_2) = 0, \tag{30c}$$

$$w'''_2(x_2) - w'''_3(x_2) = 0. \tag{30d}$$

Eqs. (28), (29) and (30) lead to a linear system with 12 equations and 12 unknowns (i.e. the amplitudes A_i, B_i and C_i). A matrix representation of this system is

$$\mathbf{G}(x_1,x_2)\mathbf{a} = \mathbf{b}(w_0,x_1,x_2), \tag{31}$$

with $\mathbf{G}$ a 12 by 12 real matrix and $\mathbf{a}$ the vector of the unknown amplitudes. The vector $\mathbf{b}$ contains the particular solutions $w_{1\mathrm{part}}$ and $w_{2\mathrm{part}}$ which depend on w_0, x_1 and x_2.

If $\det(\mathbf{G}) \neq 0$ then

$$\mathbf{a}(w_0,x_1,x_2) = \mathbf{G}^{-1}(x_1,x_2)\mathbf{b}(w_0,x_1,x_2). \tag{32}$$

Eq. (32) expresses the amplitudes as functions of x_1 and x_2. These two connecting points are obtained by solving the nonlinear system

$$f_1(w_0,x_1,x_2) = w_1(x_1) - 1 = 0, \tag{33a}$$

$$f_2(w_0,x_1,x_2) = w_2(x_2) - 1 = 0. \tag{33b}$$

The numerical resolution of this system has been carried out with Matlab, using the *fzero* function. This function tries to find a zero of (33) near X_0, X_0 being a vector of length two. Depending on λ (33) has 0 or several solutions. For small λ, the restoring force p remains linear, such that $w = w_1$ for any $x \in [0,l]$. Thus, (33) has no solution. For high λ, the restoring force p is nonlinear: the existence and the uniqueness of a solution for (33) is not trivial.

In this paper, we only search for a solution which satisfies $x_1 \in [0,l/2]$, $x_2 \in [l/2,l]$ and $x_2 = l - x_1$: the connecting points are symmetric relative to $x = l/2$. This condition is specified adjusting the X_0 vector used by the *fzero* function. Typically, $X_0 = [l/2; l/2]$ is a good candidate to easily find the symmetric connecting points. Once the connecting points are calculated, we determine the amplitudes A_i, B_i and C_i thanks to (32), the functions w_1, w_2 and w_3 thanks to (25a), (25b), (26) and finally the deflection w via (27).

3.2. Galerkin method

The Galerkin procedure (see [3]) may be seen as being derived from (3) by assuming that the modes which go to make up w are given by

$$w = \sum_{i=1}^{n} y_i \phi_i, \tag{34}$$

where each y_i is an undetermined amplitude of each shape function ϕ_i. Depending on the form of w in (34), we can perform periodic or localized buckling analysis. For a very long imperfection in the line of a strut on a cubic foundation, Whiting [24] performed the latter, using the functions predicted by the asymptotical analysis (see [23]) as test functions. The amplitudes of each shape function are determined numerically using a variable-order variable-step Adams method. In this paper we do not search for localized solutions: we use a unique test function which has the same shape as the imperfection. It means that the deflection w is searched as

$$w = y \sin\left(\frac{\pi}{l}x\right), \tag{35}$$

with $y > 0$.

Inserting δw in the dimensionless form of (3) gives

$$\int_0^l \sin\left(\frac{\pi}{l}x\right)[w'''' + \lambda(w'' + w_0'') - p(w)]\,\mathrm{d}x = 0. \tag{36}$$

Writing the restoring force as $p(w) = -w - N(w)$ yields a relation between the load λ and the amplitude y

$$\lambda = \frac{1}{a_0 + y}\left[\lambda_c y + \frac{Q(y)}{\lambda_e}\right], \tag{37}$$

with

$$Q(y) = \frac{2}{l}\int_0^l \sin\left(\frac{\pi}{l}x\right) N\left(y \sin\left(\frac{\pi}{l}x\right)\right)\mathrm{d}x. \tag{38}$$

The assumption $N(y \sin((\pi/l)x)) = N(y)\sin((\pi/l)x)$ introduced by Maltby and Calladine [14] yields $N = Q$. Such an assumption will not be introduced in this paper. However, we will see how this assumption affects the result.

Note that since the integrand function in (38) is $l/2$-periodic, the Q function does not change when the deflection is searched as $w = y \sin((n\pi/l)x)$. Then, when the imperfection is $w_0 = a_0 \sin((n\pi/l)x)$, the equilibrium paths are still given by (37) with $\lambda_e = (n\pi/l)^2$ and $\lambda_c = \lambda_e + \lambda_e^{-1}$.

In practice, the equilibrium paths predicted by the Galerkin method are plotted using (37), varying y and evaluating λ.

3.2.1. Bi-linear restoring force

Considering the bi-linear restoring force, the Q function rewrites

$$Q(y) = \frac{2\mathrm{H}(y-1)}{\pi}\left\{y\left[\arcsin\left(\frac{1}{y}\right) - \frac{\pi}{2}\right] + \left(\frac{y^2-1}{y^2}\right)^{1/2}\right\}, \tag{39}$$

where H is the Heaviside function defined by $\mathrm{H}(y-1) = 0$ if $y < 1$ and $\mathrm{H}(y-1) = 1$ if $y \geq 1$. The proof of this result is reported in Appendix A.

3.2.2. Exponential restoring force

Considering the exponential restoring force, the Q function rewrites

$$Q(y) = 2[\mathrm{I}_1(y) - \mathrm{L}_1(y)] - y, \tag{40}$$

where I_1 and L_1 are respectively the modified Bessel and Struve functions of parameter 1. The proof of this result is reported in Appendix B.

4. Theoretical and numerical results

In this section, the equilibrium paths predicted by the piecewise solution theory, the Galerkin procedure and a numerical resolution of (8) are compared. We also determine the influence of the restoring force (bi-linear or exponential) on the shape of the equilibrium paths.

4.1. Piecewise solution theory

The equilibrium paths predicted by the piecewise solution theory are depicted in Fig. 3(a) for a_0 from 0 to 1.19. For a small imperfection size, the equilibrium path shows the load increasing at first but then hits a maximum (limit point, or saddle-node bifurcation point) that is below λ_c (or equals for $a_0 = 0$), and the rest of the path asymptotically decreases to the Euler load when $\max(w) \to \infty$. Thus, the system is subcritical. Moreover, the greater the imperfection size, the greater the reduction in the maximum load. Thus the system is imperfection sensitive. For high imperfection sizes, the equilibrium path increases monotically and $\lambda \to \lambda_e < \lambda_c$ when $\max(w) \to \infty$.

From these observations we infer the existence of a critical amplitude a_{0c} such that

- if $a_0 > a_{0c}$ then the equilibrium paths do not have a limit point and the equilibrium states are stable,
- if $a_0 < a_{0c}$ then the equilibrium paths have a limit point (y_m, λ_m). For $y < y_m$ (resp. $y > y_m$) the equilibrium states are stable (resp. unstable). An unstable equilibrium state is represented in Fig. 4 by connecting the functions w_1, w_2, and w_3.

The determination of a_{0c} is reported in Section 5.

4.2. Galerkin method and numerical results

4.2.1. Bi-linear restoring force

For the bi-linear function, the equilibrium paths predicted by the Galerkin method and those obtained via a numerical resolution of (8), using the ODE45 solver from Matlab (this routine uses a variable step Runge–Kutta method), are represented in Fig. 3(b) and (c). The equilibrium paths are identical to those predicted by the piecewise solution theory (the relative error between the two theories and the numerical resolution being less than 0.1%). Since the Galerkin test function and the imperfection have the same shape, in the case of a bi-linear restoring force the deflection is an amplification of the imperfection.

4.2.2. Exponential restoring force

For the exponential profile, the equilibrium paths predicted by the Galerkin method and those obtained via a numerical resolution of (8) are represented in Figs. 5 and 6. Once again they are identical, thus the deflection w is an amplification of the imperfection. The equilibrium paths predicted by Maltby and Calladine [14] have also been reported in Fig. 5. The assumption introduced by Maltby and Calladine [14] (see Section 3.2) leads to an underestimation of the load. In Section 5 we will show that the existence of a limit point is also affected by this assumption.

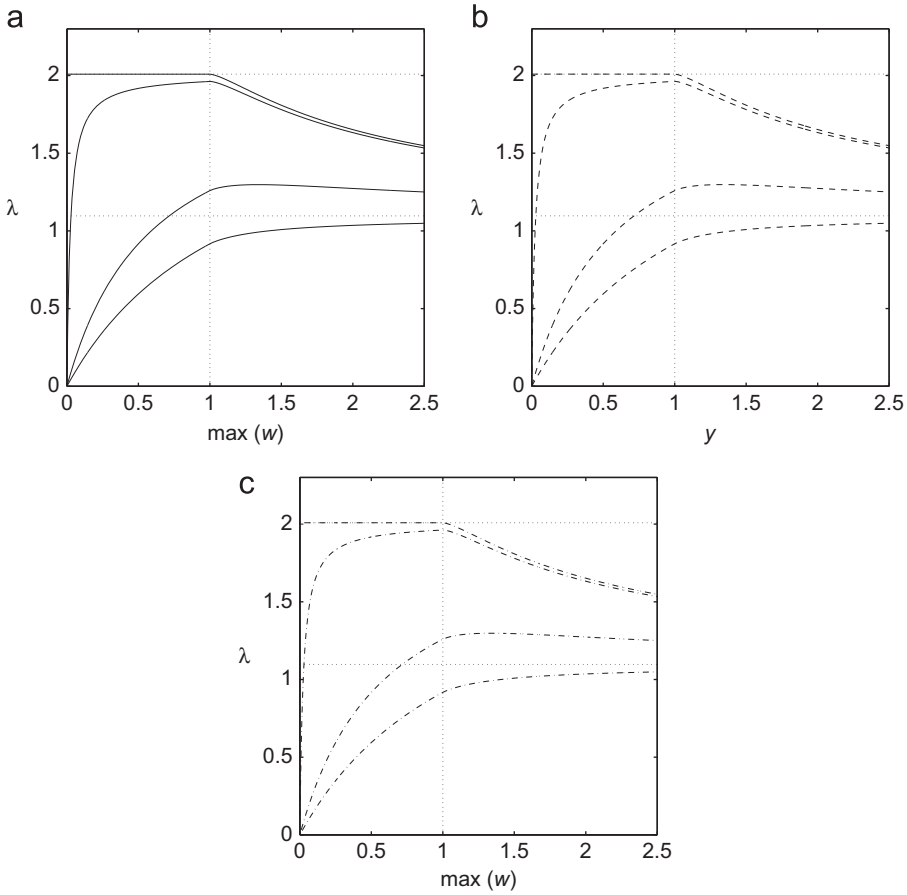

Fig. 3. Equilibrium paths predicted by (a) the piecewise solution theory, (b) the Galerkin method, (c) the numerical resolution of (8), case of a bi-linear restoring force. On each graph, the equilibrium paths are plotted (from top to bottom) for $a_0 = 0$, a_0=0.0238, a_0=0.595, a_0=1.19 and l=3. Dotted lines: critical load (upper line), Euler load (lower line), mobilization (vertical line).

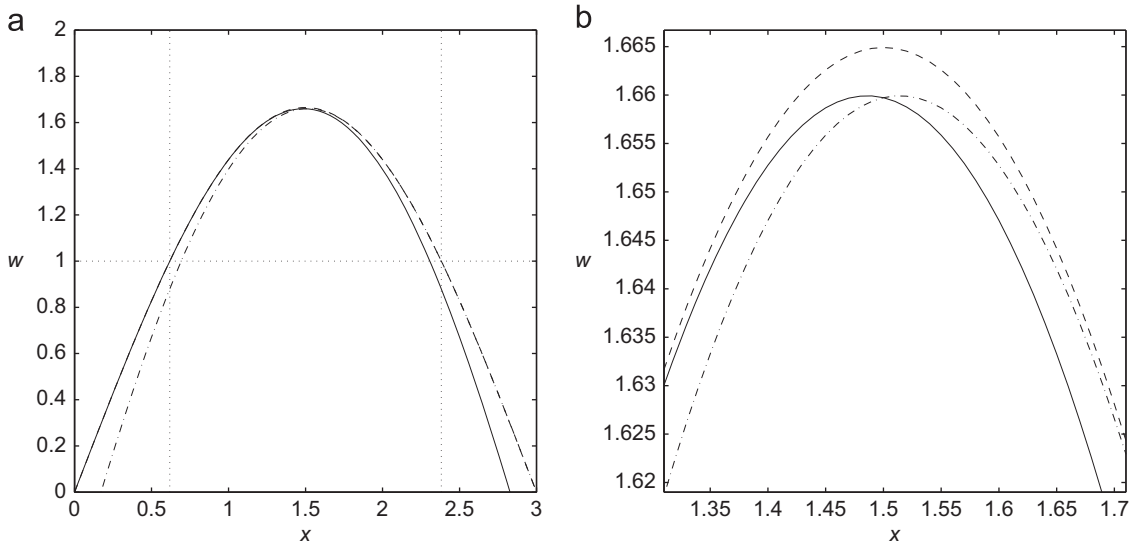

Fig. 4. Deflection predicted by the piecewise solution theory. (b) is a zoom of (a). Function w_1 (solid line), function w_2 (dashed line), function w_3 (dash-dotted line). The functions w_1 and w_2 are connected at $x = x_1 \approx 0.618$ (first vertical dotted line). The functions w_2 and w_3 are connected at $x = x_2 \approx 2.382$ (second vertical dotted line). The horizontal dotted line represents the mobilization. l=3, $a_0 = 0$, $\lambda = 1.75$.

In Fig. 5 the equilibrium paths predicted for a bi-linear restoring force have been reported in order to discuss the influence of the restoring force. It appears that the restoring force (bi-linear or exponential) has no influence on the shape of the equilibrium paths (the variations are preserved, it always exists a limit point for small imperfection sizes, the same asymptotes are recovered). Nevertheless, the equilibrium paths for an exponential profile are below the equilibrium paths for a bi-linear profile.

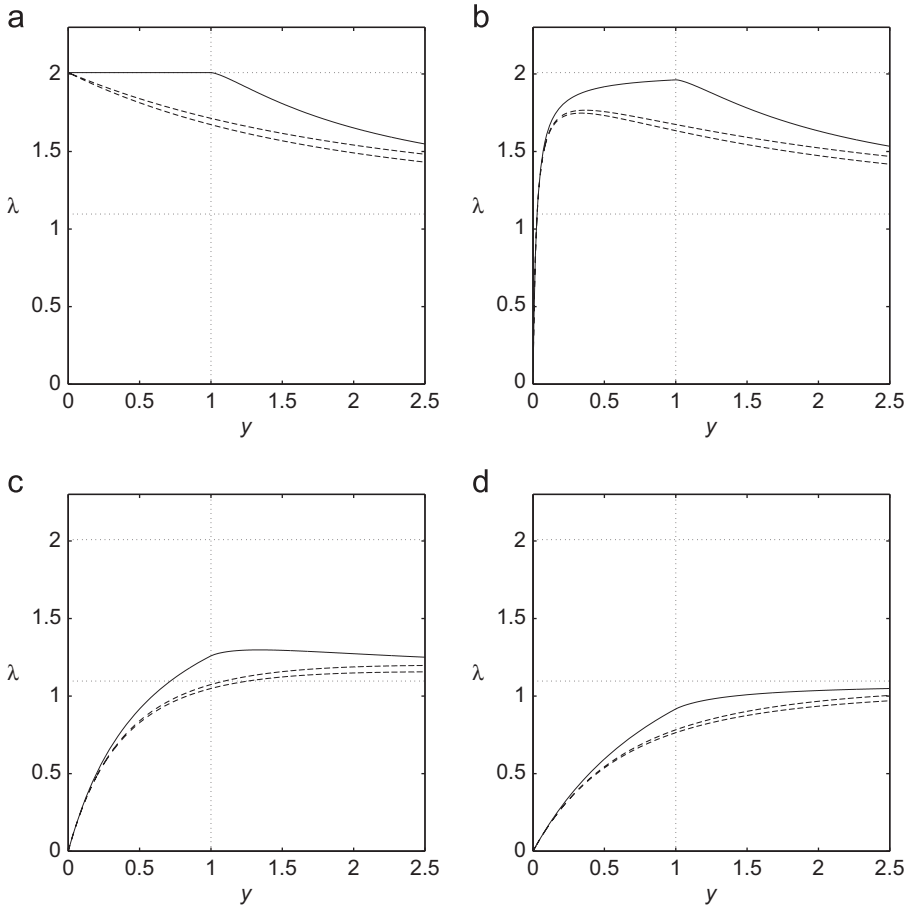

Fig. 5. Equilibrium paths predicted by the Galerkin method. Bi-linear restoring force (solid line), exponential restoring force (dashed lines). Galerkin method (upper dashed line), Galerkin method with the [14] assumption (lower dashed line). Dotted lines: critical load (upper line), Euler load (lower line), mobilization (vertical line). $l=3$, $a_0=0$ (a), $a_0=0.0238$ (b), $a_0=0.595$ (c), $a_0=1.19$ (d).

Therefore, the choice of the restoring force has a non-negligible influence on the maximal load acceptable by the system. This point is the purpose of the next section.

5. Limit point

A limit point corresponds to a maximum of λ. Therefore, if it exists, this point (y_m,λ_m) satisfies $(d\lambda/dy)(y_m)=0$, that is to say using (37)

$$(a_0+y_m)\frac{dQ}{dy}(y_m)-Q(y_m)=-a_0\lambda_c\lambda_e. \tag{41}$$

This equation yields $Q(y_m)/\lambda_e=a_0\lambda_c-(a_0+y_m)f(a_0)$ with f a function of a_0. Inserting this last expression in (37) yields

$$\lambda_m=\lambda(y_m)=\lambda_c-f(a_0). \tag{42}$$

In practice, the coordinates of a limit point are obtained by varying y_m and looking for an amplitude a_0 which satisfies (41). Fig. 7(a) represents the evolution of y_m as a function of a_0. For the two restoring forces it appears that y_m is an increasing function of a_0 and diverges for the same critical amplitude. This amplitude is determined by enforcing $y_m\to\infty$ in (41). It yields

$$a_{0c}=\frac{4}{\pi}\lambda_e^{-2}, \tag{43}$$

whose dimensional equivalent form is

$$A_{0c}=\frac{4}{\pi}\frac{L^4}{\pi^4 EI}K\Delta. \tag{44}$$

This result is of great importance since it governs the appearance of localized solutions, as demonstrated in Tveergard and Needleman [21]. In that paper, they indeed showed the close link between the existence of a limit point in the $\lambda(y)$ curve and localization, the bifurcation into a localized form occurring a little way beyond this limit point.

Considering the bi-linear restoring force, when $a_0\to 0$, Eq. (41) has an infinity of solutions y_m in $]0,1]$. This observation is coherent with the equilibrium paths depicted in Fig. 3 since the points lying on the plateau $\lambda=\lambda_c$ are a maximum.

Considering the exponential restoring force, $y_m\to 0$ when $a_0\to 0$. This result is coherent with the equilibrium paths depicted in Figs. 5(a) and 6(a) since $(0,\lambda_c)$ is a maximum.

Substituting $Q(y_m)$ by $N(y_m)=-y_m+1-e^{-y_m}$ in (41) (assumption made by [14]) and enforcing $y_m\to\infty$ yields

$$a_{0c}=\lambda_e^{-2}, \tag{45}$$

whose dimensional equivalent form is

$$A_{0c}=\frac{L^4}{\pi^4 EI}K\Delta, \tag{46}$$

which is $4/\pi$ times smaller than the exact prediction (43). This result means that a stable equilibrium (i.e. an equilibrium path without a limit point) predicted with the assumption introduced by Maltby and Calladine [14], could in fact be unstable (see Fig. 9).

Fig. 7(b) represents the evolution of the limit point λ_m as a function of a_0. Considering the two restoring forces, the same asymptotes are observed: $\lambda_m\to\lambda_e$ when $a_0\to a_{0c}$ and $\lambda_m\to\lambda_c$ when $a_0\to 0$. We also observe that the assumption introduced by [14]

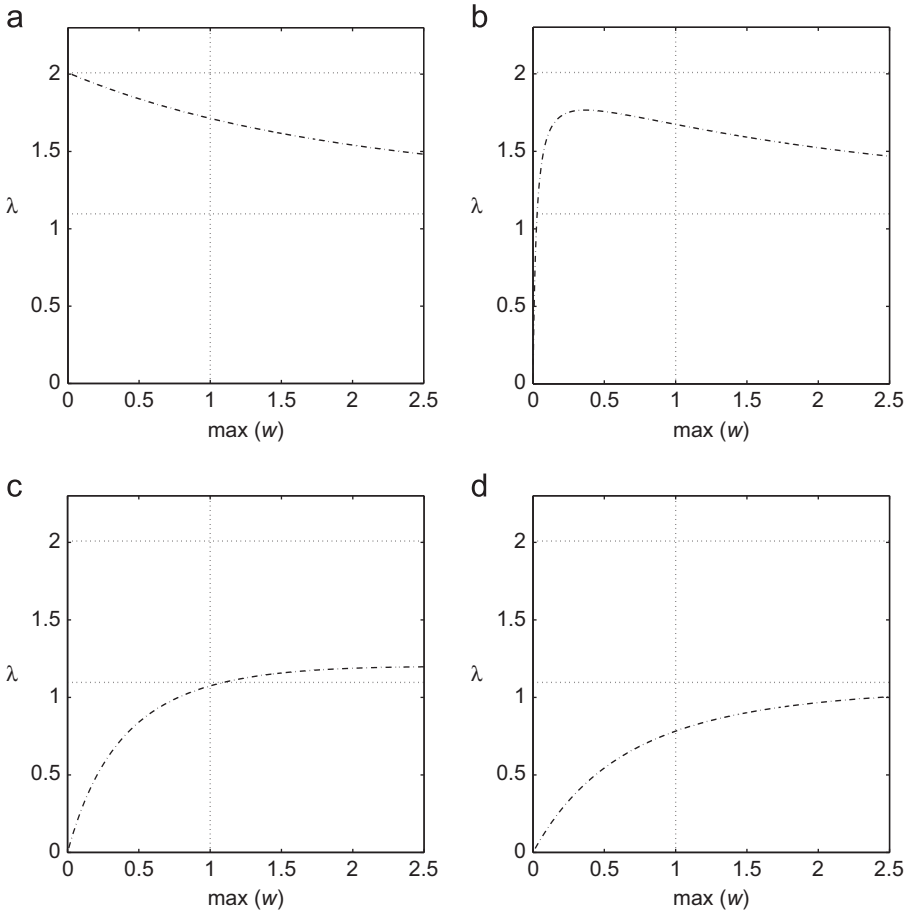

Fig. 6. Equilibrium paths obtained via a numerical resolution of (8), case of an exponential restoring force. Dotted lines: critical load (upper line), Euler load (lower line), mobilization (vertical line). $l=3$, $a_0=0$ (a), $a_0=0.0238$ (b), $a_0=0.595$ (c), $a_0=1.19$ (d).

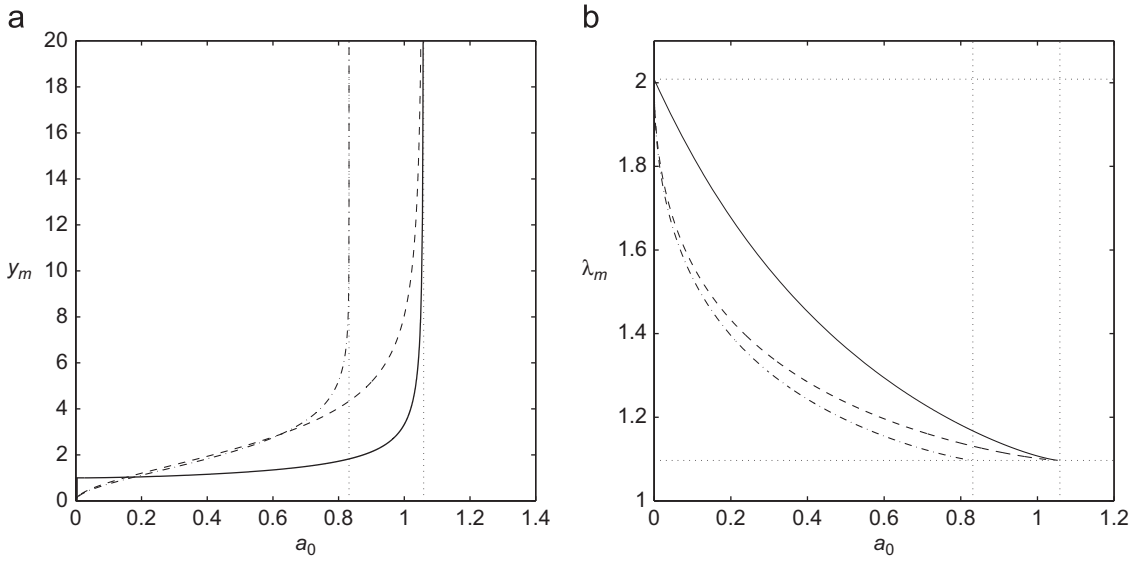

Fig. 7. Limit point as a function of the amplitude of the imperfection. Bi-linear restoring force (solid line), exponential restoring force (dashed line), exponential restoring force with the assumption introduced by [14] (dash-dotted line). Dotted lines: (a) critical amplitudes, (b) critical load (upper line), Euler load (lower line), critical amplitudes (vertical lines). $l=3$.

(see Section 3.2) leads to an underestimation of the limit load. These observations are coherent with the equilibrium paths depicted in Figs. 3, 5 and 6.

Fig. 8 shows the evolution of $\lambda_c-\lambda_m$ as a function of a_0, in a logarithmic scale. This picture allows to determine a scaling for the function f appearing in (42). Considering the bi-linear restoring force, for small amplitudes a_0, $\lambda_m-\lambda_c$ scales as

$$\lambda_m-\lambda_c \sim -a_0. \tag{47}$$

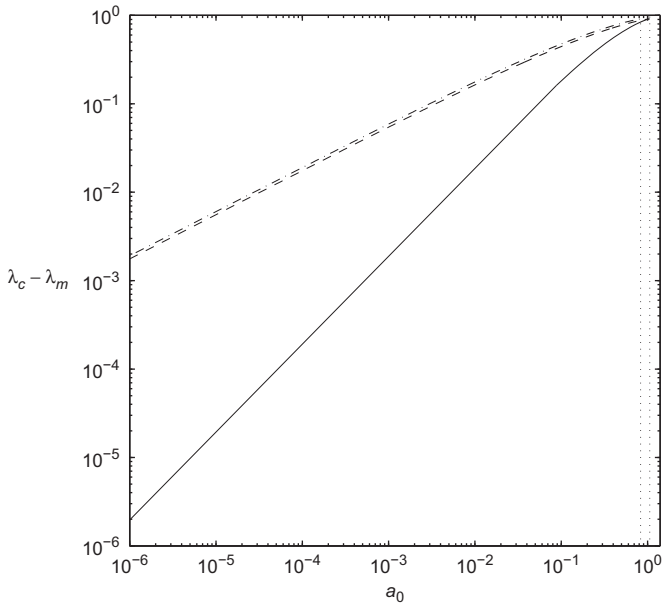

Fig. 8. Scaling of the limit point. Bi-linear restoring force (solid line), exponential restoring force (dashed line), exponential restoring force with the assumption introduced by Maltby and Calladine [14] (dash-dotted line), critical amplitudes (dotted lines). $l=3$.

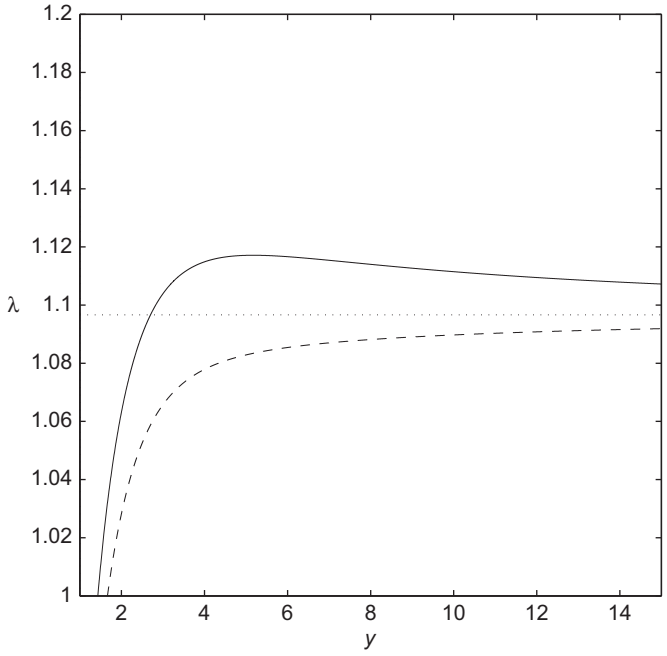

Fig. 9. Equilibrium paths predicted by the exact Galerkin method (solid curve) and the Galerkin method with the assumption introduced by Maltby and Calladine [14] (dashed line). The dotted line corresponds to the Euler load. $a_0=0.9$, $l=3$.

When the exponential restoring force is considered this scaling becomes

$$\lambda_m - \lambda_c \sim -a_0^{1/2}. \tag{48}$$

We observe in Fig. 8 that the assumption introduced by Maltby and Calladine [14] has no influence on this last scaling.

6. Conclusion

In this paper, the growth of a repeating sinusoidal imperfection in the line of a strut on a nonlinear elastic Winkler-type foundation is considered. The imperfection is introduced by considering an initially sinusoidal deformed shape with an half wavelength. The imperfection length is chosen such that the buckle mode predicted by the linear theory has the same shape as the imperfection (first buckle mode). The nonlinearities are only due to the restoring force provided by the foundation. This restoring force is expressed as a force-displacement relationship which is either a bi-linear or an exponential function. The equilibrium problem is solved using three different methods. The first one, named piecewise solution theory, is dedicated to the bi-linear profile and leads to an exact resolution of the equilibrium problem. The second one is available whatever the restoring force and is based on a Galerkin procedure. This procedure is initiated with a test function which has the same shape as the imperfection. It yields an explicit relation between the compressive load and the amplitude of the test function. This expression is an exact solution of the Galerkin equation and gives an approximate solution of the equilibrium problem. The last method is a numerical resolution of the equilibrium problem, using the ODE45 solver from Matlab. These three solving methods yield the same results: whatever the restoring force (bi-linear or exponential), the bifurcation is subcritical, the system is imperfection sensitive and the deformed shape is an amplification of the default. Moreover, it exists a critical imperfection size $a_{0c}=(4/\pi)\lambda_e^{-2}$ (λ_e being the Euler load) which does not depend on the restoring force and such that

- if $a_0 > a_{0c}$, then the equilibrium path shows the load increasing monotically and remains asymptotic to the Euler load.
- if $a_0 < a_{0c}$, then the equilibrium path shows the load increasing at first but then hits a limit point and the rest of the path is asymptotic to the Euler load.

This paper provides a better estimate of a_{0c} with respect to previous publications.

For each restoring force, an approximate mathematical rule is derived relating the imperfection size a_0 to the corresponding limit load λ_m. Considering the bi-linear profile (resp. the exponential profile) the limit point scales as $\lambda_m-\lambda_c \sim -a_0$ (resp. $\lambda_m-\lambda_c \sim -a_0^{1/2}$), where λ_c is the critical load issued from the classical linear analysis. Therefore, the scaling of the limit point depends on the regularization method.

In this paper, the restoring force and the compressive load are independent. Nevertheless, in some industrial applications (such as in drilling problems) the restoring force slightly depends on the axial compressive load. Therefore, we are currently carrying out a study with a bi-linear restoring force proportional to the axial load. First results issued from the Galerkin approach indicate that it is necessary to redefine the dimensionless parameters, leading to new scalings for the critical imperfection size and the limit load.

Appendix A. Function Q, bi-linear restoring force

The aim of this appendix is to calculate the function Q appearing in (39) when the bi-linear restoring force is considered.

Introduce H the Heaviside function defined as $H(x)=0$ if $x<0$ and $H(x)=1$ if $x\geq 0$. The restoring force p rewrites

$$p=-w-(\mathrm{Sgn}(w)-w)H(|w|-1), \tag{A.1}$$

where Sgn is the sign function. Since $p=-w-N(w)$ it comes

$$N(w)=(\mathrm{Sgn}(w)-w)\mathrm{H}(|w|-1). \tag{A.2}$$

For an imperfection with an half-wavelength, it can be assumed that $w>0$. Then, the Q function is (see (38))

$$Q(y)=-\frac{2}{l}\int_0^l \left[y\sin\left(\frac{\pi}{l}x\right)-1\right]\sin\left(\frac{\pi}{l}x\right)\mathrm{H}\left(y\sin\left(\frac{\pi}{l}x\right)-1\right)\mathrm{d}x. \tag{A.3}$$

If $y<1$ then $y\sin((\pi/l)x)-1<0$ so $\mathrm{H}(y\sin((\pi/l)x)-1)=Q=0$. Therefore, the function Q can be written as

$$Q(y)=-\frac{2\mathrm{H}(y-1)}{l}\int_0^l \left[y\sin\left(\frac{\pi}{l}x\right)-1\right]\sin\left(\frac{\pi}{l}x\right)\mathrm{H}\left(y\sin\left(\frac{\pi}{l}x\right)-1\right)\mathrm{d}x. \tag{A.4}$$

The change of variable $t=(\pi/l)x$ gives

$$Q(y)=-\frac{2}{\pi}\mathrm{H}(y-1)\int_0^{\pi}[y\sin(t)-1]\sin(t)\mathrm{H}(y\sin(t)-1)\,\mathrm{d}t. \tag{A.5}$$

The argument of the Heaviside function under the integral sign equals 0 when $\sin(t)=1/y$, that is to say for $t=t_1=\arcsin(1/y)$ and $t=\pi-t_1$. It comes that the function Q is non-zero between t_1 and $\pi-t_1$

$$Q(y)=-\frac{2}{\pi}\mathrm{H}(y-1)\int_{t_1}^{\pi-t_1}[y\sin(t)-1]\sin(t)\,\mathrm{d}t. \tag{A.6}$$

Finally, this integral yields

$$Q(y)=\frac{2}{\pi}\mathrm{H}(y-1)\left\{y\left[\arcsin\left(\frac{1}{y}\right)-\frac{\pi}{2}\right]+\left(\frac{y^2-1}{y^2}\right)^{1/2}\right\}, \tag{A.7}$$

and the result from (39) is recovered.

Appendix B. Function Q, exponential restoring force

The aim of this Appendix is to calculate the function Q appearing in (40) when the exponential restoring force is considered. For this calculus, we recall that the modified Struve and Bessel functions of parameter 1 can be expended as power series

$$\mathrm{L}_1(y)=\sum_{p=1}^{+\infty}\frac{2}{\pi}\frac{(p!)^2}{(2p+1)[(2p)!]^2}(2y)^{2p}, \tag{B.1a}$$

$$\mathrm{I}_1(y)=\sum_{p=0}^{+\infty}\frac{1}{p!(p+1)!}\left(\frac{y}{2}\right)^{2p+1}. \tag{B.1b}$$

Substituting the exponential function in (11) by its power series yields

$$p(w)=-w+\sum_{n=2}^{+\infty}\frac{(-1)^n w^n}{n!}, \tag{B.2}$$

so that

$$N(w)=\sum_{n=2}^{+\infty}\frac{(-1)^{n+1}w^n}{n!}. \tag{B.3}$$

Therefore, (38) gives

$$Q(y)=\frac{2}{l}\int_0^l\sum_{n=2}^{+\infty}\frac{(-1)^{n+1}\sin\left(\frac{\pi}{l}x\right)^{n+1}}{n!}y^n\,\mathrm{d}x. \tag{B.4}$$

Inverting the sum and integral signs and introducing the change of variable $t=(\pi/l)x$ yields

$$Q(y)=\frac{4}{\pi}\sum_{n=2}^{+\infty}\frac{(-1)^{n+1}W_{n+1}}{n!}y^n, \tag{B.5}$$

with W_n the Wallis integral

$$W_n=\int_0^{\pi/2}\sin^n(x)\,\mathrm{d}x. \tag{B.6}$$

The terms W_n are classical to calculate. For $n=2p$ and $n=2p+1$ it yields

$$W_{2p}=\frac{(2p)!}{2^{2p}(p!)^2}\frac{\pi}{2}, \tag{B.7a}$$

$$W_{2p+1}=\frac{2^{2p}(p!)^2}{(2p+1)!}. \tag{B.7b}$$

Splitting the series appearing in (B.5) into odd and even indices gives $Q(y)=\Sigma_1(y)+\Sigma_2(y)$ with

$$\Sigma_1(y)=-\frac{4}{\pi}\sum_{p=1}^{+\infty}\frac{W_{2p+1}}{(2p)!}y^{2p}, \tag{B.8a}$$

$$\Sigma_2(y)=\frac{4}{\pi}\sum_{p=1}^{+\infty}\frac{W_{2(p+1)}}{(2p+1)!}y^{2p+1}. \tag{B.8b}$$

Inserting (B.7a) and (B.8a) yields

$$\Sigma_1(y)=-2\sum_{p=1}^{+\infty}\frac{2}{\pi}\frac{(p!)^2}{(2p+1)[(2p)!]^2}(2y)^{2p}, \tag{B.9a}$$

$$\Sigma_2(y)=2\sum_{p=0}^{+\infty}\frac{1}{p!(p+1)!}\left(\frac{y}{2}\right)^{2p+1}-y. \tag{B.9b}$$

Eq. (B.1) gives

$$\Sigma_1(y)=-2\mathrm{L}_1(y), \tag{B.10a}$$

$$\Sigma_2(y)=2\mathrm{I}_1(y)-y, \tag{B.10b}$$

with respectively L_1 and I_1 the modified Struve and Bessel functions of parameter 1. Finally

$$Q(y)=\Sigma_1(y)+\Sigma_2(y)=2[\mathrm{I}_1(y)-\mathrm{L}_1(y)]-y, \tag{B.11}$$

and the result from (40) is recovered.

References

[1] Bournazel C. Vertical buckling of buried pipes. Revue de l'Institut Francais du Pétrole 1982;37(1):113–22.
[2] Croll JGA. A simplified model of upheaval thermal buckling of subsea pipelines. Thin Wall Struct 1997;29:59–78.
[3] Fox C. An introduction to the calculus of variations. New York: Dover; 1987.
[4] Hobbs RE. Pipeline buckling caused by axial loads. J Constr Steel Res 1981;1(2):2–10.
[5] Hobbs RE. In-service buckling of heated pipelines. J Transp Eng 1984;110:175–89.
[6] Hunt GW, Blackmore A. Principles of localized buckling for a strut on an elastoplastic foundation. J Appl Mech 1996;63(1):234–9.
[7] Hunt GW, Wadee MK. Comparative lagrangian formulations for localized buckling. Proc R Soc Lond A Math Phys Eng Sci 1991;434:485–502.
[8] Ju GT, Kyriakides S. Thermal buckling of offshore pipelines. J Offshore Mech Arctic Eng 1988;110:355–64.
[9] Kerr AD. On the stability of the railroad track in the vertical plane. Rail Int 1974;5:131–42.
[10] Kerr AD. Analysis of thermal track buckling in the lateral plane. Acta Mech 1978;30:17–50.
[11] Klever FJ, Van Helvoirt LC, Sluyterman AC. A dedicated finite-element model for analyzing buckling response of submarine pipelines. In: Proceedings from the offshore technology conference, Houston; 1990. 6333-MS.
[12] Leroy JM, Putot CJM. Behavior of buried flexible pipelines. In: Proceedings from the offshore mechanics and arctic engineering conference, Calgary; 1992.
[13] Maltby TC, Calladine CR. An investigation into upheaval buckling of buried pipelines: experimental apparatus and some observations. Int J Mech Sci 1995;37:943–63.
[14] Maltby TC, Calladine CR. An investigation into upheaval buckling of buried pipelines: theory and analysis of experimental observations. Int J Mech Sci 1995;37:965–83.
[15] Palmer AC, White DJ, Baumgard AJ, Bolton MD, Barefoot AJ, Finch M, Powell T, Faranski AS, Baldry JAS. Uplift resistance of buried submarine pipelines:

comparison between centrifuge modeling and full-scale tests. Geotechnique 2003;53(10):877–83.
[16] Potier-Ferry M. Foundations of elastic postbuckling theory. In: Lecture notes in physics, Buckling and post-buckling, vol. 288; 1987. p. 1–82.
[17] Schaminee PEL, Zorn NF, Schotman GJM. Soil response for pipeline upheaval buckling analyses: full-scale laboratory tests and modelling. In: Proceedings from the offshore technology conference, Houston; 1990. 6486-MS.
[18] Trautmann CH, O'Rourke TD, Kulhawy FH. Lateral force–displacement response of buried pipe. J Geotech Eng 1985;111(9):1077–92.
[19] Trautmann CH, O'Rourke TD, Kulhawy FH. Uplift force–displacement response of buried pipe. J Geotech Eng 1985;111(9):1061–76.
[20] Tveergard V, Needleman A. On the localization of buckling patterns. J Appl Mech 1981;47(3):613–9.
[21] Tveergard V, Needleman A. On localized thermal track buckling. Int J Mech Sci 1981;23:577–87.
[22] Wadee MA. Effects of periodic and localized imperfections on struts on nonlinear foundations and compression sandwich panels. Int J Solids Struct 2000;37:1191–209.
[23] Wadee MK, Hunt GW, Whiting AIM. Asymptotic and Rayleigh–Ritz routes to localized buckling solutions in an elastic instability problem. Proc R Soc Lond A Math Phys Eng Sci 1997;453:2085–107.
[24] Whiting AIM. A Galerkin procedure for localized buckling of a strut on a nonlinear elastic foundation. Int J Solids Struct 1997;34:727–39.
[25] Yun H, Kyriakides S. Model for beam-mode buckling of buried pipelines. J Eng Mech 1985;111(2):235–53.

B. PLISSEMENT D'UN FILM MINCE ATTACHÉ À UN SUBSTRAT NON-PLAN

Dans cette annexe, la publication parue dans la revue *Nature Materials*, sous le titre "Curvature-induced symmetry breaking selects elastic surface patterns" est reproduite.

nature materials

ARTICLES

PUBLISHED ONLINE: 2 FEBRUARY 2015 | DOI: 10.1038/NMAT4202

Curvature-induced symmetry breaking determines elastic surface patterns

Norbert Stoop[1], Romain Lagrange[1], Denis Terwagne[2†], Pedro M. Reis[2,3] and Jörn Dunkel[1*]

Symmetry-breaking transitions associated with the buckling and folding of curved multilayered surfaces—which are common to a wide range of systems and processes such as embryogenesis, tissue differentiation and structure formation in heterogeneous thin films or on planetary surfaces—have been characterized experimentally. Yet owing to the nonlinearity of the underlying stretching and bending forces, the transitions cannot be reliably predicted by current theoretical models. Here, we report a generalized Swift–Hohenberg theory that describes wrinkling morphology and pattern selection in curved elastic bilayer materials. By testing the theory against experiments on spherically shaped surfaces, we find quantitative agreement with analytical predictions for the critical curves separating labyrinth, hybrid and hexagonal phases. Furthermore, a comparison to earlier experiments suggests that the theory is universally applicable to macroscopic and microscopic systems. Our approach builds on general differential-geometry principles and can thus be extended to arbitrarily shaped surfaces.

Symmetry breaking and structure formation are intrinsically linked. Symmetry-breaking transitions encompass a diverse range of phenomena, from the emergence of large-scale cosmological structures[1] or the formation of sand dunes[2] to crystallization of solids[3] and the development of form and function in living organisms[4,5]. Theoretical analysis of symmetry breaking typically builds on effective nonlinear field equations that describe complex many-particle systems[6] by a few macroscopic field variables. This approach has proved fruitful in identifying generic aspects of structure formation, as exemplified by the Ginzburg–Landau theory of phase transitions[7] and Turing's description of reaction–diffusion patterns[8,9]. Generally, however, it is challenging to derive nonlinear field theories systematically[10–13] from the underlying microscopic dynamics. Instead, effective field equations are often inferred from abstract symmetry considerations and bifurcation theory[14], resulting in a large number of undetermined parameters that limit the predictive power and complicate comparison with experimental data. Here, we systematically derive and experimentally test an effective field theory that predicts quantitatively the surface-pattern selection in curved bilayer systems consisting of a stiff film on a soft substrate (Figs 1 and 2).

Buckling of thin films plays a prominent role in the morphogenesis of multilayered soft tissues, governing the wrinkling of skin[15], fingerprint formation[16] and the development of brain convolutions[17]. In addition to their biological relevance, wrinkling processes under curvature constraints are attracting considerable interest as promising techniques for nanoscale surface patterning[18], microlens array fabrication[19] and adaptive aerodynamic drag control[20]. Recent experiments and simulations suggest that wrinkling patterns may vary strongly with applied stress[21–25] and substrate curvature[20,26–30]. However, so far, the complexity of the numerically implemented tensor equations has prevented a detailed analytical understanding. Despite substantial progress in the theoretical description of planar bilayer membranes[31,32], it is unclear how curvature controls pattern selection in non-planar geometries.

The scalar field theory presented below solves this longstanding problem by providing detailed quantitative predictions for curvature- and stress-induced pattern-formation transitions. Starting from Koiter's shell theory[33], we derive a generalized fourth-order Swift–Hohenberg (GSH) equation for the normal displacement field of a film bound to an arbitrarily curved surface (Supplementary Information). In the case of a spherical geometry, our GSH theory reveals that curvature triggers a transition from labyrinth-like to hexagonal wrinkling patterns through a curvature-induced symmetry breaking in the field equation. The theory further predicts a coexistence region separating two 'pure' phases (Fig. 1a–c). Both the theoretically predicted surface patterns and the analytically predicted phase diagram agree quantitatively with data from our macroscale experiments (Figs 1d–f and 3). The GSH model implies that analogous transitions occur when the compressive stress in the film is increased. This prediction is in agreement with recent microscale experiments[28,34] (Fig. 1g–i), suggesting that the theory is universally applicable to both microscopic and macroscopic systems. As our derivation of the GSH model builds on general differential-geometric principles, it can be extended to arbitrarily shaped surfaces, thus providing a generic framework for future studies of curvature-controlled wrinkling in physical, biological and chemical systems.

Theory of thin-film deformation on soft substrates

Our derivation starts from the covariant Koiter shell equations[33], obtained from three-dimensional elasticity theory through an expansion in the film thickness $h \to 0$ (Fig. 2). Koiter's model expresses the elastic energy of a freestanding curved shell in terms of deformations of its central surface (Supplementary Information). Although the Koiter equations have been successfully used in

[1]Department of Mathematics, Massachusetts Institute of Technology, 77 Massachusetts Avenue, Cambridge, Massachusetts 02139-4307, USA. [2]Department of Civil & Environmental Engineering, Massachusetts Institute of Technology, 77 Massachusetts Avenue, Cambridge, Massachusetts 02139-4307, USA. [3]Department of Mechanical Engineering, Massachusetts Institute of Technology, 77 Massachusetts Avenue, Cambridge, Massachusetts 02139-1713, USA. †Present address: Faculté des Sciences, Université Libre de Bruxelles (ULB), Bruxelles 1050, Belgium. *e-mail: dunkel@mit.edu

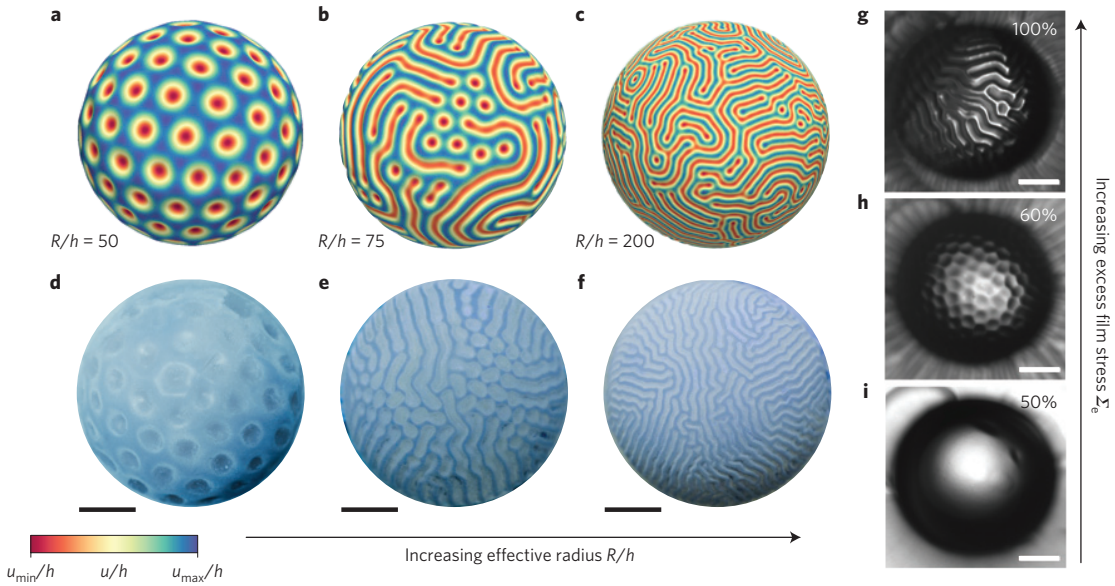

Figure 1 | Macroscopic and microscopic wrinkling morphologies of stiff thin films on spherically curved soft substrates. a–c, Theoretical predictions based on numerical steady-state solutions of equation (1). Colour red (blue) signals inward (outward) wrinkles. Simulation parameters: (**a**) $\gamma_0 = -0.029$, $a = 0.00162$, $c = 0.0025$; (**b**) $\gamma_0 = -0.04$, $a = -1.26 \times 10^{-6}$, $c = 0.002$; (**c**) $\gamma_0 = -0.02$, $a = 1.49 \times 10^{-4}$, $c = 0.0025$ (see Table 1). **d–f**, Experimentally observed patterns confirm the transition from hexagonal (**d**) to labyrinth-like wrinkles (**f**) via a bistable region (**e**) when the radius-to-thickness ratio R/h (see Fig. 2) is increased. Scale bars, 10 mm. Parameters: $E_f = 2{,}100$ kPa, $R = 20$ mm, $\nu = 0.5$ and (**d**) $E_s = 230$ kPa, $h = 0.630$ mm; (**e**) $E_s = 29$ kPa, $h = 0.14$ mm; (**f**) $E_s = 63$ kPa, $h = 0.10$ mm. **g–i**, Oxide layers on microscopic PDMS hemispheres exhibit a similar transition from hexagonal to labyrinth patterns when the excess film stress is increased through changes in the ambient ethanol concentration (indicated in per cent). Scale bars, 250 μm. Micrographs courtesy of D. Breid and A. Crosby[28].

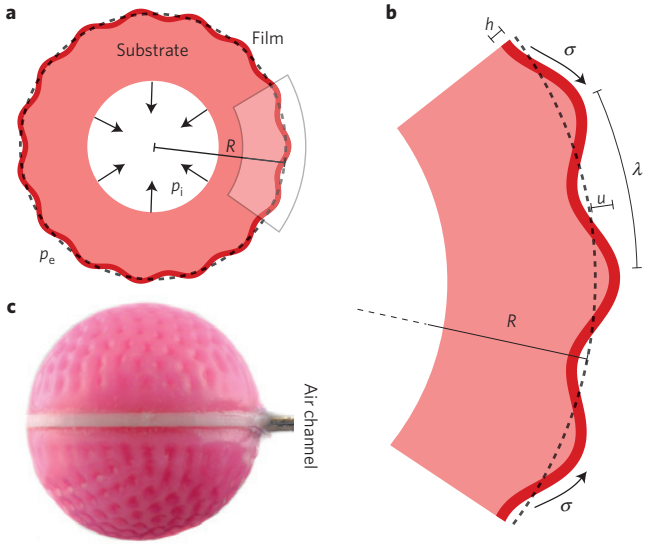

Figure 2 | Notation and experimental system. a, Schematic of a curved thin film adhering to a soft spherical substrate of outer radius R. **b**, The film (thickness h) is driven towards a wrinkling instability by the compressive film stress σ, leading to a wrinkling pattern with wavelength λ and radial displacement u. **c**, The experimental system consists of two merged hemispherical caps. An air channel allows one to tune the film stress σ through the pressure difference $\Delta p = p_e - p_i$.

computational wrinkling studies[26,27], their nonlinear tensorial structure offers limited insight beyond linear stability analysis. We found, however, that substantial analytical simplifications are possible when a stiff film (Young modulus E_f) is adhered to a soft substrate with Young modulus $E_s \ll E_f$.

As relevant to our experiments, which are described in detail below, we consider a spherical geometry with radius $R/h \gg 1$ and assume that film and substrate have the same Poisson ratio ν. The generalization to non-spherical surfaces is obtained by replacing the metric tensor appropriately (Supplementary Information). Continuity across the film–substrate interface favours deformations that are dominated by the radial displacement u (Fig. 2; from here onwards all lengths are normalized by h). Neglecting secondary lateral displacements, one can systematically expand the strain energy, which contains the original Koiter shell energy density as well as additional substrate coupling and overstress contributions, in terms of the covariant surface derivative ∇u and powers of u (Supplementary Information). Functional variation of the elastic energy with respect to u then yields a nonlinear partial differential equation for the wrinkled equilibrium state of the film. Assuming overdamped relaxation dynamics, one thus obtains the following GSH equation (Supplementary Information)

$$\partial_t u = \gamma_0 \Delta u - \gamma_2 \Delta^2 u - a u - b u^2 - c u^3 + \Gamma_1 \left[(\nabla u)^2 + 2u \Delta u \right] + \Gamma_2 \left[u (\nabla u)^2 + u^2 \Delta u \right] \qquad (1)$$

Here, Δ denotes the Laplace–Beltrami operator, involving the surface metric tensor of the sphere and Christoffel symbols of the second kind, and Δ^2 is the surface biharmonic operator[35]. The (γ_0, γ_2) terms describe stress and bending, the (a, b, c) terms comprise local film–substrate interactions and stretching contributions, and the (Γ_1, Γ_2) terms account for higher-order stretching forces. For $\Gamma_1 = \Gamma_2 = 0$, equation (1) reduces to the standard Swift–Hohenberg equation, as originally derived in the context of Rayleigh–Bénard convection[10,36]. The additional (Γ_1, Γ_2) terms will prove crucial below when matching theory and experiments. The generalization of equation (1) for arbitrary surfaces is given in Supplementary Equation (34).

The detailed derivation (Supplementary Information), combined with systematic asymptotic analysis of the planar limit $R/h \to \infty$, allows us to express the coefficients in equation (1) in terms of the standard material parameters: Poisson ratio of the film ν,

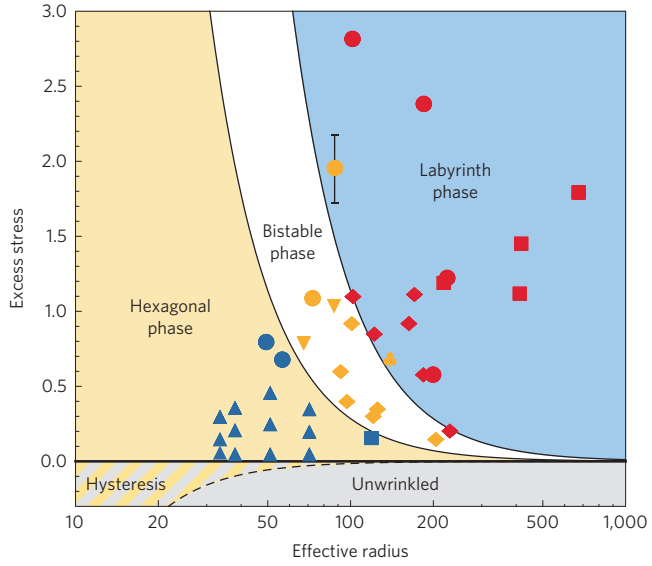

Figure 3 | Phase diagram of wrinkling morphologies. Experimental data points for hexagonal (blue), bistable (yellow) and labyrinth (red) patterns are shown for different values of curvature radius $R/h=\kappa^{-1}$ and excess film stress Σ_e. Symbols indicate the elastic moduli ratio $\eta=3E_s/E_f$ (square, $\eta=0.019$; circle, $\eta=0.036$; clubsuit, $\eta=0.041$; downtriangle, $\eta=0.055$; diamond, $\eta=0.09$; triangle, $\eta=0.328$). The data suggest that phase boundaries are independent of η in the experimentally tested range. Only the largest vertical error bars are shown (standard deviation of 12 amplitude measurements; see Methods). Horizontal error bars are smaller than the symbol size. Solid lines are theoretically predicted phase boundaries, obtained from equation (3) with parameter $c_1=0.0188$ (Table 1).

effective curvature $\kappa=h/R$, Young ratio $\eta=3E_s/E_f$, and excess stress $\Sigma_e=(\sigma/\sigma_c)-1$ (Table 1). The theory contains only a single fitting parameter, c_1, related to the cubic stretching force term cu^3. Equation (1) predicts that the unbuckled solution $u=0$ is stable for negative excess stresses $\Sigma_e<0$, whereas wrinkling occurs for $\Sigma_e\geq 0$. Linear stability analysis at $\Sigma_e=0$ and $\kappa=0$ reproduces the classical[37] pattern-wavelength relation for planar wrinkling, $\lambda/h=2\pi\eta^{-1/3}$ (Supplementary Information).

Numerical simulation of equation (1) is non-trivial owing to the metric dependence of the biharmonic operator Δ^2 (ref. 35). To compute the stationary wrinkling patterns (Fig. 1a–c) predicted by equation (1), we implemented a $\mathcal{C}^1$-continuous finite-element algorithm specifically designed for covariant fourth-order problems (Methods). A main benefit of equation (1), however, is that it enables analytical prediction of the various pattern-formation regimes.

Pattern selection

Pattern selection in the wrinkling regime $\Sigma_e\geq 0$ is a nonlinear process and, therefore, cannot be inferred from linear stability analysis. Numerical parameter scans of equation (1) yield a variety of qualitatively different stationary states that can be classified as representatives of a hexagonal phase (Fig. 1a), labyrinth phase (Fig. 1c) or intermediate coexistence phase (Fig. 1b). Qualitatively, the transition from hexagons to labyrinths can be understood through a symmetry argument: the (b,Γ_1) terms in equation (1) break the radial reflection invariance of its solutions under the transformation $u\rightarrow -u$, as also evident from the corresponding energy functional that is given in Supplementary Equation (37). As b and Γ_1 are controlled by $\kappa=h/R$ (Table 1), we expect a curvature-induced symmetry-breaking transition at some critical value of κ. Furthermore, recalling that the inclusion of similar symmetry-breaking terms causes a transition from labyrinths to hexagonal patterns in the classical Swift–Hohenberg model[36], it is plausible to expect a hexagonal phase at large curvatures κ and labyrinths at smaller values of κ in our system.

Table 1 | List of parameters for equation (1) in units $h=1$, with $\eta=3E_s/E_f$, $\gamma_2=1/12$, $\Sigma_e=(\sigma/\sigma_c)-1$ and $\kappa=h/R$.

$$\gamma_0=-\frac{\eta^{2/3}}{6}-\left[\frac{2(1+\nu)}{\eta^{2/3}}-\frac{1}{3}\right]\kappa^2$$

$$a=\frac{\eta^{4/3}}{12}+\frac{6(1+\nu)-\eta^{2/3}}{3}\kappa^2+\tilde{a}_2\Sigma_e$$

$$b=3(1+\nu)\kappa^3$$

$$c=\frac{2(1+\nu)\eta^{2/3}}{3}c_1$$

$$\Gamma_1=\frac{1+\nu}{2}\kappa$$

$$\Gamma_2=\frac{1+\nu}{2}\kappa^2$$

$$\tilde{a}_2=-\frac{\eta^{4/3}(c+3|\gamma_0|\Gamma_2)}{48\gamma_0^2}$$

The only remaining fitting parameter of the model is c_1.

To obtain a quantitative prediction for the phase boundaries, we approximate equation (1) through a standard Swift–Hohenberg equation and make use of established results from nonlinear stability analysis[38]. Assuming plane-wave solutions with amplitude $\mathcal{A}$ and wavevector k, the Γ_1 term exerts an average force $\Gamma_1\langle(\nabla u)^2+2u\Delta u\rangle_\lambda=-\Gamma_1\mathcal{A}^2k^2/2$ per wavelength λ. One may therefore approximate the Γ_1 term by an effective quadratic force $-\Gamma_1k^2u^2$, and similarly the Γ_2 term by an effective cubic force $\Gamma_2k^2u^3/2$ (Supplementary Information). Inserting for k the most unstable mode, $k_*=\sqrt{|\gamma_0|/(2\gamma_2)}$, equation (1) can be approximated by the standard Swift–Hohenberg equation

$$\partial_t\phi=-2\Delta\phi-\Delta^2\phi-A\phi-B\phi^2-\phi^3 \qquad (2)$$

where $\phi=u/u_*$, $u_*=|\gamma_0|/\sqrt{(c/3)+\Gamma_2|\gamma_0|}$, $A=3a/\gamma_0^2$, and $B=u_*\left[(b/3)+2|\gamma_0|\Gamma_1\right]/\gamma_0^2$. Nonlinear stability analysis of equation (2) yields the critical phase transition curves as functions of A and B (ref. 38). Note that the coefficients in equation (2) can be directly traced back to geometric and material parameters, whereas in many other pattern formation processes Swift–Hohenberg-type equations have been applied only in a purely phenomenological manner[6]. In terms of the original system parameters, one finds the stability criteria (Supplementary Information)

$$\begin{aligned}&\text{Hexagonal phase:} && -\kappa^2/(20c_1^2)<\Sigma_e<\kappa^2/c_1^2\\ &\text{Bistable phase:} && \kappa^2/c_1^2<\Sigma_e<4\kappa^2/c_1^2\\ &\text{Labyrinth phase:} && 4\kappa^2/c_1^2<\Sigma_e\end{aligned} \qquad (3)$$

where the parameter c_1 sets the strength of the cubic stretching force (Table 1). In the bistable coexistence phase, both hexagon and labyrinth solutions are stable, suggesting a strong dependence on initial conditions in this regime (Fig. 4).

Equation (3) confirms our qualitative symmetry argument and implies, moreover, that the pattern-formation transitions can be controlled not only by curvature, but also through the excess film stress Σ_e, in agreement with recent experimental results[28] (Fig. 1g–i).

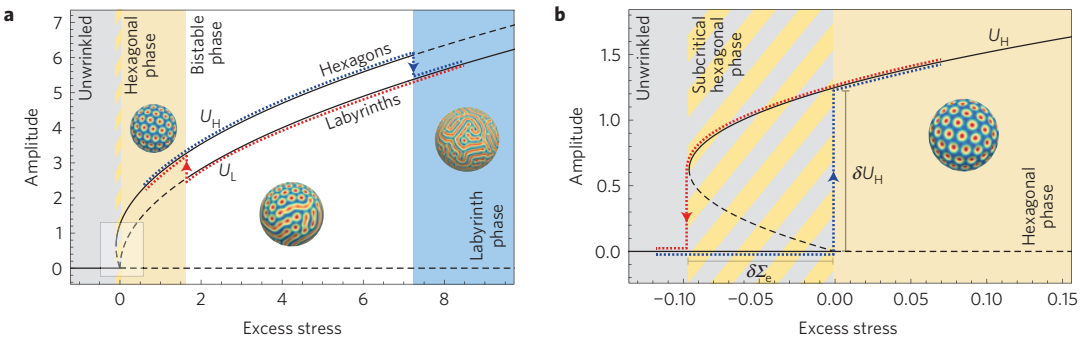

Figure 4 | Bifurcation diagram of wrinkling patterns. Stability analysis of equation (2) predicts two hysteresis cycles, shown here for $R/h = 40$. Solid (dashed) lines correspond to stable (unstable) amplitude solutions; see equation (4) and Supplementary Information. **a**, The hysteresis path across the bistable phase is realized by first decreasing (red) and subsequently increasing (blue) the excess stress Σ_e. **b**, Enlarged view of the second curvature-dependent hysteresis cycle near $\Sigma_e = 0$, corresponding to the highlighted region in **a**. Starting from a stable unwrinkled solution at $\Sigma_e < 0$, the system switches to a hexagonal state at $\Sigma_e = 0$ (blue path). When decreasing the excess stress again to negative values (red), the hexagons remain stable in the subcritical region until a critical value $\Sigma_e = -\delta\Sigma_e$ is reached. The width $\delta\Sigma_e$ and height δU_H of this hysteresis loop depend on curvature $\kappa = h/R$; see equation (4).

Comparison with experiments

We test the theoretical predictions, obtained from equations (1)–(3), by studying the wrinkling of centimetre-sized polydimethylsiloxane (PDMS)-coated elastomer hemispheres (Methods). In our experiments, wrinkling is controlled by the swelling of the film during fabrication and by manual depressurization after fabrication (Fig. 2a,c). The displacement field u, from which the excess film stress Σ_e can be estimated through amplitude measurements[32], is obtained from three-dimensional (3D) surface scans (Methods).

The experimental data confirm quantitatively the theoretically predicted curvature-induced phase transitions from hexagons to labyrinths (Figs 1 and 3). At high values of curvature $\kappa = h/R$, we find the hexagonal phase, characterized by localized spherical depressions that are typically surrounded by 6 neighbours (Fig. 1a,d), although occasional topological defects with 5 or 7 neighbours exist as required by Euler's polyhedral theorem[39]. As predicted by equation (1), experimentally observed hexagons always buckle inwards. For intermediate values of κ, the experiments further confirm coexisting domains of hexagonal and labyrinth-like patterns (Fig. 1b,e). In our simulations of equation (1), we find that the energy of such hybrid patterns remains constant asymptotically, suggesting that they are not transient but correspond to local energy minima. When the curvature is decreased, $\kappa \to 0$, at constant stress Σ_e, the experimental system transitions into the labyrinth phase (Fig. 1c,f), characterized by a network of connected ridges and extended but disconnected valleys (Fig. 1f). Equation (1) shows that this ridge–valley asymmetry is due to the small but non-vanishing symmetry-breaking effect of curvature.

Moreover, in agreement with previous microscale experiments[28] (Fig. 1g–i), equations (1) and (3) imply that the phase transition from hexagons to labyrinths can also be triggered by increasing the excess film stress $\Sigma_e = (\sigma/\sigma_c) - 1$ at constant surface curvature. The morphological phase diagram constructed from our macroscale data confirms this prediction (Fig. 3). In particular, by fixing just a single fitting parameter $c_1 = 0.0188 \pm 0.0002$, the analytical results for the two critical curves in equation (3) are in good quantitative agreement with the experimental data for a wide range of Young modulus ratios $\eta = 3E_s/E_f$ (Fig. 3). Strikingly, we find that the phase boundaries are independent of η over the range $0.019 < \eta < 0.328$ realized in our experiments, suggesting that the parameter c_1 may be a universal numerical constant independent of material properties.

Predictions for future experiments

The good agreement between theory and available experimental data encourages additional predictions that ought to be tested in future experiments. The nonlinear stability analysis of equation (2) suggests that, for sufficiently small overstress Σ_e, the hexagonal phase continues to exist even for weakly curved substrates[32] with $\kappa \ll 1$ (Fig. 3). Simulations of equation (1) for time-varying overstress $\Sigma_e(t)$ confirm that, owing to the presence of symmetry-breaking terms for $\kappa \neq 0$, hexagonal patterns always appear first after crossing the wrinkling threshold $\Sigma_e = 0$ from below. Once the hexagons have been formed, they remain stable throughout the bistable phase when the film stress is slowly increased. A similar reverse effect is observed when the film stress is slowly decreased in simulations that start from the labyrinth phase. In this case, the labyrinths persist throughout the bistable region. Equation (1) makes it possible to understand such memory effects analytically (Fig. 4).

Specifically, the above bifurcation analysis of equations (1)–(3) predicts two hysteresis cycles. The first cycle relates to the onset of wrinkling at $\Sigma_e = 0$ (Fig. 4b), whereas the second encompasses the bistable phase (Fig. 4a). The amplitude $U_H = \max u_H - \min u_H$ of the hexagonal solutions u_H grows according to a square-root law, shifted by the coefficient of the symmetry-breaking term in equation (2) (Supplementary Information),

$$U_H = \frac{3}{5}\left[Bu_* + \sqrt{(Bu_*)^2 + \frac{45\Sigma_e}{4}}\right] \tag{4}$$

where $Bu_* \simeq 3\kappa/(4c_1)$ to leading order in κ, with B and u_* as defined in equation (2). Equation (4) implies that, for $\kappa > 0$, the hexagonal phase is stable subcritically: on reducing the excess film stress from the hexagonal phase, hexagons remain stable even when the film stress is below the critical wrinkling stress σ_c (Fig. 4b). The width of the subcritical region, $\delta\Sigma_e = \kappa^2/(20c_1^2)$, and the amplitude at onset, $\delta U_H = U_H(\Sigma_e = 0) = 9\kappa/(10c_1)$, scale with κ. The bifurcation at $\Sigma_e = 0$ is transcritical, corresponding to a Lifshitz point[38]. Such bifurcations are typical of Swift–Hohenberg-type models, and have been predicted and observed in optics[40] and nonlinear biological and chemical systems[41]. For values of Σ_e in the subcritical hysteresis region, the hexagonal and the flat state are simultaneously stable in a narrow parameter range, potentially allowing for localized hexagonal patterns as found for the standard Swift–Hohenberg equation[42,43].

The detailed analysis of the second hysteresis cycle (Fig. 4a) shows that the amplitude U_L of the labyrinth solutions follows a square-root law (Supplementary Information). Starting from the labyrinth phase, the system remains in a labyrinth state when the film stress is lowered across the bistable region until one reaches the

instability threshold, located at $\Sigma_e \approx 1.75$ in the depicted example with $R/h = 40$ (red path in Fig. 4a). At that point, the system transitions into a hexagonal state. As Σ_e is increased again, the film maintains the hexagonal configuration until the stress exceeds the upper instability threshold $\Sigma_e \approx 7.5$ (blue path in Fig. 4a).

The direct verification of the two predicted hysteresis cycles poses a substantial experimental challenge, requiring high accuracy in the amplitude measurements and precise reversible tuning mechanisms for the excess film stress Σ_e. For instance, the large stress variations needed to trace out the hysteresis loops with a single sample cannot be realized with the present depressurization set-up[20]. Some preliminary experimental support for the hysteresis predictions comes from a recent study[32] of low-stress films, which pointed out the frequent appearance of hexagonal patterns when the excess stress is slowly varied from negative to positive values (see also Fig. 1g–i). These findings are consistent with the results of the above bifurcation analysis (Fig. 4a). We hope that our detailed theoretical predictions will stimulate further experimental work.

In closing, we showed that a systematically derived effective field theory provides a comprehensive quantitative description of surface-pattern formation in non-planar elastic media (see Supplementary Fig. 2 for additional examples with spatially varying curvature). The observation of similar pattern transitions in systems ranging from a few micrometres[26,28,34] to several centimetres[20,27], combined with the fact that curvature-induced pattern selection can now be understood in terms of a symmetry breaking in the effective field equations, suggests that such processes form common universality classes. The generic differential-geometric framework developed here enables a systematic classification of wrinkling phenomena in complex geometries, by examining the symmetry properties of effective higher-order differential operators built from the surface metric and film–substrate coupling forces. Moreover, equation (1) and its generalization to arbitrary shapes (Supplementary Information) provide a basis for studying weakly time-dependent phenomena such as the nucleation of wrinkling patterns under adiabatic (slow) increase of stress. Thus, in practice, the above analytical approach can help us to predict and control wrinkling processes under natural conditions, promising improved microfabrication techniques and, perhaps, even a better understanding of tissue mechanics and developmental morphogenesis.

Methods

Algorithm. The fourth-order covariant derivatives in the metric-dependent biharmonic operator Δ^2 make it challenging to solve equation (1) numerically. We simulate equation (1) by employing an extension of the finite-element scheme, based on subdivision surface basis functions. Previous studies[44,45] show that this method yields high accuracy and excellent performance for related problems in nonlinear elasticity. The underlying algorithm ensures the C^1-continuity of the basis functions, as required for the numerical integration of fourth-order equations. The method also allows for a direct computation of the various covariant derivatives. As in standard finite-element algorithms, we discretize the spherical surface with a mesh consisting of up to 50,000 triangular elements. A solution coefficient u_i is assigned to each of the $i=1,\ldots,N$ triangle vertices, such that the system state is interpolated by $u(\mathbf{r}) = \sum_{i=1}^{N} u_i N_i(\mathbf{r})$, where the N_i terms are the finite-element basis functions. For each time step $[t, t+\Delta t]$, we solve the weak form of equation (1) as a sum over individual element-wise contributions. Starting from random initial conditions with $\|u_i\|^2 < 1-a$, we integrate the dynamics of the system in time using a standard explicit Euler scheme, to obtain the system state $\{u_i\}$ at time $t+\Delta t$. We determine steady-state solutions by continuously monitoring the associated free energy. We consider the system to be in a steady state if its relative change remains below 10^{-5} for more than 10,000 successive time steps.

Experiments. Hemispherical samples were fabricated using rapid digital prototyping techniques that allow flexibility in the choice of geometrical and material parameters[20]. Samples were casted and coated using silicone-based elastomers, such as PDMS (Sylgard 184, Dow Corning), Ecoflex (Smooth-on) and vinylpolysiloxane (VPS, Zhermack), allowing us to examine a wide range of elastic moduli for film (E_f) and substrate (E_s), spanning $9 \le E_f/E_s \le 162$. Typical sample parameters are: outer radius $R = 20$ mm, radius of the inner cavity 9 mm, and film thickness $20\,\mu\text{m} \le h \le 1{,}000\,\mu\text{m}$. The inner cavity of the samples was depressurized to create a state of homogeneous compression and to trigger wrinkling of the stiff surface film. Surface profiles were measured using a NextEngine 3D Laser scanner. The excess film stress Σ_e was estimated from the pattern amplitude $\mathcal{A}$ determined in the 3D surface scans, using the established amplitude versus stress relations $\mathcal{A} = k\sqrt{\Sigma_e}$ from classical wrinkling theory[32], with $k=1$ for labyrinths and $k = 2/\sqrt{11+6\nu-5\nu^2}$ for hexagonal patterns.

Received 17 August 2014; accepted 19 December 2014; published online 2 February 2015

References

1. Bond, J. R., Kofman, L. & Pogosyan, D. How filaments of galaxies are woven into the cosmic web. *Nature* **380,** 603–606 (1996).
2. Parteli, E., Durán, O., Tsoar, H., Schwämmle, V. & Herrmann, H. J. Dune formation under bimodal winds. *Proc. Natl Acad. Sci. USA* **106,** 22085–22089 (2009).
3. Onuki, A. *Phase Transition Dynamics* (Cambridge Univ. Press, 2002).
4. Palmer, A. R. Symmetry breaking and the evolution of development. *Science* **306,** 828–833 (2004).
5. Chirat, R., Moulton, D. E. & Goriely, A. Mechanical basis of morphogenesis and convergent evolution of spiny seashells. *Proc. Natl Acad. Sci. USA* **110,** 6015–6020 (2013).
6. Aranson, I. S. & Tsimring, L. S. Patterns and collective behavior in granular media: Theoretical concepts. *Rev. Mod. Phys.* **78,** 641–692 (2006).
7. Ginzburg, V. L. & Landau, L. D. On the theory of superconductivity. *Zh. Eksp. Teor. Fiz.* **20,** 1064–1082 (1950).
8. Turing, A. M. The chemical basis of morphogenesis. *Phil. Trans. R. Soc. Lond. B* **237,** 37–72 (1952).
9. Ouyang, Q. & Swinney, H. L. Transition from a uniform state to hexagonal and striped Turing patterns. *Nature* **352,** 610–612 (1991).
10. Swift, J. & Hohenberg, P. C. Hydrodynamic fluctuations at the convective instability. *Phys. Rev. A* **15,** 319–328 (1977).
11. Paczuski, M., Kardar, M. & Nelson, D. R. Landau theory of the crumpling transition. *Phys. Rev. Lett.* **60,** 2638–2640 (1988).
12. Delprato, A. M., Samadani, A., Kudrolli, A. & Tsimring, L. S. Swarming ring patterns in bacterial colonies exposed to ultraviolet radiation. *Phys. Rev. Lett.* **87,** 158102 (2001).
13. Brenner, M. P. Chemotactic patterns without chemotaxis. *Proc. Natl Acad. Sci. USA* **107,** 11653–11654 (2010).
14. Wiggins, S. & Golubitsky, M. *Introduction to Applied Nonlinear Dynamical Systems and Chaos* Vol. 2 (Springer-Verlag, 1990).
15. Cerda, E. & Mahadevan, L. Geometry and physics of wrinkling. *Phys. Rev. Lett.* **90,** 074302 (2003).
16. Efimenko, K. *et al.* Nested self-similar wrinkling patterns in skins. *Nature Mater.* **4,** 293–297 (2005).
17. Richman, D. P., Stewart, R. M., Hutchinson, J. W. & Caviness, V. S. Mechanical model of brain convolutional development. *Science* **189,** 18–21 (1975).
18. Bowden, N., Brittain, S., Evans, A. G., Hutchinson, J. W. & Whitesides, G. M. Spontaneous formation of ordered structures in thin films of metals supported on an elastomeric polymer. *Nature* **393,** 146–149 (1998).
19. Chan, E. P. & Crosby, A. J. Fabricating microlens arrays by surface wrinkling. *Adv. Mater.* **18,** 3238–3242 (2006).
20. Terwagne, D., Brojan, M. & Reis, P. M. Smart morphable surfaces for aerodynamic drag control. *Adv. Mater.* **26,** 6608–6611 (2014).
21. Jiang, H. *et al.* Finite deformation mechanics in buckled thin films on compliant supports. *Proc. Natl Acad. Sci. USA* **104,** 15607–15612 (2007).
22. Pocivavsek, L. *et al.* Stress and fold localization in thin elastic membranes. *Science* **320,** 912–916 (2008).
23. Brau, F. *et al.* Multiple-length-scale elastic instability mimics parametric resonance of nonlinear oscillators. *Nature Phys.* **7,** 56–60 (2011).
24. Xu, F., Potier-Ferry, M., Belouettar, S. & Cong, Y. 3d finite element modeling for instabilities in thin films on soft substrates. *Int. J. Solids Struct.* **51,** 3619–3632 (2014).
25. Brau, F., Damman, P., Diamant, H. & Witten, T. A. Wrinkle to fold transition: Influence of the substrate response. *Soft Matter* **9,** 8177–8186 (2013).
26. Cao, G., Chen, X., Li, C., Ji, A. & Cao, Z. Self-assembled triangular and labyrinth buckling patterns of thin films on spherical substrates. *Phys. Rev. Lett.* **100,** 036102 (2008).
27. Li, B., Jia, F., Cao, Y-P., Feng, X-Q. & Gao, H. Surface wrinkling patterns on a core-shell soft sphere. *Phys. Rev. Lett.* **106,** 234301 (2011).
28. Breid, D. & Crosby, A. J. Curvature-controlled wrinkle morphologies. *Soft Matter* **9,** 3624–3630 (2013).
29. Schroll, R. D. *et al.* Capillary deformations of bendable films. *Phys. Rev. Lett.* **111,** 014301 (2013).

30. King, H., Schroll, R. D., Davidovitch, B. & Menon, N. Elastic sheet on a liquid drop reveals wrinkling and crumpling as distinct symmetry-breaking instabilities. *Proc. Natl Acad. Sci. USA* **109,** 9716–9720 (2012).
31. Audoly, B. & Boudaoud, A. Buckling of a thin film bound to a compliant substrate, part i: Formulation, linear stability of cylindrical patterns, secondary bifurcations. *J. Mech. Phys. Solids* **56,** 2401–2421 (2008).
32. Cai, S., Breid, D., Crosby, A. J., Suo, Z. & Hutchinson, J. W. Periodic patterns and energy states of buckled films on compliant substrates. *J. Mech. Phys. Solids* **59,** 1094–1114 (2011).
33. Ciarlet, P. G. *Mathematical Elasticity* Vol. 3 (North Holland, 2000).
34. Yin, J., Han, X., Cao, Y. & Lu, C. Surface wrinkling on polydimethylsiloxane microspheres via wet surface chemical oxidation. *Sci. Rep.* **4,** 5710 (2014).
35. Jost, J. *Riemannian Geometry and Geometric Analysis* (Springer, 2008).
36. Cross, M. C. & Hohenberg, P. C. Pattern formation outside of equilibrium. *Rev. Mod. Phys.* **65,** 851–1112 (1993).
37. Allen, H. G. *Analysis and Design of Structural Sandwich Panels* (Pergamon, 1969).
38. Golovin, A. A. & Nepomnyashchy, A. A. *Self-Assembly, Pattern Formation and Growth Phenomena in Nano-Systems* (Springer, 2006).
39. Coxeter, H. S. M. *Regular Polytopes* (Courier Dover Publications, 1973).
40. Clerc, M. G., Petrossian, A. & Residori, S. Bouncing localized structures in a liquid-crystal light-valve experiment. *Phys. Rev. E* **71,** 015205(R) (2005).
41. Kozyreff, G. & Tlidi, M. Nonvariational real Swift–Hohenberg equation for biological, chemical, and optical systems. *Chaos* **17,** 037103 (2007).
42. Lloyd, D. J. B., Sandstede, B., Avitabile, D. & Champneys, A. R. Localized hexagon patterns of the planar Swift–Hohenberg equation. *SIAM J. Appl. Dyn. Syst.* **7,** 1049–1100 (2008).
43. Burke, J. & Knobloch, E. Localized states in the generalized Swift–Hohenberg equation. *Phys. Rev. E* **73,** 056211 (2006).
44. Cirak, F., Ortiz, M. & Schröder, P. Subdivision surfaces: A new paradigm for thin-shell finite-element analysis. *Int. J. Numer. Methods Eng.* **47,** 2039–2072 (2000).
45. Stoop, N., Wittel, F. K., Amar, M. B., Müller, M. M. & Herrmann, H. J. Self-contact and instabilities in the anisotropic growth of elastic membranes. *Phys. Rev. Lett.* **105,** 068101 (2010).

Acknowledgements

This work was supported by the Swiss National Science Foundation grant No. 148743 (N.S.), by the National Science Foundation, CAREER CMMI-1351449 (P.M.R.) and by an MIT Solomon Buchsbaum Award (J.D.).

Author contributions

N.S., R.L. and J.D. developed the theory. N.S. and R.L. performed analytical calculations. N.S. implemented and performed the numerical simulations. D.T. and P.M.R. developed the experiments. N.S., R.L. and D.T. analysed data. All authors discussed the results and contributed to writing the paper.

Additional information

Supplementary information is available in the online version of the paper. Reprints and permissions information is available online at www.nature.com/reprints. Correspondence and requests for materials should be addressed to J.D.

Competing financial interests

The authors declare no competing financial interests.

nature materials

SUPPLEMENTARY INFORMATION

DOI: 10.1038/NMAT4202

Curvature-induced symmetry breaking determines elastic surface patterns

Norbert Stoop[1], Romain Lagrange[1], Denis Terwagne[2*], Pedro M. Reis[2,3], and Jörn Dunkel[1]

[1] *Department of Mathematics, Massachussetts Institute of Technology, 77 Massachusetts Avenue, Cambridge, MA 02139-4307, USA*

[2] *Department of Civil & Environmental Engineering, Massachussetts Institute of Technology, 77 Massachusetts Avenue, Cambridge, MA 02139-4307, USA*

[3] *Department of Mechanical Engineering, Massachussetts Institute of Technology, 77 Massachusetts Avenue, Cambridge, MA 02139-1713, USA*

(Dated: December 14, 2014)

We derive an effective theory for the wrinkling of thin hard films bound to arbitrarily curved soft substrates. Starting from the nonlinear Koiter shell equations, we show that the elastic equations can be reduced to a generalized Swift-Hohenberg theory, yielding Eq. (1) in the Main Text for the special case of a spherical surface geometry. Using nonlinear analysis of this effective fourth-order equation, we derive predictions for hexagonal and labyrinth-like wrinkling patterns in dependence on the film stress and the substrate curvature. To illustrate the effects of spatially varying substrate curvature on wrinkling, we present additional numerical results for a toroidal geometry.

DEFINITIONS

Let $\boldsymbol{S} = \boldsymbol{\Theta}(\theta_1, \theta_2)$ be a two-dimensional surface in $\mathbb{R}^3$, parameterized by $y = (\theta_1, \theta_2) \in \omega \subset \mathbb{R}^2$. Throughout, Greek indices $\alpha, \beta, \ldots$ take values in $\{1, 2\}$, whereas Latin indices $i, j, \ldots$ run from 1 to 3. The induced metric $a_{\alpha\beta}$ (first fundamental form) on the surface $\boldsymbol{S} = \boldsymbol{\Theta}(\theta_1, \theta_2)$ is given by

$$a_{\alpha\beta} = \boldsymbol{a}_\alpha \cdot \boldsymbol{a}_\beta = a_{\beta\alpha}, \tag{1}$$

where

$$\boldsymbol{a}_\alpha = \boldsymbol{\Theta}_{,\alpha} \equiv \partial_\alpha \boldsymbol{\Theta} \equiv \frac{\partial \boldsymbol{\Theta}}{\partial \theta_\alpha} \tag{2}$$

are the tangent vectors, and $\cdot$ denotes the Euclidean inner product on $\mathbb{R}^3$. The unit-length normal vector $\boldsymbol{n}$ is defined by

$$\boldsymbol{n} \equiv \boldsymbol{a}^3 = \frac{\boldsymbol{a}_1 \times \boldsymbol{a}_2}{|\boldsymbol{a}_1 \times \boldsymbol{a}_2|} \tag{3}$$

and characterized by the properties

$$\begin{aligned} \boldsymbol{n} \cdot \boldsymbol{n} &= 1, \qquad \boldsymbol{n} \cdot \boldsymbol{a}_\alpha = 0, \qquad \boldsymbol{n}_{,\alpha} \cdot \boldsymbol{n} = 0 \\ \boldsymbol{n}_{,\alpha} \cdot \boldsymbol{a}_\beta &= -\boldsymbol{a}_{\alpha,\beta} \cdot \boldsymbol{n}, \qquad \boldsymbol{n} \cdot \boldsymbol{n}_{,\alpha\beta} = -\boldsymbol{n}_{,\alpha} \cdot \boldsymbol{n}_{,\beta} \end{aligned}$$

The surface element is

$$d\omega = \sqrt{|\det(a_{\alpha\beta})|}\, dy \tag{4}$$

We also introduce the second and third fundamental forms $b_{\alpha\beta}$, $c_{\alpha\beta}$ with components given by

$$b_{\alpha\beta} = \boldsymbol{n} \cdot \boldsymbol{a}_{\alpha,\beta} \tag{5a}$$

$$c_{\alpha\beta} = \boldsymbol{n}_{,\alpha} \cdot \boldsymbol{n}_{,\beta} \tag{5b}$$

The second fundamental form, $b_{\alpha\beta}$, is often also referred to as the curvature tensor. The Christoffel symbols are

$$\Gamma^\sigma_{\alpha\beta} = \frac{1}{2} a^{\sigma\gamma} \left(a_{\gamma\alpha,\beta} + a_{\gamma\beta,\alpha} - a_{\alpha\beta,\delta} \right) \tag{6}$$

where $a^{\alpha\beta}$ are the components of the contravariant metric tensor, defined by $a^{\alpha\gamma} a_{\beta\gamma} = \delta^\alpha_\beta$. Introducing $\boldsymbol{a}^\alpha = a^{\alpha\beta} \boldsymbol{a}_\beta$, the following identities will be useful later:

$$\boldsymbol{n}_\alpha = -b_{\alpha\beta} \boldsymbol{a}^\beta = -b^\sigma_\alpha \boldsymbol{a}_\sigma \tag{7a}$$

$$b^\gamma_\alpha b_{\beta\gamma} = \boldsymbol{n}_{,\alpha} \cdot \boldsymbol{n}_{,\beta} = c_{\alpha\beta} \tag{7b}$$

The covariant derivative of a scalar function ψ is

$$\nabla_\alpha \psi = \psi_{,\alpha} \tag{8}$$

The gradient of ψ on the surface $\boldsymbol{S}$ has components

$$\nabla^\alpha \psi = a^{\alpha\beta} \nabla_\alpha \psi \tag{9}$$

The action of the Laplace-Beltrami operator $\triangle$ on scalar functions is defined as

$$\triangle \psi = \nabla_\alpha \nabla^\alpha \psi = a^{\gamma\delta} \psi_{,\gamma\delta} - a^{\gamma\delta} \Gamma^\lambda_{\gamma\delta} \psi_{,\lambda} \tag{10}$$

For a vector field V^α or for a $(0,1)-$tensor field V_α, the covariant derivative involves the Christoffel symbols,

$$\nabla_\alpha V^\beta = V^\beta_{,\alpha} + \Gamma^\alpha_{\beta\gamma} V^\gamma \tag{11a}$$

$$\nabla_\alpha V_\beta = V_{\beta,\alpha} - \Gamma^\gamma_{\alpha\beta} V_\gamma \tag{11b}$$

All gradients ∇ and Laplacians $\triangle$ below refer to these surface-specific differential operators.

*Current address: Faculté des Sciences, Université Libre de Bruxelles (ULB), Bruxelles 1050, Belgium

DOI: 10.1038/NMAT4202

ENERGY FUNCTIONAL

We extend the classical Koiter shell (KS) energy functional to account for film-substrate coupling and excess stresses.

Koiter shell equations

The KS equations describe the equilibrium of a thin shell (precurved plate) when the thickness h of the shell is small compared to its curvature in undeformed and deformed configurations. The KS equations follow rigorously by means of Γ-convergence from the full 3D elasticity problem in the limit $h \to 0$ [1].

In the absence of forces and boundary conditions, we assume that the shell adopts a stress-free equilibrium configuration which we call the reference configuration, parametrized by the surface map $\boldsymbol{\Theta}$, with fundamental forms $a_{\alpha\beta}, b_{\alpha\beta}$ etc. as specified above. Under the influence of forces and boundary conditions, the shell adopts a new, deformed configuration characterized by a displacement field $\boldsymbol{\Psi}$ defined with respect to the curved reference state $\boldsymbol{\Theta}$,

$$\boldsymbol{\Psi} = \Psi_1 \boldsymbol{a}^1 + \Psi_2 \boldsymbol{a}^2 + \Psi_3 \boldsymbol{a}^3 \equiv \Psi_i \boldsymbol{a}^i \tag{12}$$

For any point $y \in \omega$, its displaced position is given by $\boldsymbol{\Theta}(y) + \boldsymbol{\Psi}(y)$, and the respective surface geometry will be denoted as $a_{\alpha\beta}(\boldsymbol{\Psi}), b_{\alpha\beta}(\boldsymbol{\Psi})$ etc.

The KS energy of the shell is given by [1]

$$\mathcal{E}_{\mathrm{KS}}(\boldsymbol{\Psi}) = \mathcal{E}_b(\boldsymbol{\Psi}) + \mathcal{E}_s(\boldsymbol{\Psi}) + \mathcal{E}_f(\boldsymbol{\Psi}) \tag{13a}$$

with bending energy

$$\mathcal{E}_b = \frac{E_f}{2(1-\nu^2)} \int_\omega d\omega \, \frac{h^3}{24} C^{\alpha\beta\gamma\delta} R_{\gamma\delta}(\boldsymbol{\Psi}) R_{\alpha\beta}(\boldsymbol{\Psi}) \tag{13b}$$

stretching energy

$$\mathcal{E}_s = \frac{E_f}{2(1-\nu^2)} \int_\omega d\omega \, \frac{h}{2} C^{\alpha\beta\gamma\delta} G_{\gamma\delta}(\boldsymbol{\Psi}) G_{\alpha\beta}(\boldsymbol{\Psi}) \tag{13c}$$

and energy contributions

$$\mathcal{E}_f = -\int_\omega d\omega \, p^i \Psi_i \tag{13d}$$

due to external forces p^i (pressure, body loads, etc.). In Eqs. (13), E_f denotes the Young modulus of the film, ν its Poisson ratio and $C^{\alpha\beta\gamma\delta}$ the constitutive tensor. We focus on the case of a Kirchhoff-St. Venant material, corresponding to an extension of Hook's law to large deformations, described by

$$C^{\alpha\beta\gamma\delta} = (1-\nu)(a^{\alpha\delta}a^{\beta\gamma} + a^{\alpha\gamma}a^{\beta\delta}) + 2\nu a^{\alpha\beta}a^{\gamma\delta} \tag{14}$$

The nonlinear membrane bending and stretching strains $R_{\alpha\beta}$ and $G_{\alpha\beta}$ are given by [1]

$$R_{\alpha\beta} = b_{\alpha\beta}(\boldsymbol{\Psi}) - b_{\alpha\beta} \tag{15a}$$

$$G_{\alpha\beta} = \frac{1}{2}\left[a_{\alpha\beta}(\boldsymbol{\Psi}) - a_{\alpha\beta}\right] \tag{15b}$$

The bending energy scales with h^3 and will be small compared to the stretching contributions. We will therefore linearize $R_{\alpha\beta}(\boldsymbol{\Psi})$ in the bending energy, but keep higher-order terms in the stretching strains $G_{\alpha\beta}$.

Normal component of bending strains. The linearized bending strains read [1]

$$R_{\alpha\beta} \simeq (\boldsymbol{\Psi}_{,\alpha\beta} - \Gamma^\sigma_{\alpha\beta}\boldsymbol{\Psi}_{,\sigma}) \cdot \boldsymbol{n} \tag{16}$$

With this approximation, the normal displacement component Ψ_3 decouples from the in-plane components. Since the dominant bending contribution comes from the normal displacement Ψ_3, we may neglect the in-plane components

$$\begin{aligned} R_{\alpha\beta} &\simeq \rho_{\alpha\beta}(\Psi_3) \equiv \Psi_{3,\alpha\beta} - \Gamma^\sigma_{\alpha\beta}\Psi_{3,\sigma} - \Psi_3 c_{\alpha\beta} \\ &= \nabla_\alpha \nabla_\beta \Psi_3 - \Psi_3 c_{\alpha\beta} \end{aligned} \tag{17}$$

Normal component of stretching strains. For the stretching strains, one has [1]

$$\begin{aligned} G_{\alpha\beta} &= \frac{1}{2}\left(\nabla_\beta \Psi_\alpha + \nabla_\alpha \Psi_\beta + \boldsymbol{\Psi}_{,\alpha} \cdot \boldsymbol{\Psi}_{,\beta}\right) - b_{\alpha\beta}\Psi_3 \\ &= \frac{1}{2}(\Psi_{\alpha,\beta} + \Psi_{\beta,\alpha} + \boldsymbol{\Psi}_{,\alpha} \cdot \boldsymbol{\Psi}_{,\beta}) - \Gamma^\sigma_{\alpha\beta}\Psi_\sigma - b_{\alpha\beta}\Psi_3 \end{aligned} \tag{18}$$

The displacement derivative can be split into an in-plane and normal part,

$$\boldsymbol{\Psi}_{,\alpha} = (\Psi_{\gamma,\alpha} - \Gamma^\sigma_{\alpha\gamma}\Psi_\sigma - b_{\alpha\gamma}\Psi_3)\boldsymbol{a}^\gamma + (\Psi_{3,\alpha} + b^\gamma_\alpha \Psi_\gamma)\boldsymbol{a}^3$$

Due to the orthogonality of $\boldsymbol{a}^\alpha$ and $\boldsymbol{n} \equiv \boldsymbol{a}^3$, the nonlinear term in the stretching strains becomes

$$\boldsymbol{\Psi}_{,\alpha} \cdot \boldsymbol{\Psi}_{,\beta} = t^\delta_\alpha t_{\beta\delta} + s_\alpha s_\beta \tag{19a}$$

where

$$t_{\alpha\beta} = \Psi_{\beta,\alpha} - \Gamma^\sigma_{\alpha\beta}\Psi_\sigma - b_{\alpha\beta}\Psi_3 \tag{19b}$$

$$s_\alpha = \Psi_{3,\alpha} + b^\sigma_\alpha \Psi_\sigma \tag{19c}$$

Expanding Eqs. (19) for small in-plane displacements, $|\Psi_\alpha| \ll |\Psi_3|$, one finds to leading order

$$\boldsymbol{\Psi}_{,\alpha} \cdot \boldsymbol{\Psi}_{,\beta} \simeq \Psi_{3,\alpha}\Psi_{3,\beta} + b^\delta_\alpha b_{\beta\delta}(\Psi_3)^2$$

Using Eq. (7) and (18), we obtain

$$G_{\alpha\beta} \simeq \gamma_{\alpha\beta}(\Psi_3) \equiv \frac{1}{2}[\Psi_{3,\alpha}\Psi_{3,\beta} + c_{\alpha\beta}(\Psi_3)^2] - b_{\alpha\beta}\Psi_3 \tag{20}$$

We note that the obtained bending and stretching strains are symmetric,

$$\rho_{\alpha\beta} = \rho_{\beta\alpha}, \qquad \gamma_{\alpha\beta} = \gamma_{\beta\alpha} \tag{21}$$

Additional remarks. In our and previous [2] experiments, the film stress is imposed in two ways: (i) depressurization of the shell-substrate system and (ii) swelling of the film. Before the onset of the buckling transition, either technique creates a pre-stress in the film. The associated prestrain can be decomposed into an in-plane part $\bar{\gamma}_{\alpha\beta}$ and a bending part $\bar{\rho}_{\alpha\beta}$, with $\bar{\gamma}_{\alpha\beta} \gg \bar{\rho}_{\alpha\beta}$. Adopting the same approximations as above (Eqs. 17, 20), the prestrains remain symmetric. Restricting ourselves furthermore to equi-biaxial pre-stress without shear, $\bar{\gamma}_{\alpha\beta}$ is proportional to the metric tensor $a_{\alpha\beta}$, and we write this as

$$\bar{\gamma}_{\alpha\beta} = \bar{\gamma}\, a_{\alpha\beta} \tag{22}$$

where from now on $\bar{\gamma}$ denotes the constant of proportionality.

If the film stress due to depressurization or swelling becomes too large, the film will buckle, with an inhomogeneous deformation u around the pre-stressed state. The strains of a buckled configuration can then be expressed as

$$\gamma_{\alpha\beta}(u_0+u) = \bar{\gamma}_{\alpha\beta} + \frac{1}{2}\left(u_{,\alpha}u_{,\beta} - 2b_{\alpha\beta}u + c_{\alpha\beta}u^2\right) \tag{23a}$$

$$\rho_{\alpha\beta}(u_0+u) = \bar{\rho}_{\alpha\beta} + \nabla_\alpha\nabla_\beta u - c_{\alpha\beta}u \tag{23b}$$

To contract the strains with the constitutive tensor, we use the fact that the bending and stretching strains, Eqs. (23), are symmetric. For any symmetric $(0,2)$-tensor $\tau_{\alpha\beta}$, the contraction $\mathcal{C}(\tau)$ of $C^{\alpha\beta\gamma\delta}$ with $\tau_{\alpha\beta}$ can be written as

$$\begin{aligned}\mathcal{C}(\tau) &= C^{\alpha\beta\gamma\delta}\tau_{\alpha\beta}\tau_{\gamma\delta}\\ &= 2\left[(1-\nu)\tau^{\alpha\beta}\tau_{\alpha\beta} + \nu(\tau^\gamma_\gamma)^2\right]\\ &= 2\left(\tau_M + \tau_G\right)\end{aligned} \tag{24}$$

with

$$\begin{aligned}\tau_M &= (\tau^\gamma_\gamma)^2\\ \tau_G &= (1-\nu)\left[\tau^{\alpha\beta}\tau_{\alpha\beta} - (\tau^\gamma_\gamma)^2\right]\end{aligned} \tag{25}$$

For later use, it is convenient to introduce the identities

$$\mathcal{H} = \frac{1}{2}b^\gamma_\gamma \tag{26a}$$

$$\mathcal{K} = \det(\{a_{\alpha\beta}\})/\det(\{b_{\alpha\beta}\}) \tag{26b}$$

$$\mathcal{R} \equiv b^{\alpha\beta}b_{\alpha\beta} = c^\gamma_\gamma = 4\mathcal{H}^2 - 2\mathcal{K} \tag{26c}$$

$$\mathcal{S} \equiv b^{\alpha\beta}c_{\alpha\beta} = 2\mathcal{H}(4\mathcal{H}^2 - 3\mathcal{K}) \tag{26d}$$

$$\mathcal{T} \equiv c^{\alpha\beta}c_{\alpha\beta} = 16\mathcal{H}^2(\mathcal{H}^2 - \mathcal{K}) + 2\mathcal{K}^2 \tag{26e}$$

$\mathcal{H}$ is the mean curvature and $\mathcal{K}$ the Gaussian curvature. Most of these expressions follow directly from the contracted Gauss-Codazzi-Mainardi equations [3].

Relevant energy contributions

Bending energy density. Using the definition of the Laplace-Beltrami operator, Eq. (10), and Eq. (24) with $\tau_{\alpha\beta} = \rho_{\alpha\beta}$, the mean-curvature contribution ρ_M can be written as

$$\begin{aligned}\rho_M = \left(\rho^\gamma_\gamma\right)^2 = (\triangle u)^2 - 2\mathcal{R}u\triangle u + \mathcal{R}^2u^2 +\\ 2(\bar{\rho}^\gamma_\gamma\triangle u - \mathcal{R}\bar{\rho}^\gamma_\gamma u) + (\bar{\rho}^\gamma_\gamma)^2\end{aligned} \tag{27}$$

The ρ_G-term in Eq. (24) accounts for the energy cost due to a change of Gaussian curvature. This term is negligible if the typical wrinkling wavelengths are small compared to the local radii of curvature of the underlying surface. More precisely, in this case, one finds that Eqs. (15a,17) reduce to $\rho^\beta_\alpha \simeq b^\beta_\alpha(u)$ in leading order, where $b^\beta_\alpha(u)$ is the curvature tensor of the deformed configuration. Accordingly, Eq. (25) then yields $\rho_G = (1-\nu)\mathcal{K}(u)$. Since the Gaussian curvature $\mathcal{K}(u)$ of the deformed configuration integrates to a topological invariant for a closed surface (or when the geodesic curvature of the boundary curve is fixed), the ρ_G-term can be neglected in the variational formulation, just as in the classical Helfrich model [4]. Under these assumptions, the resulting bending energy takes the form

$$\begin{aligned}\mathcal{E}_b = \frac{E_f}{2(1-\nu^2)}\int_\omega d\omega\, \frac{h^3}{12}\left[(\triangle u)^2 + 2\mathcal{R}(\nabla u)^2 +\right.\\ (\mathcal{R}^2 - \triangle\mathcal{R})u^2 +\\ \left. 2\left(\triangle\bar{\rho}^\gamma_\gamma - \mathcal{R}\bar{\rho}^\gamma_\gamma\right)u + (\bar{\rho}^\gamma_\gamma)^2\right]\end{aligned} \tag{28}$$

where from now on the product symbol $\cdot$ as in $(\nabla u)^2 = (\nabla u)\cdot(\nabla u)$ denotes the scalar product with respect to the surface metric. To obtain Eq. (28), we used the generalized Stokes theorem[1] to rewrite the second and fourth term on the rhs. of Eq. (27).

Stretching energy density. For the stretching energy

$$\mathcal{E}_s = \frac{E_f}{2(1-\nu^2)}\int_\omega d\omega\, \frac{h}{2}\mathcal{C}(\gamma) \tag{29}$$

we find by using Eq. (24) with $\tau_{\alpha\beta} = \gamma_{\alpha\beta}$, and combining with Eqs. (22), (23) and (26),

$$\begin{aligned}\mathcal{C}(\gamma) = 2(1+\nu)\bar{\gamma}(\nabla u)^2 + 2(1+\nu)(\nabla u)^4 -\\ 2\left[(1-\nu)b^{\alpha\beta}\nabla_\alpha u\nabla_\beta u + 2\nu\mathcal{H}(\nabla u)^2\right]u +\\ \left[(1-\nu)c^{\alpha\beta}\nabla_\alpha u\nabla_\beta u + \nu\mathcal{R}(\nabla u)^2\right]u^2 +\\ 2\left[(1-\nu+\bar{\gamma}+\nu\bar{\gamma})\mathcal{R} + 4\nu\mathcal{H}^2\right]u^2 -\\ 2\left[(1-\nu)\mathcal{S} + 2\nu\mathcal{H}\mathcal{R}\right]u^3 +\\ \tfrac{1}{2}\left[(1-\nu)\mathcal{T} + \nu\mathcal{R}^2\right]u^4 + \mathcal{O}(1) + \mathcal{O}(u)\end{aligned} \tag{30}$$

[1] Note that $-\int d\omega\, \mathcal{R}u\triangle u = \int d\omega\, u(\nabla\mathcal{R})\cdot(\nabla u) + \int d\omega\, \mathcal{R}(\nabla u)^2$. Furthermore, repeated application of the Stokes theorem gives $\int d\omega\, u(\nabla\mathcal{R})\cdot(\nabla u) = \frac{1}{2}\int d\omega\, \triangle\mathcal{R}u^2$.

DOI: 10.1038/NMAT4202

where we did not explicitly write down the terms linear and constant in u, as they will not be relevant for the later analysis (see detailed remarks in *Total energy density* below).

Substrate coupling energy. In our experiments, the thin film is coupled to a curved soft substrate. To simplify further analysis, we assume from now on that the substrate has the same Poisson ratio ν as the film, as is the case in our experiments. We model the substrate coupling as a nonlinear spring by adding a substrate energy $\mathcal{E}_{sub}$ to the KS energy from Eq. (13a), where

$$\mathcal{E}_{sub} = \frac{E_s}{2}\int_\omega d\omega \left(Au + \frac{\tilde{a}}{h}u^2 + \frac{\tilde{c}}{h^3}u^4\right) \tag{31}$$

with E_s denoting the Young modulus of the substrate. The constant film thickness h could have been absorbed into the coefficients $\tilde{a}$ and $\tilde{c}$, but simplifies subsequent formulas. Note that $\mathcal{E}_{sub}$ contains a term linear in u because we are considering the state of the film-substrate system around a flat but displaced equilibrium solution u_0. This linear term gives rise to a corresponding constant normal force that is needed to balance the internal normal forces of the film.

Energy due to excess film stress. Finally, we still have to account for the excess film stress

$$\Sigma_e \equiv \frac{\sigma}{\sigma_c} - 1 \tag{32a}$$

where σ is the film stress and σ_c the critical stress needed for wrinkling. In our model, the energy due to excess film stress is included by adding a term

$$\mathcal{E}_\sigma = \frac{E_f}{2(1-\nu^2)}\int_\omega d\omega\ \frac{\tilde{a}_2}{h}\Sigma_e u^2 \tag{32b}$$

to the KS energy from Eq. (13a). The energy contribution $\mathcal{E}_\sigma$ is crucial for capturing the system behavior beyond the wrinkling instability. We discuss below how the dimensionless parameter $\tilde{a}_2$ is related to the elastic properties of the substrate. The u^2-dependence of $\mathcal{E}_\sigma$ is a classical result from elastic wrinkling theory [5], ensuring that the amplitude-stress relationship in the effective model agrees with classical wrinkling theory, as is shown in detail further below.

Total energy density. Adding the contributions due to substrate coupling, external forces and excess stress to the KS energy (13a), we obtain the total elastic energy

$$\mathcal{E} = \frac{E_f}{1-\nu^2}\bar{\mathcal{E}} \tag{33a}$$

where to leading order

$$\begin{aligned}\bar{\mathcal{E}} = \int_\omega d\omega \Big[&\frac{\gamma_0}{2}(\nabla u)^2 + \frac{\gamma_2}{2}(\triangle u)^2 + \frac{a}{2}u^2 + \frac{b}{3}u^3 + \frac{c}{4}u^4 - \\ &\frac{h}{2}\left[(1-\nu)b^{\alpha\beta}\nabla_\alpha u\nabla_\beta u + 2\nu\mathcal{H}(\nabla u)^2\right]u + \\ &\frac{h}{4}\left[(1-\nu)c^{\alpha\beta}\nabla_\alpha u\nabla_\beta u + \nu\mathcal{R}(\nabla u)^2\right]u^2\Big]\end{aligned} \tag{33b}$$

with coefficients

$$\begin{aligned}\gamma_0 &= h\bar{\gamma}(1+\nu) + \frac{h^3\mathcal{R}}{6} \\ \gamma_2 &= \frac{h^3}{12} \\ a &= h\left[(1-\nu+\bar{\gamma}+\nu\bar{\gamma})\mathcal{R} + 4\nu\mathcal{H}^2\right] + \frac{h^3(\mathcal{R}^2 - \triangle\mathcal{R})}{12} + \\ &\quad \frac{E_s(1-\nu^2)}{E_f}\frac{\tilde{a}}{h} + \frac{\tilde{a}_2}{h}\Sigma_e \\ b &= -\frac{3h}{2}\left[(1-\nu)\mathcal{S} + 2\nu\mathcal{H}\mathcal{R}\right] \\ c &= \frac{h}{2}\left[(1-\nu)\mathcal{T} + \nu\mathcal{R}^2\right] + 2\frac{E_s(1-\nu^2)}{E_f}\tilde{c}\end{aligned} \tag{33c}$$

Note that for compressive stresses $\bar{\gamma} < 0$. Thus, for sufficiently large film pre-stress, $\gamma_0 < 0$. To obtain the effective energy functional (33), the following additional simplifications and assumptions were adopted:

- **Constant terms.** We neglected all constant terms in the energy, as they will not contribute to the equations of motion, obtained by variation of the energy with respect to u.
- **Terms linear in u.** We note that the term linear in u gives rise to a inhomogeneous, constant term in the equation of motion. However, $u = 0$ always is an equilibrium solution by construction. More precisely, $u = 0$ means that the film is radially displaced by u_0, which is a fundamental solution of the problem. Therefore, the inhomogeneous term in the equation of motion has to vanish, implying that the coefficient of the energy term linear in u must be zero. This condition can be interpreted as follows: For $u = 0$ to be an equilibrium solution, the sum of all normal forces acting on the film must vanish.
- **Quartic terms.** The quartic terms in u and ∇u ensure that the effective theory remains stable above the wrinkling threshold, as these terms limit the growth of the most unstable modes. To keep the theory as simple as possible, we only include the dominant u^4-contribution and neglect terms $\propto (\nabla u)^4$.

Taking the variation of $\bar{\mathcal{E}}$ with respect to u, we obtain

$$\begin{aligned}-\frac{\delta\bar{\mathcal{E}}}{\delta u} = &\gamma_0\triangle u - \gamma_2\triangle^2 u - au - bu^2 - cu^3 + \\ &\frac{h}{2}\left\{(\nu-1)\left[b^{\alpha\beta}\nabla_\alpha u\nabla_\beta u + 2u\nabla_\beta\left(b^{\alpha\beta}\nabla_\alpha u\right)\right] + \right. \\ &\left. 2\nu\left[\mathcal{H}(\nabla u)^2 - 2\nabla\cdot(\mathcal{H}u\nabla u)\right]\right\} + \\ &\frac{h}{2}\left[(1-\nu)u\nabla_\beta\left(uc^{\alpha\beta}\nabla_\alpha u\right) - \nu\mathcal{R}u(\nabla u)^2 + \right. \\ &\left.\nu\nabla\cdot(\mathcal{R}u^2\nabla u)\right]\end{aligned} \tag{34}$$

where $\nabla\cdot$ denotes the surface divergence. We note that, for a flat Euclidean metric, the first line of Eq. (34) coincides with the Swift-Hohenberg (SH) equation, as originally derived in the context of Rayleigh-Bénard convection [6, 7]. The b-term and the first term $\propto h$ (second and third line) break the symmetry $u \to -u$, which is known to lead to a transition from labyrinth-like patterns to hexagons for SH-like equations. As both terms depend on the curvature tensor $b_{\alpha\beta}$, we can infer that regions of high curvature will show different wrinkling patterns than regions of low curvature.

We next apply Eq. (34) to derive quantitative predictions for wrinkling patterns transitions on spherical geometries, which are then compared with our experiments (Main Text). Subsequently, we still present numerical solutions for a toroidal geometry, as an example of a surface with locally varying curvature.

APPLICATION TO SPHERICAL GEOMETRIES

Using spherical coordinates $(\theta_1, \theta_2) \in [0, 2\pi) \times [0, \pi]$, a spherical surface of radius R is described by the metric tensor

$$(a_{\alpha\beta}) = \begin{pmatrix} (R\sin\theta_2)^2 & 0 \\ 0 & R^2 \end{pmatrix} \tag{35}$$

In this case, we have $\mathcal{H} = -1/R$, $\mathcal{K} = 1/R^2$. Thus

$$\mathcal{R} = 2/R^2, \qquad \mathcal{S} = -2/R^3, \qquad \mathcal{T} = 2/R^4 \tag{36}$$

Total energy density. Noting that the sphere has constant mean and Gaussian curvature $\mathcal{H}$ and $\mathcal{K}$, Eq. (36) allows to simplify the total energy density (33) considerably,

$$\bar{\mathcal{E}} = \int_\omega d\omega \left[\frac{\gamma_0}{2} (\nabla u)^2 + \frac{\gamma_2}{2} (\triangle u)^2 + \frac{a}{2}u^2 + \frac{b}{3}u^3 + \frac{c}{4}u^4 + \Gamma_1 (\nabla u)^2 u + \frac{\Gamma_2}{2} (\nabla u)^2 u^2 \right] \tag{37}$$

with coefficients

$$\begin{aligned} \gamma_0 &= h\bar{\gamma}(1+\nu) + \frac{h^3}{3R^2} \\ \gamma_2 &= \frac{h^3}{12} \\ a &= \frac{2h(1+\bar{\gamma})(1+\nu)}{R^2} + \frac{h^3}{3R^4} + \frac{E_s(1-\nu^2)}{E_f}\frac{\tilde{a}}{h} + \frac{\tilde{a}_2}{h}\Sigma_e \\ b &= \frac{3h(1+\nu)}{R^3} \\ c &= \frac{h(1+\nu)}{R^4} + 2\frac{E_s(1-\nu^2)}{E_f}\tilde{c} \\ \Gamma_1 &= \frac{h(1+\nu)}{2R} \\ \Gamma_2 &= \frac{h(1+\nu)}{2R^2} \end{aligned} \tag{38}$$

Equations of motions

To identify the equilibrium configurations, we assume that the film exhibits an overdamped relaxation dynamics. Then, the equations of motion follow by functional variation of the elastic energy (37) with respect to the displacement field u,

$$\frac{\rho}{\tau_0}\partial_t u = -\frac{\delta\mathcal{E}}{\delta u} \tag{39}$$

where ρ is the constant surface mass density of the film and τ_0 the damping-time scale. The relaxation dynamics (39) can be written in the equivalent form

$$\mu\partial_t u = -\frac{\delta\bar{\mathcal{E}}}{\delta u} \tag{40a}$$

where the coefficient

$$\mu = \frac{\rho(1-\nu^2)}{\tau_0 E_f} \tag{40b}$$

is the inverse relaxation speed. Calculating the functional derivative $\delta\bar{\mathcal{E}}/\delta u$ gives

$$\begin{aligned} \mu\partial_t u \;=\; & \gamma_0\triangle u - \gamma_2\triangle^2 u - au - bu^2 - cu^3 + \\ & \Gamma_1\left[(\nabla u)^2 + 2u\triangle u\right] + \Gamma_2\left[u(\nabla u)^2 + u^2\triangle u\right] \end{aligned} \tag{41}$$

Since we are only interested in the steady-state solutions, the exact value of μ is not relevant for our analysis. It is convenient to rewrite Eq. (41) in dimensionless form by measuring length in units of the film thickness h and time in units of $\tau_h = \mu h$. Introducing the dimensionless curvature parameter

$$\kappa = h/R \tag{42}$$

Eq. (41) reduces to

$$\begin{aligned} \partial_t u \;=\; & \gamma_0\triangle u - \gamma_2\triangle^2 u - au - bu^2 - cu^3 + \\ & \Gamma_1\left[(\nabla u)^2 + 2u\triangle u\right] + \Gamma_2\left[u(\nabla u)^2 + u^2\triangle u\right] \end{aligned} \tag{43}$$

with rescaled dimensionless parameters

$$\begin{aligned} \gamma_0 &= \bar{\gamma}(1+\nu) + \frac{\kappa^2}{3} < 0 \\ \gamma_2 &= \frac{1}{12} \\ a &= 2(1+\bar{\gamma})(1+\nu)\kappa^2 + \frac{\kappa^4}{3} + \frac{E_s(1-\nu^2)}{E_f}\tilde{a} + \tilde{a}_2\Sigma_e \\ b &= 3(1+\nu)\kappa^3 \\ c &= (1+\nu)\kappa^4 + 2\frac{E_s(1-\nu^2)}{E_f}\tilde{c} \\ \Gamma_1 &= \frac{(1+\nu)\kappa}{2} \\ \Gamma_2 &= \frac{(1+\nu)\kappa^2}{2} \end{aligned} \tag{44}$$

DOI: 10.1038/NMAT4202

Note that the covariant derivatives ∇ and $\triangle$ in Eq. (43) are now also defined with respect to the rescaled dimensionless sphere of radius $\kappa^{-1} = R/h$. In Eq. (44), we kept the term $\sim \kappa^4$ in the coefficient a. Although this higher order term is negligible, its inclusion will lead to simpler expressions when matching our model with experiments (see section *Curvature-dependence of the critical strain* $\bar{\gamma}$ below). Given the dimensionless parameters in Eq. (44), the corresponding values in physical units are recovered through the transformations

$$\begin{aligned} u &\to hu, & R &\to h/\kappa, & t &\to \mu h t \\ \gamma_0 &\to h\gamma_0, & \gamma_2 &\to h^3\gamma_2 & & \\ a &\to a/h, & b &\to b/h^2, & c &\to c/h^3 \\ \Gamma_1 &\to \Gamma_1, & \Gamma_2 &\to \Gamma_2/h & & \end{aligned} \tag{45}$$

As evident from Eq. (44), the model is specified through dimensionless parameters

$$(\kappa, \bar{\gamma}, E_s/E_f, \nu, \tilde{a}, \tilde{a}_2, \tilde{c}) \tag{46}$$

Parameter determination

The parameters (h, R, ν, E_s, E_f) can be directly measured for our experimental system. To determine the remaining parameters $(\bar{\gamma}, \tilde{a}, \tilde{a}_2, \tilde{c})$, we proceed as follows:

1. Linear stability analysis will enable us to relate γ_0 at the onset of wrinkling with the wavelength λ, which yields a relation between the critical buckling strain $\bar{\gamma}$ and the ratio E_s/E_f.

2. The value of the substrate parameter $\tilde{a}$ can be estimated from known results for the critical bulking stress in planar elasticity theory [8]. Below, we will extend the classical derivation to the weakly curved case to confirm that our model predictions agree with recent results by Cai *et al.* [9]

3. By means of nonlinear stability analysis and comparison with analytical results for the standard Swift-Hohenberg equation, we will express the parameter $\tilde{a}_2$ in terms of c, leaving $\tilde{c}$ as the only remaining fit parameter. We estimate $\tilde{c}$ by comparing our numerical simulations with the experimentally measured surface morphologies.

Critical stress $\bar{\gamma}$ *and* $\tilde{a}$

We estimate $\bar{\gamma}$ by comparing our effective theory with known results for the full elastic equations in the planar limit case $R \to \infty$. Letting $\kappa \to 0$ and linearizing Eq. (43) for a small perturbation εe^{ikx} of the unbuckled homogeneous solution, one finds the dominant unstable wave-mode

$$|k| = \sqrt{\frac{|\gamma_0|}{2\gamma_2}} = \sqrt{6|\gamma_0|} \tag{47a}$$

which selects the characteristic wavelength

$$\lambda_c = \frac{2\pi}{|k|} = \frac{2\pi}{\sqrt{6|\gamma_0|}} \tag{47b}$$

Equating λ_c with the known wrinkling wavelength λ_{el} of a planar elastic film-substrate system, which in units $h = 1$ is given by [8]

$$\lambda_{el} = 2\pi \left(\frac{E_f}{3E_s}\right)^{1/3} \tag{48}$$

we obtain

$$\gamma_0 = -\frac{1}{6}\left(\frac{3E_s}{E_f}\right)^{2/3} \tag{49}$$

The sign indicates a compressive strain, which in our terminology is negative. From Eq. (44) with $\kappa \to 0$, we find the planar estimate

$$\bar{\gamma} \simeq -\frac{1}{6(1+\nu)}\left(\frac{3E_s}{E_f}\right)^{2/3} \equiv \bar{\gamma}_p \tag{50}$$

A correction due to curvature will be discussed below.

Critical stress. The strain $\bar{\gamma}_p$ can be associated with the critical stress σ_c at the wrinkling threshold. As expressed by Eq. (22), our system is in a state of equibiaxial strains $\bar{\gamma}$ implying that, in a locally orthogonal coordinate frame, the in-plane elasticity tensor reduces to $\epsilon_{11} = \epsilon_{22} = \epsilon$, $\epsilon_{12} = \epsilon_{21} = 0$. The usual stress-strain relationship of a Hookean material then reads [10]

$$\begin{aligned} \sigma_{11} = \sigma_{22} &= \frac{E}{1-\nu^2}(\epsilon_{11} + \nu\epsilon_{22}) = \frac{E}{1-\nu}\epsilon \equiv \sigma \\ \sigma_{12} = \sigma_{21} &= 0 \end{aligned}$$

Assuming a standard linear relation between stress and strain, we expect

$$\sigma_c = k_\sigma \frac{E_f}{1-\nu}\bar{\gamma}_p \tag{51}$$

with some constant prefactor k_σ. Inserting Eq. (50), we obtain

$$\sigma_c = -\frac{k_\sigma}{6}\frac{E_f}{1-\nu^2}\left(\frac{3E_s}{E_f}\right)^{2/3} \tag{52}$$

which for $k_\sigma = 3/2$ agrees with the known critical stress of elastic wrinkling analysis [8]

$$\sigma_{c_{el}} = -\frac{E_f}{4(1-\nu^2)}\left(\frac{3E_s}{E_f}\right)^{2/3} \tag{53}$$

Estimation of $\tilde{a}$ near the critical value σ_c. In the planar limit $\kappa \to 0$, Eq. (43) exhibits a bifurcation from a uniform state to nontrivial pattern formation only if $a < a_c$, where

$$a_c = \frac{\gamma_0^2}{4\gamma_2} = \frac{1}{12}\left(\frac{3E_s}{E_f}\right)^{4/3} \tag{54}$$

At the wrinkling onset, corresponding to $a = a_c$, the film stress σ equals the critical stress σ_c so that $\Sigma_e = 0$. For the planar case, Eq. (54) thus determines the substrate parameter $\tilde{a}$ as

$$\tilde{a} = \frac{1}{4(1-\nu^2)}\left(\frac{3E_s}{E_f}\right)^{1/3} \tag{55}$$

Curvature-dependence of the critical strain $\bar{\gamma}$

Recent simulations of the full coupled elasticity equations [11] and experiments with polymer colloids [12] report wave-length reduction of pattern on curved substrates compared with the planar case. It is therefore interesting to study how the critical strain $\bar{\gamma} < 0$ depends on the curvature parameter $\kappa = h/R$ in our model.

Similar to the planar case, cf. Eq. (54), the wrinkling bifurcation occurs when

$$\frac{\gamma_0^2(\kappa)}{4\gamma_2\, a_c(\kappa)} = 1. \tag{56}$$

Recalling that $\Sigma_e = 0$ at the transition point and using the the above result for $\tilde{a}$, we can solve Eq. (56) for the critical strain $\bar{\gamma}$. Using Eq. (44) we then obtain for γ_0

$$\gamma_0 = \frac{\kappa^2}{3} - \frac{1}{6}\sqrt{\left(\frac{3E_s}{E_f}\right)^{4/3} + 24(1+\nu)\kappa^2} \tag{57}$$

which reduces to Eq. (49) in the planar case ($\kappa = 0$). For $\bar{\gamma}$, we find to $\mathcal{O}(\kappa^4)$

$$\frac{\bar{\gamma}}{\bar{\gamma}_p} = 1 + 12\kappa^2(1+\nu)\left(\frac{E_f}{3E_s}\right)^{4/3} \tag{58}$$

where $\bar{\gamma}_p$ is the critical buckling strain for the planar case, given in Eq. (50). This asymptotic scaling behavior in κ is similar to the results of Cai *et al.* [9], although the numerical prefactors and the dependence on the Poisson ratio ν differ.

According to Eq. (57), the absolute value $|\gamma_0|$ increases with curvature with a leading order correction $\sim \kappa^2$. Equation (47b) then implies that the wavelength λ_c decreases with increasing curvature, in qualitative agreement with experimental and numerical findings [11, 12]. It is interesting to note that the wavelength reduction in our model is due to the nonlinear, curvature-dependent stretching terms of the underlying KS energy, unlike the model of Yin *et al.* [13], where a wavelength reduction was obtained by assuming a curvature-dependent substrate model. Unfortunately, for the range of parameters realized in our experiments the curvature-induced wavelength reduction is below the detection threshold. We therefore did not include any curvature-dependent substrate response in our model.

γ_0	=	$-\frac{\eta^{2/3}}{6} - \left[\frac{2(1+\nu)}{\eta^{2/3}} - \frac{1}{3}\right]\kappa^2$
a	=	$\frac{\eta^{4/3}}{12} + \frac{6(1+\nu) - \eta^{2/3}}{3}\kappa^2 + \tilde{a}_2\Sigma_e$
b	=	$3(1+\nu)\kappa^3$
c	=	$\frac{2(1+\nu)\eta^{2/3}}{3}c_1$
Γ_1	=	$\frac{1+\nu}{2}\kappa$
Γ_2	=	$\frac{1+\nu}{2}\kappa^2$
$\tilde{a}_2$	=	$-\frac{\eta^{4/3}(c+3\lvert\gamma_0\rvert\Gamma_2)}{48\gamma_0^2}$

TABLE I: List of parameters for Eqs. (43) and (64) as obtained by systematic asymptotic matching to classical elastic wrinkling theory, with $\eta = 3E_s/E_f$, $\gamma_2 = 1/12$, $\Sigma_e = (\sigma/\sigma_c) - 1$, and $\kappa = h/R$ where h is the film thickness and R the radius (see Fig. 2 of Main Text). We substituted $\tilde{a}$ and $\tilde{c}$ by Eqs. (55) and (77). Focusing on the leading order contribution, we only kept terms up to $\mathcal{O}(\kappa^3)$, cf. Eq. (57). The only remaining fitting parameter of the model is c_1.

Nonlinear behavior above onset

Having determined estimates for the parameters $(\bar{\gamma}, \tilde{a})$ by analyzing the onset of wrinkling, the two remaining unknown parameters are $(\tilde{a}_2, \tilde{c})$. Aiming to further reduce the number of free parameters, we now turn to the regime beyond the wrinkling threshold, where patterns are selected by nonlinear effects. To this end, we first reduce the generalized Swift-Hohenbergy equation (43) to a standard Swift-Hohenberg (SH) equation by approximating mixed $\Gamma_{1,2}$-terms in Eq. (43) that contain both u and ∇u through effective expressions that only contain u. Assuming a typical relation between pattern amplitude and excess film stress $\Sigma_e = (\sigma/\sigma_c) - 1$, we can then exploit existing results for the stability of patterns in the SH equation to predict the morphological phase diagram of the wrinkling patterns in our experimental system.

Swift-Hohenberg approximation. To approximate Eq. (43) by a standard SH equation, we recall that γ_0 and γ_2 select the dominant (most unstable) wave number vector $k_c = \pm\sqrt{6|\gamma_0|}$, see Eq. (47a). Considering the

DOI: 10.1038/NMAT4202

limit $\kappa \to 0$ and a plane-wave solution of the form

$$u = \mathcal{A}\cos(k_c x) \tag{59}$$

the Γ_1-term in Eq. (43) exerts an average force per wavelength $\lambda = 2\pi/|k_c|$ of

$$\left\langle \Gamma_1 \left[(\nabla u)^2 + 2u\triangle u \right] \right\rangle_\lambda = -\frac{1}{2}\Gamma_1 \mathcal{A}^2 k_c^2 \tag{60}$$

where

$$\langle f(x)\rangle_\lambda \equiv \frac{1}{\lambda}\int_0^\lambda dx\ f(x) \tag{61}$$

Comparing Eq. (60) with the average force exerted by a quadratic force $f = au^2$ for the wave solution (59),

$$\langle au^2\rangle_\lambda = \frac{a\mathcal{A}^2}{2} \tag{62}$$

we can approximate the Γ_1-term by an 'equivalent' average force term of the form

$$\Gamma_1 \left[(\nabla u)^2 + 2u\triangle u \right] \approx -\Gamma_1 k_c^2 u^2 \tag{63a}$$

Similarly, the average force due to the Γ_2-term can be approximated by a cubic force. Since the Γ_2-term is antisymmetric in u, the corresponding mean force is obtained by averaging over the interval $[\lambda/4, 3\lambda/4]$, yielding

$$\Gamma_2 \left[u\,(\nabla u)^2 + u^2\triangle u \right] \approx -\frac{1}{2}\Gamma_2 k_c^2 u^3 \tag{63b}$$

With these approximations, Eq. (43) reduces to the SH equation

$$\begin{aligned} \partial_t u = {} & \gamma_0\triangle u - \gamma_2\triangle^2 u - \\ & au - \left(b + \Gamma_1 k_c^2\right) u^2 - \left(c + \frac{\Gamma_2 k_c^2}{2}\right) u^3 \end{aligned} \tag{64}$$

To facilitate direct comparison with results in the literature [14], it is convenient to rewrite Eq. (64) in the rescaled *normal form*

$$\partial_T \phi = -2\triangle_X \phi - \triangle_X^2 \phi - A\phi - B\phi^2 - \phi^3 \tag{65}$$

where

$$\begin{aligned} T &= \frac{4\gamma_2 t}{\gamma_0^2} = \frac{t}{3\gamma_0^2} \\ \triangle_X &= \frac{\triangle}{k_c^2} = \frac{\triangle}{6|\gamma_0|} \\ \phi &= \frac{u}{u_*} \\ u_* &= \sqrt{\frac{\gamma_0^2}{4\gamma_2(c + \Gamma_2 k_c^2/2)}} = \sqrt{\frac{\gamma_0^2}{(c/3) + \Gamma_2|\gamma_0|}} \\ A &= \frac{a}{a_c} = \frac{4a\gamma_2}{\gamma_0^2} = \frac{3a}{\gamma_0^2} \\ B &= \frac{2\left(b + \Gamma_1 k_c^2\right)}{\sqrt{(\gamma_0^2/\gamma_2)\,(c + \Gamma_2 k_c^2/2)}} = u_* \frac{(b/3) + 2|\gamma_0|\Gamma_1}{\gamma_0^2} \end{aligned} \tag{66}$$

with a_c given by Eq. (54).

Excess film stress. Our model accounts for the excess film stress $\Sigma_e = (\sigma/\sigma_c) - 1$ through the contribution $\tilde{a}_2\Sigma_e$ that appears in the coefficient a of the linear force, see Eq. (44). This specific functional relationship between a and Σ_e follows from the requirement that, in the planar limit $\kappa \to 0$, our model must produce the same amplitude-stress relation as classical wrinkling theory [5]. More precisely, classical planar wrinkling theory predicts that the amplitude $\mathcal{A}_{el}$ of the wrinkling solution $u = \mathcal{A}_{el}\cos(kx)$, measured in units of the film thickness h, is equal to square of the excess film stress [9],

$$\mathcal{A}_{el} = \sqrt{\Sigma_e}. \tag{67}$$

This must be equal to the amplitude $\mathcal{A}$ of the solution $u = \mathcal{A}\cos(k_c x)$ of the standard SH equation (64), which is given by [14]

$$\mathcal{A} = \frac{2}{\sqrt{3}} u_* \sqrt{1 - A} \tag{68}$$

Equating the amplitudes yields

$$A = \frac{a}{a_c} = 1 - \frac{3\Sigma_e}{4u_*^2} \tag{69}$$

Finally, considering the definition of a in Eq. (44) in the planar case $\kappa = 0$ and inserting a_c from Eq. (54), we find

$$\tilde{a}_2 = -\frac{3\gamma_2}{4u_*^2}\left(\frac{3E_s}{E_f}\right)^{4/3} \tag{70}$$

We have thus determined all parameters of the effective theory with the exception of $\tilde{c}$, which enters through both c in Eq. (44) and u_* in (70), see Eq. (66). As shown in the next section, $\tilde{c}$ can be estimated by matching our model predictions with the experiments. Table I summarizes the results for our model parameters, retaining curvature terms up to $\mathcal{O}(\kappa^3)$, and is also reproduced in Table 1 of the Main Text.

Remark. In the above derivation, we have matched the amplitude-stress relationship using the plane-wave wrinkling solution. Alternatively, one can match the amplitude-stress relationship of wrinkling patterns using the hexagonal solution of the SH equation. The general procedure is identical to the one above. The hexagonal solution u_{H} of the standard SH equation is given by [14]

$$u_{\mathrm{H}} = \mathcal{A}\left[\cos(k_c x) + 2\cos\left(\frac{k_c x}{2}\right)\cos\left(\frac{\sqrt{3}k_c y}{2}\right)\right] \tag{71}$$

with

$$\mathcal{A} = \frac{2}{15}\left[Bu_* + \sqrt{(Bu_*)^2 + 15u_*^2(1 - A)}\right] \tag{72}$$

B vanishes in the planar case, where $\kappa = 0$. Classical planar wrinkling theory predicts the same solution, Eq. (71), with amplitude [9]

$$\mathcal{A}_{el} = \frac{2}{\sqrt{11 + 6\nu - 5\nu^2}}\sqrt{\Sigma_e} \tag{73}$$

Comparing the two amplitudes, we obtain

$$A = 1 - \frac{15\Sigma_e}{(11 + 6\nu - 5\nu^2)u_*^2} \tag{74}$$

from which a and $\tilde{a}_2$ follow again by Eqs. (44) and (54).

Hence, matching amplitudes in the hexagonal phase again leads to a linear relationship between A and Σ_e, but the prefactor differs compared with the plane-wave solution considered above.

However, irrespective of the chosen matching procedure, we obtain a linear relation between $\tilde{a}_2$ and $\tilde{c}$, leaving only one fitting parameter, $\tilde{c}$. Due to the linear dependence between $\tilde{a}_2$ and $\tilde{c}$ for both hexagonal and labyrinth patterns, one can use either matching relation to fit the experiments. Since the plane-wave (labyrinth) solution (67) leads to slightly simpler formulas, we choose the plane-wave matching in the following; that is, we assume that A and Σ_e are related by Eq. (69), and $\tilde{a}_2$ is given by Eq. (70). This convention means that we must determine $\tilde{c}$ by matching the theoretically predicted phase transition curve between the bistable and labyrinth states to the corresponding experimentally measured phase transition curve. The fitting value $\tilde{c}$ then automatically fixes the theoretical prediction for the second transition curve between hexagonal and bistable phase.

Phase diagram of the wrinkling morphology

The reduction of our effective theory to a standard Swift-Hohenberg equation allows us to make approximative predictions regarding the wrinkling morphologies. For the normal form, Eq. (65), three different wrinkling phases emerge depending on the choice of parameters A and B [14]:

$$\text{Unwrinkled:} \qquad 1 - A \leq 0 \tag{75a}$$

$$\text{Hexagons:} \qquad -\frac{1}{15}B^2 < 1 - A < \frac{4}{3}B^2 \tag{75b}$$

$$\text{Bistable phase:} \qquad \frac{4}{3}B^2 < 1 - A < \frac{16}{3}B^2 \tag{75c}$$

$$\text{Labyrinths:} \qquad \frac{16}{3}B^2 < 1 - A \tag{75d}$$

We recall that the coefficient B depends on κ via Γ_1, Γ_2, b and c, see Eq. (66), while A depends on the excess film stress and κ via Eq. (69). Substituting Eqs. (69) and (66) for A and B in Eq. (75), we obtain to leading order in κ the following stability criteria:

$$\text{Unwrinkled:} \qquad \Sigma_e \leq 0 \tag{76a}$$

$$\text{Hexagons:} \qquad -\frac{\rho}{20}\kappa^2 < \Sigma_e < \rho\kappa^2 \tag{76b}$$

$$\text{Bistable phase:} \qquad \rho\kappa^2 < \Sigma_e < 4\rho\kappa^2 \tag{76c}$$

$$\text{Labyrinths:} \qquad 4\rho\kappa^2 < \Sigma_e \tag{76d}$$

where

$$\rho = \frac{1}{\left[\eta^{1/3}(1-\nu)\tilde{c}\right]^2} \tag{76e}$$

The free parameter $\tilde{c}$ is a function of $\eta = 3E_s/E_f$ and ν. The functional form of $\tilde{c} = \tilde{c}(\eta, \nu)$ determines how the phase transition lines depend on those material properties. Comparison with our experimental data suggests, however, that the phase transition lines are in fact independent of η and ν (Fig. 3 of Main Text). In this case, ρ must be independent of η and ν, which means that

$$\tilde{c} = \frac{c_1}{(1-\nu)\eta^{1/3}}, \tag{77}$$

with fit parameter c_1. Adopting the ansatz (77), we find that $c_1 = 0.0188 \pm 0.0002$ gives the best fit to the experimental data (Fig. 3 of Main Text). The resulting good agreement with the data suggests strongly that the critical curves, which separate the different wrinkling phases in our experiments, are independent of material properties.

Hysteresis

We explain how the critical curves in Fig. 4 of Main Text are obtained. To this end, recall that the amplitude of the hexagonal solutions is given by Eq. (72). Inserting Eq. (69) for A gives

$$\mathcal{A} = \frac{2}{15}\left[Bu_* + \sqrt{(Bu_*)^2 + \frac{45\Sigma_e}{4}}\right] \tag{78}$$

To compare with the labyrinth solutions, we consider the measurable difference U_H of the maximal and minimal values of the hexagonal displacement field u_H (measured in units of h). Equation (71) implies that

$$U_\mathrm{H} = \max u_\mathrm{H} - \min u_\mathrm{H} = \frac{9}{2}\mathcal{A} \tag{79}$$

The prefactor in the last expression is due to the fact that u_H assumes its minimum at $-3\mathcal{A}$ and its maximum at $+3\mathcal{A}/2$.

To calculate the corresponding quantity U_L for the labyrinth solution u_L, we assume that labyrinths are locally described by the plane-wave $u_\mathrm{L} = \mathcal{A}\cos(k_c x)$. We then obtain with Eqs. (68) and (69)

$$U_\mathrm{L} = \max u_\mathrm{L} - \min u_\mathrm{L} = 2\sqrt{\Sigma_e} \tag{80}$$

Note that U_L is independent of curvature, whereas the square-root law for U_H is shifted horizontally and vertically by the Bu_*-terms (see Fig. 4b of Main Text). To first order in curvature, we have

$$Bu_* \simeq \frac{3\kappa}{4c_1} \tag{81}$$

DOI: 10.1038/NMAT4202

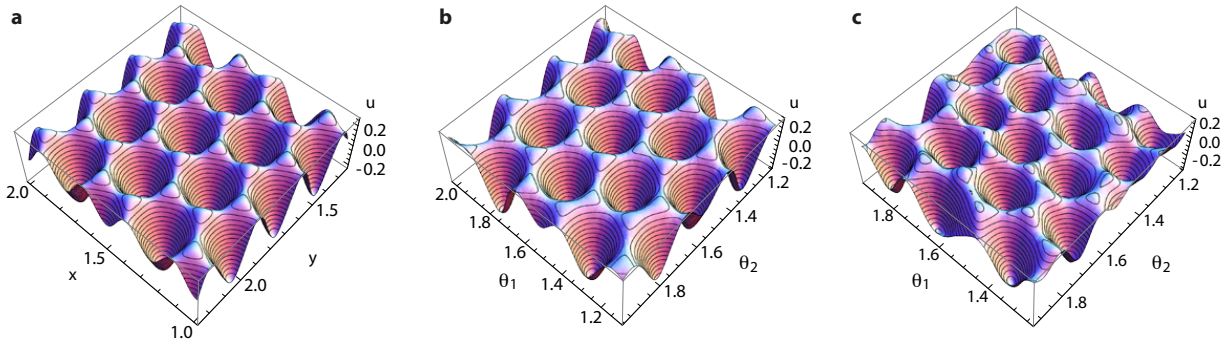

Fig. S1: Comparison of wrinkling morphologies in the hexagonal phase: (a) Planar analytical solution from Eq. (71), (b) numerical solution of the generalized Swift-Hohenberg theory from Eq. (43) (simulation parameters: $\gamma_0 = -0.08$, $a = 0.0151$, $c = 0.0095$, $R/h = 80$), and (c) 3D surface scan from experiments ($R = 20$mm, $h = 0.375$mm, $E_f = 2100$kPa, $E_s = 230$kPa). θ_1 and θ_2 denote polar angles.

yielding for the horizontal and vertical shifts (see Fig. 4b in the Main Text)

$$\delta\Sigma_e = \frac{\kappa^2}{20c_1^2}, \qquad \delta U_{\rm H} = \frac{9\kappa}{10c_1} \tag{82}$$

Based on the results for $U_{\rm L}$ and $U_{\rm H}$, we expect two hysteresis cycles (see Fig. 4 of Main Text). The first cycle is due to the shift $\delta\Sigma_e$, which creates a subcritical stability zone for the hexagonal solutions [14]. Increasing Σ_e from the unwrinkled phase, hexagons emerge at the onset $\Sigma_e = 0$. However, once they have formed, hexagons remain stable even if the excess stress Σ_e is subsequently reduced below the wrinkling onset $\Sigma_e = 0$. Only for $\Sigma_e < -\delta\Sigma_e$, hexagons loose stability and the unwrinkled solution remains as the only stable state. The second hysteresis cycle involves larger excess stresses (see Fig. 4a of Main Text). Starting from the hexagonal phase, hexagons remain stable if the excess stress is increased into the bistable phase [14]. Only if Σ_e is increased beyond the bistable-to-labyrinth transition line, hexagons loose their stability and the system jumps to a labyrinth state. Upon decreasing Σ_e from the labyrinth phase, the system adopts a different path as labyrinths remain stable throughout the bistable phase; a transition to hexagons happens when Σ_e is decreased below the critical value that separates the hexagonal from the bistable phase.

Validation of hexagonal patterns

To test our effective theory further, we compare the planar hexagon solution, Eq. (71), with the numerical solution of Eq. (43) on a spherical geometry (Fig. S1a,b). The good agreement between analytical and numerical solution confirms that the effective theory is indeed well approximated by the standard planar SH equation (65). These results corroborate that once hexagons are selected, curvature has negligible influence on their morphology. Moreover, analytical and numerical solutions compare well with the experimentally determined 3D surface scans (Fig. S1c), demonstrating that the presented effective theory is able to reproduce the morphological details of thin film buckling patterns.

TOROIDAL GEOMETRIES

We consider a torus with major radius R_1 and minor radius R_2 measured in units of h. Using Eq. (1) and the standard surface parametrization $\mathbf{S} = [(R_1 + R_2\cos\theta_2)\cos\theta_1, (R_1 + R_2\cos\theta_2)\sin\theta_1, R_2\sin\theta_2]$ with coordinates $(\theta_1, \theta_2) \in [0, 2\pi) \times [0, 2\pi)$ we obtain the metric tensor

$$(a_{\alpha\beta}) = \begin{pmatrix} (R_1 + R_2\cos\theta_2)^2 & 0 \\ 0 & R_2^2 \end{pmatrix} \tag{83}$$

Equation (5a) yields for the curvature tensor

$$(b_{\alpha\beta}) = \begin{pmatrix} -\cos\theta_2(R_1 + R_2\cos\theta_2) & 0 \\ 0 & -R_2 \end{pmatrix} \tag{84}$$

and, from Eq. (26), one finds mean and Gaussian curvature as

$$\mathcal{H} = -\frac{1}{2}\left(\frac{\cos\theta_2}{R_1 + R_2\cos\theta_2} + \frac{1}{R_2}\right) \tag{85a}$$

$$\mathcal{K} = \frac{\cos\theta_2}{R_1R_2 + R_2^2\cos\theta_2} \tag{85b}$$

Recall that the coefficients $\tilde{a}$, $\bar{\gamma}$, and $\tilde{a}_2$ were determined in the previous section using asymptotic comparison with the flat case. Hence, the expressions for these coefficients remain valid for toroidal geometries. Moreover, we observe that only the symmetry-breaking term in Eq. (34) contains contractions of the curvature tensor of first order, whereas the coefficients (33c) only depend on curvature at second or higher order. For instance, for

Fig. S 2: Wrinkling morphologies on a toroidal geometry with $R_1 = 80$ and $R_2 = 16$ for increasing excess film stress: (a) $\Sigma_e = 0.25$, (b) $\Sigma_e = 0.5$ and (c) $\Sigma_e = 2.0$. As in spherical geometries, one observes a transition from hexagonal to labyrinth-like patterns with increasing excess stress Σ_e. However, in contrast to the spherical case, the non-constant curvature on the torus can lead to local symmetry-breaking, i.e., at intermediate values of Σ_e labyrinth patterns are more likely to emerge at the inner saddle-like regions of the torus, see (b), whereas hexagons remain stable in the outer regions of the torus, where the two principal curvatures have the same sign resulting in a larger mean curvature. Simulation parameters are $\gamma_0 = -0.079$, $c = 0.075$, (a) $a = 0.017$, (b) $a = 0.016$, and (c) $a = 0.007$, using an unstructured surface triangulation with $> 26,000$ nodes.

a toroidal geometry with $R_1 = 80$, $R_2 = 16$, and $\eta = 0.33$ as shown in Fig. S2, we have $\gamma_0 = -0.079$, so that $|\gamma_0|$ is much larger than the maximum curvature correction $\max_{\theta_1,\theta_2} |\mathcal{R}/6| \approx 0.0007$. We can therefore neglect curvature corrections in the coefficients (33c).

Simulations of Eq. (34) confirm that a symmetry-breaking transition from hexagonal to labyrinth-like structures can also be observed on toroidal geometries when the excess stress is increased (Fig. S2). However, as curvature is now spatially varying, we find that the transition occurs first in the inner regions of the torus, where the principle curvatures have opposite sign (Fig. S2b). In the outside regions, where both principal components have the same sign, hexagons remain stable for relatively larger overstresses, until they become also unstable eventually (Fig. S2c).

In summary, Fig. S2 illustrates that the generalized theory derived above can be applied to arbitrarily curved surfaces.

[1] P. G. Ciarlet. *Mathematical elasticity, vol. III: Theory of shells*. North Holland, 2000.
[2] D. Breid and A. J. Crosby. Curvature-controlled wrinkle morphologies. *Soft Matter*, 9:3624–3630, 2013.
[3] M. M. Müller, M. Deserno, and J. Guven. Interface-mediated interactions between particles: A geometrical approach. *Phys. Rev. E*, 72(6):061407, 2005.
[4] W. Helfrich. Elastic properties of lipid bilayers: theory and possible experiments. *Z. Naturforsch.*, 28(11):693–703, 1973.
[5] Z. Y. Huang, W. Hong, and Z. Suo. Nonlinear analyses of wrinkles in a film bonded to a compliant substrate. *J. Mech. Phys. Solids*, 53:2101–2118, 2005.
[6] J. Swift and P. C. Hohenberg. Hydrodynamic fluctuations at the convective instability. *Phys. Rev. A*, 15(1):319–328, 1977.
[7] M. C. Cross and P. C. Hohenberg. Pattern formation outside of equilibrium. *Rev. Mod. Phys.*, 65(3):851–1112, 1993.
[8] H. G. Allen. *Analysis and Design of Structural Sandwich Panels*. Pergamon, New York, 1969.
[9] S. Cai, D. Breid, A. J. Crosby, Z. Suo, and J. W. Hutchinson. Periodic patterns and energy states of buckled films on compliant substrates. *J. Mech. Phys. Solids*, 59:1094–1114, 2011.
[10] L. D. Landau and E. M. Lifshitz. *Elasticity theory*. Pergamon Press, New York, 1975.
[11] Y. Jeong, Y.-C. Chen, M. K. Turksoy, S. Rana, G. Y. Tonga, B. Creran, A. Sanyal, A. J. Crosby, and V. M. Rotello. Tunable elastic modulus of nanoparticle monolayer films by host–guest chemistry. *Advanced Materials*, in press, doi: 10.1002/adma.201401226, 2014.
[12] G. Cao, X. Chen, C. Li, A. Ji, and Z. Cao. Self-assembled triangular and labyrinth buckling patterns of thin films on spherical substrates. *Phys. Rev. Lett.*, 100(3):036102, 2008.
[13] J. Yin, Z. Cao, C. Li, I. Sheinman, and X. Chen. Stress-driven buckling patterns in spheroidal core/shell structures. *Proc. Natl Acad. Sci.*, 105(49):19132–19135, 2008.
[14] A. A. Golovin and A. A. Nepomnyashchy. *Self-assembly, pattern formation and growth phenomena in nano-systems*. Springer, Dordrecht, 2006.

C. INTERACTION FLUIDE-STRUCTURE ENTRE DEUX CYLINDRES CONCENTRIQUES

Dans cette annexe, la publication parue dans la revue *Journal of Applied Mechanics*, sous le titre "Viscous theory for the vibrations of coaxial Cylinders : analytical formulas for the fluid forces and the modal added coefficients" est reproduite[1].

[1] Nomination par Journal of Applied Mechanics pour le prix du meilleur article 2023.

Viscous Theory for the Vibrations of Coaxial Cylinders: Analytical Formulas for the Fluid Forces and the Modal Added Coefficients

Romain Lagrange[1]
Université Paris-Saclay, CEA,
Service d'Etudes Mécaniques et Thermiques,
F-91191 Gif-sur-Yvette, France
e-mail: romain.lagrange@cea.fr

Maria Adela Puscas
Université Paris-Saclay, CEA,
Service de Thermo-hydraulique et de
Mécanique des Fluides,
F-91191 Gif-sur-Yvette, France
e-mail: maria-adela.puscas@cea.fr

This article addresses the small-amplitude forced beam vibrations of two coaxial finite-length cylinders separated by a viscous Newtonian fluid. A new theoretical approach based on an Helmholtz expansion of the fluid velocity vector is carried out, leading to a full analytical expression of the fluid forces and subsequently of the modal added mass and damping coefficients. Our theory shows that the fluid forces are linear combinations of the Fourier harmonics of the vibration modes. The coefficients of the linear combinations are shown to depend on the aspect ratio of the cylinders, on the separation distance, and on the Stokes number. As a consequence, the linear fluid forces do not have, in general, the same shape as the forced vibration mode, so that the fluid makes it possible to couple vibration modes with different wave numbers. Compared to the previous works, the present theory includes the viscous effects of the fluid, accounts for the finite length of the cylinders, does not rely on the assumption of a narrow annulus, and covers in a unique formulation all types of classical boundary conditions for an Euler–Bernoulli beam. The theoretical predictions for the modal added mass and damping coefficients (self and cross) are corroborated numerically, considering rigid, pinned-pinned, and clamped-free vibrations.
[DOI: 10.1115/1.4056910]

Keywords: vibration, fluid–structure interaction, fluid forces, coaxial cylinders, viscosity

1 Introduction

This article addresses the hydrodynamic interaction between two elongated cylinders separated by a viscous quiescent fluid. This classical fluid–structure problem has been the topic of considerable works; see the book of Refs. [1,2] and the survey of Ref. [3] for an extensive bibliography; among which significant analytical contributions were provided by [4–14]. Usually, none of the theoretical approaches is a panacea for a large spectrum of boundary conditions and geometric complexities. Therefore, the analytical calculations mainly differ from each other by the structural models introduced to account for the free or forced vibrations of the inner and outer structures (rigid, beams, shells) and the properties of the coupling fluid (inviscid, viscous). For example, in Ref. [4], the case of flexible concentric cylinders imposed harmonic breathing shell modes (modes with no longitudinal wave number) was considered. A classical acoustic fluid equation for the pressure field was solved, leading to a complex solution expressed in terms of Bessel functions. In Ref. [7], a similar study was carried out on the small-amplitude vibrations (breathing mode) of flexible coaxial shells of infinite length, leading to exact expressions for the added mass coefficients (self and cross). In the same spirit, Ref. [8] considered the small oscillations of a flexible shell (regarded as a cantilever beam with a flexible support) surrounded by a rigid shell (representative of a reactor vessel). The slender-body formulation of Ref. [15] (two-dimensional hydrodynamic mass formulas for rigid fluid-coupled bodies) was used to perform a parametric study on the effects of the boundary stiffness and the confinement (narrow gap) on the modal added mass coefficients and the natural frequencies of the coupled system. This study was extended by Ref. [16], who replaced the slender-body assumption with a wave equation for compressible and incompressible fluid flow.

One of the reasons for the high interest in the fluid-coupled cylinders problem is that the added mass of the fluid, especially for a narrow annulus, can be several times larger than the mass of the structures that constitute the boundaries of the annulus. Hence, the modal characteristics of the structures are not just modified by the presence of the fluid but are strongly affected by it. Viscous effects, which mainly occur near the interface of the structure, in a thin layer of the rotational flow, are also of great importance in the dynamic response of coupled systems. Actually, in industrial applications, like the one that motivated this study and presented later, the added mass and damping effects may be so strong that they are sometimes the only effects taken into account by engineers in the calculation of the vibrational characteristics of the system, even when the fluid is flowing.

2 Industrial Context and Motivation

The present study finds its motivations in the context of the vibrations of internal components of the Jules Horowitz Reactor. This test reactor is mainly dedicated to the research on materials and fuels for the nuclear power industry and nuclear medicine, see Ref. [17] for more details. Essentially, the internal structure of the Jules Horowitz reactor is a system of finite, coaxial cylinders immersed in a fluid. A simplified schematic diagram of the reactor is shown in Fig. 1. The reactor core is made of cylindrical fuel elements of length $L = 0.7$ m. Aluminum cylindrical guide tubes, of length 2.1 m and outer diameter $2R_1 = 40$ mm, are inserted in the free space between fuel elements to guide experimental devices to be tested. The diameter of this free space is $2R_2 = 44$ mm so that the middle part of the guide tube is relatively confined (2 mm clearance). Upstream and downstream, the guide tube is less confined, and the clearance varies between 4 and 6 mm. The fuel

[1]Corresponding author.

Contributed by the Applied Mechanics Division of ASME for publication in the Journal of Applied Mechanics. Manuscript received December 15, 2022; final manuscript received February 8, 2023; published online March 6, 2023. Tech. Editor: Pradeep Sharma.

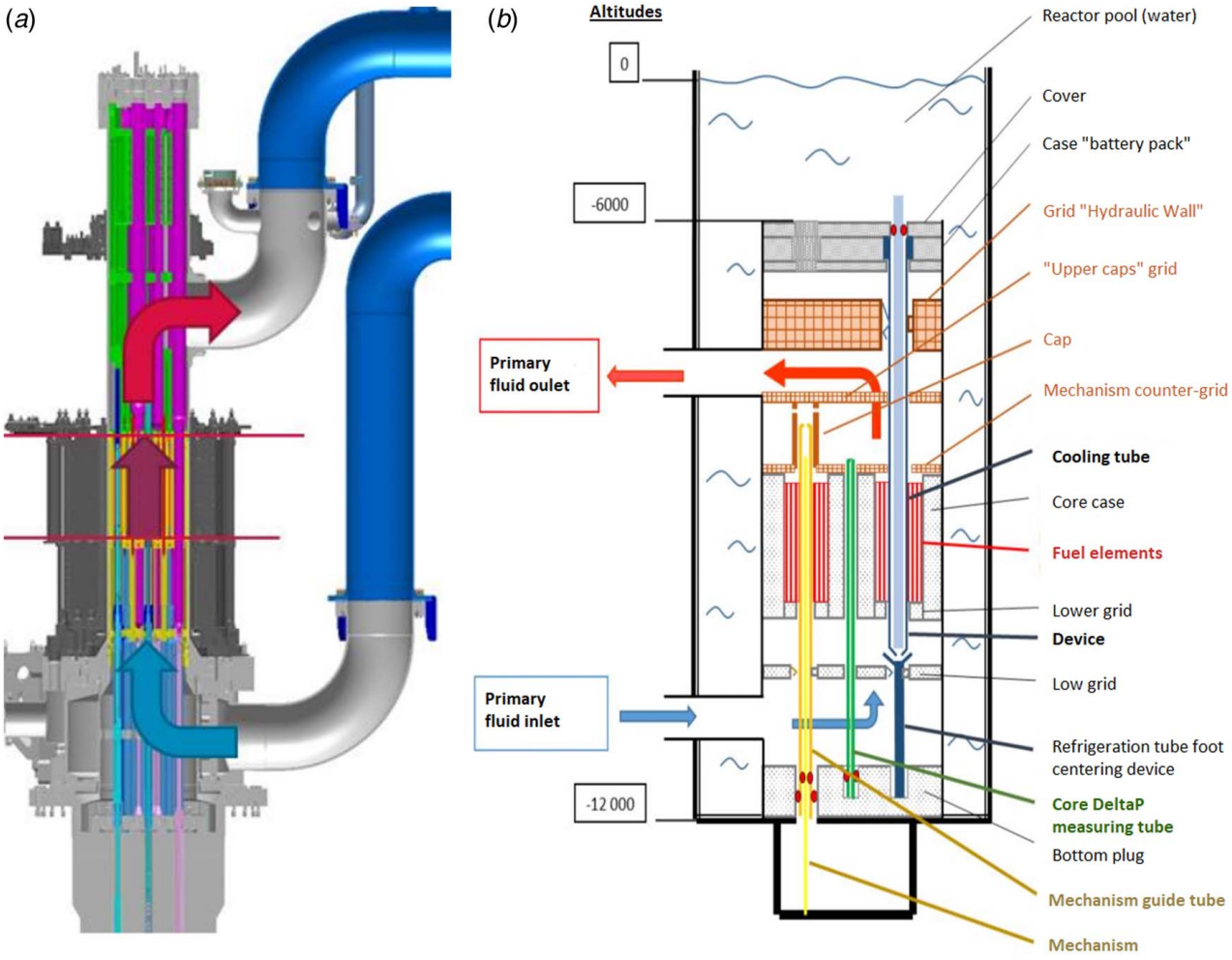

Fig. 1 Schematic diagram of the Jules Horowitz reactor, from Ref. [18]: (*a*) 3D sketch of the Jules Horowitz reactor and (*b*) axial cross section of the Jules Horowitz reactor

elements and the guide tubes are flexible and are subjected to random vibration induced by a turbulent axial flow from the primary circuit. The slender-body approximation is irrelevant here since, for instance, the middle part of the guide tube is not sufficiently slender, i.e., $L/R_1 = 35$.

This article reconsiders the analytical calculation of the hydrodynamics forces acting on coaxial elongated cylinders separated by a viscous stagnant Newtonian fluid. The cylinders are imposed small-amplitude harmonic beam vibrations.

The dynamics of the two cylinders (length L) is usually modeled by a system of forced oscillator equations. For a given couple of structural vibration modes (W_1, W_2) of cylinders ($\mathcal{C}_1, \mathcal{C}_2$), equations for the modal amplitudes (A_1, A_2) are given as follows:

$$M_{s_1}\frac{\mathrm{d}^2A_1}{\mathrm{d}T^2} + C_{s_1}\frac{\mathrm{d}A_1}{\mathrm{d}T} + K_{s_1}A_1 = \left\langle W_1, \overline{F_{T_1}} + \overline{F_{11}} + \overline{F_{12}} \right\rangle_L \tag{1a}$$

$$M_{s_2}\frac{\mathrm{d}^2A_2}{\mathrm{d}T^2} + C_{s_2}\frac{\mathrm{d}A_2}{\mathrm{d}T} + K_{s_2}A_2 = \left\langle W_2, \overline{F_{T_2}} + \overline{F_{22}} + \overline{F_{21}} \right\rangle_L \tag{1b}$$

where T, M_{s_i}, C_{s_i}, and K_{s_i} are the dimensional time, modal structural mass, damping, and rigidity coefficients, respectively. The right-hand side forcing terms in Eq. (1) represent modal forces, i.e., linear fluid forces $\overline{F_{T_i}} + \overline{F_{ij}}$ projected onto vibration modes W_i, according to the scalar product $\langle W_i, \overline{F_{ij}} \rangle_L = \int_0^L W_i \overline{F_{ij}}\,\mathrm{d}L$. The term $\overline{F_{T_i}}$ refers to a turbulent (random) linear fluid force, considered as independent of cylinder vibrations. The term $\overline{F_{ij}}$ refers to the linear fluid force acting on $\mathcal{C}_i$ due to the vibration of $\mathcal{C}_j$. This latter is assumed to be a linear combination of the modal acceleration $\mathrm{d}^2A_j/\mathrm{d}T^2$, velocity $\mathrm{d}A_j/\mathrm{d}T$, and position A_j, i.e.,

$$\left\langle W_i, \overline{F_{ij}} \right\rangle_L = -M_{ij}\frac{\mathrm{d}^2A_j}{\mathrm{d}T^2} - C_{ij}\frac{\mathrm{d}A_j}{\mathrm{d}T} - K_{ij}A_j \tag{2}$$

where M_{ij}, C_{ij}, and K_{ij} the modal added mass, damping, and rigidity coefficients, respectively (self coefficients if $i = j$, cross coefficients otherwise). As most often assumed, it is postulated that the modal added mass M_{ij} does not depend on flow velocity, whereas C_{ij} and K_{ij} are expanded as follows:

$$C_{ij} = C_{ij}^{(0)} + \hat{C}_{ij}, \quad K_{ij} = K_{ij}^{(0)} + \hat{K}_{ij} \tag{3}$$

The term $C_{ij}^{(0)}$ (resp. $K_{ij}^{(0)}$) is the modal added damping (resp. stiffness) in a still fluid, and $\hat{C}_{ij}$ (resp. $\hat{K}_{ij}$) is a complementary damping (resp. stiffness) due to fluid flow velocity. Usually, surface stiffness effects in still fluid are neglected, i.e., $K_{ij}^{(0)} = 0$, so that Eq. (1) is rewritten as follows:

$$\begin{aligned}\left(M_{s_1} + M_{11}\right)\frac{\mathrm{d}^2A_1}{\mathrm{d}T^2} + M_{12}\frac{\mathrm{d}^2A_2}{\mathrm{d}T^2} + \left(C_{s_1} + C_{11}^{(0)} + \hat{C}_{11}\right)\frac{\mathrm{d}A_1}{\mathrm{d}T} \\ + \left(C_{12}^{(0)} + \hat{C}_{12}\right)\frac{\mathrm{d}A_2}{\mathrm{d}T} + \left(K_{s_1} + \hat{K}_{11}\right)A_1 + \hat{K}_{12}A_2 = \left\langle W_1, \overline{F_{T_1}} \right\rangle_L\end{aligned} \tag{4a}$$

$$\left(M_{s_2}+M_{22}\right)\frac{\mathrm{d}^2A_2}{\mathrm{d}T^2}+M_{21}\frac{\mathrm{d}^2A_1}{\mathrm{d}T^2}+\left(C_{s_2}+C_{22}^{(0)}+\hat{C}_{22}\right)\frac{\mathrm{d}A_2}{\mathrm{d}T}$$
$$+\left(C_{21}^{(0)}+\hat{C}_{21}\right)\frac{\mathrm{d}A_1}{\mathrm{d}T}+\left(K_{s_2}+\hat{K}_{22}\right)A_2+\hat{K}_{21}A_1=\left\langle W_2,\overline{F_{T_2}}\right\rangle_L \tag{4b}$$

The modal coefficients in Eq. (4) determine the linear stability properties of the coupled system subjected to the axial flow. As a first step toward this goal, in what follows, we derive a new three-dimensional theoretical approach leading to a full analytical expression of coefficients M_{ij} and $C_{ij}^{(0)}$. These expressions are presented in dimensionless forms, see Eq. (51), introducing rescaled quantities as follows:

$$C_m^{(ij)}=\frac{M_{ij}}{L\rho R_iR_j\pi}\frac{1}{N_iN_j},\quad C_v^{(ij)}=\frac{C_{ij}^{(0)}}{L\rho R_iR_j\pi\Omega_j}\frac{1}{N_iN_j} \tag{5}$$

where N_i is the infinite norm of W_i, R_i is the radius of $\mathcal{C}_i$, Ω_i is the angular frequency of motion, and ρ is the fluid density; see Sec. 3 for precise definitions.

This new theory (i) includes the viscous effects of the fluid so that added damping is accounted for, (ii) does not rely on the assumption of a narrow annulus, contrarily to [19–22], so that it applies to all sizes of the fluid gap (some internal components of the Jules Horowitz reactor, such as the middle part of the guide tube, are highly confined; others, such as the upstream and downstream parts of the guide tube, are less so), (iii) does not rely on the slender-body approximation, contrarily to Refs. [9,10,23], so that it applies to elongated cylinders with finite aspect ratios, and (iv) considers arbitrary forced beam vibrations so that it does not only apply to a special case of boundary conditions (the boundary conditions in the Jules Horowitz project being multiple).

This article is organized as follows. In Sec. 3, we introduce the problem and the governing equations. In Sec. 4, we present the theoretical formulation to estimate the modal fluid forces and the dimensionless modal fluid added coefficients. A comparison between theoretical predictions and numerical results is presented in Sec. 5, considering rigid, pinned-pinned, and clamped-free vibrations. Finally, some conclusions are drawn in Sec. 6.

3 Definition of the Problem and Governing Equations

We consider the hydrodynamic interaction of two coaxial flexible and circular cylinders $\mathcal{C}_i$, $(i=1,2)$, with axis along $\mathbf{e}_x$, length L, radii R_i, and boundaries $\partial\mathcal{C}_i$, separated by a viscous fluid layer, as illustrated in Fig. 2. The cylinder $\mathcal{C}_i$ is imposed a harmonic displacement $\mathfrak{R}\{A_i(T)\mathbf{W}_i(X)\}$, where $\mathfrak{R}$ is the real part operator, $A_i(T)=Q_ie^{\mathrm{i}\Omega_iT}$ is the complex amplitude, i is the unit imaginary number, $\mathbf{W}_i(X)=\cos(K_iX+\delta_i)\mathbf{e}_y$ is the vibration mode, aligned with the $\mathbf{e}_y$ direction orthogonal to $\mathbf{e}_x$, K_i its wave number, δ_i its phase, and $X\in[0,L]$ the axial coordinate.

3.1 Euler Equations and Boundary Conditions. The fluid is Newtonian, homogeneous, of volume mass density ρ and kinematic viscosity ν. Assuming that the amplitude of the displacement remains small compared to the thickness of the fluid layer, i.e., $Q_i\ll R_2-R_1$, the nonlinear term of the Navier–Stokes equations is negligible. It follows that the flow expands as a linear combination of the form $\mathfrak{R}\left\{\sum_{i=1}^{2}e^{\mathrm{i}\Omega_iT}(\mathbf{V}_i,P_i)\right\}$ where $(\mathbf{V}_i,P_i)$ is the solution of the Euler equations and boundary conditions

$$\nabla\cdot\mathbf{V}_i=0 \tag{6a}$$

$$\mathrm{i}\Omega_i\mathbf{V}_i+\frac{1}{\rho}\nabla P_i-\nu\Delta\mathbf{V}_i=\mathbf{0} \tag{6b}$$

$$\mathbf{V}_i-\mathrm{i}\Omega_iQ_i\mathbf{W}_i=\mathbf{0}\quad\text{on }\partial\mathcal{C}_i \tag{6c}$$

$$\mathbf{V}_i=\mathbf{0}\quad\text{on }\partial\overline{\mathcal{C}_i} \tag{6d}$$

$$P_i=0\quad\text{at }X=0\quad\text{and}\quad X=L \tag{6e}$$

The third (resp. fourth) equation expresses the continuity of velocities at the boundary of the moving (resp. stationary) cylinder $\mathcal{C}_i$ (resp. $\overline{\mathcal{C}_i}$). The fluid force on $\mathcal{C}_i$ due to the motion of $\mathcal{C}_j$ is $\mathfrak{R}\left\{\sum_{j=1}^{2}e^{\mathrm{i}\Omega_jT}\mathbf{F}_{ij}\right\}$ and is the sum of a pressure and a viscous term, i.e.,

$$\mathbf{F}_{ij}=-\int_{\partial\mathcal{C}_i}P_j\mathbf{n}_i\,\mathrm{d}S_i+\rho\nu\int_{\partial\mathcal{C}_i}\left[\nabla\mathbf{V}_j+\left(\nabla\mathbf{V}_j\right)^T\right]\cdot\mathbf{n}_i\,\mathrm{d}S_i \tag{7}$$

In this equation, $\mathbf{n}_i$ is the outward normal unit vector to $\partial\mathcal{C}_i$, $\left(\nabla\mathbf{V}_j\right)^T$ is the transposate tensor of $\nabla\mathbf{V}_j$, and dS_i is an infinitesimal surface element of $\partial\mathcal{C}_i$. The associated linear fluid force, noted $\overline{\mathbf{F}_{ij}}$, is defined as $\mathbf{F}_{ij}=\int_0^L\overline{\mathbf{F}_{ij}}\,\mathrm{d}X$.

3.2 Dimensionless Euler Equations and Boundary Conditions. Let R_2-R_1 and Ω_i^{-1} be the characteristic length and time. We define w_i, $\mathbf{v}_i$, p_i, and $\mathbf{f}_{ij}$ as follows:

$$\mathbf{W}_i(X)=w_i\left(\frac{X}{L}\right)\mathbf{e}_y,\quad\mathbf{V}_i=Q_i\Omega_i\mathbf{v}_i,\quad P_i=\rho(R_2-R_1)Q_i{\Omega_i}^2p_i,$$
$$\mathbf{F}_{ij}=\rho\pi R_iLR_jQ_j{\Omega_j}^2\mathbf{f}_{ij} \tag{8}$$

which are the dimensionless displacement, fluid velocity, fluid pressure, and fluid force, respectively. The dimensionless vibration mode is given as follows:

$$w_i(x)=\cos(k_ix+\delta_i) \tag{9}$$

where $k_i=K_iL$ is the dimensionless wave number and $x=X/L$ is the dimensionless axial coordinate. To reduce the number of parameters of the problem, we also introduce the rescaled quantities

$$l=\frac{L}{R_1},\quad\varepsilon=\frac{R_2}{R_1},\quad\mathrm{Sk}_i=\frac{(R_2-R_1)^2\Omega_i}{\nu} \tag{10}$$

as the aspect ratio, radius ratio, and Stokes number, respectively. Introducing the dimensionless operators $\nabla^*=(R_2-R_1)\nabla$ and $\Delta^*=(R_2-R_1)^2\Delta$, the dimensionless Euler equations and boundary conditions are given as follows:

$$\nabla^*\cdot\mathbf{v}_i=0 \tag{11a}$$

$$\mathrm{i}\mathbf{v}_i+\nabla^*p_i-\frac{1}{\mathrm{Sk}_i}\Delta^*\mathbf{v}_i=\mathbf{0} \tag{11b}$$

$$\mathbf{v}_i=\mathrm{i}w_i\mathbf{e}_y\quad\text{on }\partial\mathcal{C}_i \tag{11c}$$

$$\mathbf{v}_i=\mathbf{0}\quad\text{on }\partial\overline{\mathcal{C}_i} \tag{11d}$$

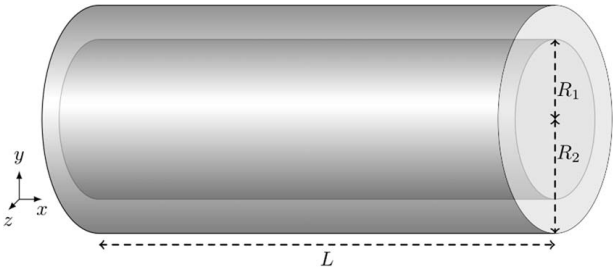

Fig. 2 Two coaxial cylinders separated by a viscous fluid layer

$$p_i = 0 \quad \text{at } x = 0 \quad \text{and} \quad x = 1 \tag{11e}$$

The dimensionless fluid force is expressed as follows:

$$\mathbf{f}_{ij} = (\varepsilon - 1)\varepsilon^{1-j}\frac{1}{\pi}\left[\int_{\partial\mathcal{C}_i} -p_j\mathbf{n}_i\,\mathrm{d}s_i + \frac{1}{\mathrm{Sk}_j}\int_{\partial\mathcal{C}_i}\boldsymbol{\tau}_j\,\mathrm{d}s_i\right] \tag{12}$$

where $\mathrm{d}s_i = \mathrm{d}S_i/(R_i L)$ and $\boldsymbol{\tau}_j = \left[\nabla^*\mathbf{v}_j + \left(\nabla^*\mathbf{v}_j\right)^T\right]\cdot\mathbf{n}_i$ is the dimensionless viscous stress vector. The associated dimensionless linear fluid force, noted $\overline{\mathbf{f}_{ij}}$, is defined as $\mathbf{f}_{ij} = \int_0^1 \overline{\mathbf{f}_{ij}}\,\mathrm{d}x$.

4 Theoretical Solution

4.1 Helmholtz Decomposition. We seek a solution of Eq. (11) as a superposition of an irrotational and a divergence-free flow (Helmholtz decomposition):

$$\mathbf{v}_i = \nabla^*\phi_i + \nabla^*\times\boldsymbol{\psi}_i \tag{13}$$

where ϕ_i and $\boldsymbol{\psi}_i$ some unknown potential and stream functions, respectively. Introducing this decomposition in Eq. (11) yields the dimensionless Euler equations:

$$\Delta^*\phi_i = 0 \tag{14a}$$

$$\nabla^*\times\left(\Delta^*\boldsymbol{\psi}_i - \mathrm{iSk}_i\boldsymbol{\psi}_i\right) - \mathrm{Sk}_i\nabla^*\left(\mathrm{i}\phi_i + p_i\right) = \mathbf{0} \tag{14b}$$

Taking the divergence and the curl of Eq. (14b) yields two equations:

$$p_i = -\mathrm{i}\phi_i \tag{15a}$$

$$\Delta^*\boldsymbol{\psi}_i + \beta_i^2\boldsymbol{\psi}_i = \mathbf{0} \quad \text{with } \beta_i = \sqrt{-\mathrm{iSk}_i} \tag{15b}$$

from which the pressure and the stream functions can be determined.

4.2 Fluid Functions. To solve the Laplace Eq. (14a) and the Helmholtz Eq. (15b), along with the boundary conditions (11c)–(11e), we introduce the dimensionless cylindrical coordinates (r, θ, x) and the associated physical basis $\mathcal{B} = (\mathbf{e}_r, \mathbf{e}_\theta, \mathbf{e}_x)$. In this basis, the displacement $w_i\mathbf{e}_y$ expands as $w_i(\cos(\theta), -\sin(\theta), 0)$ so that ϕ_i and $\boldsymbol{\psi}_i$ shall be functions of $\cos(\theta)$ and $\sin(\theta)$. Also, as the gradient and the curl operators ∇^* and $\nabla^*\times$ are first-order derivatives in x, the functions ϕ_i and $\boldsymbol{\psi}_i$ shall be linear combinations of w_i and $\mathrm{d}w_i/\mathrm{d}x$. The displacement function $w_i(x) = \cos(k_i x + \delta_i)$ is defined for $x \in [0, 1]$ and in general does not satisfy $w_i(0) = w_i(1) = 0$. In order to fulfill the pressure boundary conditions, $p_i(0) = p_i(1) = 0$, it is thus necessary to extend w_i to an odd function of period 2 whose Fourier series converges to w_i for $x \in [0, 1]$ i.e.,

$$\forall x \in [0,1], \quad w_i(x) = \sum_{n=1}^{\infty} w_{in}(x) \tag{16}$$

where

$$w_{in}(x) = b_n(k_i,\delta_i)\sin(n\pi x) \quad \text{and}$$
$$b_n(k,\delta) = 2\int_0^1 \cos(kx+\delta)\sin(n\pi x)\,\mathrm{d}x \tag{17}$$

Finally, to uncouple the $\mathbf{e}_r$ and $\mathbf{e}_\theta$ projections of the Helmholtz Eq. (15b), one should seek a stream function $\boldsymbol{\psi}_i$ whose radial and orthoradial components have the same variations in the polar coordinate r but are in phase quadrature for the angle θ. Accounting for all the aforementioned conditions, we seek fluid functions of the form $(\phi_i, \boldsymbol{\psi}_i) = \sum_{n=1}^{\infty}(\phi_{in}, \boldsymbol{\psi}_{in})$ with

$$\phi_{in}(r,\theta,x) = \Phi_{in}(r)\cos(\theta)w_{in}(x) \tag{18a}$$

$$\boldsymbol{\psi}_{in}(r,\theta,x) = \begin{pmatrix} 0 \\ 0 \\ \Psi_{in}(r)\sin(\theta) \end{pmatrix} w_{in}(x) + \frac{\varepsilon-1}{l}\begin{pmatrix} \mathrm{A}_{in}(r)\sin(\theta) \\ \mathrm{A}_{in}(r)\cos(\theta) \\ 0 \end{pmatrix}\frac{\mathrm{d}w_{in}}{\mathrm{d}x}(x) \tag{18b}$$

where the matrix notation in Eq. (18b) is used to express the components of $\boldsymbol{\psi}_{in}$ in the basis $\mathcal{B}$. Plugging Eqs. (17) and (18a) into Eq. (15a) yields a n th Fourier harmonics for the pressure field of the form

$$p_{in}(r,\theta,x) = -\mathrm{i}\Phi_{in}(r)\cos(\theta)b_n(k_i,\delta_i)\sin(n\pi x) \tag{19}$$

so that the pressure boundary conditions (11e) are automatically satisfied. The dimensionless differential operators applied to Eq. (18) are given as follows:

$$\nabla^*\phi_{in} = \begin{pmatrix} \dfrac{\mathrm{d}\Phi_{in}}{\mathrm{d}r}\cos(\theta) \\ -\frac{1}{r}\Phi_{in}\sin(\theta) \\ 0 \end{pmatrix} w_{in} + \frac{\varepsilon-1}{l}\begin{pmatrix} 0 \\ 0 \\ \Phi_{in}\cos(\theta) \end{pmatrix}\frac{\mathrm{d}w_{in}}{\mathrm{d}x} \tag{20a}$$

$$\Delta^*\phi_{in} = \left[\frac{\mathrm{d}^2\Phi_{in}}{\mathrm{d}r^2} + \frac{1}{r}\frac{\mathrm{d}\Phi_{in}}{\mathrm{d}r} + \left({\gamma_n}^2 - \frac{1}{r^2}\right)\Phi_{in}\right]\cos(\theta)w_{in} \tag{20b}$$

$$\nabla^*\times\boldsymbol{\psi}_{in} = \begin{pmatrix} \left(\frac{1}{r}\Psi_{in} - {\gamma_n}^2\mathrm{A}_{in}\right)\cos(\theta) \\ -\left(\dfrac{\mathrm{d}\Psi_{in}}{\mathrm{d}r} - {\gamma_n}^2\mathrm{A}_{in}\right)\sin(\theta) \\ 0 \end{pmatrix} w_{in} + \frac{\varepsilon-1}{l}\begin{pmatrix} 0 \\ 0 \\ \dfrac{\mathrm{dA}_{in}}{\mathrm{d}r}\cos(\theta) \end{pmatrix}\frac{\mathrm{d}w_{in}}{\mathrm{d}x} \tag{20c}$$

$$\Delta^*\boldsymbol{\psi}_{in} = \begin{pmatrix} 0 \\ 0 \\ \left[\dfrac{\mathrm{d}^2\Psi_{in}}{\mathrm{d}r^2} + \dfrac{1}{r}\dfrac{\mathrm{d}\Psi_{in}}{\mathrm{d}r} + \left({\gamma_n}^2 - \dfrac{1}{r^2}\right)\Psi_{in}\right]\sin(\theta) \end{pmatrix} w_{in} \tag{20d}$$

$$+\frac{\varepsilon-1}{l}\begin{pmatrix} \left(\dfrac{\mathrm{d}^2\mathrm{A}_{in}}{\mathrm{d}r^2} + \dfrac{1}{r}\dfrac{d\mathrm{A}_{in}}{\mathrm{d}r} + {\gamma_n}^2\mathrm{A}_{in}\right)\sin(\theta) \\ \left(\dfrac{\mathrm{d}^2\mathrm{A}_{in}}{\mathrm{d}r^2} + \dfrac{1}{r}\dfrac{\mathrm{d}\mathrm{A}_{in}}{\mathrm{d}r} + {\gamma_n}^2\mathrm{A}_{in}\right)\cos(\theta) \\ 0 \end{pmatrix}\frac{\mathrm{d}w_{in}}{\mathrm{d}x} \tag{20e}$$

where

$$\gamma_n = \mathrm{i}\frac{n\pi}{l}(\varepsilon - 1) \tag{21}$$

The magnitude of γ_n is $(n\pi/L)/(R_2 - R_1)$ so that it expresses the ratio between the wave-number of the n th Fourier component of the displacement w_i and the thickness $R_2 - R_1$ of the duct.

From Eq. (20b), the Laplace Eq. (14a) is written as follows:

$$r^2\frac{\mathrm{d}^2\Phi_{in}}{\mathrm{d}r^2} + r\frac{\mathrm{d}\Phi_{in}}{\mathrm{d}r} + \left[\left(\gamma_n r\right)^2 - 1\right]\Phi_{in} = 0 \tag{22}$$

From Eq. (20e), the Helmholtz Eq. (15b) projected onto the basis $\mathcal{B}$ has the same component along the $\mathbf{e}_r$ and $\mathbf{e}_\theta$ directions:

$$r^2\frac{\mathrm{d}^2\mathrm{A}_{in}}{\mathrm{d}r^2} + r\frac{\mathrm{d}\mathrm{A}_{in}}{\mathrm{d}r} + (\alpha_{in}r)^2\mathrm{A}_{in} = 0 \tag{23}$$

whereas the component along $\mathbf{e}_x$ is given as follows:

$$r^2\frac{\mathrm{d}^2\Psi_{in}}{\mathrm{d}r^2} + r\frac{\mathrm{d}\Psi_{in}}{\mathrm{d}r} + \left[(\alpha_{in}r)^2 - 1\right]\Psi_{in} = 0 \tag{24}$$

where

$$\alpha_{in}{}^2 = \gamma_n{}^2 + \beta_i{}^2 = \gamma_n{}^2 - \mathrm{i}\mathrm{Sk}_i \tag{25}$$

The solutions of (22)–(24) are linear combinations of Hankel functions of the first and second kind, so that the fluid functions are written as follows:

$$\begin{bmatrix} \Phi_{in}(r) \\ \Psi_{in}(r) \\ \mathrm{A}_{in}(r) \end{bmatrix} = \left[B\left(\gamma_n r, \alpha_{in} r\right)\right]\left[C\left(r_i, \gamma_n, \alpha_{in}\right)\right] \tag{26}$$

where $r_i = R_i/(R_2 - R_1)$ is the dimensionless radial coordinate of the points lying on the boundary $\partial\mathcal{C}_i$ of the moving cylinder and

$$\left[B\left(\gamma_n r, \alpha_{in} r\right)\right] = \begin{bmatrix} \mathrm{H}_1^{(1)}(\gamma_n r) & \mathrm{H}_1^{(2)}(\gamma_n r) & 0 & 0 & 0 & 0 \\ 0 & 0 & \mathrm{H}_1^{(1)}(\alpha_{in} r) & \mathrm{H}_1^{(2)}(\alpha_{in} r) & 0 & 0 \\ 0 & 0 & 0 & 0 & \mathrm{H}_0^{(1)}(\alpha_{in} r) & \mathrm{H}_0^{(2)}(\alpha_{in} r) \end{bmatrix} \tag{27}$$

For a given set of parameters r_i, γ_n, and α_{in}, the vector $[C(r_i, \gamma_n, \alpha_{in})]$ is composed of six constants determined by the conditions (11*c*) and (11*d*) at the cylinders boundaries. In terms of the fluid functions, the projection of Eqs. (11*c*) and (11*d*) onto the basis $\mathcal{B}$ yields two sets of boundary conditions:

$$\begin{cases} \dfrac{\mathrm{d}\Phi_{in}}{\mathrm{d}r} + \dfrac{1}{r}\Psi_{in} - \gamma_n{}^2 \mathrm{A}_{in} = \mathrm{i} \\ \dfrac{1}{r}\Phi_{in} + \dfrac{\mathrm{d}\Psi_{in}}{\mathrm{d}r} - \gamma_n{}^2 \mathrm{A}_{in} = \mathrm{i} \text{ at } r = r_i, \\ \Phi_{in} + \dfrac{\mathrm{dA}_{in}}{\mathrm{d}r} = 0 \end{cases} \tag{28}$$

$$\begin{cases} \dfrac{\mathrm{d}\Phi_{in}}{\mathrm{d}r} + \dfrac{1}{r}\Psi_{in} - \gamma_n{}^2 \mathrm{A}_{in} = 0 \\ \dfrac{1}{r}\Phi_{in} + \dfrac{\mathrm{d}\Psi_{in}}{\mathrm{d}r} - \gamma_n{}^2 \mathrm{A}_{in} = 0 \text{ at } r = \overline{r_i} \\ \Phi_{in} + \dfrac{\mathrm{dA}_{in}}{\mathrm{d}r} = 0 \end{cases}$$

where $\overline{r_i} = (r_1 + r_2) - r_i$ is the radial coordinate of the points lying on the boundary $\partial\overline{\mathcal{C}_i}$ of the stationary cylinder. The solution of the linear system (28) is

$$\left[C\left(r_i, \gamma_n, \alpha_{in}\right)\right] = \begin{bmatrix} \left[M\left(r_i, \gamma_n, \alpha_{in}\right)\right] \\ \left[M\left(\overline{r_i}, \gamma_n, \alpha_{in}\right)\right] \end{bmatrix}^{-1} [Q] \tag{29}$$

where $[Q] = \mathrm{i}[1\ 1\ 0\ 0\ 0\ 0]^T$ and

$$\left[M\left(r, \gamma, \alpha\right)\right] = \begin{bmatrix} \gamma \mathrm{H}_1^{(1)\prime}(\gamma r) & \gamma \mathrm{H}_1^{(2)\prime}(\gamma r) & \dfrac{\mathrm{H}_1^{(1)}(\alpha r)}{r} & \dfrac{\mathrm{H}_1^{(2)}(\alpha r)}{r} & -\gamma^2 \mathrm{H}_0^{(1)}(\alpha r) & -\gamma^2 \mathrm{H}_0^{(2)}(\alpha r) \\ \dfrac{\mathrm{H}_1^{(1)}(\gamma r)}{r} & \dfrac{\mathrm{H}_1^{(2)}(\gamma r)}{r} & \alpha \mathrm{H}_1^{(1)\prime}(\alpha r) & \alpha \mathrm{H}_1^{(2)\prime}(\alpha r) & -\gamma^2 \mathrm{H}_0^{(1)}(\alpha r) & -\gamma^2 \mathrm{H}_0^{(2)}(\alpha r) \\ \mathrm{H}_1^{(1)}(\gamma r) & \mathrm{H}_1^{(2)}(\gamma r) & 0 & 0 & \alpha \mathrm{H}_0^{(1)\prime}(\alpha r) & \alpha \mathrm{H}_0^{(2)\prime}(\alpha r) \end{bmatrix} \tag{30}$$

In Eq. (30), the prime subscript notation on the Hankel functions stands for the derivative with the r variable. Finally, plugging Eq. (29) into Eq. (26) yields an expression of the fluid functions

$$\begin{bmatrix} \Phi_{in}(r) \\ \Psi_{in}(r) \\ \mathrm{A}_{in}(r) \end{bmatrix} = \left[B\left(\gamma_n r, \alpha_{in} r\right)\right]\begin{bmatrix} \left[M\left(r_i, \gamma_n, \alpha_{in}\right)\right] \\ \left[M\left(\overline{r_i}, \gamma_n, \alpha_{in}\right)\right] \end{bmatrix}^{-1} [Q] \tag{31}$$

4.2.1 Inviscid Limit, $\mathrm{Sk_i} \to \infty$, i.e., $|\alpha_{in}| \to \infty$. The particular case of an inviscid fluid is recovered from the present viscous theory by taking the limit $\mathrm{Sk}_i \to \infty$ so that $|\alpha_{in}| \to \infty$. In such a case, the stream function vanishes, i.e., $\boldsymbol{\psi}_i = \mathbf{0}$, whereas the potential function is given as follows:

$$\phi_{in}^{(\mathrm{POT})}(r, \theta, x) = \Phi_{in}^{(\mathrm{POT})}(r)\cos(\theta) w_{in}(x) \tag{32}$$

where $\Phi_{in}^{(\mathrm{POT})}$ is the solution of the Laplace equation:

$$r^2 \frac{\mathrm{d}^2 \Phi_{in}^{(\mathrm{POT})}}{\mathrm{d}r^2} + r \frac{\mathrm{d}\Phi_{in}^{(\mathrm{POT})}}{\mathrm{d}r}\left[\left(\gamma_n r\right)^2 - 1\right]\Phi_{in}^{(\mathrm{POT})} = 0 \tag{33}$$

For the inviscid problem, the boundary conditions (28) reduce to

$$\frac{\mathrm{d}\Phi_{in}^{(\mathrm{POT})}}{\mathrm{d}r} = \mathrm{i} \text{ at } r = r_i, \quad \frac{\mathrm{d}\Phi_{in}^{(\mathrm{POT})}}{\mathrm{d}r} = 0 \text{ at } r = \overline{r_i} \tag{34}$$

so that the inviscid potential function is given as follows:

$$\Phi_{in}^{(\mathrm{POT})}(r) = \left[B^{(\mathrm{POT})}\left(\gamma_n r\right)\right]\begin{bmatrix} \left[M^{(\mathrm{POT})}\left(r_i, \gamma_n\right)\right] \\ \left[M^{(\mathrm{POT})}\left(\overline{r_i}, \gamma_n\right)\right] \end{bmatrix}^{-1} \left[Q^{(\mathrm{POT})}\right] \tag{35}$$

where $\left[Q^{(\mathrm{POT})}\right] = i\begin{bmatrix} 1 & 0 \end{bmatrix}^T$ and

$$\left[B^{(\mathrm{POT})}\left(\gamma_n r\right)\right] = \begin{bmatrix} \mathrm{H}_1^{(1)}(\gamma_n r) \mathrm{H}_1^{(2)}(\gamma_n r) \end{bmatrix} \tag{36}$$

$$\left[M^{(\mathrm{POT})}\left(r, \gamma\right)\right] = \begin{bmatrix} \gamma \mathrm{H}_1^{(1)\prime}(\gamma r) \gamma \mathrm{H}_1^{(2)\prime}(\gamma r) \end{bmatrix} \tag{37}$$

4.2.2 Slender-Body Limit, $\mathrm{l} \to \infty$, i.e., $|\gamma_n| \to 0$. The particular case of infinitely long cylinders has been covered by Ref. [10] who solved the two-dimensional viscous fluid problem by the mean of a stream function solution of a Laplace equation. The solution of Ref. [10] is recovered from the present three-dimensional theory by taking the limit $l \to \infty$ so that $|\gamma_n| \to 0$. In such a case, one has to disregard the pressure boundary conditions (11*e*) and consequently the Fourier expansion of w_i introduced in Eq. (16). In such a case, the fluid functions reduce to

$$\phi_i^{(2D)}(r, \theta) = \Phi_i^{(2D)}(r)\cos(\theta) \tag{38a}$$

$$\boldsymbol{\psi}_i^{(2D)}(r, \theta) = \Psi_i^{(2D)}(r)\sin(\theta)\mathbf{e}_x \tag{38b}$$

where $\Psi_i^{(2D)}$ and $\Psi_i^{(2D)}$ are solutions of the Laplace and the Helmholtz equations:

$$r^2 \frac{\mathrm{d}^2 \Phi_i^{(2D)}}{\mathrm{d}r^2} + r \frac{\mathrm{d}\Phi_i^{(2D)}}{\mathrm{d}r} - \Phi_i^{(2D)} = 0 \tag{39a}$$

$$r^2 \frac{\mathrm{d}^2 \Psi_i^{(2D)}}{\mathrm{d}r^2} + r \frac{\mathrm{d}\Psi_i^{(2D)}}{\mathrm{d}r} + \left[\left(\beta_i r\right)^2 - 1\right]\Psi_i^{(2D)} = 0 \tag{39b}$$

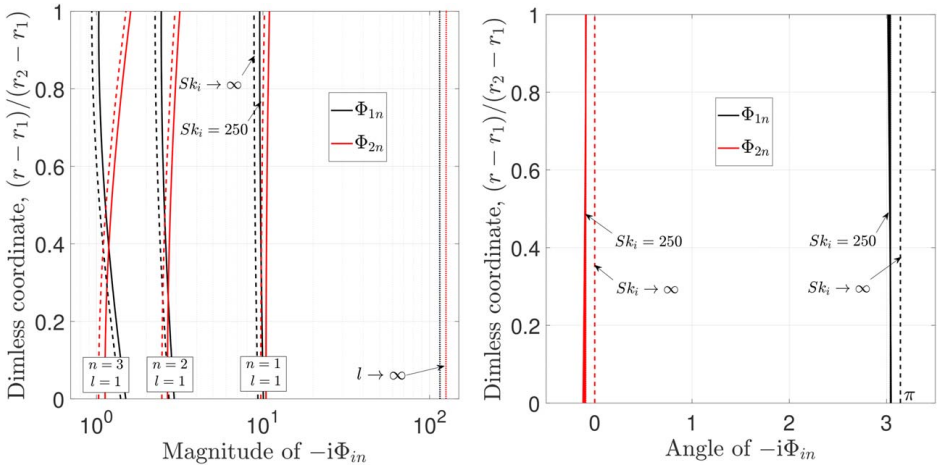

Fig. 3 Magnitude and angle of $-\mathrm{i}\Phi_{in}$ in the thickness of the duct, for $i=1$ (black), $i=2$ (red) and $n \in \{1, 2, 3\}$. The solid lines correspond to a Stokes number $\mathrm{Sk}_i = 250$ and an aspect ratio $l=1$. The dashed lines correspond to the inviscid limit $\mathrm{Sk}_i \to \infty$. The dotted lines correspond to the limit of infinitely long cylinders, $l \to \infty$, for $\mathrm{Sk}_i = 250$. On the right picture, the solid and dotted lines are indistinguishable. The radius ratio is $\varepsilon = 1.1$. (Color version online.)

For the two-dimensional fluid problem, the boundary conditions (28) reduce to

$$\left|\begin{array}{l} \dfrac{\mathrm{d}\Phi_i^{(2D)}}{\mathrm{d}r} + \dfrac{1}{r}\Psi_i^{(2D)} = \mathrm{i} \\ \dfrac{1}{r}\Phi_i^{(2D)} + \dfrac{\mathrm{d}\Psi_i^{(2D)}}{\mathrm{d}r} = \mathrm{i} \end{array}\right. \text{at } r = r_i, \qquad \left|\begin{array}{l} \dfrac{\mathrm{d}\Phi_i^{(2D)}}{\mathrm{d}r} + \dfrac{1}{r}\Psi_i^{(2D)} = 0 \\ \dfrac{1}{r}\Phi_i^{(2D)} + \dfrac{\mathrm{d}\Psi_i^{(2D)}}{\mathrm{d}r} = 0 \end{array}\right. \quad (40)$$

at $r = \overline{r_i}$

so that the fluid functions are given as follows:

$$\begin{bmatrix} \Phi_i^{(2D)}(r) \\ \Psi_i^{(2D)}(r) \end{bmatrix} = \left[B^{(2D)}(r,\beta_i r)\right] \begin{bmatrix} \left[M^{(2D)}(r_i,\beta_i)\right] \\ \left[M^{(2D)}(\overline{r}_i,\beta_i)\right] \end{bmatrix}^{-1} \left[Q^{(2D)}\right] \quad (41)$$

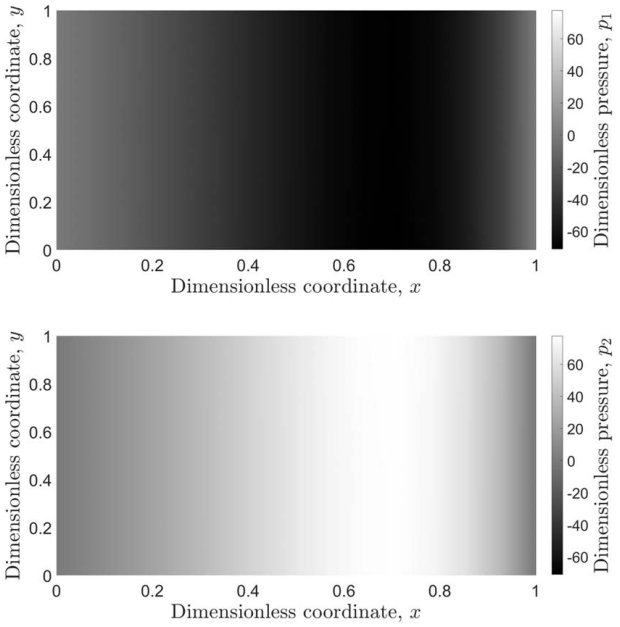

Fig. 4 Color map of the dimensionless pressure field $\Re\{p_i\}$ generated by the motion of C_i, which vibrates in the first mode of a clamped-free beam. The aspect ratio is $l=4$. The Stokes number is number $\mathrm{Sk}_i = 250$. The radius ratio is $\varepsilon = 1.1$.

where $\left[Q^{(2D)}\right] = \mathrm{i}\begin{bmatrix} 1 & 1 & 0 & 0 \end{bmatrix}^T$ and

$$\left[B^{(2D)}(r,\beta_i r)\right] = \begin{bmatrix} r & \dfrac{1}{r} & 0 & 0 \\ 0 & 0 & \mathrm{H}_1^{(1)}(\beta_i r) & \mathrm{H}_1^{(2)}(\beta_i r) \end{bmatrix} \quad (42a)$$

$$\left[M^{(2D)}(r,\beta)\right] = \begin{bmatrix} 1 & -\dfrac{1}{r^2} & \dfrac{\mathrm{H}_1^{(1)}(\beta r)}{r} & \dfrac{\mathrm{H}_1^{(2)}(\beta r)}{r} \\ 1 & \dfrac{1}{r^2} & \beta\mathrm{H}_1^{(1)\prime}(\beta r) & \beta\mathrm{H}_1^{(2)\prime}(\beta r) \end{bmatrix} \quad (42b)$$

By having determined the fluid functions, we now proceed with analyzing the variations of $-\mathrm{i}\Phi_{in}$, which is, according to Eq. (19), directly related to the pressure field p_i in the duct. In Fig. 3, we show that the magnitude and the angle of $-\mathrm{i}\Phi_{in}$ do not vary that much with the radial coordinate r, so that p_i is at the first-order constant in the thickness of the duct. The amplitude of p_i increases with the aspect ratio l of the cylinders, whereas the Stokes number Sk_i mainly affects the phase shift between p_i and w_i. Finally, for two cylinders vibrating in the same mode, i.e., $w_1 = w_2$, with the same frequency, i.e., $\mathrm{Sk}_1 = \mathrm{Sk}_2$, the pressures p_1 and p_2 have similar amplitudes and are in phase opposition. As a consequence, p_1 and p_2 tend to cancel each other out so that the total pressure in the duct is close zero. In Fig. 4, we show the pressure field in the half-plane $(\mathbf{e}_x, \mathbf{e}_y)$, $y > 0$, when C_i vibrates in the first mode of a clamped-free configuration. As expected from the variations of $-\mathrm{i}\Phi_{in}$, we recover that the pressure mostly varies along the x-direction and that $\Re\{p_1\} \approx -\Re\{p_2\}$.

4.3 Linear Fluid Forces. The viscous stress vector at the cylinders boundaries is obtained by substituting the Helmholtz decomposition (13) in $\boldsymbol{\tau}_j = \left[\nabla^* \mathbf{v}_j + \left(\nabla^* \mathbf{v}_j\right)^T\right] \cdot \mathbf{e}_r$. By using the boundary conditions (28), the components of $\boldsymbol{\tau}_{jn}$ in the basis $\mathcal{B}$ simplify to

$$\boldsymbol{\tau}_{jn} = \begin{pmatrix} 0 \\ \left(\alpha_{jn}{}^2\Psi_{jn} - \gamma_n{}^2\Phi_{jn}\right)\sin(\theta) \\ 0 \end{pmatrix} w_{jn} + \frac{\varepsilon - 1}{l} \times \begin{pmatrix} 0 \\ 0 \\ \left(2\dfrac{\mathrm{d}\Phi_{jn}}{\mathrm{d}r} + \dfrac{\Phi_{jn} + \Psi_{jn}}{r} - \left(\alpha_{jn}{}^2 + \gamma_n{}^2\right)\mathrm{A}_{jn}\right)\cos(\theta) \end{pmatrix} \frac{\mathrm{d}w_{jn}}{\mathrm{d}x} \quad (43)$$

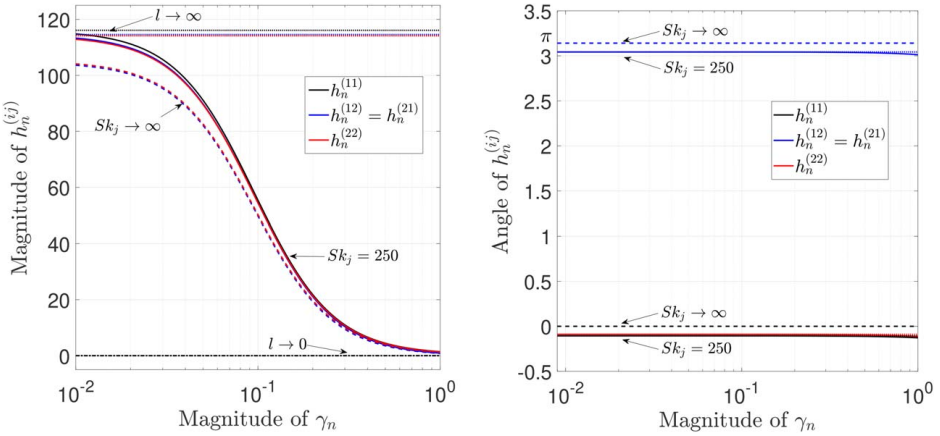

Fig. 5 Magnitude and angle of $h_n^{(ij)}$ as functions of $|\gamma_n|$, for $i=j=1$ (black), $i=j=2$ (red) and $i\neq j$ (blue). The solid lines correspond to a Stokes number $Sk_j=250$. The dashed lines (black and red are indistinguishable) correspond to the inviscid limit $Sk_j\to\infty$. The dotted lines correspond to the limit of infinitely long cylinders, $l\to\infty$, for $Sk_j=250$. The dashed-dotted line corresponds to the limit of infinitely short cylinders, $l\to 0$. On the right picture, the solid, dotted, and dash-dotted lines are indistinguishable. The radius ratio is $\varepsilon=1.1$. (Color version online.)

Plugging Eq. (43) and the pressure equation (15*a*) into Eq. (12) and assuming small displacement and deformation of the cylinders, i.e., $\mathbf{n}_i \approx (-1)^{i+1}\mathbf{e}_r$, show that the linear fluid force is aligned with the direction of motion, i.e., $\overline{\boldsymbol{f}_{ij}} = \overline{f_{ij}}\mathbf{e}_y$, with

$$\overline{f_{ij}} = (-1)^{i+1}(\varepsilon-1)\varepsilon^{1-j}\sum_{n=1}^{\infty}\mathrm{i}\left[\Phi_{jn}(r_i)+\frac{{\gamma_n}^2\Phi_{jn}(r_i)-{\alpha_{jn}}^2\Psi_{jn}(r_i)}{{\gamma_n}^2-{\alpha_{jn}}^2}\right]w_{jn} \tag{44}$$

The term $\mathrm{i}\Phi_{jn}(r_i)$ arises from the integration of the pressure field on the circumference of $\partial\mathcal{C}_i$, whereas the second term entering in the sum sign arises from the integration of the $\mathbf{e}_y$ component of the viscous stress vector $\boldsymbol{\tau}_{jn}$. From Eq. (44), the linear fluid force $\overline{f_i} = \overline{f_{i1}} + \overline{f_{i2}}$ acting on the cylinder $\mathcal{C}_i$ is written as follows:

$$\begin{bmatrix}\overline{f_1}\\ \overline{f_2}\end{bmatrix} = (\varepsilon-1)\sum_{n=1}^{\infty}\begin{bmatrix}h_n^{(11)} & h_n^{(12)}\\ h_n^{(21)} & h_n^{(22)}\end{bmatrix}\begin{bmatrix}b_{1n}\\ b_{2n}\end{bmatrix}\sin(n\pi x) \tag{45}$$

where $b_{jn} = b_n(k_j, \delta_j)$ is the n th Fourier coefficient of $w_j = \cos(k_j x + \delta_j)$, see Eq. (17) and

$$h_n^{(ij)} = h_n^{(ji)} = (-1)^{i+1}\varepsilon^{1-j}\mathrm{i}\left[\Phi_{jn}(r_i)+\frac{{\gamma_n}^2\Phi_{jn}(r_i)-{\alpha_{jn}}^2\Psi_{jn}(r_i)}{{\gamma_n}^2-{\alpha_{jn}}^2}\right] \tag{46}$$

In Eq. (45), $h_n^{(ij)}$ acts as a transfer function, which relates the fluid force on $\mathcal{C}_i$ to the n th Fourier harmonics of w_j. Since α_{jn} depends on the Stokes number, $h_n^{(ij)}$ is actually a function of $(\varepsilon,\gamma_n,\mathrm{Sk}_j)$.

In Fig. 5, we show the evolution of the magnitude and the angle of $h_n^{(ij)}$ as functions of $|\gamma_n|$. We observe that the magnitude decreases monotonically from the asymptotic limit of an infinitely long cylinder ($|\gamma_n|\to 0$, i.e., $l\to\infty$) to the limit of an infinitely short cylinder ($|\gamma_n|\to\infty$, i.e., $l\to 0$). This decrease indicates that the n th Fourier harmonics of the vibration mode is all the more amplified that the aspect ratio l of the cylinders is large. For a given aspect ratio l of the cylinders, this decrease also indicates that the fluid has a different effect on the Fourier harmonics of the vibration mode, amplifying its low-order harmonics more than its large ones. As a direct consequence, the shape of the linear fluid force $\overline{f_{ij}}$ is generally different from that of the vibration mode w_j. The proximity of the curves drawn for $\mathrm{Sk}_j=250$ and $\mathrm{Sk}_j\to\infty$ (inviscid limit) shows that the Stokes number has a very weak effect on the magnitude of $h_n^{(ij)}$. Actually, the Stokes number mainly affects the angle of $h_n^{(ij)}$, which is poorly sensitive on $|\gamma_n|$. Finally, we shall note that the magnitude of $h_n^{(ij)}$ does not depend that much on the values of the indices i and j. It follows that the linear fluid force acting on $\mathcal{C}_i$, due to the motion of $\mathcal{C}_j$, has the same magnitude as the linear fluid force acting on $\mathcal{C}_j$, due to the motion of $\mathcal{C}_i$, providing that the two cylinders vibrate in the same mode. Still, the angle of $h_n^{(ij)}$ indicates that $\overline{f_{ii}}$ and $\overline{f_{ij}}$, $i\neq j$, are in phase opposition.

4.4 Modal Fluid Forces and Matrix of the Dimensionless Modal Fluid Added Coefficients. The modal fluid force $\langle\overline{w_i},\overline{f_i}\rangle$ is defined as the projection of $\overline{f_i}$ onto a vibration mode $\overline{w_i}(x)$, i.e.,

$$\langle\overline{w_i},\overline{f_i}\rangle = \int_0^1 \overline{w_i}(x)\overline{f_i}(x)\,\mathrm{d}x \tag{47}$$

where

$$\overline{w_i}(x) = \cos\left(\overline{k_i}x + \overline{\delta_i}\right) \tag{48}$$

From Eq. (45), it follows that the modal fluid forces are written as follows:

$$\begin{bmatrix}\langle\overline{w_1},\overline{f_1}\rangle\\ \langle\overline{w_2},\overline{f_2}\rangle\end{bmatrix} = (\varepsilon-1)\sum_{n=1}^{\infty}\int_0^1\begin{bmatrix}h_n^{(11)}\overline{w_1}(x) & h_n^{(12)}\overline{w_1}(x)\\ h_n^{(21)}\overline{w_2}(x) & h_n^{(22)}\overline{w_2}(x)\end{bmatrix} \times\begin{bmatrix}b_{1n}\\ b_{2n}\end{bmatrix}\sin(n\pi x)\,\mathrm{d}x \tag{49}$$

Introducing the n th Fourier coefficient $\overline{b_{in}}$ of $\overline{w_i}$, Eq. (49) simplifies to

$$\begin{bmatrix}\langle\overline{w_1},\overline{f_1}\rangle\\ \langle\overline{w_2},\overline{f_2}\rangle\end{bmatrix} = \frac{(\varepsilon-1)}{2}\sum_{n=1}^{\infty}\begin{bmatrix}h_n^{(11)}\overline{b_{1n}} & h_n^{(12)}\overline{b_{1n}}\\ h_n^{(21)}\overline{b_{2n}} & h_n^{(22)}\overline{b_{2n}}\end{bmatrix}\begin{bmatrix}b_{1n}\\ b_{2n}\end{bmatrix} \tag{50}$$

By splitting $\langle\overline{w_i},\overline{f_i}\rangle$ as $\langle\overline{w_i},\overline{f_{i1}}\rangle + \langle\overline{w_i},\overline{f_{i2}}\rangle$, we introduce the dimensionless normalized modal mass and damping coefficients, defined as $C_m^{(ij)} - \mathrm{i}C_v^{(ij)} = \langle\overline{w_i},\overline{f_{ij}}\rangle/(N_iN_j)$, where $N_j = \sup_{x\in[0,1]}(|w_j|)$ is the infinite norm of the mode w_j. From Eq. (50), the modal matrix

eventually is written as follows:

$$\begin{bmatrix} C_m^{(11)} - \mathrm{i}C_v^{(11)} & C_m^{(12)} - \mathrm{i}C_v^{(12)} \\ C_m^{(21)} - \mathrm{i}C_v^{(21)} & C_m^{(22)} - \mathrm{i}C_v^{(22)} \end{bmatrix} = \frac{(\varepsilon - 1)}{2} \times \sum_{n=1}^{\infty} \begin{bmatrix} h_n^{(11)} \dfrac{\overline{b_{1n}} b_{1n}}{\overline{N_1} N_1} & h_n^{(12)} \dfrac{\overline{b_{1n}} b_{2n}}{\overline{N_1} N_2} \\ h_n^{(21)} \dfrac{\overline{b_{2n}} b_{1n}}{\overline{N_2} N_1} & h_n^{(22)} \dfrac{\overline{b_{2n}} b_{2n}}{\overline{N_2} N_2} \end{bmatrix} \tag{51}$$

4.5 Euler–Bernoulli Beam Vibration Modes. So far the theory has been derived for a vibration mode w_j of the form $w_j = \cos(k_j\, x + \delta_j)$. Considering the classical boundary conditions of an Euler–Bernoulli beam, the shape of w_j is expressed as follows:

$$w_j(x) = \chi_j^{(1)} \cosh(\lambda_j x) + \chi_j^{(2)} \cos(\lambda_j x) + \chi_j^{(3)} \sinh(\lambda_j x) + \chi_j^{(4)} \sin(\lambda_j x) \tag{52}$$

so that b_{jn} is obtained from the superposition of trigonometric modes with different wave numbers, leading to

$$b_{jn} = \chi_j^{(1)} b_n(\mathrm{i}\lambda_j, 0) + \chi_j^{(2)} b_n(\lambda_j, 0) + \chi_j^{(3)} (-\mathrm{i}) b_n\left(\mathrm{i}\lambda_j, -\frac{\pi}{2}\right) + \chi_j^{(4)} b_n\left(\lambda_j, -\frac{\pi}{2}\right) \tag{53}$$

The expansion of Eq. (53) then reduces to

$$\begin{aligned} b_{jn} = &-2\frac{\pi\left(\left(\pi^2 n^2 - \lambda_j{}^2\right)\cosh(\lambda_j)(-1)^n - \pi^2 n^2 + \lambda_j{}^2\right) n}{\pi^4 n^4 - \lambda_j{}^4} \chi_j^{(1)} \\ &-2\frac{\pi\left(\left(\pi^2 n^2 + \lambda_j{}^2\right)\cos(\lambda_j)(-1)^n - \pi^2 n^2 - \lambda_j{}^2\right) n}{\pi^4 n^4 - \lambda_j{}^4} \chi_j^{(2)} \\ &-2\frac{\pi\left(\pi^2 n^2 - \lambda_j{}^2\right)\sinh(\lambda_j)(-1)^n n}{\pi^4 n^4 - \lambda_j{}^4} \chi_j^{(3)} \\ &-2\frac{\pi\left(\pi^2 n^2 + \lambda_j{}^2\right)\sin(\lambda_j)(-1)^n n}{\pi^4 n^4 - \lambda_j{}^4} \chi_j^{(4)} \end{aligned} \tag{54}$$

for $\lambda_j \neq n\pi$ and

$$b_{jn} = \frac{-\cosh(n\pi)(-1)^n + 1}{n\pi} \chi_j^{(1)} - \frac{(-1)^n \sinh(n\pi)}{n\pi} \chi_j^{(3)} + \chi_j^{(4)} \tag{55}$$

for $\lambda_j = n\pi$. Obviously, the mode used for the projection is written as follows:

$$\overline{w_i}(x) = \chi_i^{(1)} \cosh(\overline{\lambda_i} x) + \chi_i^{(2)} \cos(\overline{\lambda_i} x) + \overline{\chi_i^{(3)}} \sinh(\overline{\lambda_i} x) + \overline{\chi_i^{(4)}} \sin(\overline{\lambda_i} x) \tag{56}$$

so that the Fourier coefficient $\overline{b_{in}}$ appearing in Eq. (51) is simply given by either Eqs. (54) or (55), replacing λ_j by $\overline{\lambda_i}$, $\chi_j^{(3)}$ by $\overline{\chi_i^{(3)}}$, and $\chi_j^{(4)}$ by $\overline{\chi_i^{(4)}}$.

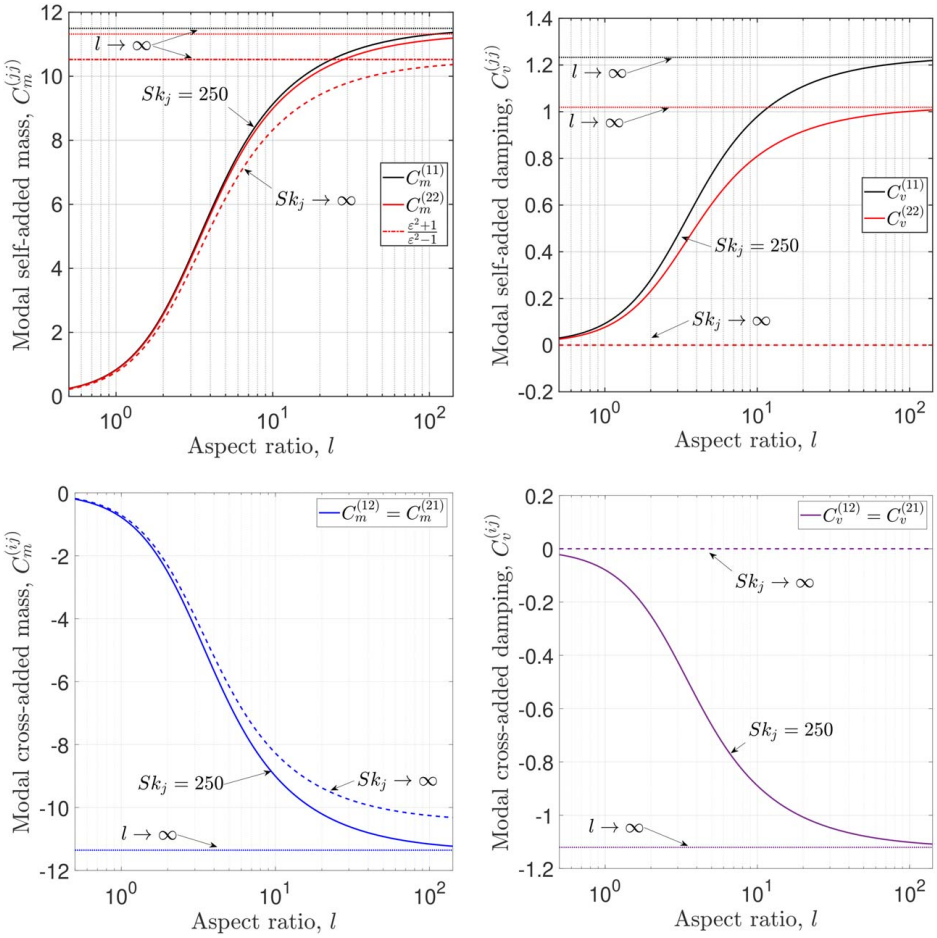

Fig. 6 Modal self and cross-added mass and damping coefficients as functions of the aspect ratio, l, for $i = j = 1$ (black), $i = j = 2$ (red), and $i \neq j$ (blue and purple). The cylinder C_j vibrates in a rigid mode. The solid lines correspond to a Stokes number $Sk_j = 250$. The dashed lines (black and red are indistinguishable) correspond to the inviscid limit $Sk_j \to \infty$. The dotted lines correspond to the limit of infinitely long cylinders, $l \to \infty$, for $Sk_j = 250$. The radius ratio is $\varepsilon = 1.1$. (Color version online.)

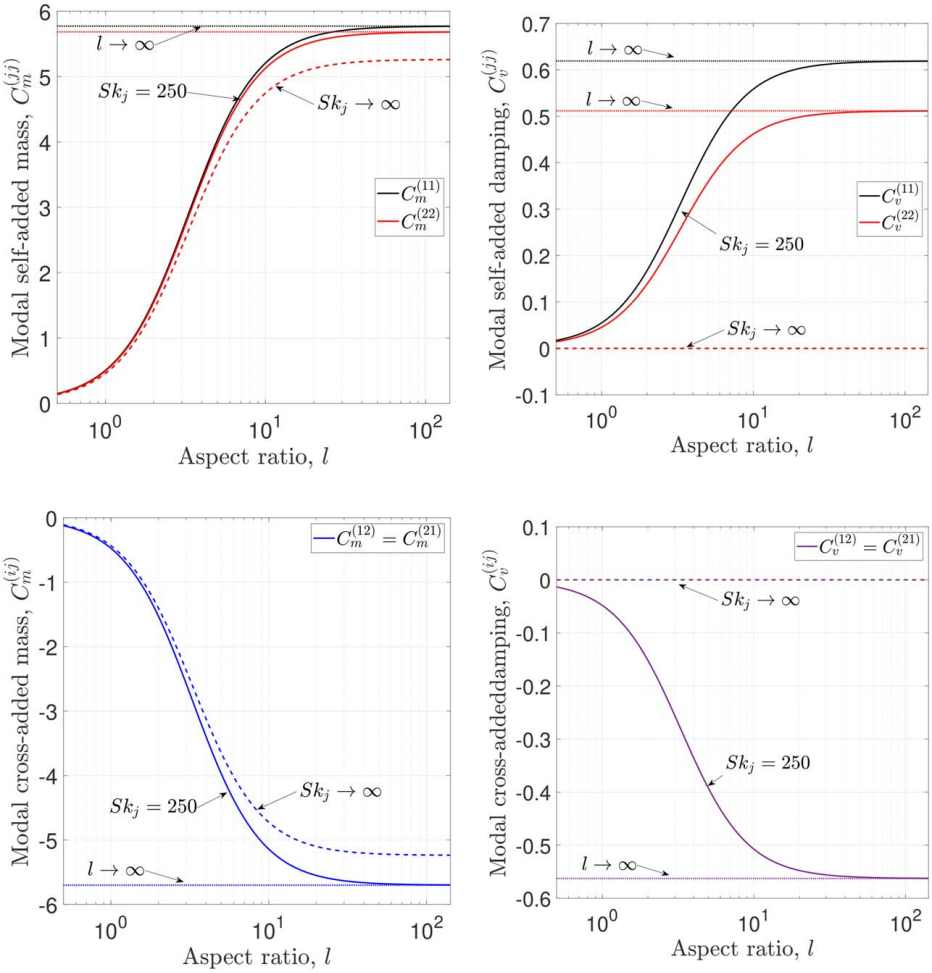

Fig. 7 Modal self and cross-added mass and damping coefficients as functions of the aspect ratio, l, for $i=j=1$ (black), $i=j=2$ (red), and $i \neq j$ (blue and purple). The cylinder $\mathcal{C}_j$ vibrates in the first mode of a pinned-pinned beam. The solid lines correspond to a Stokes number $\mathrm{Sk}_j = 250$. The dashed lines (black and red are indistinguishable) correspond to the inviscid limit $\mathrm{Sk}_j \to \infty$. The dotted lines correspond to the limit of infinitely long cylinders, $l \to \infty$, for $\mathrm{Sk}_j = 250$. The radius ratio is $\varepsilon = 1.1$. (Color version online.)

Equation (51) along with Eqs. (54) and (55) constitute a full analytical expression of the modal added coefficients. This expression shows that the added coefficients depend on the characteristics of the imposed vibrations, through the Fourier coefficients b_{jn}, on the aspect ratio l, on the radius ratio ε, and on the Stokes number, through the transfer function term $h_n^{(ij)}$, given by Eq. (46). In Figs. 6–8, we show the evolution of the modal coefficients (taking $\overline{w_i} = w_i$), as functions of the aspect ratio l, when $\mathcal{C}_j$ ($j=1$ or $j=2$) vibrates in a rigid mode (Fig. 6), i.e., $w_j = 1$, in the first mode of a pinned-pinned beam (Fig. 7), i.e., $w_j = \sin(\pi x)$, and in the first mode of a clamped-free beam (Fig. 8), i.e., w_j given by Eq. (52), where $\lambda_j = 1.8751$, $\chi_j^{(1)} = 1$, $\chi_j^{(2)} = -1$, $\chi_j^{(3)} = -\sigma$, $\chi_j^{(4)} = \sigma$, and $\sigma = 0.73410$. In all cases, we observe that the self (resp. cross) added coefficients are positive (resp. negative) monotonic increasing (resp. decreasing) functions of the aspect ratio, with an horizontal asymptote corresponding to the slender-body limit, see Sec. 4.2.2, as $l \to \infty$. More importantly, the comparison of the curves plotted for $\mathrm{Sk} = 250$ and $\mathrm{Sk} \to \infty$ (inviscid fluid) shows that the added mass coefficients (self and cross) are weakly influenced by the viscosity, contrary to the damping coefficients (which obviously vanish as $\mathrm{Sk} \to \infty$).

Finally, in Fig. 9, we show that the linear fluid forces $\overline{f_{ij}}$ do not have the same shape as the forced vibration mode (here, the first mode of a clamped-free beam), especially for low values of the aspect ratio l. This is of course related to the fact that the pressure field is imposed to vanish at $x=0$ and $x=1$, which is not necessarily the case of the imposed displacement (for a clamped-free beam, $w_j(1) \neq 0$). In such a case, the transfer function $h_n^{(ij)}$, see Eq. (46) and the discussion in Sec. 4.3, affects differently the Fourier harmonics of the imposed vibration mode, so that the fluid makes it possible to couple modes with different wave numbers.

After presenting the theoretical approach, we now proceed to its evaluation by comparing the predictions with numerical simulations.

5 Numerical Assessment

The numerical simulations of the Navier–Stokes equations are performed with the open-source code TRIOCFD, a computational fluid dynamics code for incompressible or quasi-incompressible fluids, coupled with an arbitrary Lagrange–Euler module. In our simulations, the Navier–Stokes equations are time discretized using a backward Euler scheme of the first order. A hybrid finite element volume method, see Refs. [24,25], for unstructured grids is used for the space discretization. The nonlinear convective term is approximated using a second-order MUSCL scheme upwind. Discrete linear systems are solved using iterative solvers from the PETSc library. The discretization of the domain is based on MGCADSurf-MGTetra mesh generator of the SALOME platform. The reader is referred to Refs. [23,24,26,27] for additional details on the code TRIOCFD.

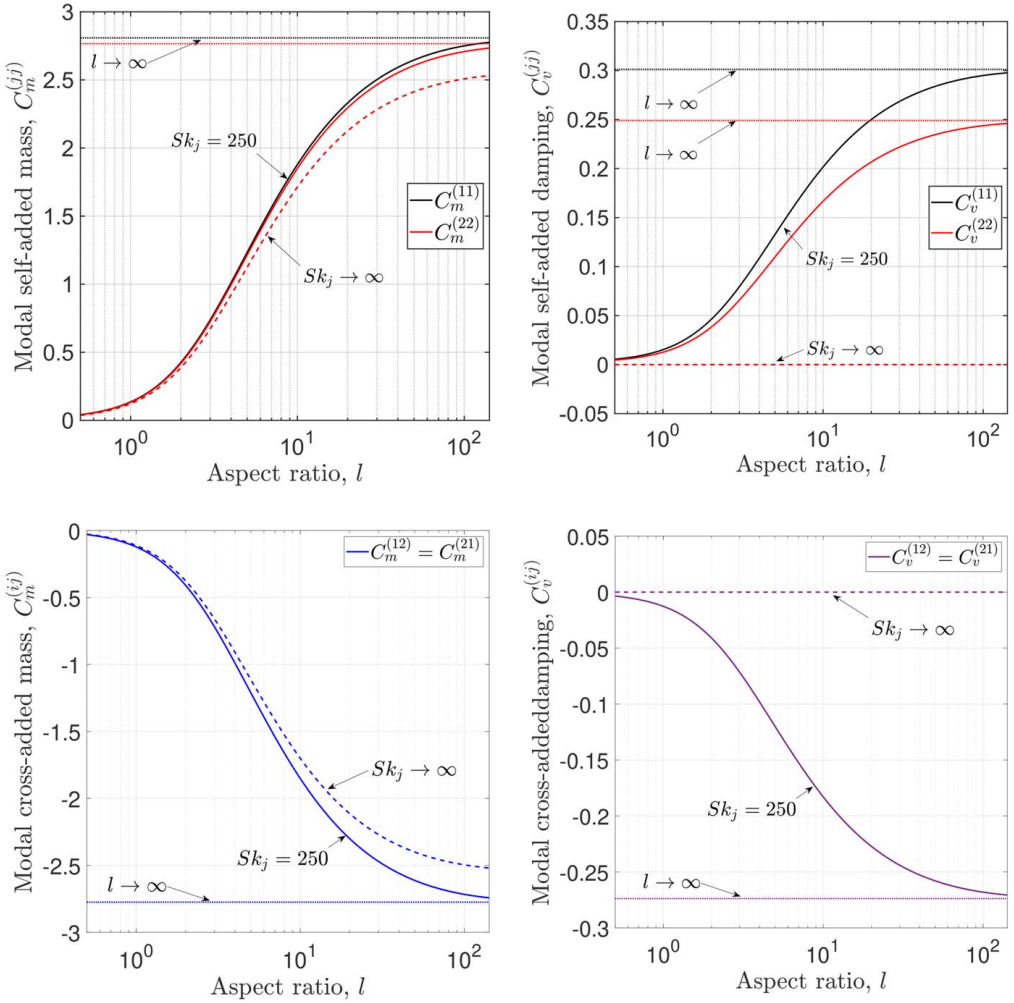

Fig. 8 Modal self and cross-added mass and damping coefficients as functions of the aspect ratio, l, for $i=j=1$ (black), $i=j=2$ (red), and $i \neq j$ (blue and purple). The cylinder $\mathcal{C}_j$ vibrates in the first mode of a clamped-free beam. The solid lines correspond to a Stokes number $Sk_j=250$. The dashed lines (black and red are indistinguishable) correspond to the inviscid limit $Sk_j \to \infty$. The dotted lines correspond to the limit of infinitely long cylinders, $l \to \infty$, for $Sk_j=250$. The radius ratio is $\varepsilon = 1.1$. (Color version online.)

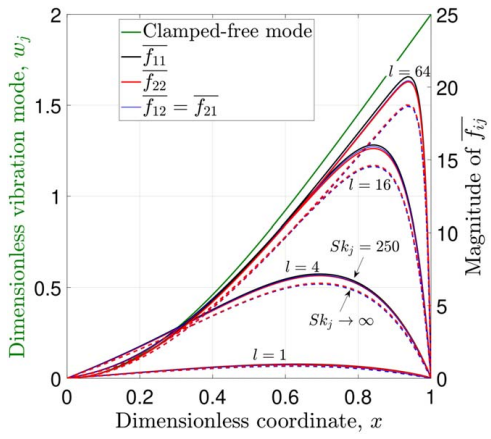

Fig. 9 Magnitude of $\overline{f_{ij}}$ as function of the dimensionless axial coordinate x, for an aspect ratio $l \in \{1, 4, 16, 64\}$, for $i=j=1$ (black), $i=j=2$ (red), and $i \neq j$ (blue). The cylinder $\mathcal{C}_j$ vibrates in the first mode of a clamped-free beam. The solid green line indicates the shape of the vibration mode. The solid lines correspond to a Stokes number $Sk_j=250$. The dashed lines (black and red are indistinguishable) correspond to the inviscid limit $Sk_j \to \infty$. The radius ratio is $\varepsilon = 1.1$. (Color version online.)

5.1 Numerical Setup. The numerical domain consists of two coaxial cylinders $\mathcal{C}_j$ with radii R_j and lengths L_j, see Fig. 2. Either the inner or the outer cylinder is imposed a displacement of the form $\mathbf{W}(X)\sin(\Omega T)$, whereas a zero pressure field is set on $X=0$ and $X=L$. The fluid domain is closed with wall boundaries (zero velocity) in the $\mathbf{e}_y$ and $-\mathbf{e}_y$ directions. Simulations are performed under an imposed displacement of amplitude $W=5\cdot10^{-5}$ [uol] (units of length) and a forcing frequency $\Omega/(2\pi)=10$ [uof] (units of frequency). The inner radius is $R_1=0.02$ [uol], and the radius of the outer cylinder is $R_2=0.022$ [uol]. The fluid properties are $\nu=1.007\times10^{-6}$ [uol]^2/ [uot] and $\rho=1000$ [uom]/[uol]^3, where [uom] stands for units of mass. Given this set of parameters, the Stokes number is sufficiently low, i.e., $Sk_j=250$, to be representative of a viscous fluid.

5.2 Fluid Force Matrix Structure. As a first evaluation of the theoretical predictions, we consider the case in which either the inner or the outer cylinder is imposed a rigid, a pinned-pinned, or a clamped-free mode of vibration (first mode). The aspect ratio is fixed to $l=15$, setting $L_1=0.3$ [uol] and $L_2=0.31$ [uol] in the numerical simulations. For such an aspect ratio, the mesh is composed of 9 million tetrahedrons; the time-step is 1×10^{-4} [uot] (units of times) and the CPU time is approximately 5 h. The modal added coefficients are obtained from the projection of the

Table 1 Cylinders vibrating in a rigid mode

Rigid	Present theory	Numerics TRIOCFD	Relative deviation (%)
	$\begin{pmatrix} 9.93-1.07\mathrm{i} & -9.80+0.968\mathrm{i} \\ -9.80+0.968\mathrm{i} & 9.78-0.880\mathrm{i} \end{pmatrix}$	$\begin{pmatrix} 9.92-1.12\mathrm{i} & -9.84+1.03\mathrm{i} \\ -9.79+1.08\mathrm{i} & 9.83-1.01\mathrm{i} \end{pmatrix}$	$\begin{pmatrix} 0.10+4.5\mathrm{i} & 0.41+6.0\mathrm{i} \\ 0.10+10\mathrm{i} & 0.99+13\mathrm{i} \end{pmatrix}$

Note: Matrix of the dimensionless fluid added coefficients. The aspect ratio is $l = 15$, the radius ratio is $\varepsilon = 1.1$, and the Stokes number is $\mathrm{Sk} = 250$.

Table 2 Pinned-pinned cylinders vibrating in the first mode

Pinned-pinned	Present theory	Numerics TRIOCFD	Relative deviation (%)
	$\begin{pmatrix} 5.50-0.590\mathrm{i} & -5.44+0.540\mathrm{i} \\ -5.44+0.540\mathrm{i} & 5.42-0.490\mathrm{i} \end{pmatrix}$	$\begin{pmatrix} 5.41-0.610\mathrm{i} & -5.44+0.560\mathrm{i} \\ -5.35+0.560\mathrm{i} & 5.43-0.520\mathrm{i} \end{pmatrix}$	$\begin{pmatrix} 1.7+3.3\mathrm{i} & 0.00+5.3\mathrm{i} \\ 1.2+5.3\mathrm{i} & 0.20+7.7\mathrm{i} \end{pmatrix}$

Note: Matrix of the dimensionless modal fluid added coefficients. The aspect ratio is $l = 15$, the radius ratio is $\varepsilon = 1.1$, and the Stokes number is $\mathrm{Sk} = 250$.

Table 3 Clamped-free cylinders vibrating in the first mode

Clamped-free	Present theory	Numerics TRIOCFD	Relative deviation (%)
	$\begin{pmatrix} 2.17-0.230\mathrm{i} & -2.14+0.210\mathrm{i} \\ -2.14+0.210\mathrm{i} & 2.13-0.190\mathrm{i} \end{pmatrix}$	$\begin{pmatrix} 2.19-0.240\mathrm{i} & -2.15+0.220\mathrm{i} \\ -2.13+0.240\mathrm{i} & 2.12-0.220\mathrm{i} \end{pmatrix}$	$\begin{pmatrix} 0.90+4.2\mathrm{i} & 0.50+4.5\mathrm{i} \\ 0.50+12\mathrm{i} & 0.50+13\mathrm{i} \end{pmatrix}$

Note: Matrix of the dimensionless modal fluid added coefficients. The aspect ratio is $l = 15$, the radius ratio is $\varepsilon = 1.1$, and the Stokes number is $\mathrm{Sk} = 250$.

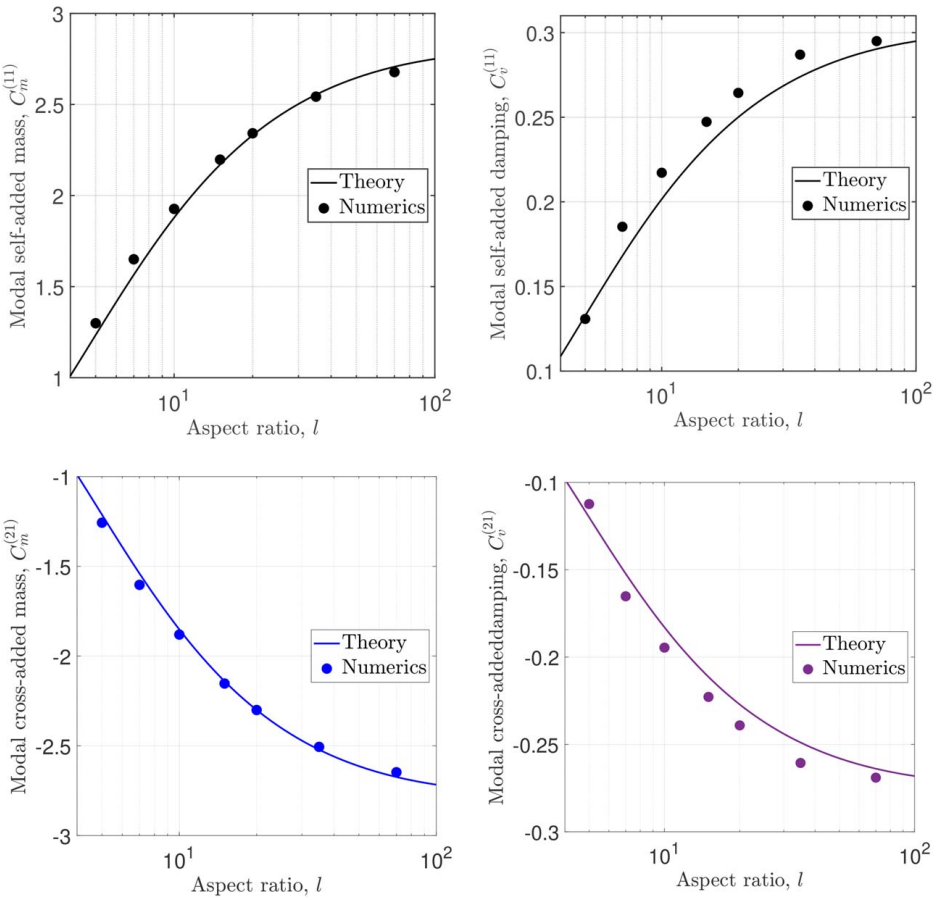

Fig. 10 Modal self and cross-added mass and damping coefficients as functions of the aspect ratio, *l*. The cylinder $\mathcal{C}_1$ vibrates in the first mode of a clamped-free beam. The Stokes number is $\mathrm{Sk}_1 = 250$. The radius ratio is $\varepsilon = 1.1$.

numerical fluid forces onto the same vibration mode as that imposed, i.e., $w_i = \overline{w_i}$. The modal coefficients of the first (resp. second) column of the matrix (51) are extracted from the numerical fluid forces acting on the two cylinders, when the vibration mode is imposed onto the inner (resp. outer) cylinder, the outer (resp. inner) cylinder being fixed.

The results of the comparative study between numerical and theoretical predictions are given in Table 1 for the rigid vibration, in Table 2 for the pinned-pinned vibration, and in Table 3 for the clamped-free vibration. Whatever the type of vibration, we observe an excellent agreement between numerical and theoretical predictions, whether for the added mass or for the added damping coefficients. The relative deviation between theoretical and numerical predictions actually arises from two causes. First, the theoretical approach is fully linear since the convective term of the Navier–Stokes equations is neglected. In our numerical simulations, this term is nonzero even if it is retained as small as possible by imposing a small-amplitude vibration. Second, some relative deviations given in our tables are computed from small values of added coefficients, especially for the damping terms. Tiny differences between numerical and theoretical predictions on such small values automatically yield important relative deviations that should be considered with a critical eye.

5.3 Clamped-Free Cylinders Vibrating in the First Mode. As a second evaluation of the theoretical predictions, we consider the case in which the inner cylinder vibrates in the first mode of a clamped-free beam, considering various values of the aspect ratio l and a low Stokes number, i.e., $\mathrm{Sk}_j = 250$, representative of a viscous fluid. The numerical simulations are performed setting $L_1 \in \{0.1, 0.14, 0.2, 0.3, 0.4, 0.7, 1.4\}$ [uol] and $L_2 \in \{0.11, 0.15, 0.21, 0.31, 0.41, 0.71, 1.41\}$ [uol] so that the aspect ratio is $l \in \{5, 7, 10, 15, 20, 35, 70\}$. The modal added coefficients are obtained from the projection of the numerical fluid forces onto the same vibration mode as that imposed, i.e., $w_i = \overline{w_i}$.

The results of the comparative study between numerical and theoretical predictions are shown in Fig. 10. There again, an excellent agreement is observed between the two approaches, whether for the added mass or for the added damping coefficients. More specifically, the variations of the coefficients with the aspect ratio are correctly reproduced, thus validating our analytical formulation (51) for the modal added coefficients.

6 Conclusion

In the present work, we have considered the fluid–structure interaction problem of two coaxial cylinders, separated by a viscous Newtonian fluid and imposed small-amplitude harmonic beam vibrations. A new theoretical approach based on the Helmholtz expansion of the fluid velocity vector is carried out, leading to a full analytical expression of the modal fluid forces along with the associated mass and damping coefficients. This new theory, which includes the viscous effects of the fluid, does not rely on the assumption of a narrow gap, accounts for the aspect ratio of the cylinders, and applies to all types of classical boundary conditions, thus extending considerably the results of Refs. [21,22]. The new theoretical approach shows that the fluid forces are linear combinations of the Fourier harmonics of the vibration modes. The coefficients of the linear combination depend on the aspect ratio of the cylinders, on the separation distance, and on the Stokes number. The theoretical predictions for the modal self and cross-added mass and damping coefficients are corroborated numerically, considering rigid, pinned-pinned, and clamped-free vibrations. This study shall foster further analytical developments to include the effect of axial fluid flow on the added coefficients and determine subsequent linear stability properties of the coupled system.

Conflict of Interest

There are no conflicts of interest.

Data Availability Statement

The datasets generated and supporting the findings of this article are obtainable from the corresponding author upon reasonable request.

References

[1] Paidoussis, M. P., 2014, *Fluid-Structure Interactions: Slender Structures and Axial Flow*, Vol. 1, 2nd ed., Elsevier, London.
[2] Paidoussis, M. P., 2016, *Fluid-Structure Interactions. Volume 2: Slender Structures and Axial Flow*, 2nd ed., Academic Press, London, UK.
[3] Brown, S. J., 1982, "A Survey of Studies Into the Hydrodynamic Response of Fluid-Coupled Circular Cylinders," J. Pressure. Vessel. Technol., **104**(1), pp. 2–19.
[4] Magrab, E. B., and Burroughs, C., 1971, "Forced Harmonic and Random Vibrations of Concentric Cylindrical Shells Immersed in Acoustic Fluids," J. Acoust. Soc. Am., **52**(3), pp. 858–864.
[5] Chen, S. S., and Wambsganss, M. W., 1972, "Parallel-Flow-Induced Vibration of Fuel Rods," Nucl. Eng. Des., **18**(2), pp. 253–278 .
[6] Levin, L., and Milan, D., 1973, "Coupled Breathing Vibrations of Two Thin Cylindrical Coaxial Shells in Fluid," Vibration Problems in Industry, International Symposium, Keswick, UK.
[7] Krajcinovic, D., 1974, "Vibrations of Two Coaxial Cylindrical Shells Containing Fluid," Nucl. Eng. Des., **30**(2), pp. 242–248.
[8] Bowers, G., and Horvay, G., 1974, "Beam Modes of Vibration of a Thin Cylindrical Shell Flexibly Supported and Immersed in Water Inside of a Coaxial Cylindrical Container of Slightly Larger Radius," Nucl. Eng. Des., **26**(2), pp. 291–298.
[9] Chen, S. S., Wambsganss, M. W., and Jendrzejczyk, J. A., 1976, "Added Mass and Damping of a Vibrating Rod in Confined Viscous Fluids," ASME J. Appl. Mech., **43**, pp. 325–329.
[10] Yeh, T. T., and Chen, S. S., 1978, "The Effect of Fluid Viscosity on Coupled Tube/fluid Vibrations," J. Sound. Vib., **59**(3), pp. 453–467.
[11] Au-Yang, M. K., 1976, "Free Vibration of Fluid-Coupled Coaxial Cylindrical Shells of Different Lengths," ASME J. Appl. Mech., **43**(3), pp. 480–484.
[12] Au-Yang, M. K., 1977, "Generalized Hydrodynamic Mass for Beam Mode Vibration of Cylinders Coupled by Fluid Gap," ASME J. Appl. Mech., **44**(1), pp. 172–173.
[13] Au-Yang, M. K., 1986, "Dynamics of Coupled Fluid-Shells," J. Vib. Acoust. Stress Reliab. Des., **108**(3), pp. 339–347.
[14] Paidoussis, M., and Ostoja-Starzewski, M., 1981, "Dynamics of a Flexible Cylinder in Subsonic Axial Flow," AIAA. J., **19**(11), pp. 1467–1475.
[15] Fritz, R. J., 1972, "The Effect of Liquids on the Dynamic Motions of Immersed Solids," J. Eng. Ind., **94**(1), pp. 167–173.
[16] Horvay, G., and Bowers, G., 1975, "Influence of Entrained Water Mass on the Vibration Modes of a Shell," J. Fluid. Eng., **97**(2), pp. 211–216.
[17] Bergamaschi, Y., Bouilloux, Y., Chantoin, P., Guigon, B., Bravo, X., Germain, C., Rommens, M., and Tremodeux, P., 2002, "Jules Horowitz Reactor, Basic Design," Proceedings of ENC, San Carlos de Bariloche, Argentina, Nov. 3–8.
[18] Laurens, M., "Présentation IFS. Bloc Pile RJH, 2020," TA–6515496 Ind. A.
[19] Mateescu, D., and Paidoussis, M. P., 1984, "Annular-Flow-Induced Vibrations of an Axially Variable Body of Revolution in a Duct of Variable Crosssection," Proceedings of the ASME Symposium on Flow-Induced Vibrations, ASME Winter Annual Meeting, M. P. Paidoussis and M. K. Au-Yang, eds., New Orleans, LA, ASME, New York, Vol. 4, pp. 53–69.
[20] Paidoussis, M. P., Mateescu, D., and Sim, W. -G., 1990, "Dynamics and Stability of a Flexible Cylinder in a Narrow Coaxial Cylindrical Duct Subjected to Annular Flow," ASME J. Appl. Mech., **57**(1), pp. 232–240.
[21] Lagrange, R., and Puscas, M. A., 2022, "Hydrodynamic Interaction Between Two Flexible Finite Length Coaxial Cylinders: New Theoretical Formulation and Numerical Validation," ASME J. Appl. Mech., **89**(8), p. 081006.
[22] Lagrange, R., Puscas, M. A., Piteau, P., Delaune, X., and Antunes, J., 2022, "Modal Added-Mass Matrix of an Elongated Flexible Cylinder Immersed in a Narrow Annular Fluid, Considering Various Boundary Conditions. New Theoretical Results and Numerical Validation," J. Fluids Structures, **114**, p. 103754.
[23] Panunzio, D., Puscas, M.-A., and Lagrange, R., 2022, "FSI-Vibrations of Immersed Cylinders. Simulations With the Engineering Open-Source Code TrioCFD. Test Cases and Experimental Comparisons," Comptes Rendus. Mécanique, **350**(G3), pp. 451–476 .
[24] Angeli, P. E., Puscas, M. A., Fauchet, G., and Cartalade, A., 2017, "FVCA8 Benchmark for the Stokes and Navier-Stokes Equations With the TrioCFD Code–Benchmark Session," Finite Volumes for Complex Applications VIII—Methods and Theoretical Aspects, Lille, France, June 12–16, pp. 181–202.
[25] Fiorini, C., Després, B., and Puscas, M. A., 2020, "Sensitivity Equation Method for the Navier-Stokes Equations Applied to Uncertainty Propagation," Int. J. Numerical Methods Fluids, **93**, pp. 71–92.
[26] Puscas, M. A., Monasse, L., Ern, A., Tenaud, C., and Mariotti, C., 2015, "A Conservative Embedded Boundary Method for an Inviscid Compressible Flow Coupled With a Fragmenting Structure," Int. J. Numerical Methods Eng., **103**, pp. 970–995.
[27] Donea, J., Huerta, A., Ponthot, J. P., and Rodríguez-Ferran, A., 2004, "Arbitrary Lagrangian–Eulerian Methods," *Encyclopedia of Computational Mechanics*, E. Stein, R. Borst, and T. J. R. Hughes, eds., American Cancer Society.

D. INTERACTION FLUIDE-STRUCTURE ENTRE DEUX CYLINDRES PARALLÈLES

Dans cette annexe, la publication parue dans la revue *Journal of Fluids and Structures*, sous le titre "A new analytical approach for modeling the added mass and hydrodynamic interaction of two cylinders subjected to large motions in a potential stagnant fluid" est reproduite.

Journal of Fluids and Structures 77 (2018) 102–114

Contents lists available at ScienceDirect

Journal of Fluids and Structures

journal homepage: www.elsevier.com/locate/jfs

A new analytical approach for modeling the added mass and hydrodynamic interaction of two cylinders subjected to large motions in a potential stagnant fluid

Romain Lagrange [a,*], Xavier Delaune [a], Philippe Piteau [a], Laurent Borsoi [a], José Antunes [b]

[a] Den-Service d'études mécaniques et thermiques (SEMT), CEA, Université Paris-Saclay, F-91191, Gif-sur-Yvette, France
[b] Centro de Ciências e Tecnologias Nucleares, Instituto Superior Técnico, Universidade de Lisboa, Estrada Nacional 10, Km 139.7, 2695-066 Bobadela LRS, Portugal

ARTICLE INFO

Article history:
Received 25 April 2017
Received in revised form 2 October 2017
Accepted 1 December 2017

Keywords:
Potential flow
Added mass
Fluid force
Cylinders interaction

ABSTRACT

A potential theory is presented for the problem of two moving circular cylinders, with possibly different radii, large motions, immersed in an perfect stagnant fluid. We show that the fluid force is the superposition of an added mass term, related to the time variations of the potential, and a quadratic term related to its spatial variations. We provide new simple and exact analytical expressions for the fluid added mass coefficients, in which the effect of the confinement is made explicit. The self-added mass (resp. cross-added mass) is shown to decrease (resp. increase) with the separation distance and increase (resp. decreases) with the radius ratio. We then consider the case in which one cylinder translates along the line joining the centers with a constant speed. We show that the two cylinders are repelled from each other, with a force that diverges to infinity at impact. We extend our approach to the case in which one cylinder is imposed a sinusoidal vibration. We show that the force on the stationary cylinder and the vibration displacement have opposite (resp. identical) axial (resp. transverse) directions. For large vibration amplitudes, this force is strongly altered by the nonlinear effects induced by the spatial variations of the potential. The force on the vibrating cylinder is in phase with the imposed displacement and is mainly driven by the added mass term. The results of this paper are of particular interest for engineers who need to understand the essential features associated with the vibration of a solid body in a still fluid.

1. Introduction

The interaction between a fluid and moving bodies is a fundamental problem which finds many applications, for example in turbomachinery (Furber and Ffowcswilliams, 1979), fish schooling (Nair and Kanso, 2007), heat exchangers tube banks (Chen, 1975, 1977), vibration of flexible risers (Le Cunff et al., 2002), biomechanics of plants (De Langre, 2008), or energy harvesting (Doare and Michelin, 2011; Singh et al., 2012; Michelin and Doare, 2013; Virot et al., 2016) from flapping flags (Eloy et al., 2008)… The reader should refer to the book of Païdoussis et al. (2014) for a complete bibliography of important works in this field. A classical approach to understand the fluid dynamics surrounding interacting bodies is to consider a potential flow model, in which viscous, rotational vortex and wake effects are disregarded. For large Reynolds numbers and

* Corresponding author.
E-mail address: romain.lagrange@cea.fr (R. Lagrange).

https://doi.org/10.1016/j.jfluidstructs.2017.12.002
0889-9746/

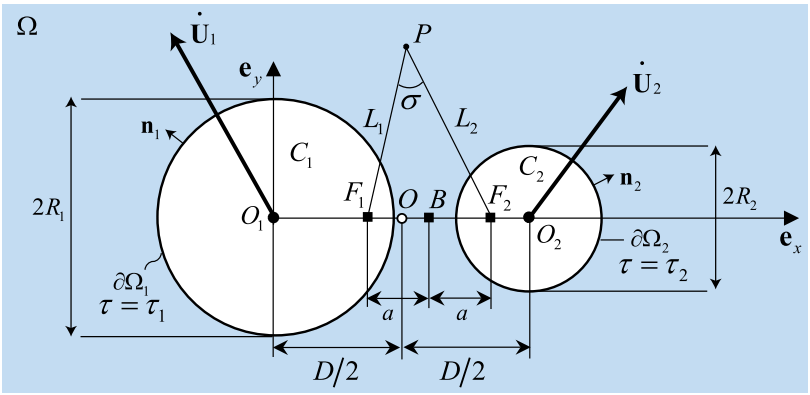

Fig. 1. Schematic diagram of the system: two moving circular cylinders $\mathcal{C}_i$ with radii R_i, centers O_i, velocities $\dot{\mathbf{U}}_i\,(T)$, are immersed in an inviscid fluid Ω. The motions of $\mathcal{C}_i$ generate an incompressible and irrotational flow. The instantaneous center-to-center distance is D. The bipolar coordinates $\sigma \in [0, 2\pi]$ and $\tau = \ln(L_1/L_2)$ are used to track the position of a fluid particle P. The points (B, F_1, F_2) are defined in such a way that points lying on the cylinder boundaries $\partial\Omega_i$ have bipolar coordinates $\tau = \tau_i$.

outside the boundary layers, the potential flow theory is expected to provide a good approximation of the solution, or some of its related characteristics as the added-mass, see Chen (1987). The very first discussions of potential flows around two circular cylinders probably originate from Hicks (1879), who studied the motion of a cylindrical pendulum inside another cylinder filled with fluid. To solve this problem, Hicks considered the potential due to flow singularities distributed over the fluid domain and the cylinder surfaces. The strengths and locations of the singularities were expressed as a set of iterative equations and the potential in an integral form, suitable for numerical computation (Lamb, 1945). Many investigators (Greenhill, 1882; Basset, 1888; Carpenter, 1958; Birkhoff, 1960; Gibert and Sagner, 1980; Landweber and Shahshahan, 1991) then tried to clarify and simplify the method of singularities by Hicks to derive a more tractable expression for the fluid potential. Still, this approximate method remains difficult to apply and as the gap between the cylinders becomes small, a high density of singularities is necessary for the solution to converge. More recently, analytical approaches based on complex analysis and conformal mapping methods (Wang, 2004; Burton et al., 2004; Tchieu et al., 2010) have overcome this problem and general theories to determine the flow through multiple bodies have been proposed (Scolan and Etienne, 2008; Crowdy, 2006, 2010). The two cylinders problem can be solved in this framework, but here we provide a more flexible method which yields new analytical and simplified expressions for the added mass coefficients. We also show that the large motions of the cylinders generate some strong spatial variations of the potential which produce nonlinear inertial effects of the fluid forces.

This paper is organized as follows. Section 2 presents the problem of two parallel circular cylinders immersed in an inviscid fluid and introduces the governing dimensionless numbers. In Section 3, we solve the potential flow problem, provide analytical expressions of the added mass terms and determine the fluid force on the cylinders. In Section 4 we test our predictions against published results and consider the case of a vibrating cylinder. Finally, some conclusions are drawn in Section 5.

2. Definition of the problem

Let $\mathcal{C}_i$, $(i = 1, 2)$, be two circular cylinders with radii R_i, immersed in an inviscid fluid of volume mass density ρ. We aim to determine the 2D flow generated by the arbitrary motions of $\mathcal{C}_i$, (Fig. 1). For convenience we introduce rescaled quantities to reduce the number of parameters of the problem. We use R_2 to normalize lengths, some characteristic speed V_0 to normalize velocities and $\rho {V_0}^2$ to normalize pressures. We define

$$r = \frac{R_1}{R_2},\ d = \frac{D}{R_2},\ \mathbf{u}_i = \frac{\mathbf{U}_i}{R_2},\ t = \frac{TV_0}{R_2},\ p = \frac{P}{\rho {V_0}^2},\ \mathbf{f}_i = \frac{\mathbf{F}_i}{\rho {V_0}^2 R_2}, \tag{1}$$

as the radius ratio, the dimensionless center-to-center distance, cylinder displacement, time, fluid pressure and fluid force, respectively. We also introduce the dimensionless separation distance, $\varepsilon = d - (r + 1)$ such that $\varepsilon = 0$ corresponds to cylinders in contact.

3. Theoretical model

3.1. Fluid equations

It is assumed that the fluid is inviscid and the flow generated by the motion of the circular cylinders is incompressible and irrotational. We thus model the flow with a potential function φ which satisfies the Laplace equation

$$\Delta\varphi = 0 \quad \text{in } \Omega, \tag{2}$$

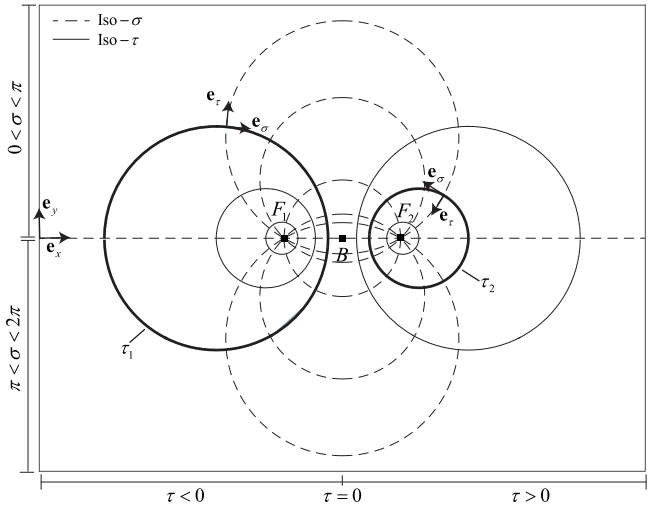

Fig. 2. Bipolar coordinate system. The dashed circles are iso-values of σ while the solid circles are iso-values of τ. The two foci points F_i are defined such that $\partial\Omega_i$ has a coordinate τ_i. The points on the x-axis have $\sigma = \pi$ if they lie in between F_1 and F_2, and $\sigma = 0$ otherwise.

and the inviscid boundary conditions

$$(\nabla\varphi - \dot{\mathbf{u}}_i) \cdot \mathbf{n}_i = 0 \quad \text{on } \partial\Omega_i. \tag{3}$$

In the above eqs., Ω is the fluid domain and $\mathbf{n}_i$ is the outward normal unit vector to $\partial\Omega_i$ (Fig. 1). To account for an unperturbed fluid at infinity we also require that

$$\varphi \to 0 \quad \text{at infinity.} \tag{4}$$

The fluid pressure p is derived from the unsteady Bernoulli equation

$$p - p_\infty = -\left(\frac{\partial\varphi}{\partial t} + \frac{(\nabla\varphi)^2}{2}\right), \tag{5}$$

where p_∞ is the pressure at infinity. The fluid force on $\mathcal{C}_i$ is obtained by integration of (5) on $\partial\Omega_i$

$$\mathbf{f}_i = \int_{\partial\Omega_i} \left(\frac{\partial\varphi}{\partial t} + \frac{(\nabla\varphi)^2}{2}\right) \mathbf{n}_i ds_i, \tag{6}$$

where ds_i is an infinitesimal element of integration.

The fluid equations must be solved on the instantaneous configuration to account for the possible large displacements of $\mathcal{C}_i$. This leads us to define a coordinate system based on the kinematics of $\mathcal{C}_i$ and in which the fluid eqs. can be solved analytically.

3.2. Bipolar coordinates

Let (B, F_1, F_2) be three points defined as $\mathbf{OB} = x_B\mathbf{e}_x$ and $\mathbf{BF_1} = -a\mathbf{e}_x$ and $\mathbf{BF}_2 = a\mathbf{e}_x$, $a > 0$. From these three points, we introduce the bipolar coordinates $\sigma \in [0, 2\pi[$ and $\tau \in \mathbb{R}$ to track the position of a fluid particle, as shown in Fig. 1. Since the iso-τ contours are circles with centers on the x-axis (Fig. 2), one can align $\partial\Omega_i$ with an iso-contour τ_i by setting the position of B and F_i. In Appendix A, we show that

$$x_B = \left(r^2 - 1\right)/(2d), \tag{7a}$$

$$a = \sqrt{d^2 - (1+r)^2}\sqrt{d^2 - (1-r)^2} \Big/ (2d), \tag{7b}$$

yield iso-contours for the two cylinders

$$\tau_1 = -\sinh^{-1}(a/r) \quad \text{and} \quad \tau_2 = \sinh^{-1}(a). \tag{7c}$$

Introducing $(\mathbf{e}_\sigma, \mathbf{e}_\tau)$ as the coordinate system basis, see Fig. 2, Appendix A, the outward normal unit vector $\mathbf{n}_i$ to $\partial\Omega_i$ is

$$\mathbf{n}_i = (-1)^{i-1}\mathbf{e}_\tau(\sigma, \tau_i), \tag{8}$$

and the infinitesimal measure ds_i of $\partial\Omega_i$ is

$$ds_i = \kappa_{\sigma\tau_i} d\sigma, \tag{9}$$

with $\kappa_{\sigma\tau} = a/(\cosh(\tau) - \cos(\sigma))$.

Finally, the gradient and the Laplace operators in bipolar coordinates are

$$\nabla\varphi = \frac{1}{\kappa_{\sigma\tau}}\left(\frac{\partial\varphi}{\partial\sigma}\mathbf{e}_\sigma + \frac{\partial\varphi}{\partial\tau}\mathbf{e}_\tau\right), \tag{10a}$$

$$\Delta\varphi = \left(\frac{1}{\kappa_{\sigma\tau}}\right)^2\left(\frac{\partial^2\varphi}{\partial\sigma^2} + \frac{\partial^2\varphi}{\partial\tau^2}\right). \tag{10b}$$

3.3. Solution of the fluid equations

In bipolar coordinates the fluid Eqs. (2)–(4) read

$$\frac{\partial^2\varphi}{\partial\sigma^2} + \frac{\partial^2\varphi}{\partial\tau^2} = 0 \quad \text{in } \Omega, \tag{11a}$$

$$\frac{\partial\varphi}{\partial\tau} = g_{ix}\dot{u}_{ix} + g_{iy}\dot{u}_{iy} \quad \text{on } \tau = \tau_i,\ i = 1, 2, \tag{11b}$$

$$\varphi \to 0 \quad \text{as } (\sigma, \tau) \to (0, 0), \tag{11c}$$

with $\dot{u}_{ix}$, $\dot{u}_{iy}$ the $\mathbf{e}_x$ and $\mathbf{e}_y$ components of $\dot{\mathbf{u}}_i$, respectively. In (11), g_{ix} and g_{iy} are the 2π periodic functions with Fourier components $g_{in} = -2nae^{-n|\tau_i|}$

$$g_{ix}(\sigma) = \kappa_{\sigma\tau_i}\mathbf{e}_x \cdot \mathbf{e}_\tau(\sigma, \tau_i) = -a\frac{\cos(\sigma)\cosh(\tau_i) - 1}{(\cosh(\tau_i) - \cos(\sigma))^2} = \sum_{n=1}^{\infty} g_{in}\cos(n\sigma), \tag{12a}$$

$$g_{iy}(\sigma) = \kappa_{\sigma\tau_i}\mathbf{e}_y \cdot \mathbf{e}_\tau(\sigma, \tau_i) = -a\frac{\sin(\sigma)\sinh(\tau_i)}{(\cosh(\tau_i) - \cos(\sigma))^2} = \sum_{n=1}^{\infty} g_{in}\,\mathrm{sign}(\tau_i)\sin(n\sigma). \tag{12b}$$

The fluid problem being linear in $\dot{u}_{ix}$ and $\dot{u}_{iy}$, the potential φ is a superposition of two functions φ_x and φ_y, solutions of (11) for $\dot{u}_{iy} = 0$ and $\dot{u}_{ix} = 0$, respectively. The calculus of φ_x and φ_y is reported in Appendix B for the sake of clarity. We find that the potential is

$$\begin{aligned}
\varphi = {} & \dot{u}_{1x}\sum_{n=1}^{\infty}\varphi_{1n}\left[\cos(n\sigma)\cosh(n(\tau - \tau_2)) - \cosh(n\tau_2)\right] \\
& + \dot{u}_{1y}\sum_{n=1}^{\infty}(-\varphi_{1n})\sin(n\sigma)\cosh(n(\tau - \tau_2)) \\
& + \dot{u}_{2x}\sum_{n=1}^{\infty}\varphi_{2n}\left[\cos(n\sigma)\cosh(n(\tau - \tau_1)) - \cosh(n\tau_1)\right] \\
& + \dot{u}_{2y}\sum_{n=1}^{\infty}\varphi_{2n}\sin(n\sigma)\cosh(n(\tau - \tau_1)) \\
= {} & \dot{\mathbf{u}}_1 \cdot \mathbf{h}_1 + \dot{\mathbf{u}}_2 \cdot \mathbf{h}_2,
\end{aligned} \tag{13}$$

with φ_{in} given by (B.4).

The calculation of the fluid pressure follows from the Bernoulli equation (5), leading to

$$p - p_\infty = -\left(\ddot{\mathbf{u}}_1 \cdot \mathbf{h}_1 + \ddot{\mathbf{u}}_2 \cdot \mathbf{h}_2 + p_q\right), \tag{14}$$

with

$$\begin{aligned}
p_q &= \dot{\mathbf{u}}_1 \cdot \frac{\partial\mathbf{h}_1}{\partial t} + \dot{\mathbf{u}}_2 \cdot \frac{\partial\mathbf{h}_2}{\partial t} + \frac{\left[\nabla(\dot{\mathbf{u}}_1 \cdot \mathbf{h}_1 + \dot{\mathbf{u}}_2 \cdot \mathbf{h}_2)\right]^2}{2}, \\
&= -(\dot{\mathbf{u}}_1 \cdot \nabla\mathbf{h}_1 + \dot{\mathbf{u}}_2 \cdot \nabla\mathbf{h}_2) \cdot \dot{\mathbf{u}}_0 + \frac{\left[\nabla(\dot{\mathbf{u}}_1 \cdot \mathbf{h}_1 + \dot{\mathbf{u}}_2 \cdot \mathbf{h}_2)\right]^2}{2},
\end{aligned} \tag{15}$$

and $\dot{\mathbf{u}}_0 = (\dot{\mathbf{u}}_1 + \dot{\mathbf{u}}_2)/2$. The terms $\ddot{\mathbf{u}}_i \cdot \mathbf{h}_i$ come from the time variation of the fluid potential due to the motion of the cylinders. The term p_q is quadratic in $(\dot{\mathbf{u}}_1, \dot{\mathbf{u}}_2)$ and comes from the spatial variations of the fluid potential. This variation is due to the

motion of the cylinders (first right hand side term of (15)) and to the convective term of the Navier–Stokes equation (last RHS term).

The integration of (14) on $\partial\Omega_i$ yields the fluid force on $\mathcal{C}_i$

$$\begin{pmatrix} f_{1x_0} \\ f_{1y_0} \\ f_{2x_0} \\ f_{2y_0} \end{pmatrix} = -\pi \left[C_a\right] \begin{pmatrix} \ddot{u}_{1x_0} \\ \ddot{u}_{1y_0} \\ \ddot{u}_{2x_0} \\ \ddot{u}_{2y_0} \end{pmatrix} + \begin{pmatrix} f_{1qx_0} \\ f_{1qy_0} \\ f_{2qx_0} \\ f_{2qy_0} \end{pmatrix}, \tag{16}$$

with $[C_a]$ the added mass matrix

$$[C_a] = \begin{pmatrix} m_{11} & 0 & m_{12} & 0 \\ 0 & m_{11} & 0 & -m_{12} \\ m_{12} & 0 & m_{11} & 0 \\ 0 & -m_{12} & 0 & m_{11} \end{pmatrix}, \tag{17a}$$

$$m_{11} = \sum_{n=1}^{\infty} \frac{4na^2 e^{-2n\tau_2}}{\tanh\left[n\left(\tau_2 - \tau_1\right)\right]}, \tag{17b}$$

$$m_{12} = \sum_{n=1}^{\infty} \frac{-4na^2 e^{-n(\tau_2 - \tau_1)}}{\sinh\left[n\left(\tau_2 - \tau_1\right)\right]}. \tag{17c}$$

These are new analytical expressions for the self and cross-added mass terms m_{11} and m_{12}. The self-added mass m_{11} relates the fluid force on $\mathcal{C}_i$ to its own acceleration. The cross-added mass m_{12} relates the fluid force on $\mathcal{C}_i$ to the acceleration of $\mathcal{C}_j$, $j \neq i$. These new expressions have the advantage of making explicit the effect of the confinement on the added mass terms: m_{11} and m_{12} depend on a and τ_i, which are functions of the separation distance, according to (7).

The terms $\mathbf{f}_{iq}$ are quadratic in $(\dot{\mathbf{u}}_1, \dot{\mathbf{u}}_2)$ and come from the integration of p_q on $\partial\Omega_i$

$$\mathbf{f}_{iq} = \int_0^{2\pi} p_q\left(\sigma, \tau_i\right) \mathbf{n}_i \kappa_{\sigma\tau_i} d\sigma. \tag{18}$$

These quadratic terms (computed numerically, see Appendix C) represent the part of the fluid force due to the spatial variations of the fluid potential.

Finally, note that if the cylinders are subject to an incident unsteady flow $\mathbf{v}_\infty(t)$, the fluid potential modifies to

$$\varphi = \mathbf{v}_\infty \cdot \mathbf{OM} + \left(\dot{\mathbf{u}}_1 - \mathbf{v}_\infty\right) \cdot \mathbf{h}_1 + \left(\dot{\mathbf{u}}_2 - \mathbf{v}_\infty\right) \cdot \mathbf{h}_2, \tag{19}$$

where $\mathbf{OM}$ is the position vector of the fluid particle P. The first right hand side term ensures that $\nabla\varphi \to \mathbf{v}_\infty$ far from the cylinders. The other terms follow from (13) where $\dot{\mathbf{u}}_i - \mathbf{v}_\infty$ is the velocity of $\mathcal{C}_i$ in the reference frame attached to the incident flow. Noting $[I]$ the identity matrix, the fluid force is

$$\begin{pmatrix} f_{1x_0} \\ f_{1y_0} \\ f_{2x_0} \\ f_{2y_0} \end{pmatrix} = \pi \left(\left[C_a\right] + \left[I\right]\right) \begin{pmatrix} \dot{v}_{\infty x_0} \\ \dot{v}_{\infty y_0} \\ \dot{v}_{\infty x_0} \\ \dot{v}_{\infty y_0} \end{pmatrix} - \pi \left[C_a\right] \begin{pmatrix} \ddot{u}_{1x_0} \\ \ddot{u}_{1y_0} \\ \ddot{u}_{2x_0} \\ \ddot{u}_{2y_0} \end{pmatrix} + \begin{pmatrix} f_{1qx_0} \\ f_{1qy_0} \\ f_{2qx_0} \\ f_{2qy_0} \end{pmatrix}, \tag{20}$$

where p_q and $\mathbf{f}_{iq}$ are given by (15)–(18) under the change $\dot{\mathbf{u}}_i \to \dot{\mathbf{u}}_i - \mathbf{v}_\infty$. The Eq. (20) is similar to the Morison equation (Morison et al., 1950), which gives the inline force on a body subject to an unsteady flow. From an experimental stand point, (20) shows that $[C_a]$ can be extracted either from the force on cylinders vibrating in a fluid at rest or from the force on fixed cylinders subject to an unsteady fluid flow.

4. Results

4.1. Added mass

In the previous section, we have obtained new simple analytical expressions for the added mass coefficients m_{11} and m_{12}. Their evolution with the separation distance ε and the radius ratio r is shown in Fig. 3. We find that m_{11} (resp. m_{12}) decreases (resp. increases) monotonically with the dimensionless separation distance, and increases (resp. decreases) with the radius ratio. When the cylinders are in close proximity, i.e. $\varepsilon \to 0$, the confinement is maximum and the added mass coefficients become unbounded, as expected. When the two cylinders are far apart, i.e. $\varepsilon \to \infty$, they both behave like an isolated cylinder in an infinite fluid domain, $m_{11} \to 1$ and $m_{12} \to 0$. To validate our observations, we have reported in Fig. 3 the theoretical predictions of the literature (Mazur, 1970; Landweber and Shahshahan, 1991), for $r = 1$. Unlike the current method, Mazur (1970) used a conformal mapping method to solve the potential problem and extracted the added mass coefficients from

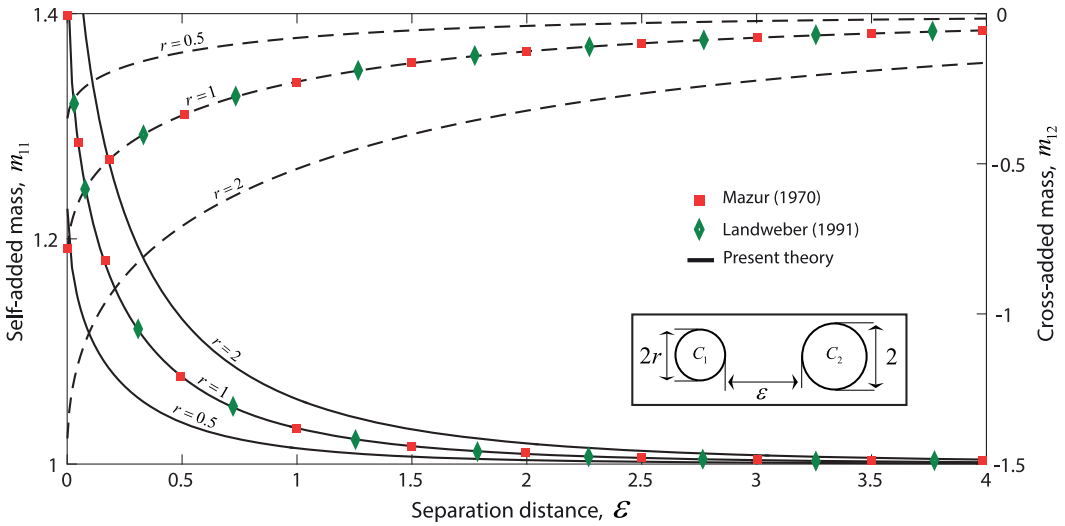

Fig. 3. Self-added mass m_{11} (solid lines) and cross-added mass m_{12}, given by Eq. (17), as functions of the separation distance ε and the radius ratio r.

Table 1
Added mass coefficients from various references. Note that Gibert's theory (Gibert and Sagner, 1980) is slightly off as it relies on an asymptotic expansion that is valid for large ε. The table is given for $\varepsilon = 1$ and $r = 1$.

	Present reference	Païdoussis et al. (1984)	Chen (1978)	Suss (1977)	Dalton and Helfinstine (1971)	Gibert and Sagner (1980)
m_{11}	1.0319	1.0320	1.0325	1.0328	1.0313	1.0250
m_{12}	−0.2269	−0.2269	−0.2265	−0.2266	−0.2245	−0.2250

the kinetic energy of the fluid. On his side, Landweber and Shahshahan (1991) extended the method of images by Hicks (1879), Herman (1887) and extracted the added mass coefficients from the fluid force acting on the cylinders. We obtain an excellent agreement with those authors (and some others reproduced in Table 1), thereby validating our prediction for m_{11} and m_{12}.

4.2. Quadratic fluid force

4.2.1. Uniform linear motion

The fluid force is the superposition of an added mass term and a quadratic term $\mathbf{f}_{iq}$. In the previous section, we have validated the prediction for the added mass term and we now proceed with assessing the validity of $\mathbf{f}_{iq}$. To do so we consider the case in which $\mathcal{C}_1$ is stationary while $\mathcal{C}_2$ translates along the line joining the centers with a constant characteristic speed V_0. The dimensionless displacement is written $\mathbf{u} = t\mathbf{e}_x$ with $t = TV_0/R_2$ the dimensionless time. The y-component of the fluid force is $f_{iy} = 0$ by symmetry.

In Fig. 4, we plot f_{ix}, given by Eq. (16), as a function of the separation distance ε. We find that f_{1x} (resp. f_{2x}) is negative (resp. positive) so that the cylinders are repelled from each other. The magnitude of this repelling force decreases monotonically with ε, and increases with the radius ratio r. When the cylinders are near contact, the force f_{ix} becomes singular and diverges to infinity. When the cylinders are far apart the fluid force on $\mathcal{C}_i$ vanishes, a result known as the d'Alembert's paradox. In Fig. 4 the results by Bampalas and Graham (2008) and Landweber and Shahshahan (1991) are presented for comparison. In Bampalas and Graham (2008) the force is computed using a Möbius conformal mapping and a series of image singularities. Here again, we find an excellent agreement with those authors thereby validating our expression (18) for $\mathbf{f}_{iq}$.

4.2.2. Sinusoidal vibrations

Thus far, we have successfully compared the results of our model to those found in the literature. We now proceed with extending those results to the case in which $\mathcal{C}_1$ is stationary while $\mathcal{C}_2$ is imposed a sinusoidal vibration with amplitude U_0 and angular frequency Ω. We choose $V_0 = \Omega R_2$ as the characteristic speed so that the dimensionless displacement writes $\mathbf{u}(t) = u_0 \sin(t)\,\mathbf{u}_0$, with $\mathbf{u}_0 = \cos(\gamma)\,\mathbf{e}_{x_0} + \cos(\gamma)\,\mathbf{e}_{y_0}$. Here $\gamma = (\mathbf{e}_{x_0}, \mathbf{u}_0)$ is the angle made by the line joining the centers in the initial configuration and the direction of vibration. The initial separation distance is $\varepsilon_0 = 1$ and three vibration amplitudes are considered, $u_0 = \{0.1, 0.5, 0.9\}$. The time evolution of the fluid force is shown in Figs. 5 and 6 for $\gamma = 0$ and $\gamma = \pi/4$, respectively. Note that for $\gamma = 0$ the problem is symmetric about the x-axis, such that $f_{iy} = 0$ and we only show the evolution of f_{ix}. For $\gamma = \pi/4$ the fluid force is represented through its components (f_{ix_0}, f_{iy_0}) in the initial basis $(\mathbf{e}_{x_0}, \mathbf{e}_{y_0})$.

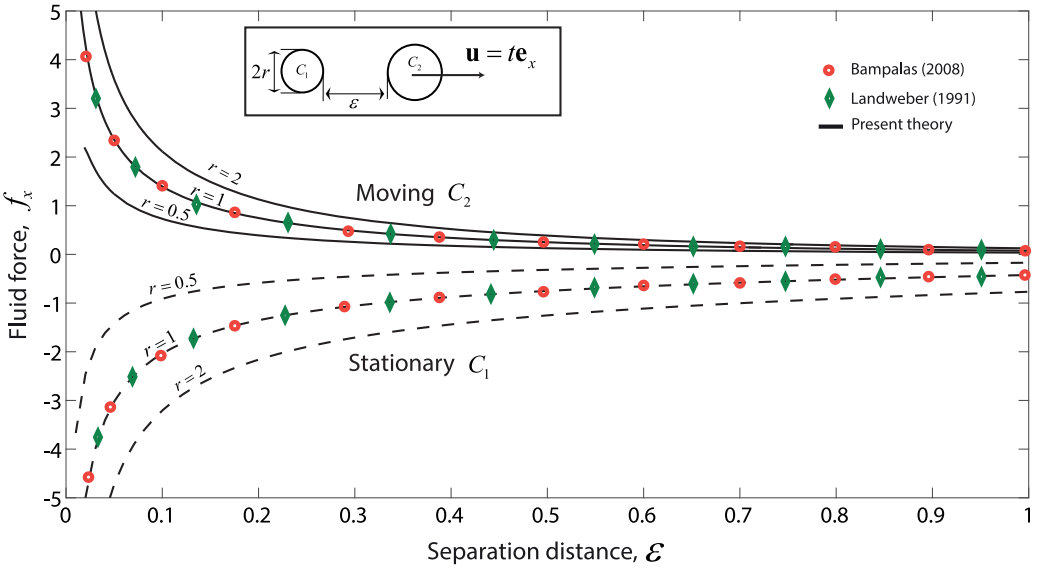

Fig. 4. Fluid force, computed from Eq. (16), as a function of the separation distance ε and the radius ratio r. The cylinder $\mathcal{C}_1$ is stationary. The cylinder $\mathcal{C}_2$ translates along the line joining the centers with a constant speed.

For both cases ($\gamma = 0$, $\gamma = \pi/4$) we find that f_{1x} and u_{2x} have opposite signs, see Figs. 5(a) and 6(a). Thus, the fluid always pushes the stationary cylinder in an axial direction that is in phase opposition with the vibration displacement. On the contrary, f_{1y} and u_{2y} have the same sign, see Fig. 6(b), such that the fluid pushes the stationary cylinder in a transverse direction that is in phase with the imposed displacement. We also observe that $\mathbf{f}_1$ has a high harmonic distortion due to the non-negligible effect of the quadratic term $\mathbf{f}_{1q}$, see Fig. 5(b). It follows that the force on the stationary cylinder is due both to the time and spatial variations of the fluid potential.

The force $\mathbf{f}_2$ on the moving cylinder has the same direction as the imposed displacement, see Figs. 5(c) and 6(c–d). The quadratic term $\mathbf{f}_{2q}$ remains negligible, see Fig. 5(d), such that $\mathbf{f}_2$ has a low harmonic distortion and approximates to $\mathbf{f}_2 = -\pi m_{11}\ddot{\mathbf{u}}_2$. Thus, the force on the moving cylinder is mainly due to the time variations of the fluid potential. Finally, we note that the magnitude $|\mathbf{f}_i|$ is maximum as the distance between the cylinders is minimum, and it increases with the radius ratio. This is of course related to a confinement effect which induces an increase of the added mass terms $|m_{11}|$ and $|m_{12}|$, as already pointed out in Section 4.1.

The online movies ($r = 0.5$, $u0 = 0.9$) show the fluid pressure distribution and its time evolution as the cylinder vibrates. As expected, a positive (resp. negative) pressure appears in the wake of the moving cylinder as it decelerates (resp. accelerates).

5. Conclusion

We have considered the problem of two moving circular cylinders immersed in an inviscid fluid. A potential theory based on a bipolar coordinate system shows that the fluid force on the cylinders is the superposition of an added mass term and a quadratic term. The added mass term comes from the time variations of the fluid potential while the quadratic term is related to its spatial variations. We provide new simple and exact analytical expressions for the fluid added mass coefficients, in which the effect of the confinement is made explicit. The self-added mass m_{11} (resp. cross-added mass m_{12}) decreases (resp. increases) with the separation distance and increases (resp. decreases) with the radius ratio. When the separation distance tends to zero, the confinement is maximum and the added mass coefficients m_{11} and m_{12} diverge to infinity. When the two cylinders are far apart, the added mass coefficients are those of a single cylinder in a fluid of infinite extent, $m_{11} \to 1$ and $m_{12} \to 0$. We then consider the case in which one cylinder is stationary while the other is translating along the line of centers with a constant speed. Our results indicate that the fluid forces are repulsive, diverge to infinity when the cylinders are in contact, and decrease to zero as they separate. These observations are in excellent agreement with published results. Finally, we consider the case in which one cylinder is fixed while the other is imposed a sinusoidal vibration. We show that the force on the stationary cylinder and the vibration displacement have opposite axial directions but identical transverse directions. This force is strongly altered by the nonlinear effects due to the spatial variations of the fluid potential. On the other hand, the force on the vibrating cylinder is mainly due to the time variations of the potential.

Acknowledgment

The authors would like to thank Prof. C. Eloy for his valuable comments and suggestions to improve the manuscript.

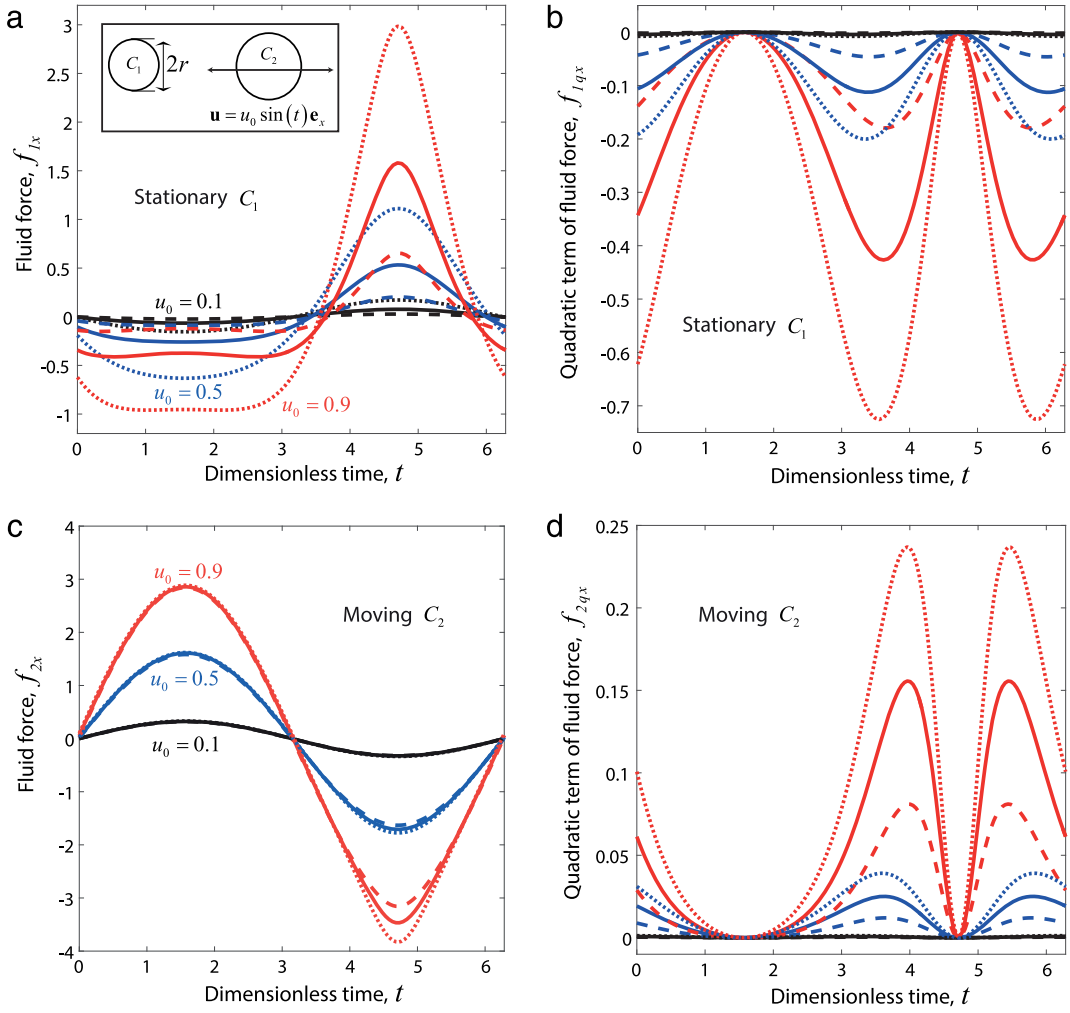

Fig. 5. Fluid force, computed from Eq. (16), as a function of the dimensionless time t. The cylinder $\mathcal{C}_1$ is stationary. The cylinder $\mathcal{C}_2$ vibrates along the line joining the centers with a dimensionless amplitude u_0. The radius ratios are: $r = 0.5$ (dashed lines), $r = 1$ (solid lines), $r = 2$ (dotted lines). The dimensionless vibration amplitudes are $u_0 = 0.1$ (black color), $u_0 = 0.5$ (blue color) and $u_0 = 0.9$ (red color). The initial separation distance is $\varepsilon_0 = 1$. The temporal and spatial evolutions of the fluid pressure and velocity fields for $r = 0.5$ and $u_0 = 0.9$ can be observed in the corresponding movies. (For interpretation of the references to color in this figure legend, the reader is referred to the web version of this article.)

Appendix A. Relations between coordinates

The relations between the cartesian coordinates (x_0, y_0) (initial configuration), (x, y) (instantaneous configuration) and the bipolar coordinates (σ, τ) are, see Fig. A.1

$$\begin{pmatrix} x_0 \\ y_0 \end{pmatrix} = \frac{1}{2}\begin{pmatrix} u_{1x_0} + u_{2x_0} \\ u_{1y_0} + u_{2y_0} \end{pmatrix} + \mathbf{P}\begin{pmatrix} x \\ y \end{pmatrix}, \tag{A.1}$$

$$\begin{pmatrix} x \\ y \end{pmatrix} = \begin{pmatrix} x_B + a\sinh(\tau)/(\cosh(\tau) - \cos(\sigma)) \\ a\sin(\sigma)/(\cosh(\tau) - \cos(\sigma)) \end{pmatrix} = \mathbf{g}(\sigma, \tau), \tag{A.2}$$

$$\begin{pmatrix} \sigma \\ \tau \end{pmatrix} = \begin{pmatrix} \pi - 2\tan^{-1}\left(\dfrac{2ay}{a^2 - (x - x_B)^2 - y^2 + \sqrt{\left(a^2 - (x - x_B)^2 - y^2\right)^2 + 4a^2y^2}}\right) \\ \dfrac{1}{2}\ln\left(\dfrac{(x - x_B + a)^2 + y^2}{(x - x_B - a)^2 + y^2}\right) \end{pmatrix}, \tag{A.3}$$

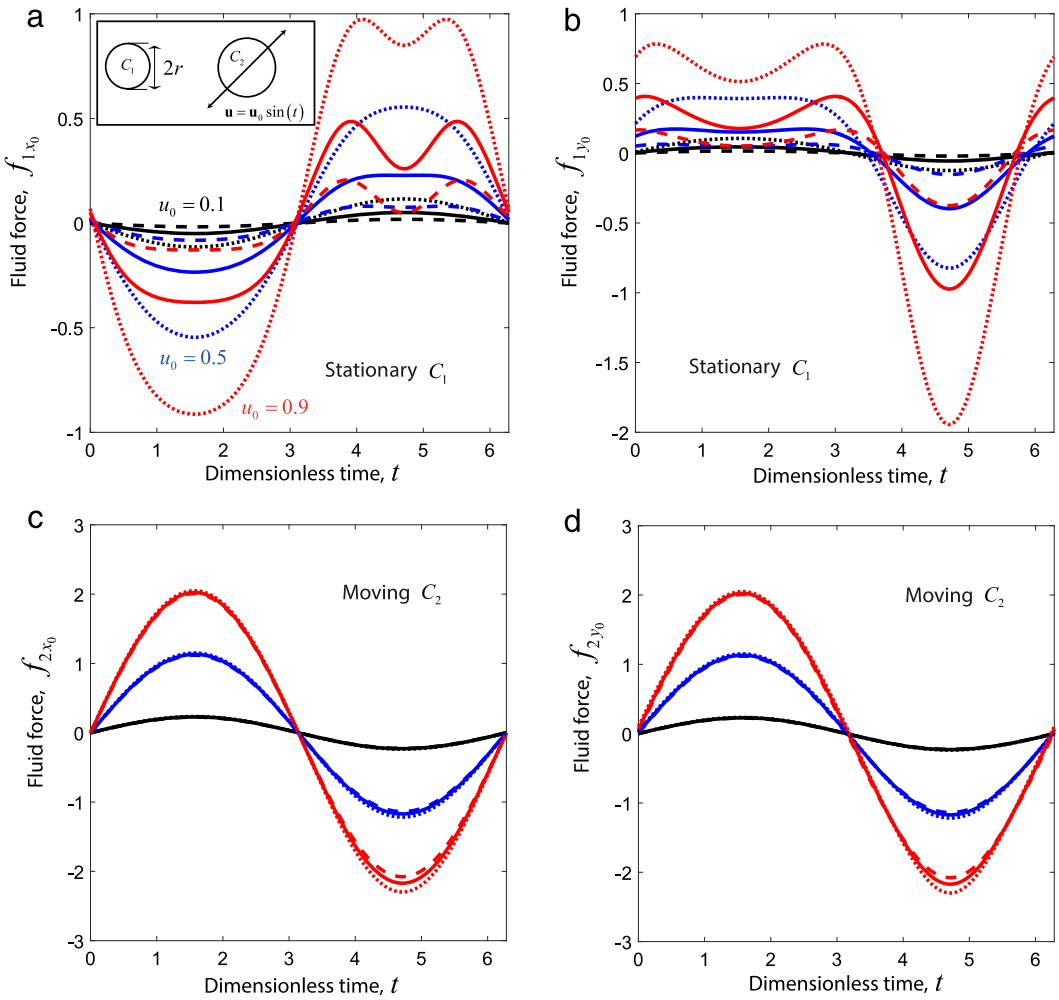

Fig. 6. Fluid force, computed from Eq. (16), as a function of the dimensionless time t. The cylinder $\mathcal{C}_1$ is stationary. The cylinder $\mathcal{C}_2$ vibrates along the direction $(\mathbf{e}_{x_0}, \mathbf{u}_0) = \pi/4$ with a dimensionless amplitude u_0. Same legend as Fig. 5.

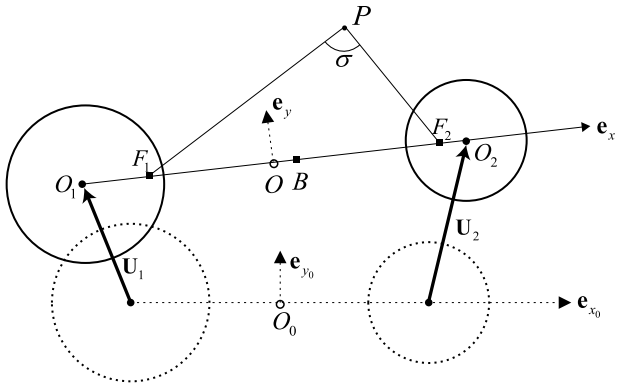

Fig. A.1. Coordinate systems used for the two cylinders problem. The dashed lines represent the initial configuration whose frame of reference is $(O_o, \mathbf{e}_{x_0}, \mathbf{e}_{y_0})$. In this frame a fluid particle P has cartesian coordinates (x_0, y_0). The solid lines represent the instantaneous configuration whose frame of reference is $(O, \mathbf{e}_x, \mathbf{e}_y)$. In this frame a fluid particle P has cartesian coordinates (x, y) and bipolar coordinates (σ, τ).

with

$$\mathbf{P} = \frac{1}{\sqrt{\left(d_0 + u_{2x_0} - u_{1x_0}\right)^2 + \left(u_{2y_0} - u_{1y_0}\right)^2}} \begin{pmatrix} d_0 + u_{2x_0} - u_{1x_0} & -\left(u_{2y_0} - u_{1y_0}\right) \\ u_{2y_0} - u_{1y_0} & d_0 + u_{2x_0} - u_{1x_0} \end{pmatrix}, \tag{A.4}$$

the passage matrix from the basis $\left(\mathbf{e}_{x_0}, \mathbf{e}_{y_0}\right)$ to $\left(\mathbf{e}_x, \mathbf{e}_y\right)$.

From (A.2) it follows that

$$y^2 + \left[x - \left(x_B + a\coth\left(\tau\right)\right)\right]^2 = \left(a/\sinh\left(\tau\right)\right)^2, \tag{A.5}$$

so that iso-τ contours are circles of radius $a/\sinh\left(\tau\right)$ and center at $x = x_B + a\coth\left(\tau\right)$. To align $\partial\mathcal{C}_i$ with an iso-contour τ_i we thus require

$$x_B + a\coth\left(\tau_1\right) = -d/2, \tag{A.6a}$$
$$a/\sinh\left(\tau_1\right) = -r, \tag{A.6b}$$
$$x_B + a\coth\left(\tau_2\right) = d/2, \tag{A.6c}$$
$$a/\sinh\left(\tau_2\right) = 1, \tag{A.6d}$$

which yields the solution (7) for x_B, a and τ_i.

The bipolar unit vectors $\mathbf{e}_\sigma$ and $\mathbf{e}_\tau$ shown in Fig. 2 are expressed in the basis $\left(\mathbf{e}_x, \mathbf{e}_y\right)$ as

$$\mathbf{e}_\sigma = \frac{1}{|\partial\,\mathbf{g}/\partial\sigma|}\frac{\partial\,\mathbf{g}}{\partial\sigma} = \frac{1}{\cosh\left(\tau\right) - \cos\left(\sigma\right)} \begin{pmatrix} -\sin\left(\sigma\right)\sinh\left(\tau\right) \\ \cos\left(\sigma\right)\cosh\left(\tau\right) - 1 \end{pmatrix}, \tag{A.7a}$$

$$\mathbf{e}_\tau = \frac{1}{|\partial\,\mathbf{g}/\partial\sigma|}\frac{\partial\,\mathbf{g}}{\partial\tau} = \frac{1}{\cosh\left(\tau\right) - \cos\left(\sigma\right)} \begin{pmatrix} 1 - \cos\left(\sigma\right)\cosh\left(\tau\right) \\ -\sin\left(\sigma\right)\sinh\left(\tau\right) \end{pmatrix}. \tag{A.7b}$$

Appendix B. Determination of the fluid potential

B.0.3. Determination of φ_x

The functions φ_x and φ_y are determined with a separation of variables method with a 2π periodic function of σ, Alassar and El-Gebeily (2009).

For $\dot{u}_{iy} = 0$, the fluid Eqs. (11a) and (11c) are automatically satisfied by the potential function

$$\begin{aligned}\varphi_x = {} & \dot{u}_{1x}\sum_{n=1}^{\infty}\varphi_{1xn}\left[\cos\left(n\sigma\right)\cosh\left(n\left(\tau - \tau_2\right)\right) - \cosh\left(n\tau_2\right)\right] \\ & + \dot{u}_{2x}\sum_{n=1}^{\infty}\varphi_{2xn}\left[\cos\left(n\sigma\right)\cosh\left(n\left(\tau - \tau_1\right)\right) - \cosh\left(n\tau_1\right)\right].\end{aligned} \tag{B.1}$$

The first terms in the brackets are harmonic, 2π periodic in σ and yield a zero fluid velocity at one of the cylinder boundary. The second constant terms are added to ensure that φ_x vanishes at infinity, i.e. as $(\sigma, \tau) \to (0, 0)$.

The boundary condition (11b) yields two equations for φ_{ixn}

$$\sum_{n=1}^{\infty}\varphi_{1xn} n\cos\left(n\sigma\right)\sinh\left(n\left(\tau_1 - \tau_2\right)\right) = g_{1x}, \tag{B.2a}$$
$$\sum_{n=1}^{\infty}\varphi_{2xn} n\cos\left(n\sigma\right)\sinh\left(n\left(\tau_2 - \tau_1\right)\right) = g_{2x}, \tag{B.2b}$$

whose solutions are obtained by taking the scalar product

$$\left\langle f, h\right\rangle = \frac{1}{\pi}\int_0^{2\pi} f\left(\sigma\right) h\left(\sigma\right) d\sigma, \tag{B.3}$$

of both sides by $\cos\left(n\sigma\right)$, leading to

$$\varphi_{1xn} = \frac{\left\langle\cos\left(n\sigma\right), g_{1x}\left(\sigma\right)\right\rangle}{n\sinh\left(n\left(\tau_1 - \tau_2\right)\right)} = \frac{-2nae^{n\tau_1}}{n\sinh\left(n\left(\tau_1 - \tau_2\right)\right)} = \varphi_{1n}, \tag{B.4a}$$
$$\varphi_{2xn} = \frac{\left\langle\cos\left(n\sigma\right), g_{2x}\left(\sigma\right)\right\rangle}{n\sinh\left(n\left(\tau_2 - \tau_1\right)\right)} = \frac{-2nae^{-n\tau_2}}{n\sinh\left(n\left(\tau_2 - \tau_1\right)\right)} = \varphi_{2n}. \tag{B.4b}$$

B.0.4. Determination of φ_y

For $\dot{u}_{ix} = 0$, the fluid Eqs. (11a) and (11c) are automatically satisfied by the potential function

$$\varphi_y = \dot{u}_{1y} \sum_{n=1}^{\infty} \varphi_{1yn} \sin(n\sigma) \cosh(n(\tau - \tau_2)) + \dot{u}_{2y} \sum_{n=1}^{\infty} \varphi_{2yn} \sin(n\sigma) \cosh(n(\tau - \tau_1)). \tag{B.5}$$

The boundary condition (11b) yields two equations for φ_{iyn}

$$\sum_{n=1}^{\infty} \varphi_{1yn} n \sin(n\sigma) \sinh(n(\tau_1 - \tau_2)) = g_{1y}, \tag{B.6a}$$

$$\sum_{n=1}^{\infty} \varphi_{2yn} n \sin(n\sigma) \sinh(n(\tau_2 - \tau_1)) = g_{2y}, \tag{B.6b}$$

whose solution are obtained by taking the dot product of both sides by $\sin(n\sigma)$

$$\varphi_{1yn} = \frac{\langle \sin(n\sigma), g_{1y}(\sigma) \rangle}{n \sinh(n(\tau_1 - \tau_2))} = \frac{2nae^{n\tau_1}}{n \sinh(n(\tau_1 - \tau_2))} = -\varphi_{1n}, \tag{B.7a}$$

$$\varphi_{2yn} = \frac{\langle \sin(n\sigma), g_{2y}(\sigma) \rangle}{n \sinh(n(\tau_2 - \tau_1))} = \frac{-2nae^{-n\tau_2}}{n \sinh(n(\tau_2 - \tau_1))} = \varphi_{2n}. \tag{B.7b}$$

Appendix C. Strategy for coding

In this Appendix, we give the relevant equations and a strategy for coding the fluid force (16) on the cylinders

$$\begin{pmatrix} f_{1x_0} \\ f_{1y_0} \\ f_{2x_0} \\ f_{2y_0} \end{pmatrix} = -\pi [C_a] \begin{pmatrix} \ddot{u}_{1x_0} \\ \ddot{u}_{1y_0} \\ \ddot{u}_{2x_0} \\ \ddot{u}_{2y_0} \end{pmatrix} + \begin{pmatrix} f_{1qx_0} \\ f_{1qy_0} \\ f_{2qx_0} \\ f_{2qy_0} \end{pmatrix}. \tag{C.1}$$

The very first step is to define the initial configuration by setting some values to the radius ratio r and the center-to center distance d_0. Note that d_0 must be greater than $r + 1$ to avoid contact between the cylinders. Then, the cylinders are imposed a particular kinematics by setting some values to the x_0 and y_0 components of the displacement vectors. For example, in the case of Section 4.2.2, the cylinder $\mathcal{C}_1$ is stationary, i.e. $u_{1x_0} = u_{1y_0} = 0$, while $\mathcal{C}_2$ is imposed a sinusoidal vibration, i.e. $u_{2x_0} = \sin(t)$, $u_{2y_0} = 0$, with t a free parameter. The velocity and the acceleration of the cylinders follow from the derivatives of u_{ix_0} and u_{iy_0}. From the initial configuration and the kinematics of the cylinders, we compute the instantaneous center-to-center distance d

$$d = \sqrt{(d_0 + u_{2x_0} - u_{1x_0})^2 + (u_{2y_0} - u_{1y_0})^2}, \tag{C.2}$$

and the position a of the foci points of the bipolar coordinate system

$$a = \sqrt{d^2 - (1+r)^2} \sqrt{d^2 - (1-r)^2} / (2d). \tag{C.3}$$

Having determined a, the instantaneous bipolar coordinates of the cylinders are given by (7c)

$$\tau_1 = -\sinh^{-1}(a/r) \quad \text{and} \quad \tau_2 = \sinh^{-1}(a). \tag{C.4}$$

The coefficients m_{11} and m_{12} of the added mass matrix $[C_a]$ follow from the analytical expressions (17)

$$m_{11} = \sum_{n=1}^{\infty} \frac{4na^2 e^{-2n\tau_2}}{\tanh[n(\tau_2 - \tau_1)]}, \tag{C.5a}$$

$$m_{12} = \sum_{n=1}^{\infty} \frac{-4na^2 e^{-n(\tau_2 - \tau_1)}}{\sinh[n(\tau_2 - \tau_1)]}. \tag{C.5b}$$

At this point, the added-mass term of the fluid force is determined and we are left with the computation of the quadratic term $\mathbf{f}_{iq}$. This term is given by (18) and its components are

$$f_{iqx} = (-1)^{i-1} a \int_0^{2\pi} p_q \frac{1 - \cos(\sigma)\cosh(\tau_i)}{[\cosh(\tau_i) - \cos(\sigma)]^2} d\sigma, \quad i = 1, 2, \tag{C.6a}$$

$$f_{iqy} = (-1)^{i-1} a \int_0^{2\pi} p_q \frac{-\sin(\sigma)\sinh(\tau_i)}{[\cosh(\tau_i) - \cos(\sigma)]^2} d\sigma, \quad i = 1, 2, \tag{C.6b}$$

with, see (15)

$$p_q = -\frac{1}{2}[A]\begin{pmatrix} \dot{u}_{1x} + \dot{u}_{2x} \\ \dot{u}_{1y} + \dot{u}_{2x} \end{pmatrix} + \frac{1}{2}[A]^T[A], \tag{C.7}$$

$$[A] = \begin{pmatrix} \dot{u}_{1x} & \dot{u}_{1y} \end{pmatrix} \begin{pmatrix} \frac{\partial h_{1x}}{\partial x} & \frac{\partial h_{1x}}{\partial y} \\ \frac{\partial h_{1y}}{\partial x} & \frac{\partial h_{1y}}{\partial y} \end{pmatrix} + \begin{pmatrix} \dot{u}_{2x} & \dot{u}_{2y} \end{pmatrix} \begin{pmatrix} \frac{\partial h_{2x}}{\partial x} & \frac{\partial h_{2x}}{\partial y} \\ \frac{\partial h_{2y}}{\partial x} & \frac{\partial h_{2y}}{\partial y} \end{pmatrix}, \tag{C.8}$$

and, see (13)

$$\mathbf{h}_1 = \sum_{n=1}^{\infty} \varphi_{1n} [\cos(n\sigma)\cosh(n(\tau - \tau_2)) - \cosh(n\tau_2)]\mathbf{e}_x + \sum_{n=1}^{\infty} (-\varphi_{1n}) \sin(n\sigma)\cosh(n(\tau - \tau_2))\mathbf{e}_y, \tag{C.9a}$$

$$\mathbf{h}_2 = \sum_{n=1}^{\infty} \varphi_{2n} [\cos(n\sigma)\cosh(n(\tau - \tau_1)) - \cosh(n\tau_1)]\mathbf{e}_x + \sum_{n=1}^{\infty} \varphi_{2n} \sin(n\sigma)\cosh(n(\tau - \tau_1))\mathbf{e}_y. \tag{C.9b}$$

A chain rule between the bipolar coordinates (σ, τ) and the cartesian coordinates (x, y), see (A.3), is used to compute the partial derivatives in $[A]$. By plugging (C.7) into (C.6), the integrals f_{iqx} and f_{iqy} are computed numerically and the components f_{iqx_0} and f_{iqy_0} are obtained from the relation

$$\begin{pmatrix} f_{iqx_0} \\ f_{iqy_0} \end{pmatrix} = \mathbf{P} \begin{pmatrix} f_{iqx} \\ f_{iqy} \end{pmatrix}, \tag{C.10}$$

with $\mathbf{P}$ the passage matrix given by (A.4).

Finally, the sum of the added mass and quadratic terms yields the fluid force on the cylinders.

Appendix D. Supplementary data

Supplementary material related to this article can be found online at https://doi.org/10.1016/j.jfluidstructs.2017.12.002.

References

Alassar, R.S., El-Gebeily, M.A., 2009. Inviscid flow past two cylinders. ASME Trans. J. Fluid Eng. 131, 054501.

Bampalas, N., Graham, J.M.R., 2008. Flow-induced forces arising during the impact of two circular cylinders. J. Fluid Mech. 616, 205–234.

Basset, A.B., 1888. A Treatise on Hydrodynamics. Deighton, Bell and Co.

Birkhoff, G., 1960. Hydrodynamics, second ed. Princeton University Press, Princeton, New Jersey.

Burton, D.A., Gratus, J., Tucker, R.W., 2004. Hydrodynamic forces on two moving discs. Theoret. Appl. Mech. 31, 153–188.

Carpenter, L.H., 1958. On the motion of two cylinders in an ideal fluid. J. Res. Nat. Bur. Stand. 61, 83–87.

Chen, S.S., 1975. Vibration of nuclear fuel bundles. Nucl. Eng. Des. 35, 399–422.

Chen, S.S., 1977. Dynamics of heat exchanger tube banks. J. Fluid. Eng. 99, 462–469.

Chen, S.S., 1978. Crossflow-induced vibrations of heat exchanger tube banks. Nucl. Eng. Des. 47, 67–86.

Chen, S.S., 1987. Flow-induced Vibration of Circular Cylindrical Structures. Hemisphere Publishing.

Crowdy, D.G., 2006. Analytical solutions for uniform potential flow past multiple cylinders. Eur. J. Mech. B Fluids 25, 459–470.

Crowdy, D.G., 2010. A new calculus for two-dimensional vortex dynamics. Theor. Comput. Fluid Dyn. 24, 9.

Dalton, C., Helfinstine, R.A., 1971. Potential flow past a group of circular cylinders. Trans. ASME J. Basic Eng. 93, 636–642.

De Langre, E., 2008. Effects of wind on plants. Annu. Rev. Fluid Mech. 40, 141–168.

Doare, O., Michelin, S., 2011. Piezoelectric coupling in energy-harvesting fluttering flexible plates: Linear stability analysis and conversion efficiency. J. Fluids Struct. 27, 1357–1375.

Eloy, C., Lagrange, R., Souilliez, C., Schouveiler, L., 2008. Aeroelastic instability of cantilevered flexible plates in uniform flow. J. Fluid Mech. 611, 97–106.

Furber, S.B., Ffowcswilliams, J.E., 1979. Is the Weis-Fogh principle exploitable in turbomachinery? J. Fluid Mech. 94, 519–540.
Gibert, R.J., Sagner, M., 1980. Vibration of structures in a static fluid medium. La Houille Blanche 1/2, 204–262.
Greenhill, A.G., 1882. Functional images in cartesians. Quaterly J. Pure Appl. Math. 18, 231.
Herman, R.A., 1887. On the motion of two spheres in fluid and allied problem. Quaterly J. Pure Appl. Math. 22, 204–262.
Hicks, W.M., 1879. On the motion of two cylinders in a fluid. Quaterly J. Pure Appl. Math. 16, 113–140, 193–219.
Lamb, H., 1945. Hydrodynamics, sixth ed. Dover, New York.
Landweber, L., Shahshahan, A., 1991. Added masses and forces on two bodies approaching central impact in an inviscid fluid. In: Technical Rep. 346. Iowa Institute of Hydraulic Research.
Le Cunff, C., Biolley, F., Fontaine, E., Etienne, S., Facchinetti, M.L., 2002. Vortex-induced vibrations of risers: Theoretical, numerical and experimental investigation. Oil Gas Sci. Technol. 57, 59–69.
Mazur, V.Y., 1970. Motion of two circular cylinders in an ideal fluid. Izvestiya Akademii Nauk SSSR, Mekhanika Zhidkosti I Gaza 6, 80–84.
Michelin, S., Doare, O., 2013. Energy harvesting efficiency of piezoelectric flags in axial flows. J. Fluid Mech. 714, 489–504.
Morison, J.R., O Brien, M.P., Johnson, J.W., Schaaf, S.A., 1950. The force exerted by surface waves on piles. Petroleum Trans. Am. Inst. Min. Eng. 189, 149–154.
Nair, S., Kanso, E., 2007. Hydrodynamically coupled rigid bodies. J. Fluid Mech. 592, 393–411.
Païdoussis, M.P., Mavriplis, D., Price, S.J., 1984. A potential-flow theory for the dynamics of cylinder arrays in cross-flow. J. Fluid Mech. 146, 227–252.
Païdoussis, M.P., Price, S.J., De Langre, E., 2014. Fluid-Structure Interactions: Cross-Flow-Induced Instabilities. Cambridge University Press.
Scolan, Y.M., Etienne, S., 2008. On the use of conformal mapping for the computation of hydrodynamic forces acting on bodies of arbitrary shape in viscous flow. Part 2: multi-body configuration. J. Eng. Math. 61, 17–34.
Singh, K., Michelin, S., De Langre, E., 2012. Energy harvesting from axial fluid-elastic instabilities of a cylinder. J. Fluids Struct. 30, 159–172.
Suss, S., 1977. Stability of a Cluster of Flexible Cylinders in Bounded Axial Flow, Ph.D. Thesis. McGill.
Tchieu, A.A., Crowdy, D., Leonard, A., 2010. Fluid-structure interaction of two bodies in an inviscid fluid. Phys. Fluids 22, 107101.
Virot, E., Amandolese, X., Hemon, P., 2016. Coupling between a flag and a spring-mass oscillator. J. Fluids Struct. 65, 447–454.
Wang, Q.X., 2004. Interaction of two circular cylinders in inviscid fluid. Phys. Fluids 16, 4412.